# Micro Free-Flow Isoelectric Focusing

by

Jacob William Albrecht
B.S. Chemical Engineering, University of Nebraska - Lincoln (2001)
M.S. Chemical Engineering Practice, Massachusetts Institute of Technology (2004)

Submitted to the Department of Chemical Engineering
in partial fulfillment of the requirements for the degree of
Doctor of Philosophy in Chemical Engineering
at the
MASSACHUSETTS INSTITUTE OF TECHNOLOGY
January 2008
[February 2008]



Author.....
Department of Chemical Engineering
January 10, 2008

Certified by.....
Klavs F. Jensen
Warren K. Lewis Professor of Chemical Engineering
Professor of Materials Science and Engineering
Thesis Supervisor

Accepted by.....
William M. Deen
Carbon P. Dubbs Professor of Chemical Engineering
Chairman, Committee for Graduate Students

# Micro Free-Flow Isoelectric Focusing

by
Jacob William Albrecht

Submitted to the Department of Chemical Engineering on January 10, 2008
in partial fulfillment of the requirements for the degree of
Doctor of Philosophy in Chemical Engineering

## Abstract

To unravel the complexity of cellular systems, protein prefractionation tools can be used to reduce cell lysate complexity and increase assay sensitivity. Rapid free flow isoelectric focusing (FF-IEF) is achieved in a microfluidic device by isolating the electrodes from the focusing region with porous buffer regions. Moving the electrodes enables the use of large electric fields without the detrimental effects of bubble formation in the focusing region of the device. The anode and cathode porous buffer regions, which are formed by acrylamide functionalized with immobilized pH groups, allow ion transport while providing buffering capacity. Thermo-electric cooling mitigates the effects of Joule heating on sample focusing at high field strengths (~500V/cm). This localized cooling was observed to increase device performance. Rapid focusing of low molecular weight isoelectric point markers proteins and protein complexes demonstrate the versatility of the technique. Simulations provide insight into and predict device performance based on a well-defined sample composition.

This thesis also presents the first implementation of cascaded stages for a microfabricated free-flow isoelectric focusing device. Both analytical and computational models for IEF suggest device performance will be improved by utilizing multiple stages to reduce device residence time. These predictions are shown to be valid by using focusing of small IEF markers as a demonstration. We also show focusing of fluorescently tagged proteins under different channel geometries, with the most efficient focusing occurring in the cascaded design, as predicted by theory. An additional aim of this work is to demonstrate the compatibility of cascaded FF-IEF with common bioanalytical tools. As an example, outlet fractions from cascaded FF-IEF were analyzed by SDS-PAGE. Processing of whole cell lysate followed by immunoblotting for cell signaling markers demonstrates the reduction of albumin from samples, as well as the enrichment of apoptotic markers.

Commercial FF-IEF equipment requires multiple inlets to approximate the linear pH gradient commonly used in IEF. These inlets require many premixed pH buffers and a dedicated pumping system, increasing system cost and complexity. As an alternative approach, a preparative scale FF-IEF microfluidic device is also designed and tested. The advantages of the divergent IEF design versus a rectangular design are demonstrated using pH indicators to visualize the formation of pH gradients within the devices. Theoretical and experimental observations indicate that using a divergent channel circumvents many of the difficulties associated with preparative FF-IEF equipment. Protein pI markers are used to demonstrate the devices ability to fractionate samples, even in the presence of salt levels too high for conventional IEF techniques. The devices process complex biological samples, fractionating whole cell lysate at a rate of 2mL/hr. The device performance is further analyzed by 2-D gels of the fractionated outlets to show that cell lysate can be enriched based on pI. These findings

underscore the promise of small, inexpensive, and disposable FF-IEF devices in proteomics and systems biology research.

**Thesis Supervisor: Klavs F. Jensen**
**Warren K. Lewis Professor of Chemical Engineering**
**Professor of Materials Science and Engineering**

# Acknowledgements

. I must first acknowledge my advisor Klavs F. Jensen for his unwavering support and advice. He has exceeded every expectation I could have for an academic "father" with his insight, dedication, and good humor. My committee, Bill Deen, Scott Manalis, and Forest White were the best I could ask for, providing direction before I knew I needed it, and offering suggestions when I was simply baffled. I also thank professors Peter Sorger, Michael Yaffe, and Hidde Ploegh: their enthusiasm and vision for cross-disciplinary research is the *foundation* of innovation.

In the trenches, I could not have completed this thesis without the direct support of John Tolsma (Numerica Technologies) for assistance with Jacobian; Hang Lu, Jamil El-Ali for his unique encoragement, Suzanne Gaudet, Jian Wen, Annemarthe Van der Veen, Renuka Sastry, Chris and Kerry Love, Gerry Ostheimer, Dan Pregibon, and Erik Wilker. I owe this thesis to their excellent collaborative work and practical suggestions. I am (figuratively) in debt to the National Institutes of Health (P50-GM68762) for funding and the gifted staff of the MIT MTL for microfabrication support.

I also thank Sabrina Spencer, Laura Sontag-Kleiman, Bree Aldrich, John Burke, Matt Lazzara, Brian Taff, and the rest of the CDP subgroup for their valuable assistance and conversation. These research collaborators and friends supported a work which has amused and exercised five years of my life, and which, however inadequate to my own wishes, I finally delivered to the curiosity and candor of the public.

The KFJ group has been an amazing place to work. I want to thank Andrea and Michiel for the espresso breaks, Jane, Brandon, Saif, Eddie, Nico, Jerry, Sam, Jon, Vicky, Kevin, Hemant, and Nick for their camaraderie, Ling, Mahmooda, Linlin, and Kishori for the spicy snacks and good times in 66-513, Alina for her conversation, patience, and help. Last but not least, Joan Chisholm for her conversation, patience, and help, plus chocolate!

I would like to thank the rest of the amazing support staff gluing the department together. Steve, Suzanne, Mary, Mary, Iris, Anne, Jen, Katie, Beth, and Gwen were especially remarkable for their outstanding performance.

My time at MIT would have been miserable if not for the social juggernaut that is the ChE grad student community: I owe Theis, Jane, KC Wood, Ben Wang, $G^3$ Beckham, EA, Bernezy, Mox,, RDB, Tmon, Shannan, Sunny, Brandon and Kenzie (+1) Blackwell, Sty, Joe, Erin, and Charlotte Lowry, Sharon, Cindy, Chris Tommaso, DD, Amy Lewis, Shuga, Jose, Huan, Micah, and the rest of cheme-2002 for making the most stressing times into the best times. The ChE guys and gals of all years maintain critical mass: Dr. Dre, Wally, Patches O'Pregibon, Rocko, Thurber, Sharms, Jie, Scott, Earl, Andy, Curt, Rob, cheme-meat, and founder Brad as well as Nate, Lino, Kevin, Jamie, Megan, et al. know what it's about. Also, "crafty" Kristin Mattern, Katharina, Andy and Michelle Miller, and Ben_Wang, for always entertaining lunch banter, G$, Joe C, Chop, Verp, Karlaj, John Lock, Fred, The Raj, and the rest of BPT for Tuesday zen.

I'd like to recognize "angry" Dave Q, Earl (again), Dave F, Craig, Mariah, Will, Val, Mike, Tiff, Sara, & Kelly, and the rest of the extraordinary eartenders; also Sara C for consistently exuding cool.

I thank my friends and fishing buddies from UNL: Dave, Sean, Andy, and Matt for the best cribbage games and canoe mishaps; and Jake O for reminding me to take it easy.

Finally, I would like to thank my family: Mom, Dad, Tris and Sarah, the Albrecht clan, and the Bops. Their encouragement and support throughout my life has meant everything to me.

# Table of Contents

# List of Figures

# List of Tables

# Chapter 1: Introduction

## *1.1. Background and Motivation*

### 1.1.1. Biochemical Understanding and Systems Biology

The problems currently faced by researchers in systems biology are due to the complex, coordinated regulation of hundreds of proteins and genes in signaling pathways. To unravel the complexity of signaling networks, status of the cell must be studied on the basis of its many interacting components. Nucleic acids (DNA and RNA) control which genes are available and expressed--fundamental to all cell processes, but work on a slower time scale than protein-protein events. Quantitative PCR and microarrays are now established technology to determine genomic and transcriptional status, but new high-throughput technologies for measuring protein status have yet to be accepted. Signaling proteins carry signals through complex covalent (phosphorylation, cleavage, etc.) and non-covalent (receptor-ligand, complex formation, translocation) interactions. Understanding the intracellular signaling network requires new tools and techniques to maximize research productivity.

### 1.1.2. Limitations of Proteomic Approaches

The growth of proteomics has been checked by the lack of fast, highly reproducible, high resolution analysis that is currently available for DNA sequencing. Compared to DNA, proteins are more complex, harder to separate, have highly variable physical properties, are more difficult to detect, and are less stable. The fact that many signaling proteins have low abundance (~1000 copies per cell [98]) further exacerbates efficient separation and detection.

Modern capillary separations of proteins are highly efficient, with many millions of theoretical plates [108]. But separations in a single dimension are best suited for purification of abundant molecules. Cellular proteins are expressed with a large range of concentrations, spanning 6 to 9 orders of magnitude [98]. To successfully identify low-abundance proteins, multiple separation steps must be used. Orthogonal separations offer a way to theoretically multiply [41, 44] the resolutions of different methods to achieve higher peak capacities. Integrating two or more batch or time-dependent columns requires a tradeoff between range and resolution. Parallel second-dimension separations reduce range while preserving the separation

resolution but at added expense and complexity [41]. Compared to slab-gel techniques, capillary separation methods better exploit the sensitivity achievable with mass spectrometers [109]. Samples separated by a 2-D gel must be identified, cut out, and digested in gel.[69] Another disadvantage of gel or large scale liquid IEF is the high levels of additives such as urea (up to 8M) [19, 110, 103] needed to promote protein solubility and prevent precipitation at the isoelectric point. Urea, ampholytes, detergents and other additives must be removed prior to subsequent separations and detection; especially MS [63, 127].

Phosphorylated proteins are used in many cell signaling processes such as antigen display [135] and androgen receptor activity. [45] Phosphate groups change the mass by roughly 80 Da [35], but the pI is shifted towards a lower pH (typically around 0.1-0.5 pH units [18, 23, 92]). Considering that a typical resolution in a modern capillary isoelectric focusing unit is approximately 0.01 pH units [110], phosphorylated proteins are easily resolved by isoelectric focusing.

### 1.1.3. Isolation of Organelles

Because the cell is compartmentalized into specialized organelles, analysis of a homogenized sample destroys information of their interaction. For example, it has been shown [62] that during type II apoptosis Cytochrome *c*, which is normally present in mitochondria, diffuses out into the cytoplasm. As fragile as proteins are, the cell's organelles are even more delicate. Fractionating the cell into its organelles requires careful lysis and manipulation of the sample. Conventional organelle separation has been achieved with centrifugation in a sucrose density gradient. These separations typically form fractions consisting of five main groups of cell homogenate: cytosol, very light membranes (lysosomes, peroxisome, light endosomes), light membranes (golgi, light mitochondria, heavy endosomes), heavy membranes (heavy mitochondria, rough endoplasmic reticulum), and nuclear/cytoskeletal material. However density gradient centrifugation has poor resolution and complete separation is practically impossible. [96] Newer methods of separating organelles include immunoisolation: using antibodies attached to a support (a solid surface or magnetic bead) to bind and hold an organelle. Another approach is to use flow cytometry on organelles tagged with a particular fluorescent dye or ligand.

### 1.1.4. Use of Microfabricated Devices

The success of the human genome project was due chiefly to the advent of massively parallel capillary electrophoresis (CE) units which could operate in a semi-automated fashion. Recent and continuing advances in DNA sequencing through CE will likely render slab gel electrophoresis obsolete [72]. Microfabrication offers ways of miniaturizing traditional fluidic systems to take advantage of the physics available on small length scales (e.g. laminar flow, low thermal resistance). The motivation of lab-on-a-chip device development has been to increase the speed and efficiency of common lab procedures through miniaturization.[34] Much work has been done since the mid-1970's to establish methods of fabricating channels, valves, pumps, and interconnects on a chip. [101] From there, separation and detection procedures were standardized and integrated on a chip. [3] Capillary electrophoresis with the now common T or double T-injector has been done on chip for over a decade, [48, 101] and is now able to achieve sub-millisecond separation times. [59] However, these devices are far from perfect. Typical disadvantages of microdevices include long prototyping times, detection difficulties, unwanted electroosmotic flow (EOF), and non-specific binding of molecules. Non-specific binding and EOF are due to the high surface-to-volume ratio found in microdevices, and must be addressed through surface modification. [101, 10] Device passivation has been, and will continue to be, one of the major issues in miniaturization. To date, separations on a chip have been detected with optical (fluorescent microscopy, non-fluorescent microscopy, UV absorbance, IR spectroscopy), electrical (conductivity [106], charge field effect [38] , impedance [5], and changes in potential [91]), and mass measurement through cantilever resonance [13, 12, 14], or by integration with mass spectrometry. [134]

## *1.2. Prior Work in Isoelectric Focusing*

### 1.2.1. Progress of Isoelectric Focusing

The phenomenon of isoelectric focusing (IEF) of protein mixtures has been observed for nearly 50 years [68]. For simple systems with linear pH gradients, the concentration profile of an arbitrary ampholyte was determined analytically for steady state [118], and later for the transient case [130]. A partial derivation and solution for an ideal ampholyte is in the next section. More recently, rigorous numerical simulations of 140 ampholyte molecules [89] has

been performed on PCs requiring computation times of over a week. On the macroscale, the earliest isoelectric focusing devices experienced difficulties arising from non-linear ph gradients, Joule heating, as well as long separation times. [19] The current state-of-the-art large scale IEF prefractionation equipment has worked around these issues but still require some external cooling and high-voltages.

Capillary isoelectric focusing (CIEF) has been an area of extensive research with several review papers covering recent progress [64, 31, 110]. All CIEF devices to date [110, 3, 11, 50] involve filling the entire capillary with sample and ampholyte prior to applying an electric field. Because of the large voltages applied electroosmotic flow (EOF) becomes a major factor in reducing resolution, and must be reduced by surface modification. [51]

Isoelectric focusing with free flow fractionation (IEF-FFF) was first theoretically proposed in 1983 by J.C. Giddings and colleagues [42] and in more general terms in 1984 by Janca and Chmelik [61] but wasn't realized until 1989. [22, 121] These large high voltage devices suffered from long separation times and lower separation efficiencies due to Joule heating and convective disturbances. As effective as IEF may be, its real utility lies in the fact that it separates molecules based on different criteria (ionizable sidechains instead of charge to mass ratio) than conventional electrophoresis. This key quality enables IEF to be used most effectively as part of a multi-dimensional separation process.

### 1.2.2. Subcellular Fractionation with Electrophoresis

Of the modern methods of organelle separation, free-flow electrophoresis (FFE) benefits most from the unique physics available on the microscale. The inherent gentleness of FFE makes it ideal for isolating delicate cellular debris [70]. FFE works by sorting organelles by their particular charge, and can be further modified by including a density gradient, called density gradient electrophoresis or using organelle specific antibodies. Zischka et al. [140] have used FFE to isolate *S. cerevisiae* mitochondria for subsequent analysis. Weber and Bocek have used continuous FFE to separate amyloglucosidase isoforms in IEF mode and rat liver organelles by isotachophoresis. [129] Mohr and Volkl [86, 126] have isolated mouse liver peroxisomes and later peroxisomal subpopulations by immune free flow electrophoresis (IFFE). The principle behind IFFE is that immunoglobulins, when bound to the surface of an organelle, drastically reduce its electrophoretic mobility, enabling separation.

However, nearly all FFE of organelles has been done with bench size (separation chamber size: 50 by 10 cm) commercially available devices. A simple FFE device fabricated in silicon by Raymond et al. [99] demonstrates the possibility of miniaturized devices. Recently on the microscale, it has been shown that mitochondria and peroxisome populations can be concentrated by isoelectric focusing. [78, 79]

### 1.2.3. IEF as a Prefractionation Technique

Because IEF preserves sample concentration while separating orthogonally to other separation techniques, it is ideally suited as a prefractionation technique. Several commercial devices exist to perform IEF. BioRad's Rotofor uses functionalized polyacrylamide membranes to define 20 chambers in a rotating cylinder to fractionate samples[4]. Preparative IEF with the Rotofor has also been used with orthogonal liquid phase separation and detection tools such as HPLC and MALDI-TOF [127] or MS/MS. [63] Invitrogen's ZOOM apparatus uses a cassette of IPG strips in a manner more convenient than traditional protocol for IPG strips. Another IEF prefractionation tool recently developed is "off-gel" [105, 85] electrophoresis, where liquid compartments are placed in contact with a common IPG strip. As voltage is applied to the strip, proteins in the liquid compartments enter the strip and migrate to their pI. Diffusion transports the isoelectric species out of the strip and into another compartment where it is collected at the end of a run. These batch IEF systems typically require three hours or more for focusing to complete.

In order to continuously focus samples, commercial free flow isoelectric focusing (FF-IEF) devices have been developed and marketed. The original "octopus" FF-IEF device developed by Weber and colleagues [129, 70] is now marketed and sold by Becton-Dickinson. This device uses over a dozen inlets to artificially establish a protein gradient and collects samples in 96 outlets.

### 1.2.4. Microfabricated FF-IEF Devices

With the aim of mitigating the disadvantages of large scale, commercial FF-IEF devices, researchers have begun to explore microfluidics as a platform for FF-IEF. Microfabricated FF-IEF (μFF-IEF) devices are attractive as simple, inexpensive, and disposable prefractionation devices that can either be integrated with separation techniques on chip, process hazardous or radio-labeled samples, or compliment existing orthogonal separation techniques, such as SDS-

PAGE or capillary electrophoresis. Of the earliest [81, 80, 16] studies of FF-IEF on a chip, the devices used a non-linear pH gradient tailored to the pI of the sample (BSA). On the microscale, power consumption, cooling efficiency, and separation times were all improved compared to larger devices. Problems with band broadening and shifting were attributed to parasitic electroosmotic flow and pH gradient breakdown. More recent micro FF-IEF devices have been shown to separate and concentrate fluorescent dyes [67], proteins [81, 133], protein complexes [1], and organelles [79]. Recent advances such as active cooling [1] and electrode isolation using polyacrylamide [67, 1, 66] have overcome the classic problems of Joule heating and bubbles from electrolysis.

## 1.3. Limitations of IEF

Despite the powerful separation and concentration abilities of IEF, it has several limitations. For isoelectric focusing, nonionic and zwitterionic surfactants are almost exclusively used. IEF can only tolerate dilute (if any) concentrations of ionic surfactant. Ionic surfactants (such as SDS) drastically alter the charge of proteins. The high levels of SDS used in SDS-PAGE irreversibly change electrophoretic behavior of the proteins in any sample. Large scale liquid-phase devices (such as IEF) and 2-D gels typically require buffers with a high content of urea and other compounds such as dithiothreitol as well as precipitation inhibitors [19, 110]. These components, along with the ampholyte solution, should be removed prior to a second dimension analysis [63]. In the case of detection by mass spectroscopy, the removal of the ampholytes is a requirement.

Practical challenges to micro-FF-IEF design and operation with a uniform electric field include removal or isolation of bubble-forming electrolysis products at the electrode interface, stable pH gradient formation, and Joule heating. To mitigate the effect of electrolysis in these microdevices, researchers have used non-gassing electrodes [81], diffusion potentials at the junction of two different solutions [16, 80, 116], or electrode isolation using either fabricated structures with high hydrodynamic resistance [133] or photopatterned polyacrylamide [66, 67, 1, 2]. To stabilize the pH gradient formation within the device, buffer sheath flow has been used [67, 81, 66]. Another challenge for micro-FF-IEF devices is the task of collecting liquid fractions of different pI ranges for subsequent processing by orthogonal techniques such as capillary

electrophoresis, SDS-PAGE, and immunoblotting (western blotting). This world-to-chip interface is a non-trivial challenge for microfluidics.

## 1.4. Present Molecular Biology Techniques

To better define the scope and goals of this thesis, it is useful to outline the techniques presently used to study intracellular processes. Individual cell measurement techniques, such as FACS and fluorescent microscopy have brought to light the microheterogeneity of cell cultures, and are making strides in determining the true kinetics of cell signaling. However, these techniques suffer from the limited number of simultaneous measurements and from the trade off between throughput and direct cell observation. Because of these limitations, population averaged measurements from fixed or lysed cells are useful to determine interactions between many proteins in cell signaling networks.

### 1.4.1. SDS-PAGE

Sodium docecylsulfate (SDS) is used as a laboratory detergent to make proteins soluble through strong interaction resulting in protein unfolding. As it binds, SDS imparts a negative charge roughly proportional to the molecular weight of the protein [40], while masking the protein's intrinsic charge. When used with polyacrylamide gel electrophoresis (PAGE), the migration of the protein within the gel matrix is used to separate proteins based on molecular weight, with smaller proteins migrating faster than large bulky proteins. SDS-PAGE typically uses a reducing agent such as 2-mercapotethanol or dithiothreitol to break disulfide bonds between protein chains.

### 1.4.2. Two-Dimensional Gel Electrophoresis

A powerful technique to separate proteins across multiple dimensions, two-dimensional (2-D) gel electrophoresis, is capable of resolving thousands of protein spots. [39] Figure 1-1 shows the steps involved in the running typical 2-D gel. Immobilized pH gradient (IPG) strips are commonly used for the first dimension, replacing tube gels formerly used in 2-D electrophoresis. These strips are pre-cast polyacrylamide with immobilized buffering groups to establish a pH gradient across the length of the strip. They are packaged and sold as freeze-dried strips for use with dedicated IEF power supplies. The strips are hydrated overnight typically in 8M urea, 2M thiourea, plus surfactant and reducing agent. The protein sample is added to a

reservoir in fluidic contact with the strip. Isoelectric focusing begins with equilibration of the sample with the strip at a low applied current (~50 μA/ strip). The voltage is usually increased in a linear or step-wise gradient to typically 3500V over the period of 2 hours and held overnight. The large variety of sample compositions and the caprice of biological systems ensure that no two focusing operations are alike; samples must be carefully monitored (using the dye bromophenol blue as an indicator of focusing) to achieve the best separation. Typical focusing times range from 6-16 hours, but shorter or longer times are not uncommon.

Once focusing is judged to be complete, the strip is washed to remove urea and introduce SDS. The strip is loaded onto a SDS-PAGE gel, and voltage is applied across the second dimension of the strip. The proteins migrate into the polyacrylamide matrix as in SDS-PAGE and are separated by molecular weight, typically in 1 to 2 hours. Once this second dimension is complete, the gel may be either imaged using any one of a variety of stains or transferred to a membrane for western blotting.

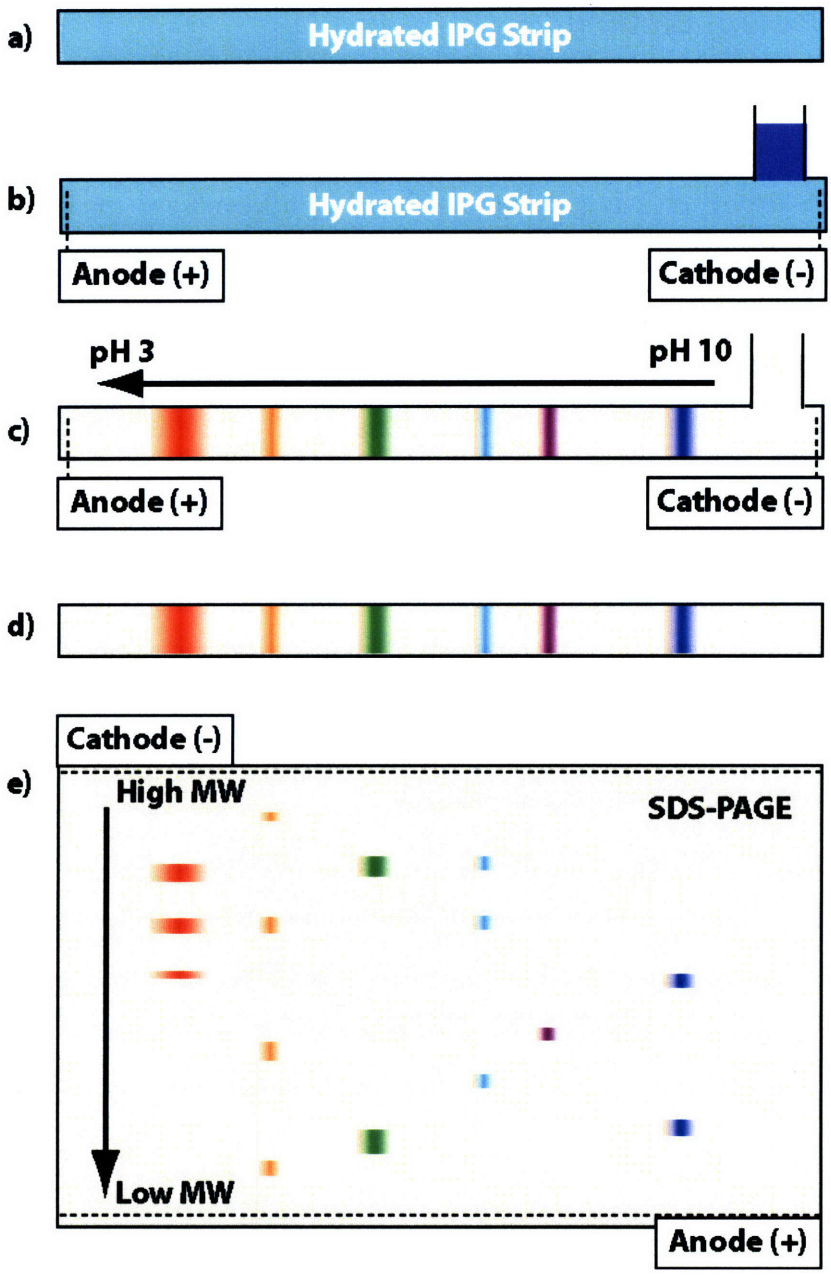


**Figure 1-1: Steps in 2-D gel electrophoresis. a) Dried polyacrylamide strips with an immobilized pH gradient are hydrated with sample or sample buffer. b) In the case of cup loading the sample, a liquid reservoir is attached to the cathodic end of the strip. c) An electric potential is applied, pulling protein through the strip until it reaches its isoelectric point. The blue dye added to the sample and hydration buffer leaves the strip, as an indicator of the focusing progress. d) The strip is washed and SDS is added to give all proteins a uniformly negative charge. e) The strip is loaded into a SDS-PAGE gel for a size based separation.**

### 1.4.3. Western Blotting

Western blotting, also known as immunoblotting is a technique to determine the presence of any protein target using an antibody specific for that target. To run a western blot, the proteins in a SDS-PAGE or 2-D gel are transferred to a membrane made of nitrocellulose or polyvinylidene fluoride (PVDF) by placing the membrane underneath the gel and applying a voltage across the of the gel-membrane stack. The transferred proteins are permanently bound to the membrane surface; when the membrane is immersed in a buffer with antibodies, specific binding can occur. This specific binding can be detected by probing with a secondary antibody that is bound to a fluorescent or chemiluminescent moiety. The signal from this moiety can be detected and quantified.

Population averaged assays such as western blotting relies upon antibody binding in order to detect the analyte of interest. This assumes i) that a validated antibody exists, and ii) it is specific for only that analyte or analyte isoform, assumptions that are not necessarily true.

### 1.4.4. Electromobility Shift Assay

Electromobility shift assays (EMSA) are used to determine the activity of transcription factors present in cell lysate. EMSA's are typically used with $P^{32}$-labeled or fluorescent [77, 93] DNA and polyacrylamide gels with a low cross-linker density. As a transcription factor binds to the DNA, and the loss of mobility can be measured. Efforts to enhance this technique involve using transcription factor-specific antibodies to further change mobility (super-shift assays) for target validation. [37]

### 1.4.5. Mass Spectroscopy

Mass spectroscopy has proven to be an invaluable tool for systems biology. Unlike other techniques, mass spectroscopy does not need a prior understanding or assumption of the underlying biological system to measure proteomic data. When coupled to HPLC, MS/MS is capable of subfemtomole detection limits. [83] A recent example of coupling separation and detection methods is the study of phosphorylation events in cell signaling cascades, critical to unraveling kinase activity in signaling networks. Ficarro et al. [35] have used immobilized metal-affinity chromatography (IMAC) columns coupled to MS/MS to study the phosphoproteome of *S. cerevisiae*. IMAC columns used in conjunction with phoshotyrosine

immunoprecipitation [137] have identified new targets in brain [58] and breast [71] cancer. However, IMAC and the MS ion detector itself have a bias for peptides with acidic residues, reducing the sensitivity for neutral and basic peptides.

## 1.5. Thesis Objectives

This thesis aims to demonstrate the viability of μFF-IEF as a prefractionation technique for systems biology. The specific objectives of this work are the following:

Overcome physical limitations of μFF-IEF

Develop practical fabrication procedures for μFF-IEF devices

Contribute to the underlying theory of μFF-IEF

Increase μFF-IEF throughput for general protein separation

Separate new types of analytes

Demonstrate compatibility of high throughput μFF-IEF with conventional tools

## 1.6. Thesis Framework

This thesis is organized into four sections: i) theory of IEF and FF-IEF, ii) the use of functionalized gels and active cooling to enable micro FF-IEF separations, iii) the use of cascaded stages to enhance separation resolution, and iv) scale up of μFF-IEF for large volume fractionation. The following chapter on theory will discuss the mechanisms of IEF in greater detail. This theory will be used in subsequent chapters to provide the motivation for microdevice design and experimental setup. The final goal, the fractionation of whole cell lysate followed by subsequent analysis is achieved using large, high throughput devices.

# Chapter 2: Theory and Simulation of IEF

## 2.1. Phenomena of Isoelectric Focusing

Isoelectric focusing was first described by Kolin [68] in 1955 and then mathematically by Svensson [118] in 1961. Isoelectric focusing of amphoteric molecules is the product of two major phenomena: electrophoretic forces, and the equilibrium of ionizable moieties such as carboxyl (R-COO-) and amino (R-NH3+) groups at a given pH. Amphoteric molecules (such as proteins) can carry a net charge that is a function of pH. Figure 2-1 illustrates how these two effects give rise to the phenomena of isoelectric focusing for an arbitrary protein. Qualitatively, IEF sweeps protein away from both electrodes concentrating it at its isoelectric point. Because proteins have a wide variety of compositions (and therefore pI's) a complex biological sample can be separated into isoelectric fractions without dilution.

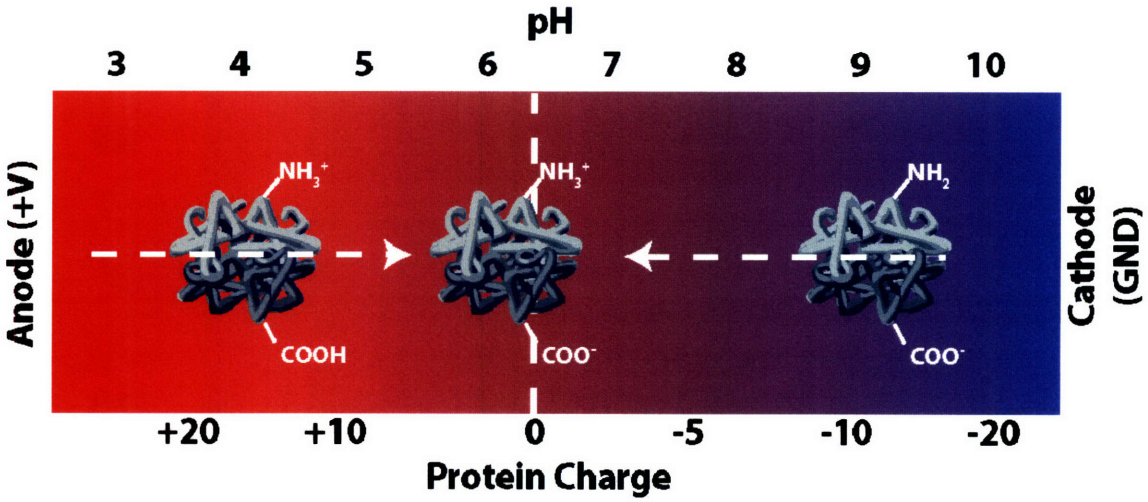


**Figure 2-1: Phenomena of Isoelectric Focusing. An arbitrary ampholyte is repulsed from both the anode and cathode, until it reaches a pH where has no net charge.**

## 2.2. Equations for IEF

The equations underlying isoelectric focusing begin with conservation equations using an expression for flux due to electrophoresis. Also required are equations for sample conductivity and local electric field. Rigorous mathematical models of isoelectric focusing [8, 9, 90, 87, 88, 107, 97, 89, 16] make three main assumptions:

1) Rapid pH equilibrium of the ampholyte subspecies

2) Electrolysis of water alone at the electrode surface

3) Electroneutrality is preserved

These assumptions are valid for practically all isoelectric focusing conditions. [107, 16]

### 2.2.1. Species Conservation Equations

Electrophoretic separations are possible because molecules (especially proteins) have a unique blend of functional groups whose electrical charge is sensitive to pH. This gives each ionic species in a mixture a distinct electrophoretic flux. Adding fluxes from convection and diffusion yields the Nernst-Planck flux equation, given by Equation 2-1.

$$\boldsymbol{N}_i = C_i \mathbf{v} - D_i \nabla C_i + \boldsymbol{E} \mu_i C_i \qquad \textbf{2-1}$$

Here, the last term defines the electrophoretic flux, with electrophoretic mobility $\mu_i$ ($m^2$/(V-s) in SI units), the electric field $\boldsymbol{E}$, and species concentration $C_i$. Inserting Equation 2-1 into the conservation equation, the general equation of species conservation for isoelectric focusing (or any other electrophoretic force) is:

$$\frac{DC_i}{Dt} = \nabla \cdot \left( D_i \nabla C_i - \boldsymbol{E} \mu_i C_i \right) + R_i \qquad \textbf{2-2}$$

### 2.2.2. Electroneutrality and pH Equilibrium

Local conductivity is defined by Equation 2-3:

$$\sigma_0 = F \sum_i z_i^2 \mu_i C_i \qquad \textbf{2-3}$$

Where $F$ is Faraday's constant (96,500 Coulombs/mole). Conservation of charge leads to a current balance, given by Equation 2-4:

$$\boldsymbol{J} = \sigma_0 \boldsymbol{E} - F \sum_i z_i D_i \nabla C_i + \sum_i z_i C_i \boldsymbol{v} \qquad \textbf{2-4}$$

The final relationship needed for isoelectric focusing is the chemical equilibrium of an ampholyte at a given pH. For the case of a biprotic molecule (used in subsequent models), $A$, the equilibrium reactions are given by Equation 2-5.

$$K^+ = \frac{k^+_{forward}}{k^+_{reverse}} = \frac{[AH][H^+]}{[AH_2^+]} \qquad K^- = \frac{k^-_{forward}}{k^-_{reverse}} = \frac{[A^-][H^+]}{[AH]} \qquad \textbf{2-5}$$

$$AH_2^+ \xleftrightarrow{K^+} AH + H^+ \xleftrightarrow{K^-} A^- + 2H^+$$

For activity coefficients near unity, the charged subspecies concentrations are related to each other through the equilibrium constants and pH (rewritten here as the Henderson-Hasselbalch in Equation 2-6):

$$pH = pK^+ - log\left(\frac{[AH_2^+]}{[AH]}\right) = pK^- - log\left(\frac{[AH]}{[A^-]}\right) \qquad \textbf{2-6}$$

The constraint of electroneutrality in the system is defined as conservation of charge for all species present in the system, shown here as Equation 2-7:

$$[\mathrm{H}^+] - \frac{K_w}{[\mathrm{H}^+]} + f([\mathrm{H}^+], C, K^+, K^-) = 0 \qquad \textbf{2-7}$$

Where the last term in Equation 2-7 is the sum of average charge for all species, and can be written for a biprotic ampholyte as:

$$f([\mathrm{H}^+], C, K^+, K^-) = \sum_i \left( \frac{\left( \sum_j \frac{j \cdot [\mathrm{H}^+]^j}{\prod_{k=1}^{j} K^+_{i,k}} - \sum_l l \cdot \frac{\prod_{k=1}^{l} K^-_{i,k}}{[\mathrm{H}^+]^l} \right) C_i}{\left( 1 + \sum_j \frac{j \cdot [\mathrm{H}^+]^j}{\prod_{k=1}^{j} K^+_{i,k}} + \sum_l l \cdot \frac{\prod_{k=1}^{l} K^-_{i,k}}{[\mathrm{H}^+]^l} \right)} \right) \qquad \textbf{2-8}$$

The equations for the equilibrium of each state of the ampholyte molecule, conservation of charge (Equation 2-4), electroneutrality (Equation 2-7) and species conservation equations (Equation 2-2) are all coupled. Because some of these coupled equations are algebraic constraints, not differential equations, the system is known as a differential-algebraic equation (DAE) system and can only be efficiently solved with specialized DAE software such as Jacobian (Numerica Technologies, Cambridge, MA).

### 2.2.3. Total Component Balances

To avoid the complexity of considering every subspecies in the system ($AH_2^+$, $AH$, and $A^-$ in Equation 2-5), a total component balance was used in the analytical and numerical models for IEF. When the subspecies conservation equations (Equation 2-2), each with a reaction term describing the conversion of one species to another. Equation 2-9 redefines the electrophoretic mobility as proportional to charge.

$$\mu_i = z_i \cdot \omega_i \qquad \textbf{2-9}$$

Here $z_i$ is the molecule's charge as a function of pH, and $\omega$ is the mobility coefficient, assumed to be constant. Equation 2-10 shows the conservation equations of each of the subspecies in Equation 2-5. Each subspecies is assumed to have identical diffusivity $D_A$ and mobility coefficient $\omega_A$. This treatment is similar to the use of total component material balances used by Olander [95] for mass transport with chemical equilibrium.

$$\frac{D[AH_2^+]}{Dt} = \nabla \cdot \left(D_A \nabla [AH_2^+] - \boldsymbol{E}\omega_A [AH_2^+]\right) - k^+_{forward}[AH_2^+] + k^+_{reverse}[AH][H^+]$$

$$\frac{D[AH]}{Dt} = D_A \nabla^2 [AH] - k^-_{forward}[AH] + k^-_{reverse}[A^-][H^+] + k^+_{forward}[AH_2^+] - k^-_{reverse}[AH_2^+][H^+] \qquad \textbf{2-10}$$

$$\frac{D[A^-]}{Dt} = \nabla \cdot \left(D_A \nabla [A^-] + \boldsymbol{E}\omega_A [A^-]\right) + k^-_{forward}[AH] - k^-_{reverse}[A^-][H^+]$$

The subspecies equations in Equation 2-10 can be summed to eliminate the reaction terms and the derivative can be expanded to yield Equation 2-11.

$$\frac{D[A_{tot}]}{Dt} = D_A \nabla^2 [A_{tot}] - \omega_A \nabla \boldsymbol{E} [AH_2^+] + \omega_A \nabla \boldsymbol{E} [A^-] \qquad \textbf{2-11}$$

Here $A_{tot}$ is the sum of each of the subspecies, defined by Equation 2-12.

$$[A_{tot}] = [AH_2^+] + [AH] + [A^-] \qquad \textbf{2-12}$$

Using Equation 2-12 with Equation 2-6, the subspecies may also be expressed as a function of hydrogen ion concentration and $A_{tot}$ in Equation 2-13.

$$[AH_2^+] = \frac{[A_{tot}][H^+]^2}{K^+K^-\left(1+\frac{[H^+]}{K^-}+\frac{[H_2]^2}{K^+K^-}\right)}$$

$$[AH] = \frac{[A_{tot}][H^+]}{K^-\left(1+\frac{[H^+]}{K^-}+\frac{[H_2]^2}{K^+K^-}\right)} \qquad \textbf{2-13}$$

$$[A^-] = \frac{[A_{tot}]}{\left(1+\frac{[H^+]}{K^-}+\frac{[H_2]^2}{K^+K^-}\right)}$$

Substituting these relationships, Equation 2-11 becomes Equation 2-14.

$$\frac{D[A_{tot}]}{Dt} = D_A\nabla^2[A_{tot}] - \omega_A\nabla\left(\boldsymbol{E}[A_{tot}]\frac{\left(\frac{[H^+]^2}{K^+K^-}-1\right)}{\left(1+\frac{[H^+]}{K^-}+\frac{[H^+]^2}{K^+K^-}\right)}\right) \qquad \textbf{2-14}$$

Equation 2-11 is a total component balance for species *A*, using the electrophoretic mobility for its charged subspecies using changes in $H^+$ concentration and electric field. This equation is similar to Equation 2-2 but with an electrophoretic mobility that is not assumed to be constant.

Analytical solutions to Equation 2-2 are only available in idealized cases with this total component balance, and will be explored in the next section for a linear pH gradient. Most purely analytical analysis of isoelectric focusing has been done before the late 1970's. Notable exceptions include modeling IEF in tapered capillaries [113], and with moving pH gradients. [112]

### 2.2.4. Zeta Potential

In microchannels, the surface chemistry of the device plays a large role in the overall device performance. Figure 2-2 shows a diagram and plot of the counterion distribution and electric potential near a charged surface. At a charged surface, counterions in solution screen the surface charge, eventually negating its influence on the bulk liquid. The Nernst potential (the electrical potential at the surface) is screened by counter ions in solution. The electrical potential at a distance of one counterion, called the Stern layer or Outer Helmholtz Plane is known as the Stern potential. The zeta ($\zeta$) potential is defined as the electrical potential at the no-slip boundary. Because this is the surface potential exposed to the moving liquid, the zeta potential is the most relevant property for fluid-surface interactions based on charge. Mobile counterions balancing the surface charge will move upon application of an electric field.

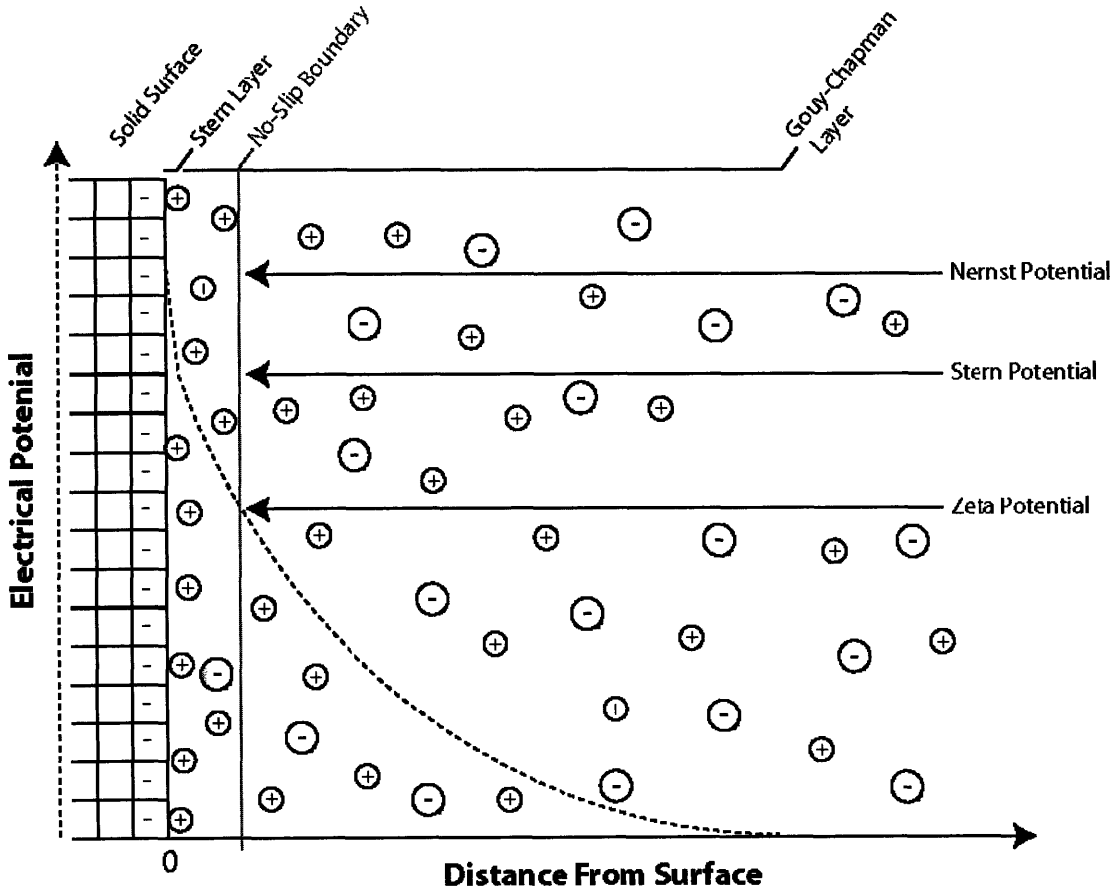


**Figure 2-2: Electrical potentials at the interface between a charged surface and an electrolyte. A plot of electrical potential versus distance from surface is overlaid with a diagram of ions in solution.**

To approximate the zeta potential, $\zeta$, as a linear function of surface charge density, $\sigma_m$, the Helmholtz approximation for a planar surface is given by Equation 2-15.

$$\sigma_m = \varepsilon\varepsilon_0\kappa\zeta \qquad \textbf{2-15}$$

Here, $\varepsilon$ is the relative permittivity of the medium, and $\varepsilon_0$ is the permittivity of free space. The Debye parameter, $\kappa$, is (units of inverse length), defined by Equation 2-16.

$$\kappa = \sqrt{\frac{2F^2 I}{\varepsilon\varepsilon_0 RT}} \qquad \textbf{2-16}$$

The Debye length for a system can be thought of as the length scale where the characteristic time for ion diffusion time is on the same order as the time scale for electrostatic interactions. For a sphere of radius $R$, Equation 2-17 describes the relationship between surface charge density and zeta potential:

$$\sigma_m = \varepsilon\varepsilon_0\zeta\left(\frac{1}{R} + \kappa\right) \qquad \textbf{2-17}$$

The ionic strength, $I$, is a function of all charged species in solution, and is defined by Equation 2-18:

$$I = 0.5\sum z_i^2 C_i \qquad \textbf{2-18}$$

To relate $\zeta$ to the total charge on a surface, we first define surface charge density as:

$$\text{Plane: } \sigma_m = \frac{zq}{A} \qquad \text{Sphere: } \sigma_m = \frac{zq}{4\pi R^2} \qquad \textbf{2-19}$$

In Equation 2-19, the product of valence, $z$, and the elementary charge, $q$, is the total charge of a surface with area $A$, the total charge of a spherical particle or molecule. Next, subtracting Equations 2-15 or 2-17 from 2-19, $\zeta$ may now be expressed as a function of valence, $z$:

$$\text{Plane: } \zeta = \frac{zq}{A\varepsilon\varepsilon_0\kappa} \qquad \text{Sphere: } \zeta = \frac{zq}{4\pi R\varepsilon\varepsilon_0}\left(\frac{1}{1+R\kappa}\right) \qquad \textbf{2-20}$$

Equation 2-20 will be used in subsequent analyses to describe electrophoretic mobility for particles moving through a liquid medium, as well as for liquid convention over a solid surface.

### 2.2.5. Electroosmotic Flow

Electroosmotic flow (EOF) is the result of applied electric fields in microchannels. Surface charges are balanced by mobile counterions, which move in response to the application of an electric field. While ions in the bulk fluid do not become separated, the viscous drag of migrating mobile counterions beyond the no-slip plane (shown in Figure 2-2) results in bulk fluid flow. Compared to electrophoresis, the physics and relative transport are identical; however, in EOF, the movement relative to the observer is reversed: the chamber is stationary while the liquid is conveyed by the electric field. Figure 2-3 illustrates the principle of electroosmotic flow.

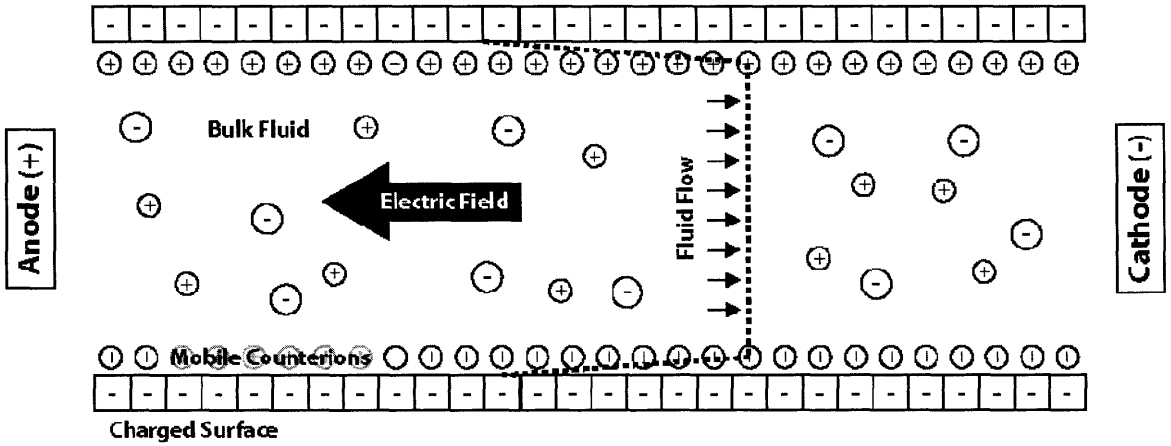


**Figure 2-3: Diagram of electroosmotic flow. In the bulk fluid, cations are drawn toward the cathode, and anions towards the anode. However, the electroneutrality constraint prevents separation of anions and cations in the bulk liquid. Mobile cations near the negatively charged surface are drawn towards the cathode, resulting in a uniform bulk fluid flow against the direction of the electric field.**

Electroosmotic flow velocity $U_{EOF}$ for a dilute system is given by Equation 2-21:

$$U_{EOF} = -\frac{\varepsilon\varepsilon_0\zeta}{\eta}E \qquad \textbf{2-21}$$

Where $\eta$ is the dynamic viscosity of the liquid. Changes in the double layer thickness result affect the zeta potential. Because $\kappa$ varies with the square root of the ionic strength, a simple correction factor to normalize electroosmotic mobility to a standard ionic strength may be added to Equation 2-21:

$$U_{EOF} = -\frac{\varepsilon\varepsilon_0\zeta_{std}}{\eta}\sqrt{\frac{I_1}{I_{std}}}E \qquad \textbf{2-22}$$

Figure 2-4 plots the electroosmotic mobility inside a 50 micron glass capillary as a function of pH with and without the correction factor for differences in ionic strength as measured by Thormann et al. [124]. From this data the pKa of the silica surface was estimated to be ~5, meaning that at high pH, the silica surface is highly charged. This implies that with a pH gradient in a glass channel, there will also be a gradient in electroosmotic mobility.

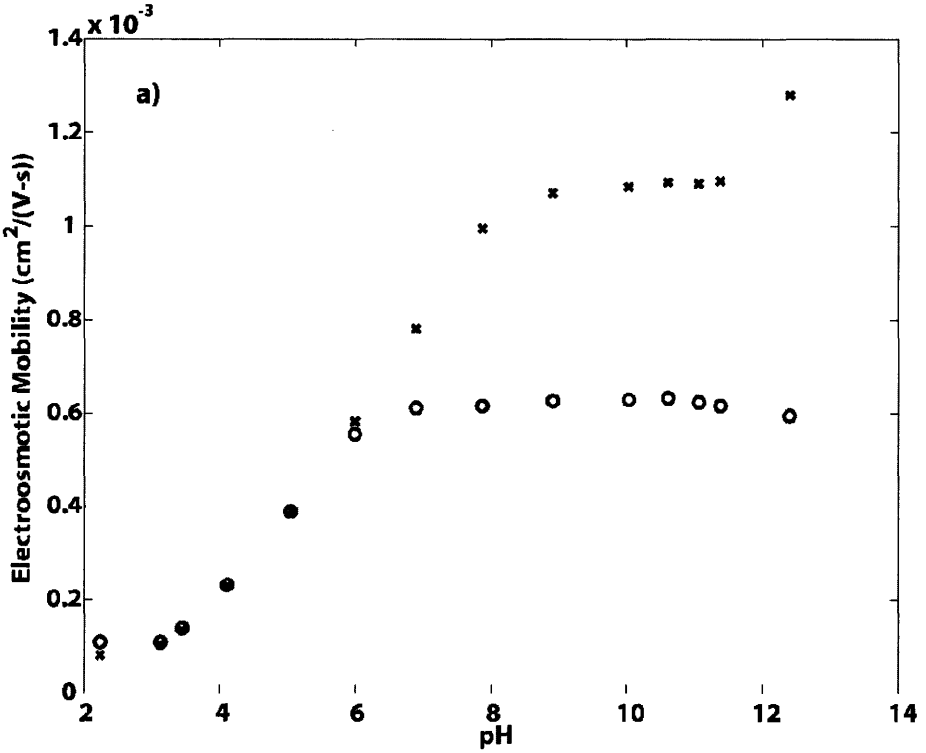


b)

| pH | I (mM) |
|---|---|
| 2.23 | 22.4 |
| 3.12 | 36.3 |
| 3.44 | 38.2 |
| 4.11 | 39.7 |
| 5.04 | 40.5 |
| 5.99 | 44.6 |
| 6.89 | 66.1 |
| 7.87 | 105.8 |
| 8.91 | 118.5 |
| 10.03 | 120.3 |
| 10.61 | 121.4 |
| 11.06 | 124.1 |
| 11.38 | 128.4 |
| 12.4 | 187.8 |

**Figure 2-4: Electroosmotic flow measured by Thormann et al. [124] a) Plot of observed electroosmotic mobility versus pH (open circles) and electroosmotic mobility normalized to 40.5 mM ionic strength (solid x's). b) Table of ionic strengths at each pH measurement.**

In a closed channel, EOF will induce a pressure gradient across the width of the channel. This pressure gradient can induce fluid recirculation in the channel. A pressure driven, parabolic flow profile will disrupt the resolution of the separation. Rhodes et. al. observed this electrohydrodynamic distortion of sample streams in free flow zone electrophoresis [102]. An effective diffusion of the analyte can be expressed as a lateral diffusion problem in chromatography, as derived by Giddings [43], where species are only present in the mobile phase with a parabolic flow profile, and channel height $h$.

$$D_T = D + \frac{U_{EOF}{}^2 h^2}{210D} \qquad \textbf{2-23}$$

This effective diffusion and Equation 2-21 can be substituted into the expression for peak width for the analytical case to yield the expression for band broadening in EOF [66]:

$$\sigma = \sqrt{\frac{D}{\omega Ep} + \frac{Eh^2}{210D}\left(\frac{\varepsilon\varepsilon_0\zeta}{\eta}\right)^2} \qquad \textbf{2-24}$$

Taking the derivative of this equation, setting it equal to zero, solving for $E$ results in the optimum electric field as a function of diffusion constant and channel height, given by Equation 2-25. This equation assumes that there are no other dispersive effects.

$$E = \pm\frac{\sqrt{210}\cdot D\eta}{h\varepsilon\varepsilon_0\zeta} \qquad \textbf{2-25}$$

From Equation 2-25, the optimal electrical field is related to channel height and the physical properties of the system. This relationship with channel height illustrates the importance of device geometry on focusing performance.

### 2.2.6. Electrokinetic Instability

As an electric field is applied parallel to a conductivity gradient, as is the case for IEF, electrokinetic instabilities are possible. These instabilities arise to the unequal concentrations of mobile ions, generating unequal forces throughout the volume of the fluid. The electrical force acting on a mobile charge density $\rho_f$ in solution when added to the Navier-Stokes equation becomes Equation 2-26:

$$\rho\left(\frac{D\mathbf{v}}{Dt}\right) = -\nabla P + \eta\nabla^2\mathbf{v} + \rho_f\mathbf{E} \qquad \textbf{2-26}$$

Taylor and McEwan [120] analyzed the stability of two immiscible liquids with different conductivities. Such volumetric effects are more difficult to suppress in IEF, because unlike EOF, conductivity gradients are an unavoidable consequence of isoelectric focusing. Instabilities may develop at high electric fields across regions of differing conductivity [55, 53, 54], linear stability analysis by Baygents and Baldessari [6] yields an electrical equivalent for the Rayleigh number (electric instability relative to viscous stabilization), shown in Equation 2-27.

$$Ra_e = \frac{\varepsilon\varepsilon_0 E^2 d^2}{\eta D}\frac{\Delta\sigma}{\sigma_0} \qquad \textbf{2-27}$$

Here, the conductivity difference $\Delta\sigma$ occurs over distance $d$, and may diffuse with diffusivity $D$. For stress-free boundary conditions, the theoretical critical electric Rayleigh

numbers Baygents and Baldessari calculated were as low as $10^4$. Other numerical models have been used to describe and predict periodic instabilities in microgeometries.[75]

### 2.2.7. Multi-peak Approach

Under some circumstances, multiple peaks are observed to originate from the electrodes, focus, and coalesce at the pI. This behavior is the result of electrophoretic stacking as analytes are swept towards the isoelectric point gradually reducing the electrophoretic mobility. Multipeak focusing has been observed both experimentally and theoretically, especially in systems with a nonlinear pH gradient. Large gradients in electrophoretic fluxes with respect to position cause the stacking. This phenomenon manifests itself as a moving front.

## *2.3. Analytical Solution for an Idealized Case*

An ideal ampholyte focusing in a pre-defined pH gradient will be focused in a manner shown in Figure 2-5:

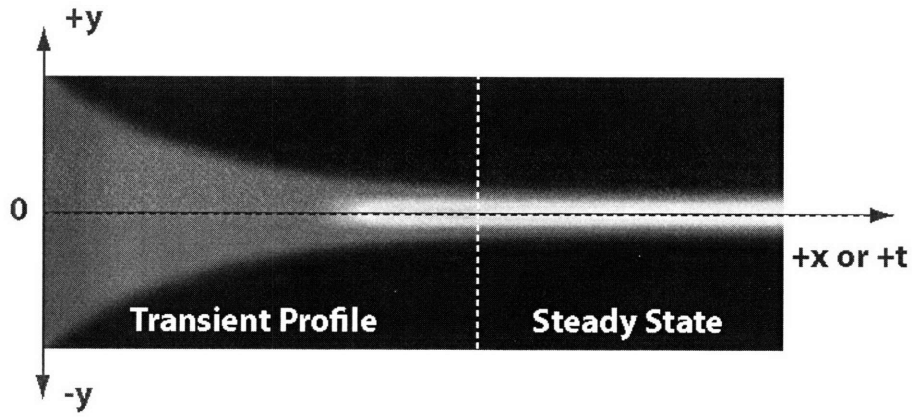


**Figure 2-5: Focusing of an ideal ampholyte in two dimensions.**

For a system with a transverse electric field in the $y$ direction and flow $\boldsymbol{v}$ in the $x$ direction, $\boldsymbol{E}$ becomes a scalar, $E$. This simplification requires the assumption of constant conductivity to ensure a uniform field across the channel. Further simplifying the model to describe only uniform flow in the x direction and a linear pH gradient generated by an ampholyte solution in the y direction only, Equation 2-2 becomes:

$$\boldsymbol{v}\frac{\partial C}{\partial x} = D\frac{\partial^2 C}{\partial y^2} - E\omega C\frac{\partial z}{\partial y} - E\omega\frac{\partial C}{\partial y}z \qquad \textbf{2-28}$$

Alternatively, Equation 2-28 can be written as a pseudo-time dependent system with uniform flow in the x direction only ($t = x/v$ ):

$$\frac{\partial C}{\partial t} = D\frac{\partial^2 C}{\partial y^2} - E\omega C\frac{\partial z}{\partial y} - E\omega\frac{\partial C}{\partial y}z \qquad \textbf{2-29}$$

### 2.3.1. Steady State Solution

Imposing a steady state condition which implies a fully-focused (i.e. $\partial C/\partial x = 0$) state, Equation 2-29 reduces to Equation 2-30:

$$0 = D\frac{d^2 C}{dy^2} - E\omega C\frac{dz}{dy} - E\omega\frac{dC}{dy}z \qquad \textbf{2-30}$$

A first order Taylor series can be used to approximate *dz/dy* as a constant, *-p,* around the isoelectric point. For most proteins this approximation works only for pH near the pI. However, for an analytical solution, it must be assumed to be equal to the total change in charge of the species divided by the channel distance. The slope is also a function of conductivity [19, 17], which must be assumed constant. Setting the linear relationship in Equation 2-31:

$$z = \frac{z_{\max} - z_{\min}}{L}\left(y_{pI} - y\right) = p\left(y_{pI} - y\right) \qquad \textbf{2-31}$$

Equation 2-30 can be non-dimensionalized to Equation 2-33:

$$\Theta = C/C_{max} \qquad \eta = y/L \qquad Pe_e = E\omega pL^2/D \qquad \textbf{2-32}$$

$$0 = \frac{1}{Pe_e}\frac{d^2\Theta}{d\eta^2} - \Theta - \frac{d\Theta}{d\eta}\left(\eta - \eta_{pI}\right) \qquad \textbf{2-33}$$

Here $Pe_e$ is the electrophoretic equivalent of the Peclet number; electrophoretic flux divided by diffusive flux. The key assumptions of constant conductivity and a linear charge/slope relationship are typically valid for proteins in a linear pH gradient with low conductivity [118]. The solution to this simplified ODE is a Gaussian concentration distribution with standard deviation $\sigma$ around the isoelectric point:

$$C(y) = C_{max}\, exp\left(-\frac{\left(y - y_{pI}\right)^2}{2\sigma^2}\right) \qquad \textbf{2-34}$$

The maximum concentration *Cmax* is related to the total species present in a given cross-section of the channel by Equation 2-35:

$$C_{max} = \frac{1}{\sigma\sqrt{2\pi}} \int C(y)dy \qquad \textbf{2-35}$$

The variance of the distribution is given by Equation 2-36:

$$\sigma^2 = \frac{D}{\omega Ep} = \frac{L^2}{Pe_e} \qquad \textbf{2-36}$$

The number of theoretical plates, an assessment of separation efficiency [44], is given by Equation 2-37:

$$N = \frac{L^2}{\sigma^2} = Pe_e \qquad \textbf{2-37}$$

The system peak capacity is the maximum number of bands that can be separated. If minimum width for separation of each component is set at say, 3 $\sigma$ or 87% of the total distribution, the peak capacity is given by Equation 2-38. This result is equivalent to the results of Vesterberg and Svensson [125] and Rilbe [104] for the minimum resolvable difference in pI. Here, we also define resolution, *Res*, also equivalent to the peak capacity:

$$\frac{\Delta pI_{min}}{\Delta pH} = 3\sqrt{\frac{D}{E\omega L\Delta z}} = \frac{1}{Res} \qquad \textbf{2-38}$$

Note the peak capacity varies with the square of the electrophoretic Peclet number. Thus if the number of theoretical plates was reduced by half, the peak capacity would be reduced by only 30%. The possibility of increasing total peak capacity through stream splitting and refocusing will be explored in section 2.6.

### 2.3.2. Transient Solution

Non-dimensionalizing the pseudo-time dependent case, with a linear pH gradient, Equation 2-29 becomes Equation 2-39:

$$\frac{\partial\Theta}{\partial\tau} = \frac{1}{Pe_e}\frac{\partial^2\Theta}{\partial\eta^2} - \Theta - \frac{\partial\Theta}{\partial\eta}(\eta - \eta_{pI}) \qquad \textbf{2-39}$$

Where time is scaled by *Eωp* ($\tau$=*Eωpt*). Solving Equation 2-39 by using Fourier transforms [30, 130], the transient concentration profile is determined by Equation 2-40.

$$C(y,t)=e^{E\omega pt}\left[\Psi\left(\frac{y_{pI}\left(1-e^{-E\omega pt}\right)+e^{-E\omega pt}-y}{\frac{\sigma}{L}\sqrt{1-e^{-2E\omega pt}}}\right)+\Psi\left(\frac{y-y_{pI}\left(1-e^{-E\omega pt}\right)}{\frac{\sigma}{L}\sqrt{1-e^{-2E\omega pt}}}\right)-1\right] \quad \textbf{2-40}$$

$$\Psi(x)=\frac{1}{\sqrt{2\pi}}\int_{-\infty}^{x}e^{-z^2/2}dz$$

This analytical transient solution was published in 1974 [130]. For Equation 2-40, it should be noted that as $t$ becomes infinite, the exponential term also approaches infinity. Accordingly, the bracketed term drops to approximately zero. At large values of $t$, floating point error becomes significant, making it difficult to use Equation 2-40 in numerical simulations.

## 2.4. Numerical Solutions in a Static Linear pH Gradient

To simulate the focusing of single species in a static, linear pH gradient, with variable salt concentration and parabolic flow, finite element modeling software (FEMLAB or COMSOL Mulitphysics, COMSOL, Burlington, MA) was used to create models for steady-state focusing in a two dimensional rectangular channel with a salt (NaCl) in solution. The model parameters are listed in Table 2-1.

**Table 2-1: Model parameters used for IEF in a static pH gradient**

| Parameter | FEMLAB Name | Value | Units |
|---|---|---|---|
| F | F | 96485 | Coul/mol |
| D | D | 5.94E-11 | $m^2/s$ |
| $\omega$ | Omega | 2.31E-09 | $m^2/V\text{-}s$ |
| $\varepsilon\varepsilon_0$ | ee0 | 7.083e-10 | Coul/V-m |
| $\mu_{Na}$ | Upos | 7.35E-08 | $m^2/V\text{-}s$ |
| $\mu_{Cl}$ | Uneg | 7.91E-08 | $m^2/V\text{-}s$ |
| R | R | 4.00E-09 | m |
| T | Temp | 298 | K |
| $R_c$ | Rc | 8.3145 | j/mol-K |
| $k_B$ | kb | 1.38E-23 | $m^2kg/s^2\text{-}K$ |
| q | q | 1.60E-19 | Coul |
| V | Voltage | 2 | V |
| $C_{NaCl}$ | Cs0 | 8 | $mol/m^3$ |

Focusing of small molecules in a pseudo 3-D geometry modeled using a preestablished flow profile was performed to observe the effects of flow profile on focusing dynamics. Time dependent 2-D geometry, a channel cross-section of 50 by 1000 microns was created to model the focusing chamber. In addition to this channel, a 50 by 500 micron gel was modeled on either side of the channel. Beyond this, there is a region of high conductivity (a ten fold higher salt concentration) and the electrode surface. To capture the fluid flow profile in the device (liquid in the center of the channel flows faster than near the edges) the dimensional form of fully developed Navier-Stokes flow was used. [26] Equation 2-41 relates the unidirectional local fluid velocity $v_x$, to the average velocity, $U$, between parallel plates spaced a distance of $2H$ apart.

$$\nabla^2 v_x = \frac{-3U}{H^2} \qquad \textbf{2-41}$$

To use fluid flow in the COMSOL model, a Poisson function, Equation 2-42, with a homogeneous source (representing pressure normal to the channel cross-section) as used to create a profile within the focusing channel with a height of 50 microns ($H = 25\text{x}10^{-6}$m) which

was then used to determine the coefficient, $d_a$, for the time derivative of the conservation equation.

$$-\nabla^2 d_a = \frac{3U}{H^2} = \frac{3 \cdot 0.6667}{\left[25 \cdot 10^{-6}\right]^2} = 3.2 \cdot 10^9 \qquad \textbf{2-42}$$

This time derivative coefficient, termed mass coefficient in COMSOL, varies from 0 at the no-slip boundary to 1 at the center of the channel, with an average value of 0.66. This term effectively recaptures the fluid velocity profile normal to the 2-D model geometry. To approximate a 3D channel, the time dependent solver evaluated 20 seconds of focusing starting from a homogeneous concentration of 0.2 mM BSA.

### 2.4.1. Models for Protein and Small Molecule Focusing

Using published titration data for bovine serum albumin (BSA), a FEMLAB model was created to describe protein mobility. MATLAB was used to fit the tabular data to a continuous rational function. Using BSA as the model species for IEF, three electrophoresis models were created. BSA's charge with respect to pH (extrapolated to zero ionic strength) was calculated by Linderstrøm-Lang and Nielsen [76]. Table 2-2 lists the charge of BSA as function of pH as well as the estimated charge using Equation 2-43.

$$z_{est}(pH) = \frac{-1.184pH^5 + 47.28pH^4 - 748.5pH^3 + 5858pH^2 - 22640pH + 34370}{pH^2 - 18.55pH + 92.45} \qquad \textbf{2-43}$$

**Table 2-2: Charge as a function of pH for BSA.**

| pH | z | $z_{est}$ |
|---|---|---|
| 3 | 58 | 54.68 |
| 3.5 | 35.5 | 31.97 |
| 4 | 13 | 15.34 |
| 4.2 | 3 | 10.16 |
| 4.5 | 1.7 | 3.78 |
| 5 | -1.5 | -3.74 |
| 6.5 | -10.5 | -13.20 |
| 7 | -14 | -15.84 |
| 10 | -32 | -47.48 |
| 10.85 | -37 | -56.76 |
| 11 | -44 | -59.94 |
| 12 | -84 | -100.00 |

Equation 2-43 uses fitting constants with fewer significant figures than more precise rational fit calculated with MATLAB ($R^2$= 0.996). The truncated constants result in a poorer fit ($R^2$= 0.978) were used for ease of coding and because it resulted in a minimal shift in the pI, 4.722 versus 4.756.

Using Equation 2-43 to calculate $z$ for a theoretical BSA-like protein, the surface charge and zeta potential could be estimated for a spherical particle with a radius equal to the hydrodynamic radius, $r$, of BSA, using the Stokes-Einstein relationship given in Equation 2-52

$$r = \frac{k_B T}{6\pi\eta D} \qquad \textbf{2-44}$$

The radius is a function of Boltzmann's constant, $k_B$, and using the diffusion constant for BSA, $5.94 \times 10^{-11}$ $m^2/s$ [76], this value is 4.1 nm. These values are used with three models for electrophoresis.

There are many analytical and numerical models for electrokinetic phenomena [28] each with their own assumptions. Three of the simplest analytical models were chosen to simulate BSA focusing, to both to validate the numerical focusing model and to select the appropriate model for future work. Figure 2-6 is a diagram of a spherical charged particle in an electric field. Salient features of electrophoresis considered by the analytical models are: charge screening by

counterions, convective redistribution of the counterions, distortion of the electric field due to an insulating particle, and the surface conductivity of the particle's electric double layer.

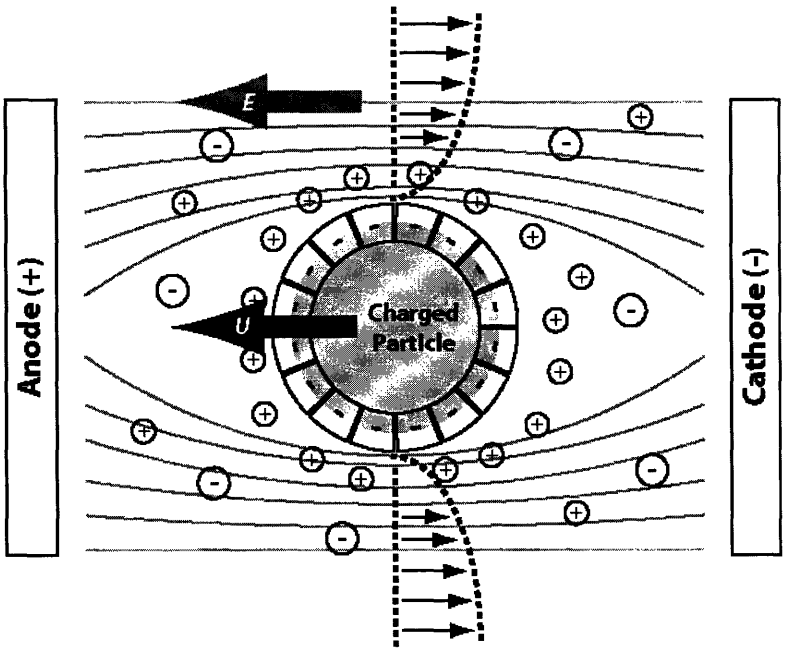


**Figure 2-6: Diagram of particle electrophoresis. A solid, non conducting particle will distort the local electric field, *E* shown in gray. Fluid (black arrows and dotted lines) will move around the particle as it moves toward the anode with velocity *U*. At high mobilities and low ionic strength, the envelope of mobile counterions may be distorted by convection.**

## Einstein Approximation

The most basic relationship between electrophoretic mobility and charge considers only a point charge and is given by the Einstein relation shown in Equation 2-45. This simplistic model assumes only a point charge with no influence on the electric field or fluidic resistance.

$$\mu = \frac{U}{E} = \frac{z_i D_i F}{R_c T} \qquad \textbf{2-45}$$

Equation 2-45 is the simplest and most direct relationship between electrophoretic mobility and diffusion. Here, $R_c$ is the ideal gas constant, $T$ is absolute temperature, and $F$ is Faraday's constant.

## Helmholtz-Smoluchowski Approximation

To take the double layer into account for a surface with $R\kappa \gg 1$, Smoluchowski determined the relationship between mobility and electric field, shown in Equation 2-46.

$$\mu = \frac{U}{E} = \frac{\varepsilon\varepsilon_0}{\eta}\zeta \qquad \textbf{2-46}$$

Unlike Equation 2-45, this relationship accounts for the charge screening of counterions. However, it is not without its limitations. In addition to the assumption for particle size relative to double layer thickness, does not consider disturbance of the counterions due to convection, and it does not consider the particle's influence on the electric field, nor surface conductivity.

## Hückel-Onsager Approximation

Equation 2-47 is the analog of Equation 2-46 valid for $R\kappa \ll 1$ is known as the Hückel-Onsager equation for electrophoresis.

$$\mu = \frac{U}{E} = \frac{2\varepsilon\varepsilon_0\zeta}{3\eta} \qquad \textbf{2-47}$$

In this case, because of the small size of the particle relative to the double layer thickness, the convective disturbance of the counterions is not relevant. However, like Equation 2-46, Equation 2-47 also ignores surface conductivity.

## Henry Approximation

A more universal model for electrophoresis that interpolates between the Helmholtz-Smoluchowski and Hückel-Onsager for any value of $R\kappa$ was presented by DC Henry in 1931 [49] shown in Equation 2-48.

$$\mu = \frac{U}{E} = \frac{\varepsilon\varepsilon_0\zeta}{\eta} f(\kappa R) \qquad \textbf{2-48}$$

Here the $f(\kappa R)$ term is a sinusoidal function that varies between 2/3 and 1, effectively linking Equations 2-46 and 2-47 over all values of $R\kappa$. The exact definition of this function is given by Equation 2-49:

$$f(\kappa R) = 1 + \frac{(\kappa R)^2}{16} - \frac{5(\kappa R)^3}{48} - \frac{(\kappa R)^4}{96} + \frac{(\kappa R)^5}{96} - \left[\frac{(\kappa R)^4}{8} - \frac{(\kappa R)^6}{96}\right] e^{\kappa R}\int_{\infty}^{\kappa R}\frac{e^{-t}}{t}dt \qquad \textbf{2-49}$$

An explicit expression that approximates Equation 2-49 to within 1% was first published by Oshima in 1994 [94, 27], shown in Equation 2-50:

$$f(\kappa R) \cong \frac{2}{3}\left[1+\frac{1}{2}\left(1+\frac{2.5}{\kappa R(1+2exp(-\kappa R))}\right)^{-3}\right] \qquad \textbf{2-50}$$

While useful for any combination of particle size and double layer thickness, Equation 2-48 neglects electric field distortions and surface conductivity effects.

## Levich Approximation

To consider effects such as surface conductivity and ion convection around an migrating sphere, Levich [73] expanded the Helmholtz-Smoluchowski approximation:

$$\mu = \frac{U}{E} = \frac{\frac{\varepsilon\varepsilon_0\zeta}{\eta}}{1+\frac{\varepsilon\varepsilon_0\zeta\sigma_m}{\eta\sigma R}+\frac{|\sigma_m|u}{\sigma R}} \qquad \textbf{2-51}$$

Like Equation 2-46, Equation 2-51 is valid for particles with radii much larger than the double layer. However, two correction terms are present in the denominator. The first, $\frac{\varepsilon\varepsilon_0\xi\sigma_m}{\eta\sigma R}$, represents the ratio of ionic relaxation time to particle convection and corrects for the redistribution of ions due to particle convection. The second term, $\frac{|\sigma_m|u}{\sigma R}$, uses the mobility of the mobile counterions, $u$, to correct for the surface conductivity of the particle.

### 2.4.2. Results for Various Focusing Models

The mobility of BSA was calculated using the various focusing models using Equations and 2-20 and 2-43 to calculate charge with respect to channel position, assuming a linear pH gradient of 3 to 10 from anode to cathode. Using the electrophoresis models outlined previously, the calculated mobility for the Einstein, Henry, and Levich models are plotted in Figure 2-7.

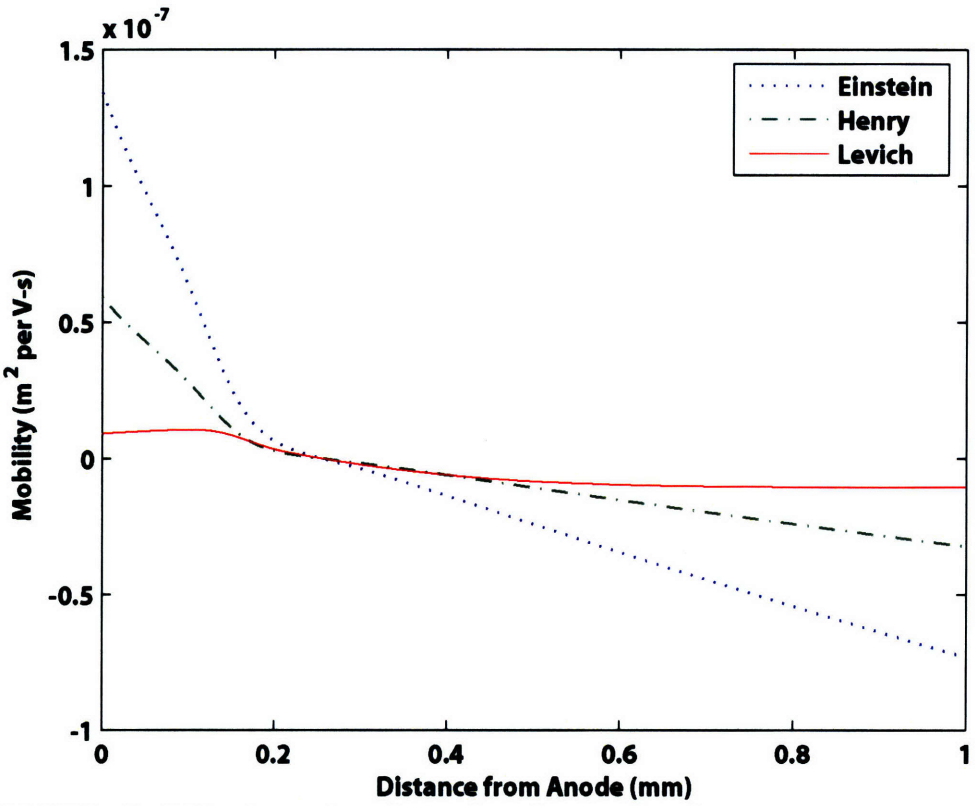


**Figure 2-7: Mobilities for BSA using various electrophoresis approximations.**

For each of the three selected models, the concentration of BSA across the midplane of the channel was plotted with respect to the distance from the anodic end of the channel. Figure 2-8 plots the BSA focusing using the Einstein approximation. In this case, a sharp, focused peak rapidly forms following the multi-peak approach. Figure 2-9 plots the BSA focusing using the Henry approximation. Here, focusing also occurs via a multi-peak approach, but the final peak is much wider, with a lower peak concentration of 1.3 mM versus 3.5 mM for the Einstein model. Figure 2-10 plots the BSA focusing using the Levich approximation. In this case the lower mobility results in more gradual focusing, resulting in an asymmetric peak with a maximum concentration of 1.35 mM.

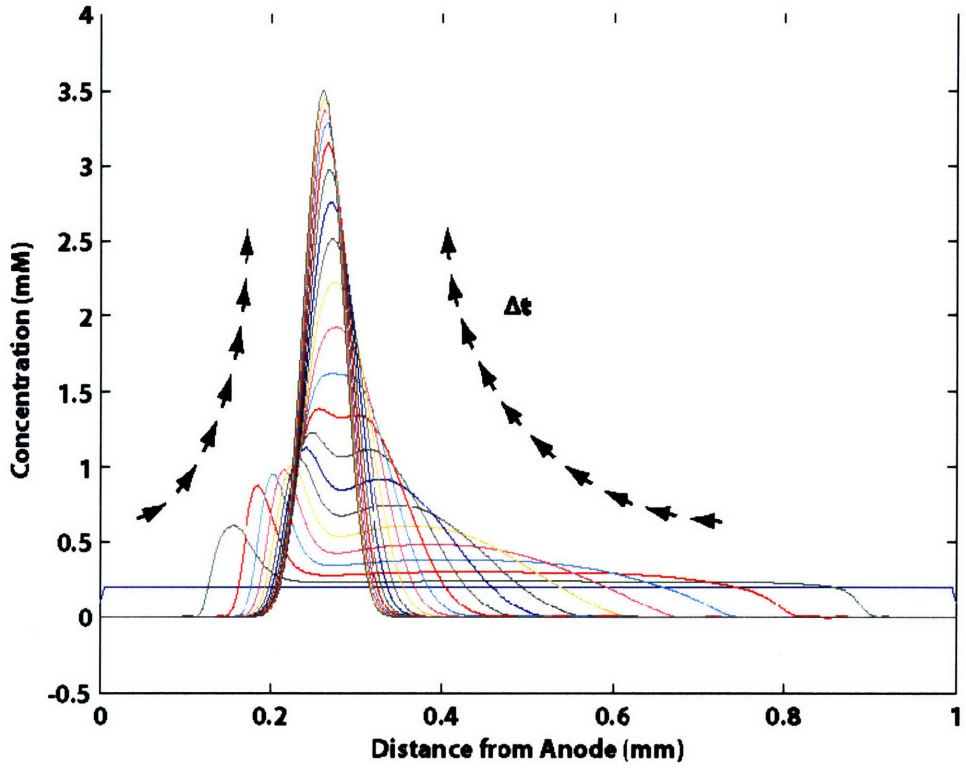


**Figure 2-8: BSA focusing using the Einstein approximation. The output of the time dependent solver is plotted as multiple overlapping lines at from time 0 to 20 seconds, in one second increments.**

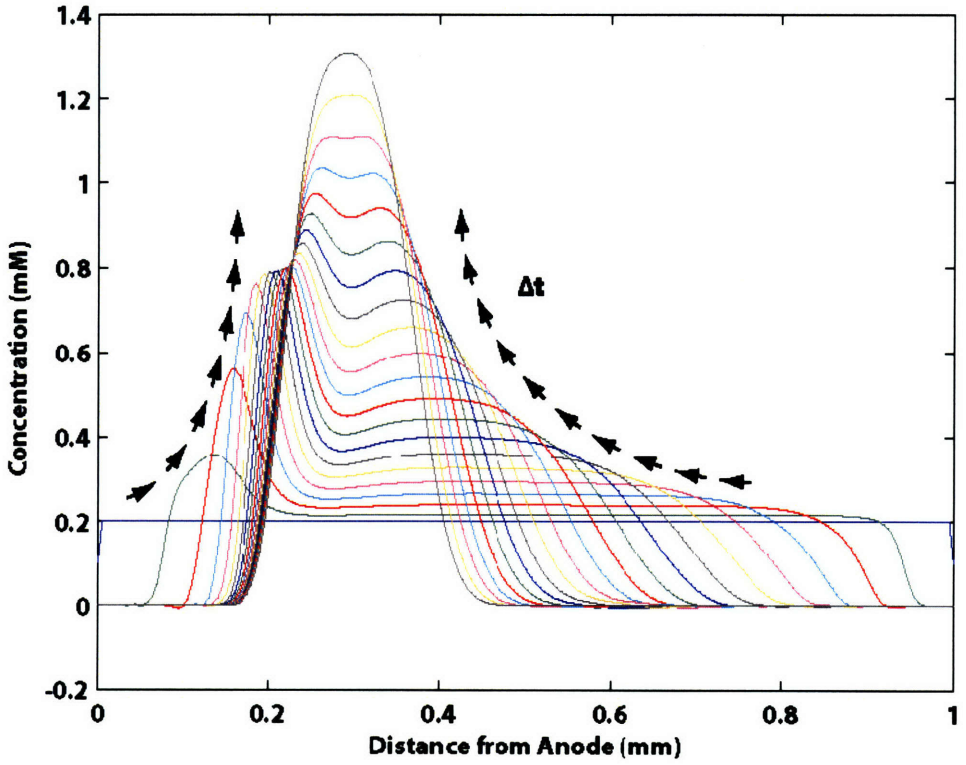


**Figure 2-9: BSA focusing using the Henry approximation. The output of the time dependent solver is plotted as multiple overlapping lines at from time 0 to 20 seconds, in one second increments.**

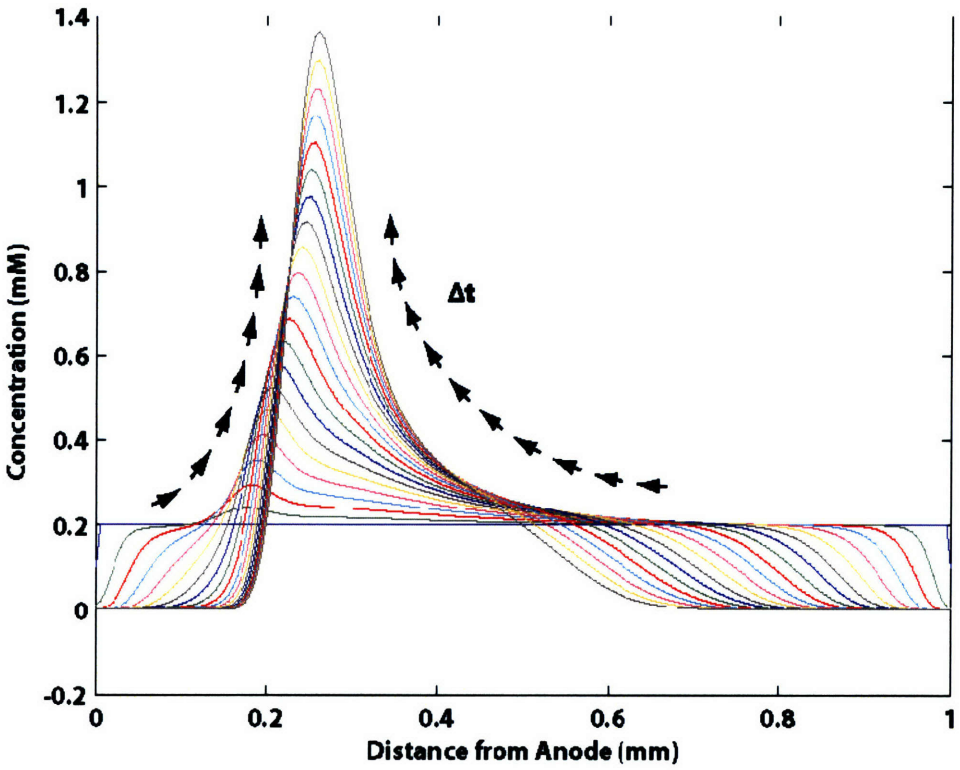


**Figure 2-10: BSA focusing using the Levich approximation. The output of the time dependent solver is plotted as multiple overlapping lines at from time 0 to 20 seconds, in one second increments.**

For the conductivity of the sample used, the $R\kappa$ for BSA was calculated to be 1.16. At this value of $R\kappa$, the Levich is expected to be a poor model for electrophoresis. Rejecting the Einstein approximation due to its point charge assumption, the Henry approximation was selected as the best model of the three for protein electrophoresis. The Henry approximation is used to calculate protein mobility for numerical solutions in a dynamic pH gradient. The good agreement with experimental results for BSA focusing in Chapter 3 of this thesis confirms the utility of Equation 2-48.

## 2.5. Numerical Solutions in a Dynamic pH Gradient

To describe IEF without an assumed linear pH gradient, a numerical simulation was written to be able to describe all species present in the focusing sample. Conservation equations for many (up to 150) species present in the sample were used in conjunction with constraints for pH equilibrium and electroneutrality. The resulting system of equations formed a set of differential-algebraic equations (DAE), which were integrated numerically by DAE software

(Jacobian, Numerica Technologies, Cambridge, MA). The Jacobian code that was used to create the model is available in Appendix B.2 The pI of the $i^{th}$ theoretical ampholyte is given by Equation 2-52:

$$pI_i = \frac{(i-1)(pI_{\max} - pI_{\min})}{(N-1)} + pI_{\min} \qquad \textbf{2-52}$$

Here, $N$ is the total number of theoretical ampholytes, typically 140. The pI range defined by $pI_{min}$ and $pI_{max}$, typically pH 3 to 10.

### 2.5.1. Model Structure

Figure 2-11 shows the structure of a simplified model with 14 species and 25 spatial grid points, the most complex matrices that the Jacobian analysis environment could display. With respect to scaling, the number of equations, $N_{Eq}$, scales according to Equation 2-53:

$$N_{Eq} = (4N_{Comp} + 11)(N_{Grid} + 1) + 2 \qquad \textbf{2-53}$$

The complexity of the system scales linearly with respect to both the number of components ($N_{Comp}$) and the number of finite difference points ($N_{Grid}$+1). The system was found to be quite sparse, with 99.7% of the matrix empty. Because the Jacobian analysis environment could not display or export this volume of data, custom MATLAB programs were written to parse and post process the results, as well as provide Jacobian consistent initialization values. These programs are available in Appendix B.3.

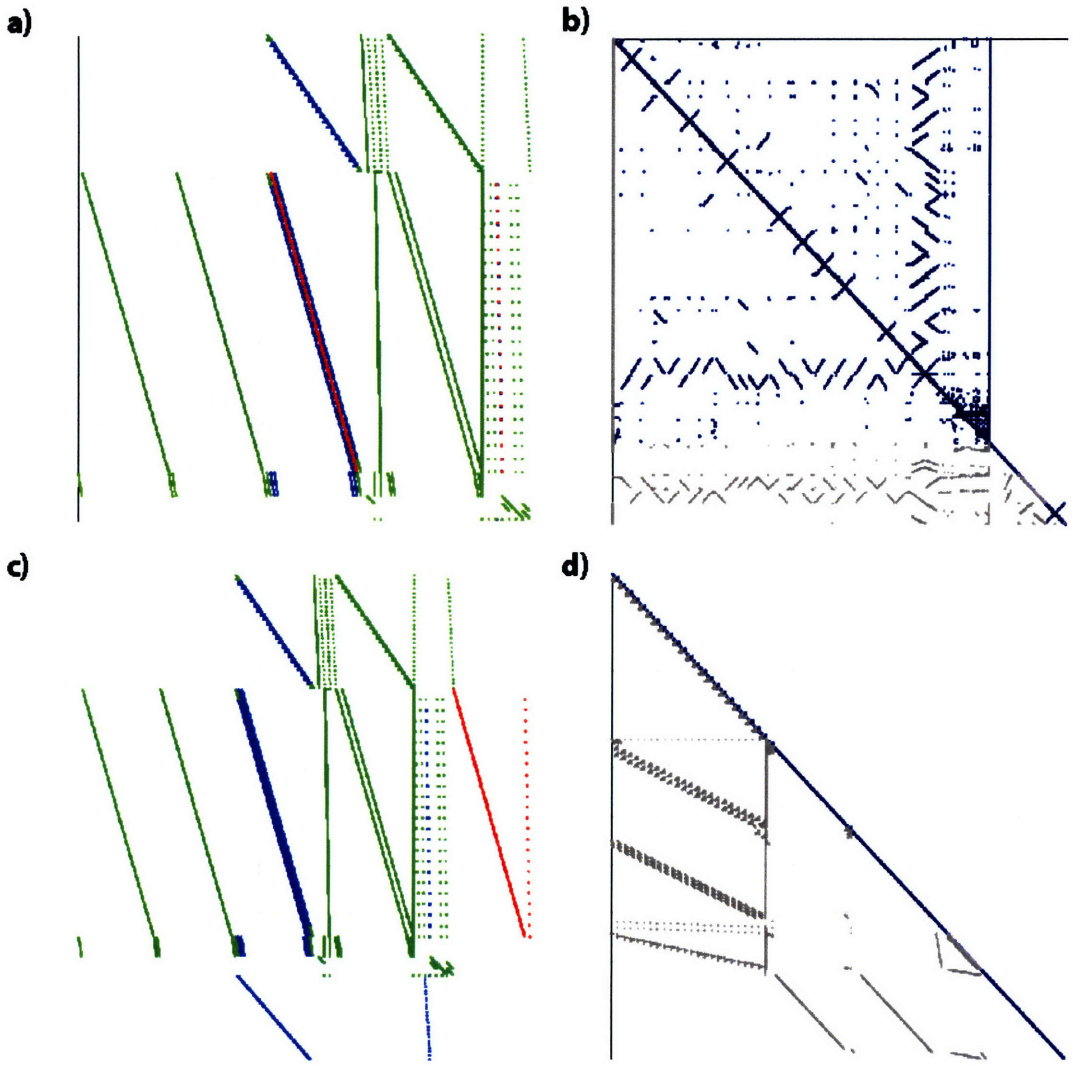


**Figure 2-11: Scarcity pattern of the Jacobian for the dynamic IEF simulation. a) Unpermuted Jacobian of the DAE system. Green: algebraic variables, blue: differential variables, red: time derivatives. b) Permuted Jacobian of the DAE. Blue: fully determined block, gray: off-diagonal entry. c) Unpermuted Jacobian of the initialization conditions. d) Permuted Jacobian of the initialization conditions.**

### 2.5.2. Model Evaluation

In evaluating the model for IEF, two considerations were addressed: validating the model with published results, and evaluating the assumptions of negligible 2D current fluxes and current due to ionic diffusion. To validate the model, previously published results [9, 97, 88] were reproduced exactly. No flux boundary conditions were used, allowing no species to leave the channel. To satisfy the electrophoretic flux terms, a slight change in pH was required. To ensure that the contribution to current due to ionic conductivity was negligible, steady-state results from the Jacobian simulation were used to estimate the second term in Equation 2-4. For

the most extreme case of fully focused ampholytes at 500V/cm, the current due to the diffusive flux was calculated to be 140 times smaller than the current due to the applied field.

### 2.5.3. Focusing Dynamics

The results for a typical simulation are shown in Figure 2-12. Over the course of the simulation, the slight pH non uniformity at the edges of the channels increases, and stabilizes, eventually becoming a linear gradient. As species migrate and focus, the lower mobility of the isoelectric species means that they reduce the conductivity of the sample. This agrees with the experimental observations of IEF. Figure 2-12 shows the dynamics of IEF for three selected ampholytes (#20, #50, and #120) of the 140 modeled, as well as the pH and conductivity profiles. At time zero, 100V is applied to the system. After approximately 5 seconds, the focusing reaches steady state.

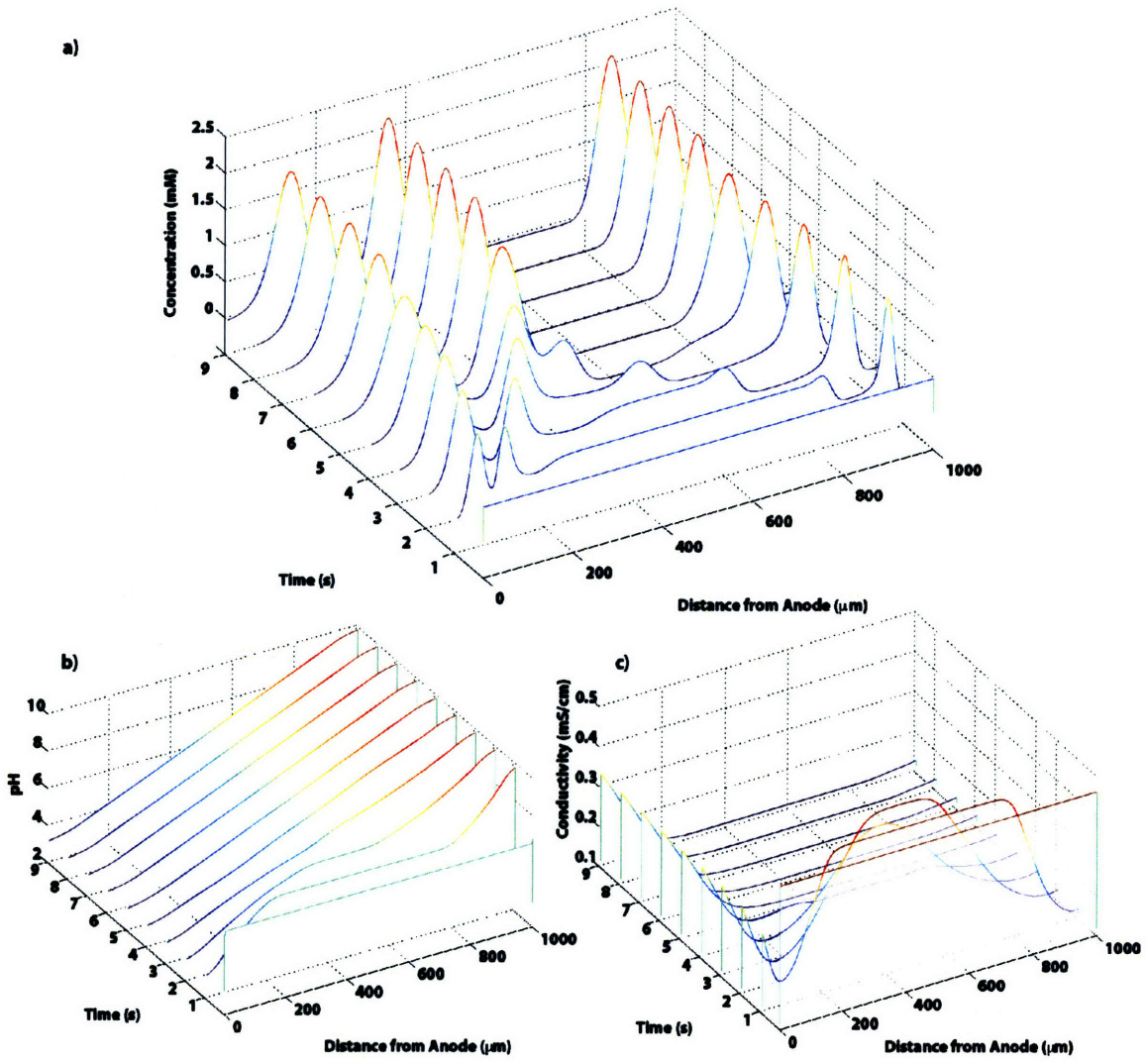


**Figure 2-12: Dynamics of IEF model with a fixed 1mm channel. a) Focusing of three selected biprotic ampholytes with respect to time. b) pH gradient with respect to time. c) Conductivity profile with respect to time.**

### 2.5.4. Pseudo-2D Approximation

This model treats the steady state two dimensional (2-D) focusing in the device as a transient one dimensional (1-D) problem. This pseudo-2-D formulation greatly simplified the computation, but is unable to represent two dimensional effects present in the device, principally two-dimensional current fluxes. Therefore, an additional model was written in Comsol Multiphysics with MATLAB (Comsol, Inc, Burlington, MA) to evaluate the effect of variable sample conductivity in two spatial dimensions.

The conductivity calculated from the transient 1-D Jacobian simulation was entered into COMSOL Multiphysics as a stationary 2-D conductivity. Figure 2-13 shows the difference

between the current calculated from this 2-D stationary model and the 1-D transient models. Applied voltage here is 50V, with the initial current density maximum of 6.23-6.21 A/m$^2$. The minimum current density was 3.53-3.66 A/m$^2$. To convert between time and space, a uniform fluid flow rate of 33 μm/sec was used. The maximum difference at 50 V (an average electric field of 500 V/cm) was found to be 3.5%, meaning that the transient model overpredicted current by at most 3.5%. With lower voltages, this difference was reduced.

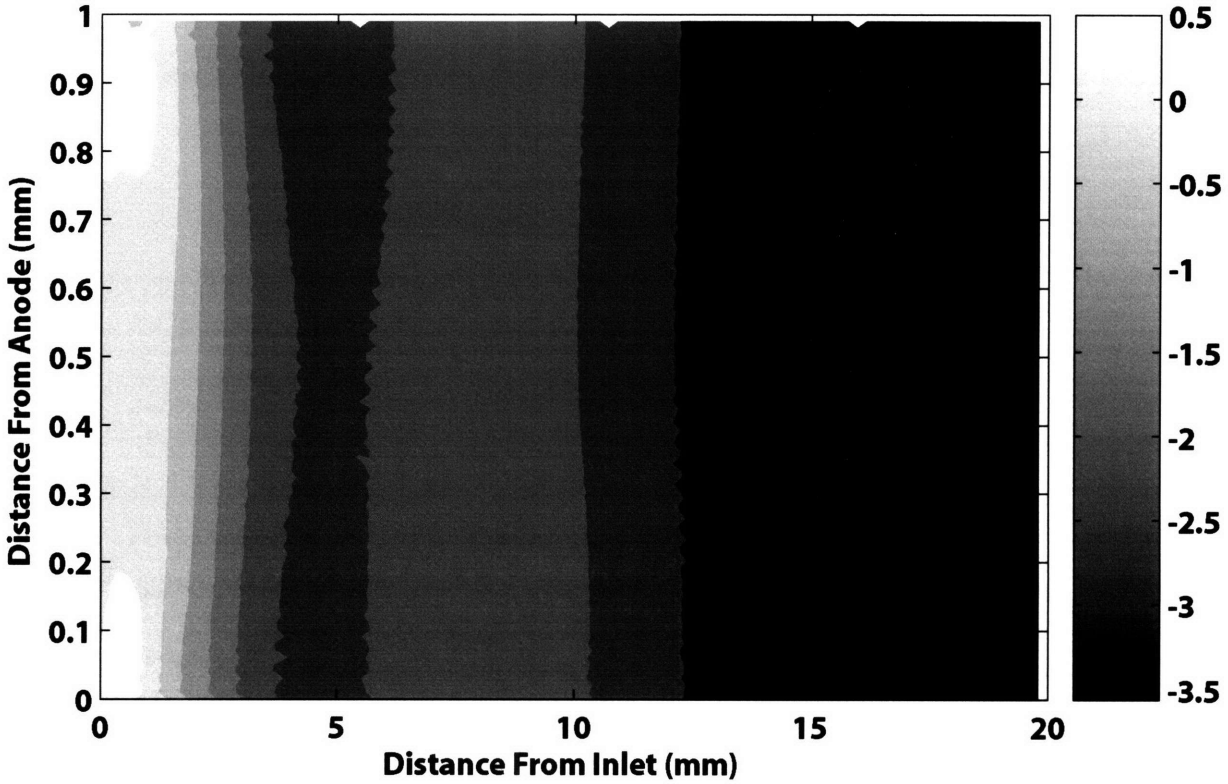


**Figure 2-13: Validity of pseudo 2D approach. The contour map plots the difference (%) between the current densities calculated for a 2-D stationary model and 1-D transient model.**

### 2.5.5. Conductivity Approximation

To calculate the local electric field for each spatial point, Equation 2-54 and 2-55 were used across the *n* spatial points. This equation is a simplified form of Equation 2-4, as it assumes that ions moving in response to the applied voltage are the only contribution to the electrical current, and that ionic diffusion does not contribute to the electric current.

$$E_n = \frac{J}{\sigma_{0,n}} \qquad \textbf{2-54}$$

$$\sigma_{0,n} = F \cdot \left( \left[H^+\right]_n \cdot \omega_H + \frac{K_w}{\left[H^+\right]_n} \cdot \omega_{OH} + \sum_i \frac{\beta_{i,n} C_{i,n} \cdot \omega_i}{(1+\beta_{i,n})} \right)$$

$$\beta_{i,n} = \frac{\left[H^+\right]_n}{K^+_{i,1}} \cdot \left( 1 + 2\frac{\left[H^+\right]_n}{K^+_{i,2}} \right) + \frac{K^-_{i,1}}{\left[H^+\right]_n} \cdot \left( 1 + 2\frac{K^-_{i,2}}{\left[H^+\right]_n} \right) \qquad \textbf{2-55}$$

This abbreviated expression for bulk conductivity was found to reduce the simulation time, as the coupling between species concentration and electric field is somewhat reduced.

To ensure that the contribution to current due to ionic diffusivity was negligible, results from the simulation were used to calculate the second term in Equation 2-4. The result is shown in Equation 2-56:

$$Error_J = \frac{\sigma_0 \boldsymbol{E} - F\sum_i z_i D_i \nabla C_i}{\sigma_0 \boldsymbol{E}} - 1 \qquad \textbf{2-56}$$

Figure 2-14 shows the current density error with and without the diffusive current term versus focusing time for simulations with various channel widths at a constant electric field, 100 V/cm. In all cases, the error was calculated to be less than 1%, confirming the assumption of Equation 2-54. As the focusing reaches steady state, the focused species have a higher diffusive flux, resulting in a larger current density error. Similarly, IEF in narrower channels also results in higher diffusive fluxes, consistently leading to greater errors for simulations with narrower channels.

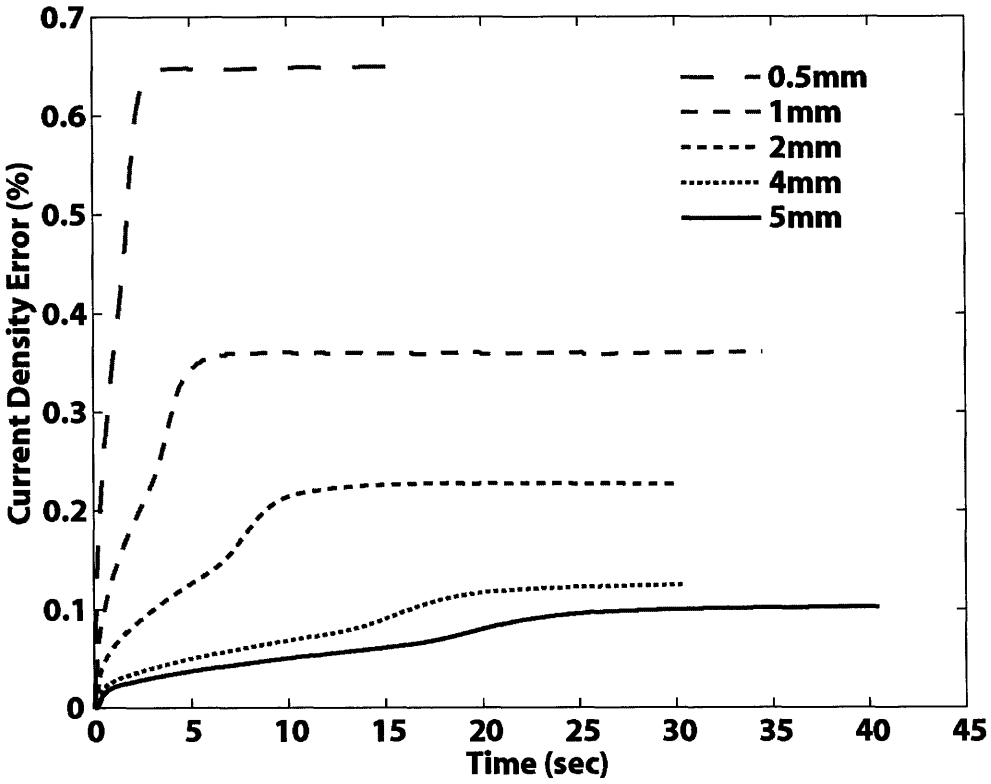


**Figure 2-14: Current density error for various channel widths as a function of focusing time. Assuming that ion diffusion in negligible in IEF results in small (<1%) errors in the calculated current density. The error increases as IEF reaches steady state, and is greater for narrow channel widths.**

### 2.5.6. Temperature Dependence

To examine the effect of temperature changes on the focusing sample, the model was run for different temperatures. Considered were two different factors altering electrophoretic behavior: change in sample conductivity (a strong function of temperature), and the change in the diffusivity of the species assuming a Stokes-Einstein dependence on temperature, as defined by Equation 2-45. The relationship between mobility and temperature was assumed to follow the relationship given by Equation 2-57, where the mobility increases by 2% per degree Kelvin. This heuristic is used for typical ions around 25°C [74].

$$\omega_i(T) = \omega_{i,0}(1 + 0.02(T - 298°K)) \qquad \text{2-57}$$

The focusing resolution is defined by Equation 2-38, where a Gaussian fit was used to calculate the standard deviation of ampholyte #70 of 140. Time to steady state was calculated as the time for the current density to reach 99% of its final value. By virtue of numerical modeling,

the effect of temperature on conductivity and ion diffusion can be examined independently of each other. Seven simulations at 10 V/cm and various combinations of mobility and diffusion temperature adjustments were analyzed. Figure 2-15 summarizes the results of these simulations in a matrix of conductivity (electrophoretic mobility) adjustment versus diffusion adjustment for focusing at three different temperatures: 0, 25, and 45 °C.

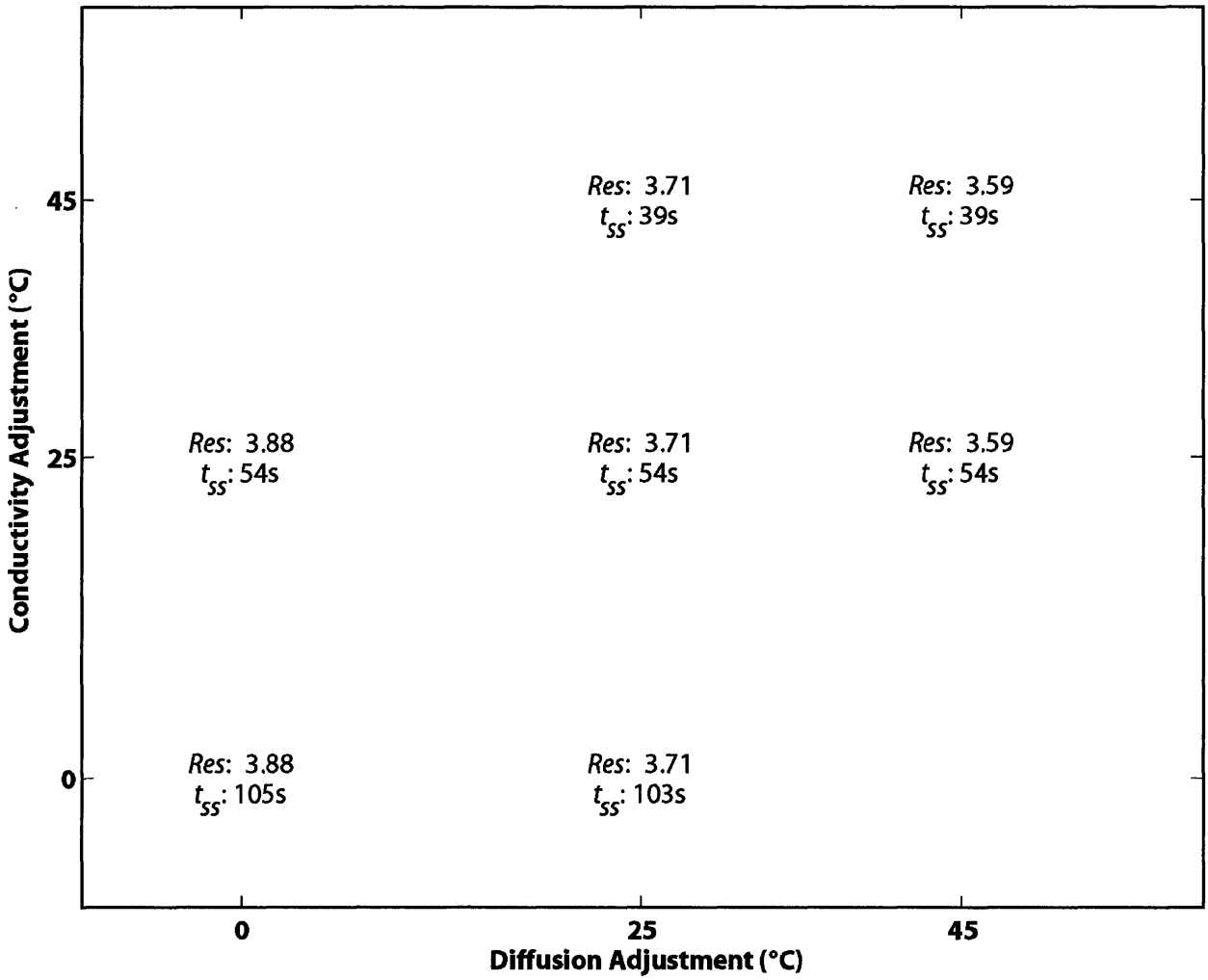


**Figure 2-15: Modeling results for temperature changes to modeling parameters. Resolution and time to steady state are shown to be functions of thermal effects on diffusion and conductivity, respectively.**

From Figure 2-15, it is apparent that the focusing resolution and time to reach steady state are remarkably independent. Resolution increases with decreasing species diffusivity, whereas the time to reach steady state decreases with increasing sample conductivity.

## 2.6. IEF Dynamics and Focusing Distances

The distance between the electrodes is a critical parameter for both the focusing time and resolution. To explore various channel geometries, six simulations were analyzed for several linear and non-linear channel geometries. Figure 2-16 summarizes these simulations where, for each case, the average electric field is held constant at 100 V/cm and the channel width is equal to 3 mm after 180 seconds of simulated focusing. The current density is plotted in Figure 2-16b as a metric of focusing as it approaches steady state; lower current density is an indication of more complete and resolved focusing.

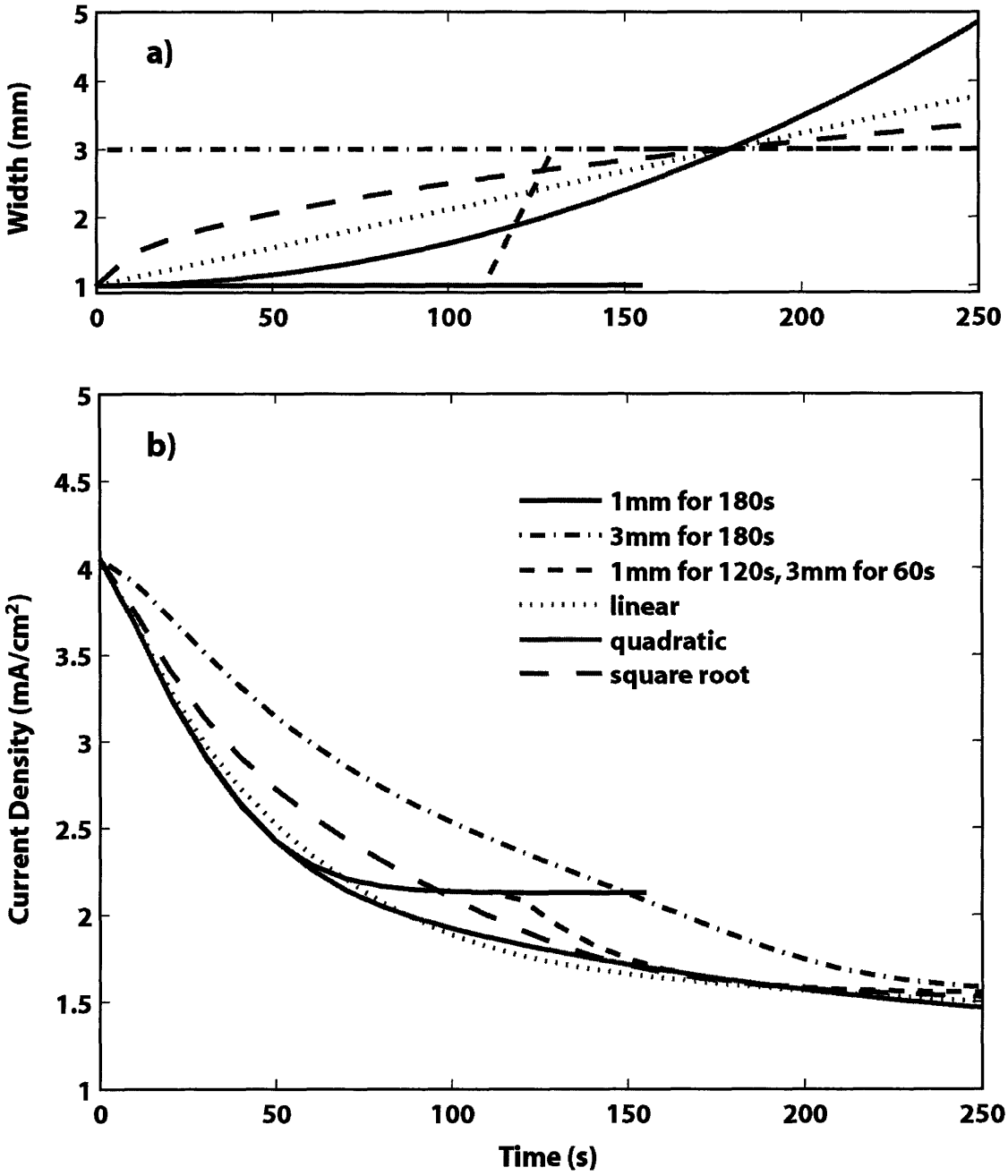


**Figure 2-16: Focusing dynamics for channels of various geometries. a) Channel width with respect to focusing time. b) Current density as a function of channel width with respect to time.**

From Figure 2-16, the geometries that appear to most efficiently focus (i.e. Have the lowest current density with respect to time) are the linear and quadratic diverging channels. Channels with a width that diverges with respect to the square root of time and channels with a step change from 1 to 3 mm appear to be not as efficient, but are an improvement over the 3 mm

channel. These interesting initial findings warranted further simulation of unconventional channel geometries for FF-IEF.

### 2.6.1. Cascaded IEF

For the case of a suddenly widening channel, Figure 2-17 shows the motivation behind cascaded IEF. Figure 2-17 shows a contour map of species concentration (components #60, #70, and #80 of 140 theoretical ampholytes) with respect to position and focusing time at 100 V/cm. The fast focusing time (5 seconds) in Figure 2-17b compared to Figure 2-17a (roughly 20 seconds) highlights the faster time scale of focusing for narrower channels. However, in Figure 2-17a, these three components can be fully resolved after 20 seconds, whereas in Figure 2-17b, they can never be fully resolved. Coupling the fast, low resolution focusing channel width with the high resolution focusing width in Figure 2-17c reduces the time to resolve the ampholytes by half, while maintaining the higher resolution of the wider channel.

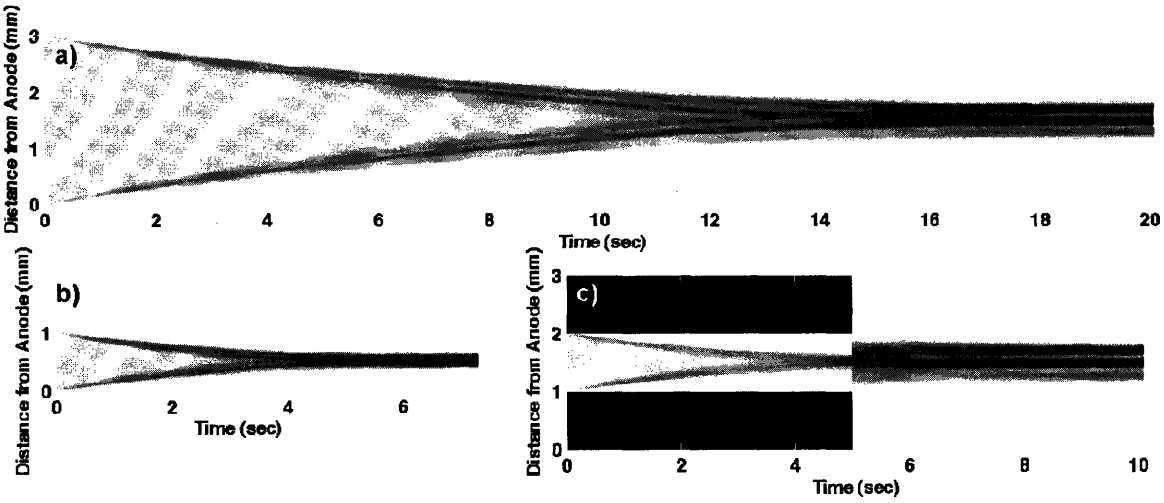


**Figure 2-17: Isoelectric focusing for various channel widths. The spatial concentration of ampholyte # 60 (cyan), 70 (blue), and 80 (red) are plotted with respect to focusing time. a) Focusing in a 3 mm channel at 100 V/cm requires approximately 20 seconds to reach steady state. b) Focusing in a 1 mm channel at 100 V/cm requires approximately 6 seconds to reach steady state. c) Utilizing a 3 mm focusing channel after focusing in a 1 mm focusing channel for 5 seconds requires a total of 10 seconds to focus.**

To test the scaling predictions used in Equations 2-38 and 2-39, several simulations were run at various widths and constant average electric field (100V/cm). Figure 2-18 shows the results of these simulations, plotting the time to reach steady state ($t_{ss}$, Figure 2-18a) and resolution *Res* (from a Gaussian fit of one of the ampholytes, Figure 2-18b) versus channel width

for the simulations. A nearly linear relationship (exponent of 0.908) exists between focusing time and channel width, as predicted by scaling arguments. The relationship between resolution and channel width also follows the predicted power law behavior, with a fitted exponent of 0.488 versus 0.5 for the analytical case. From the solid lines in Figure 2-18, a wider FF-IEF channel has the effect of increasing both focusing resolution and focusing time. These results indicate that the effects of pH gradient formation and changes in conductivity do not significantly alter the idealized focusing behavior of simple ampholytes, underscoring the usefulness of the analytical expressions for IEF.

For comparison, the simulation was made where the channel was instantly widened from 1 to 3 mm after 5 seconds (Figure 2-18, open circles) is plotted with the single, straight channel data. The results show that the higher resolution of the 3 mm channel can be reached in half the time (8.70 versus 17.49 seconds to steady state) when the average electric field is held constant at 100 V/cm.

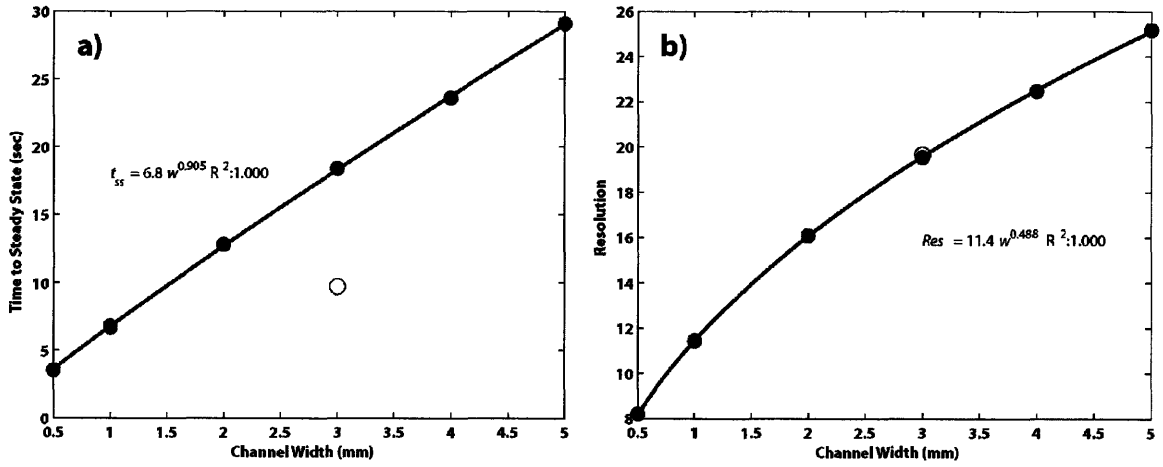


**Figure 2-18: Dynamics of the IEF simulation with respect to channel size. The results of simulations (solid circles) were fitted to two-parameter power law equations of the form $y=aw^b$ (solid lines). The time to reach steady state, a) is nearly linear ($w^{0.908}$) with respect to the channel width. The resolution b) at steady state, as defined by Equation (1), increased with nearly the square-root of the channel width ($w^{0.488}$). These findings are consistent with analytical expressions for IEF. A simulation of focusing for 5 sec at 1 mm followed by focusing at 3 mm (open circles) shows that high resolution can be reached in much less time.**

The dynamics of IEF under a step change from 1 mm to 3 mm for protein IEF was examined with other simulations. Figure 2-19 shows the simulated focusing of BSA under three different geometry configurations at identical field strengths: 1 mm, 3 mm, and 1 mm followed

by focusing at 3 mm. The protein focusing follows the "double-peak approach" observed by others [122, 20, 19, 7]: peaks form at both electrodes, move toward the pI, and coalesce. To better quantify focusing, the simulation used low electric fields (5 V/cm for each case) for slow, low resolution focusing that allowed a Gaussian fit to the data. The resolution (from a Gaussian fit, $R^2 > 0.999$) of the focusing is 1.6 times greater for the longer channel. Transitioning from a shorter to a longer channel reaches this higher-resolution steady state in 40% less time than the 3 mm case. These results demonstrate that the predictions for small amphoteric molecules in terms of channel geometry and residence time also extend to large proteins with complicated electrophoretic behavior.

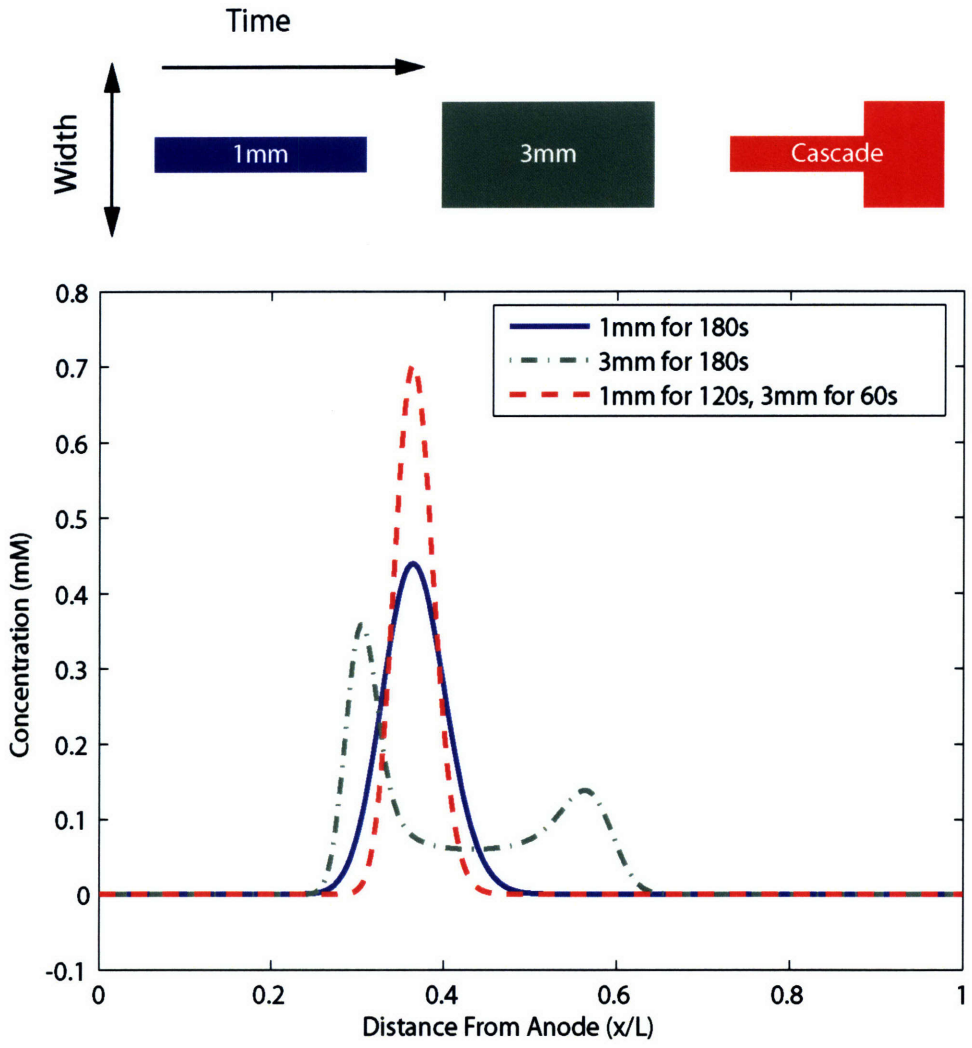


**Figure 2-19: Simulated focusing of a protein in channels of different widths. Solid line is steady state focusing after 3 min in a 1 mm wide channel; dash-dot line is a 3 mm channel, incomplete after 3 min. Dashed line is focusing in a 1 mm channel for 2 min, followed by a 3 mm channel for 1 minute. This more resolved steady state is reached in 40% less time.**

### 2.6.2. Divergent IEF

For the case of IEF in a diverging channel, the relationship between focusing time and channel distance is no longer linear. This is due to the fluid slowing as it enters a progressively larger channel. Assuming uniform flow across the width of the channel at all times, the relationship between channel distance and focusing time can be derived.

For a symmetric, linearly diverging channel with angle $\alpha$ on each side and with initial width $w_0$ and length $L$, the channel width as a function of length, $w$, is defined by Equation 2-57. This relationship can be rearranged to solve for $L$ in Equation 2-35.

$$w = 2L\tan(\alpha) + w_0 \qquad \textbf{2-57}$$

$$L = \frac{w - w_0}{2\tan(\alpha)} \qquad \textbf{2-58}$$

Assuming an inlet velocity of $U_0$, and uniform flow across the width of the channel, the rate that a slug of liquid will flow down the length of the channel at a given time is assumed to diminish proportionately with a change in $w$, as given by Equation 2-59. The assumption of uniform flow is valid when there is sufficient external pressure on the outlets of the device.

$$\frac{dL}{dt} = U(t) = \frac{U_0 w_0}{w} = \frac{U_0 w_0}{2L\tan(\alpha) + w_0} \qquad \textbf{2-59}$$

The rate that the channel diverges can be determined by substituting Equation 2-59 into Equation 2-57:

$$\frac{dw}{dt} = 2\tan(\alpha)\frac{dL}{dt} = 2\tan(\alpha)U(t) = \frac{2\tan(\alpha)U_0 w_0}{2L\tan(\alpha) + w_0} = \frac{2\tan(\alpha)U_0 w_0}{w} \qquad \textbf{2-60}$$

Integrating and solving for $w$ yields the relationship between channel width and residence time, shown in Equation 2-61.

$$w(t) = \sqrt{\left(4\tan(\alpha)U_0 w_0 t + w_0^2\right)} \qquad \textbf{2-61}$$

From Equation 2-61, we see that for a channel diverging linearly in space, the fluid inside will experience a change in channel width with respect to the square root of time.

For the case of FF-IEF in a diverging channel, the model was modified to simulate a diverging channel initially at 1 mm, and diverging at an angle, $\alpha$, of 20 degrees. Because the divergent channel can never reach steady state, Figure 2-20 shows focusing resolution after 150 seconds of focusing for various inlet velocities. The relationship between resolution and inlet

velocity shows a trend that increases with less than the square root of inlet velocity, meaning that the resolution at higher flowrates is lower than expected from simple analytical expressions.

Figure 2-21 shows more detailed results of focusing in these channels at an inlet flow rate of 6 mm/s. Here, the longer focusing time and diverging channel enable fast, complete separation of the sample. At this flowrate, the resolution at the end of 150 seconds of focusing was calculated to be 59.7. Of note is the wishbone shaped focusing profile, instead of the more linear approach to focusing observed in Figure 2-16. From these results, the divergent channel is shown to be an effective alternative to cascaded FF-IEF devices.

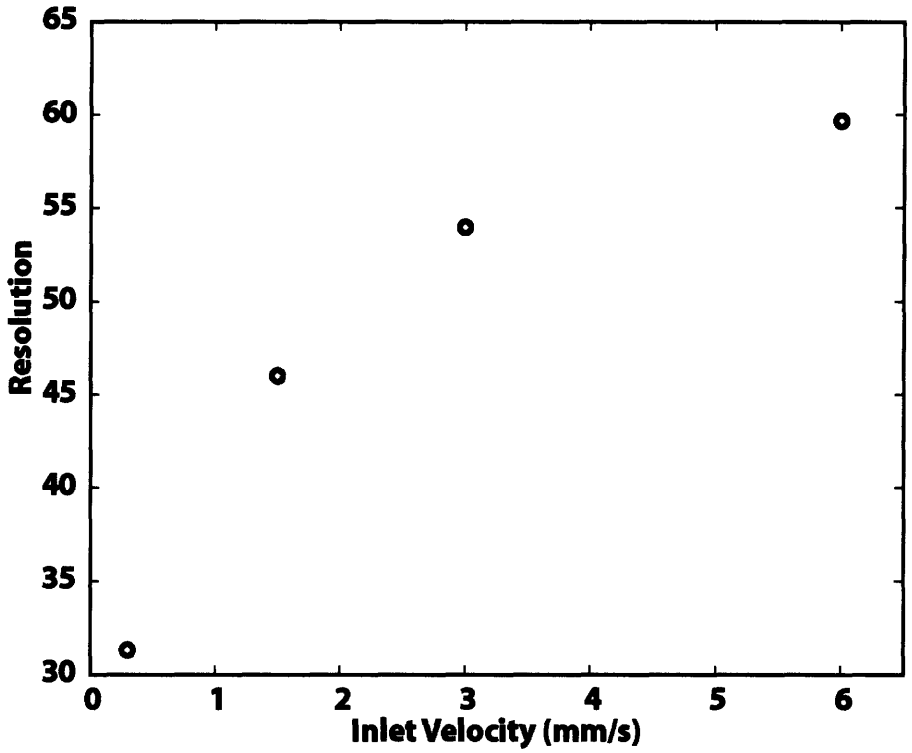


**Figure 2-20: Resolution versus inlet velocity for a 20 degree diverging channel.**

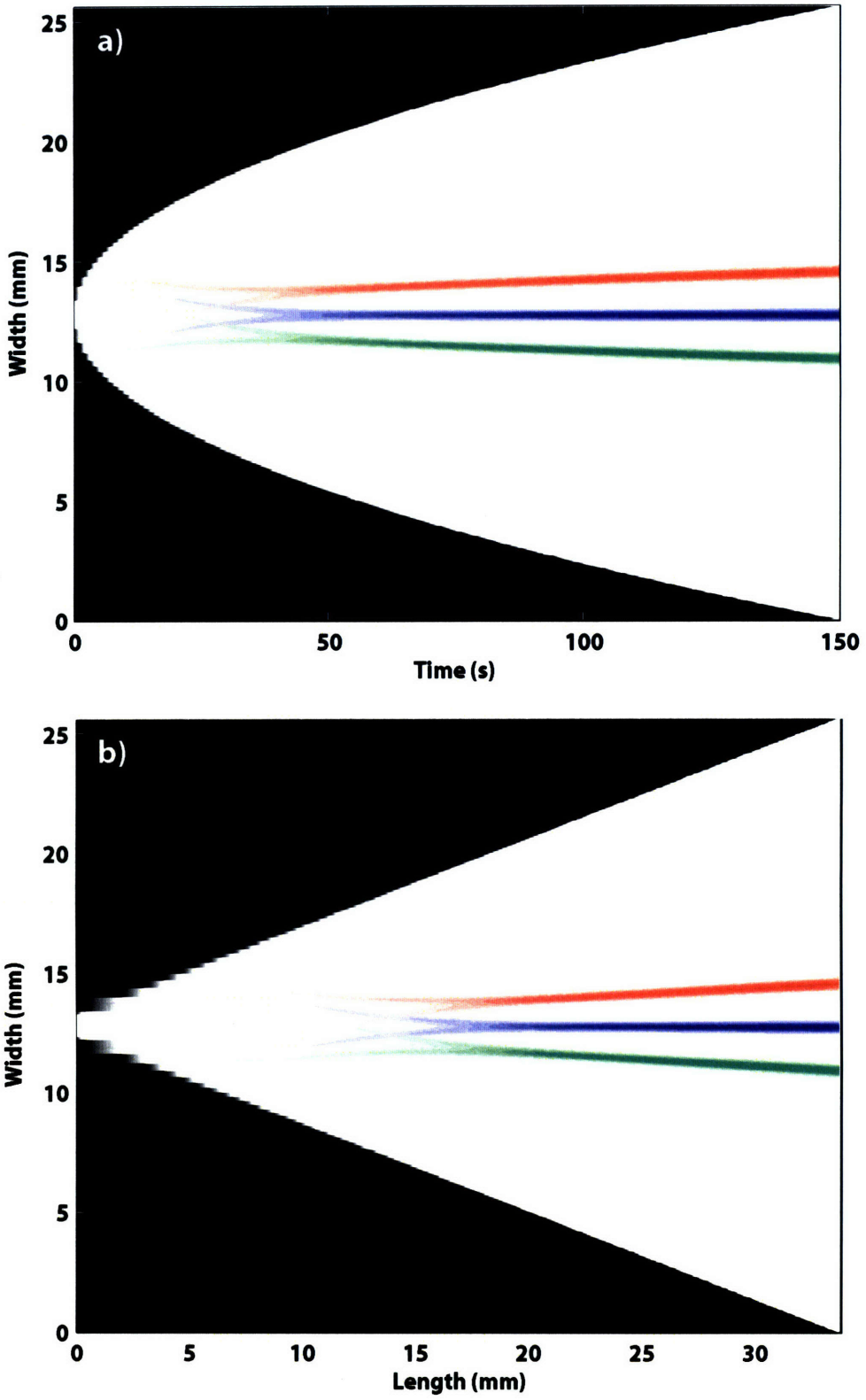


**Figure 2-21: Isoelectric focusing for a divergent channel. The spatial concentration of ampholyte # 60 (green), 70 (blue), and 80 (red) are plotted with respect to a) focusing time and b) distance from inlet. The species are focused and separated at 100 V/cm with an inlet flowrate of 6 mm/s.**

## 2.7. Conclusions

In this chapter, models for isoelectric focusing and particle electrophoresis were summarized and used to identify important parameters governing the quality of FF-IEF separations. In addition, detailed numerical simulations were developed to predict focusing behavior in linear and non-linear channel geometries and at various changes in temperature. The model was simplified from literature in order to quickly examine multiple conditions. From the analysis of various operating parameters, channel geometry was identified as an important factor. These conclusions lead to models for cascaded and divergent FF-IEF stages. These findings will be used develop original FF-IEF device designs in subsequent sections.

# Chapter 3: FF-IEF Enhanced by Active Cooling and Functionalized Gels

This chapter describes the use of active cooling and functionalized gels to enable simple and disposable micro free flow isoelectric focusing (μFF-IEF) devices. Rapid free flow isoelectric focusing is achieved in a microfluidic device by separating the electrodes from the focusing region with porous buffer regions. Moving the electrodes outside the sample channel enables the use of large electric fields without the detrimental effects of bubble formation in the focusing region. The anode and cathode porous buffer regions, which are formed by acrylamide functionalized with immobilized pH groups, allow ion transport while providing buffering capacity. Thermo-electric cooling mitigates the effects of Joule heating on sample focusing at high field strengths (~500V/cm). This localized cooling was observed to increase device performance. Rapid focusing of low molecular weight isoelectric point markers, Protein G-Mouse IgG complexes , and transcription factor – DNA complexes demonstrate the versatility of the technique. Simulations provide insight into and predict device performance based on a well-defined sample composition.

## *3.1. Introduction*

As a separation technique, isoelectric focusing (IEF) is used to sort and concentrate a sample into sub-fractions based on isoelectric point (pI). IEF also has the advantage of acting orthogonally to size based separations (e.g., SDS-PAGE), making it very attractive for low-resolution prefractionation and concentration. However IEF in a gel, as it is most commonly used, requires several hours of focusing at high voltages. Microscale IEF has been shown to operate much more quickly [47, 67, 81, 116, 133, 32], making micro-IEF devices desirable tools in simplifying complex biological samples for enhancing the sensitivity of subsequent detection assays. Unfortunately, the processing of biologically relevant sample volumes (~100 μL) remains a challenge for microfabricated batch separation techniques.

Free flow electrophoresis (FFE) [42, 100] works by applying an electric field perpendicular to a sample as it flows through a rectangular channel. With FFE, continuous operation allows sample volumes much larger than the device operating volume to be fractionated and collected. Isoelectric focusing is an ideal mode of electrophoresis for use in

FFE as it concentrates species as they are focused to their isoelectric point. In this way, sample complexity can be reduced without losses associated with dilution. Losses associated with non-specific adhesion can be mitigated by using a large sample volume relative to the device surface area, reducing the importance of surface passivation. Also, a wide, open sample channel increases the tolerance for complex biological samples, as organelles [79] and protein aggregates can be focused in the device without clogging.

There are technical challenges to constructing these devices due to the relatively large amount of electrical energy that must be delivered to the focusing sample. The primary barrier is in applying voltages high enough to create the electric field strengths needed for focusing. With the sample in direct contact with metal electrodes [79, 81], electrolysis of water creates bubbles in the channel when voltages above ~3V are applied. Recently, several groups have devised designs to surmount this barrier by isolating the metal electrodes. Fabricated wells [85, 105] above an immobilized pH gradient gel have been used to fractionate samples. For microfabricated channels, a fabricated array of channels with high hydrodynamic resistance [136, 99, 133, 60, 36] served as the electrical interface for the sample channel. Hydrogel channels formed by casting agarose around a nylon filament were shown to allow transverse electric fields of 5 to 10 V/cm [46]. Kohlheyer et al. [67, 66] used photopolymerized acrylamide within a glass device as an ion bridge, in conjunction with buffer sheath flows, to perform rapid IEF and zone electrophoresis.

A second challenge to device performance is Joule heating of the sample when large voltages are applied. Typically, conventional IEF uses active cooling to counteract heating effects, while microscale devices have relied on the high heat transfer inherent to microdevices to keep the sample at reasonable operating temperatures. However, assuming isothermal operation is not necessarily true for microsystems with high applied voltages. Because Joule heating increases roughly with the voltage squared, higher applied voltages require much more heat dissipation, perhaps more than what is possible by natural convective cooling to the environment. Models for Joule heating in microfluidic channels [21] have explored the effect of insulating material as well as autothermal (runaway) liquid heating.

Here, we design and test a device to perform free flow IEF. Our approach involves fabricating thin gel slabs within a PDMS device, not only as structural material, but as a chemically significant part of the device. Our design motivations were to improve upon previous

work [67, 81, 133, 79] not necessarily in terms of resolution, but in terms of allowing for non-ideal samples, lowering hydraulic resistance, and simplifying fabrication and operation. Heat transfer from the device is also a key concern; active heat transfer should be employed to prevent overheating of the device at high applied voltages.

## 3.2. Materials and Methods

### 3.2.1. Design and Fabrication

The free flow IEF device (Figure 3-1) was designed to have a sample channel defined by a porous material capable of allowing ion conduction between the sample channel and the electrode buffer, while preventing unwanted fluid convection between the two regions. The porous material should ideally have no electroosmotic flow as well as very small pores to facilitate ion conduction. Other characteristics, such as good mechanical strength and inertness were desired to improve device durability. The design was based on a PDMS channel bordered by posts to define placement of the porous material without the need for a photo-polymerization mask. The need for a high degree of anisotropy in the device (tall posts around a rectangular sample channel) as well as the height of the sample channel led to the fabrication of the device in PDMS. Small liquid reservoirs were located on either side of the device contained catholyte and anolyte as well as platinum electrodes, which were connected to an external power source.

The bulk of the device was fabricated using standard soft lithography techniques [33]. Briefly, a silicon wafer was coated with a layer of SU-8 2050 (MicroChem, Newton, MA), which was pattered using a 5080dpi transparency mask (Pageworks, Cambridge, MA). Next, Sylgard 184, (Dow Chemicals, Midland, MI) was cast over the SU-8 mold and cured at 70°C for two hours. Two different heights of PDMS were used in the devices, 1 mm for the area beneath the thermoelectric element, and 3 mm for the inlet and outlet connections. To create these differing heights, a glass platform approximately 18 mm wide by 75 mm long was created from a glass microscope slide. This platform was placed into the uncured PDMS. Spacers 1 mm thick were glued to either of the extreme ends of the platform. Due to subtle drifting, the platform was periodically repositioned over the wafer during curing. After curing, the PDMS was peeled off of the master; individual devices were cut out, and fluidic connections were punched using a 20 gauge Luer stub adapter (Becton-Dickinson, Sparks, MD). When a 23 gauge Luer stub adapter was inserted in to these holes, the connection was self-sealing; no epoxy or glue was necessary.

Next, the devices were treated with oxygen plasma for 40 seconds prior to permanently bonding to a 25x40mm glass cover-slip (VWR, West Chester, PA).

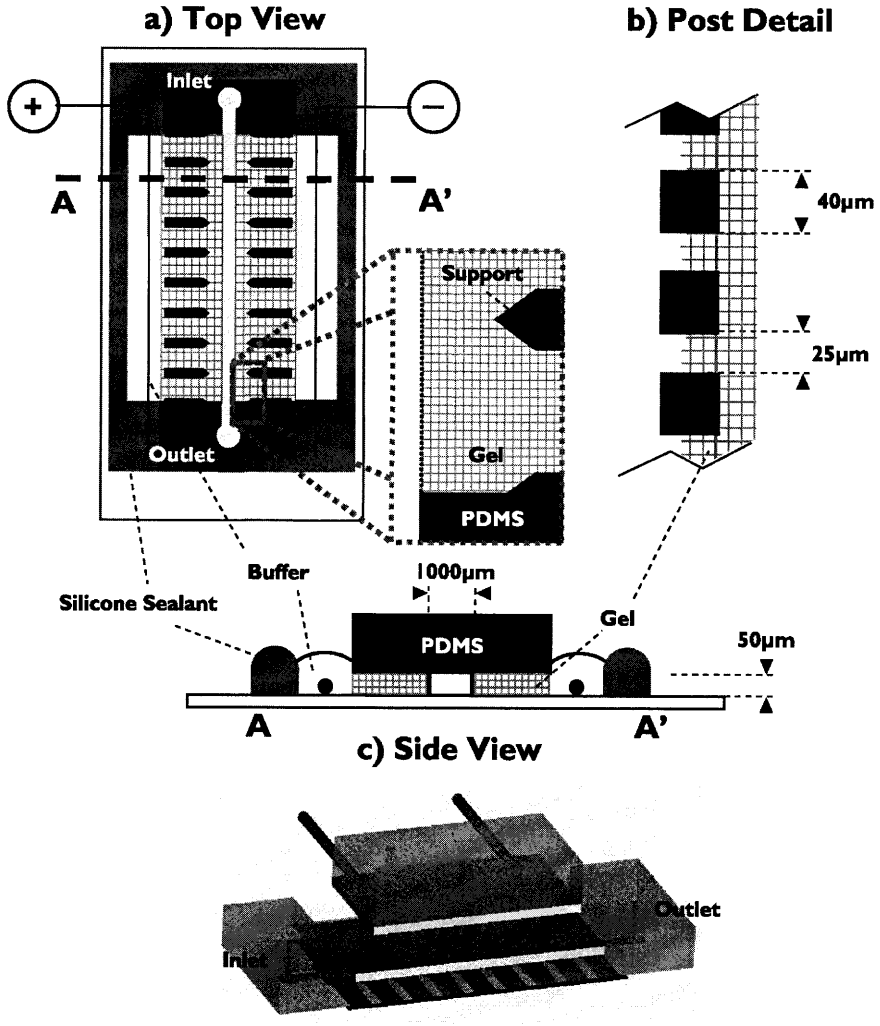


Figure 3-1: Layout of transverse IEF device. Top view (a) shows the PDMS device with the sample channel bordered by left and right porous material regions (cross hatched areas) and anode and cathode, respectively. Silicone sealant (solid gray) is used to form the reservoirs for the anolyte and catholyte buffers, as well as to hold the platinum electrodes in place. The sample channel is 1mm wide, 20 mm long, and 50μm deep. It is separated from the gel sections by 40 μm × 40 μm, 50 μm tall posts (b) spaced 25μm apart (307 posts on each side of the channel). Larger elongated post structures (0.75 x 3 mm rectangle with 0.75 mm equilateral triangle) support the fragile post array and the porous regions. The device presented has a single inlet and single outlet. Side view (c) shows the device in cross-section (not to scale). A rendering of the device with a thermo electric cooler (d) illustrates the placement of the cooling module, heat spreaders, and water cooled chip.

### 3.2.2. Gel Casting

The gel was cast inside the device on each side of the sample channel (Figure 3-1b) after the PDMS had been sealed to the glass substrate. In order to ensure that the PDMS surfaces regained their hydrophobicity following the plasma treatment, there was a 24 hour wait before gel casting. Surface tension effects at the post structures (Figure 3-1b) confined the gel and prevented penetration into the sample channel during casting.

Polyacrylamide has been used in other microfluidic applications [47, 132, 52, 67] and is usually patterned by UV initiated polymerization. The present device was designed to avoid this step. In this case, ammonium persulfate (APS, VWR, West Chester, PA) was used the free radial initiator. Since oxygen inhibits acrylamide polymerization and has a high permeability in PDMS [84], thorough oxygen removal procedures were required. To remove oxygen, the PDMS devices were placed in a vacuum oven at 70°C and 50 mmHg for more than 8 hours. Subsequently, the devices were kept under nitrogen. The monomer solution used in the polyacrylamide devices tested was 15% total acrylamide (15% T), with 3% of the acrylamide present as bis-acrylamide (3% C) (PlusOne ReadySol IEF, GE Healthcare, Piscataway, NJ). Solutions containing acrylamide are neurotoxic and should be handled with caution. Immobilines (pKa 3.6 and pKa 9.3, GE Healthcare) were added to the monomer solution to a final concentration of 12 mM. For the anode side gel, 1 mL of this monomer solution was mixed with 80 μL 1% v/v Triton X-100 (EMD Chemicals, Gibbstown, NJ), 3 μL 1 M $Na_2SO_3$ (Mallinckrodt Baker, Phillipsburg, NJ), 3 μL 1M Na2S2O5 (Mallinckrodt Baker), 2 μL 230 mM $CoBr_2$ (Sigma-Aldrich, St. Louis, MO), 2 μL TEMED (EMD Chemicals) and 6 μL 10% ammonium persulfate (APS, EMD Chemicals), in this order. The cathode side gel had a slightly different recipe, the proportion was 1000:40:3:3:2:1:6, for the reagents, respectively. There were two reasons for the different recipes: i) the cathode gel mixture had a lower surface tension due to the pKa 9.3 Immobiline, so less Triton was necessary, and ii) only the basic form of TEMED accelerates polymerization, so more is needed for low pH gels. Cobalt, sulfite, and metabisulfite levels were adjusted to scavenge oxygen quickly [138]. After adding APS as the initiator and TEMED as the polymerization accelerator, the liquid mixture was introduced to the side of the device, where it was drawn in by capillary action. Surface tension held the monomer solution at the post array, long enough for the gel mixture to become crosslinked; approximately 40 seconds.

### 3.2.3. Device Packaging and Operation

Platinum wires (0.5 mm diameter, Alfa Asear, Ward Hill, MA) were used to connect the electrode reservoirs to a high voltage electrophoresis power supply (VWR, West Chester, PA). Silicone sealant (ASI 502, American Sealants Inc, Fort Wayne, IN) was used to fix the wires in place and to form reservoirs for the anolyte and catholyte buffers. The anolyte used was 20 mM phosphoric acid with 0.4% w/v hydroxypropyl methyl cellulose (HPMC, Fluka, Buchs, Switzerland); the catholyte was 20 mM lysine and 20 mM arginine (1X IEF Cathode Buffer, Bio-Rad, Hercules, CA) in 0.4% HPMC. To reduce protein adsorption and electroosmotic flow [131], the channel was incubated with a 1% w/v solution of poly(vinyl alcohol) (PVA, MW 146-186kDa, 87-89% hydrolyzed, Sigma-Aldrich) at room temperature overnight. Sample buffers were pulled through the device using a syringe pump (EW-74901-10, Cole-Parmer, Vernon Hills, IL) set to withdrawal mode. At the inlet of device, a 200 μL pipette tip was simply inserted into the PDMS. This sample reservoir was easily refilled by pipetting samples into the top of the pipette tip. Different samples could also be "queued" by using 10 μL of perfluorodecalin (Sigma-Aldrich) as a spacer. The negative pressure applied to the outlet of the device was sufficient to ensure steady operation without adversely affecting the polyacrylamide gel. In separate trials, to ensure that there was no fluid convection through the gel, a suspension of fluorescent beads flowing through the device (6 μm, Duke Scientific, Palo Alto, CA) without an applied voltage were not observed to focus hydrodynamically or to slow as they moved down the sample channel.

Joule heating was counteracted by active cooling with a miniature thermo-electric cooler (TE-35-0.6-1.0, TE Technology, Traverse City, MI) placed on top of the device. Although cooling through the PDMS side of the device is much less efficient (the thermal resistance is roughly 60 times greater than the glass coverslip) it was necessary in order to observe focusing within the device. The cold side of the TE module was separated from the focusing channel by a 0.6 mm thick silicon heat spreader and 1 mm thick layer of PDMS. The hot side of the TE device was cooled by water flowing through a custom made PDMS and silicon chip. To assemble these chips, PDMS was cured around a small piece of glass (approximately 5 by 13 by 1 mm high) to create a rectangular chamber. After curing, the PDMS was cut to the size of the silicon heat sink (approximately 8 by 20 by 4 mm high) and fluidic connections were punched out on opposite corners of the chamber. The PDMS and silicon chip were treated with oxygen

plasma for 1 minute to ensure adequate bonding. The cooling rate of the TE module was adjusted by varying the water flowrate through the PDMS and silicon chip (1-3 mL/min). This sealed chip was affixed to the top (hot side) of the TE module with a thermal joint compound (Type 120, Wakefield Engineering, Pelham, NH) and 5-minute epoxy (Devcon, Danvers, MA). A separate power supply (Protek 3015B, Tempe, AZ) was used to supply 3V and 0.75A to the module. The cooling rate at this amperage was measured to be between 0.35 and 0.88 W, depending on the water flowrate used.

### 3.2.4. Dye, Protein, and DNA Preparation

Dye focusing experiments were conducted with fluorescent low molecular weight pI markers (isoelectric points: 3.5, 5.1, 7.2, 7.6, and 9.5, Fluka, Buchs, Switzerland) and fluorescein disodium salt, (EMD Chemicals, Gibbstown, NJ),). Markers were used at a final concentration of 1 mg/mL and a final fluorescein concentration of 13.3 μM was used. In all cases, Ampholine 3-10 was mixed to a final concentration of 2% in deionized water (Millipore, Billerica, MA). To reduce EOF and increase solubility, HPMC and Triton were added to final concentrations of 0.2% w/v and 0.1% v/v, respectively.

For protein focusing experiments, FITC BSA (Sigma-Aldrich) was used at 130 μg/mL (~2μM) in 2% Ampholine 3-10, and with 0.2% w/v HPMC in deionized water. Because of the low ionic strength and BSA's proclivity for nonspecific adhesion, Triton was used at a final concentration of 0.5% v/v. For affinity IEF experiments, Alexa 488 conjugated Protein G (Invitrogen, Carlsbad, CA) and chromatographically purified Mouse IgG (Invitrogen) were mixed in phosphate buffered saline (PBS, Invitrogen). For all experiments, the concentration of Protein G was held constant at 20 μg/mL (1 mM). To remove any free dye in solution, 0.5 mL of Protein G (20 μg/mL) was dialyzed using a dialysis cassette (Slide-A-Lyzer 3500 MWCO, Pierce Biotechnology, Rockford, IL) in 500 mL of PBS for 16 hours. Ampholine 3-10 was added to a final concentration of 2% prior to the addition of IgG. The mixture was allowed to react for a minimum of 15 minutes prior to focusing. For pure Protein G and low levels of IgG (5 μg/mL), no Triton or HPMC was added to the mixture. For high levels of IgG (22 μg/mL), Triton was added to 0.1% v/v to reduce agglomeration and precipitation at the complex's pI. In the event of excessive precipitation at high levels of IgG, the device was flushed with 100 μL of 1% Triton to remove adsorbed protein.

For mobility shift assay measurements (EMSA), recombinant human NF-kB p50 subunit (rhNFkB, Promega, Madison, WI) was used according to the manufacturer's EMSA protocol. Instead of radio-labeled DNA, synthesized dsDNA (Integrated DNA Technologies, Coralville, IA) was used. The unlabeled consensus biding sequence was 5' AGTTGAGGGGACTTTCCCAGGC 3' and was used at 300 nM as a binding competitor. The unlabeled mutant binding sequence was 5' AGTTGAGCCGACTTTTACAGGC 3' used at 300 nM as a non-specific competitor. The labeled consensus sequence had a Cy3 fluorophore covalently bound to the 5' end of the sequence and was used at 15 nM.

### 3.2.5. Mitochondrial Preparation

Mitochondria from HeLa cells were crudely prepared by lysing the cells mechanically in a hypotonic buffer, and separating the organelles by centrifugation. For each experiment ~$3.25\times10^6$ cells were lysed in a low salt buffer (10mM HEPES pH 7.4, 1mM EDTA, 70 mM sucrose, 210 mM Mannitol, and 10mg/ml of leupeptin, pepstatin, chemostatin (Sigma-Aldrich) and suspended in 0.5 mL EGTA buffer, and kept on ice. The membrane potential specific dye JC-1 (JC-1 assay kit, Invitrogen, Carlsbad, CA) was used to stain the mitochondria for visualization. With the JC-1 assay kit, CCCP (carbonyl cyanide 3-chlorophenylhydrazone) was used to depolarize the membrane prior to staining for a negative control. Both the control and untreated mitochondrial preparations were made to have a final concentration of 2% Ampholine in EGTA buffer. The sample introduced to the IEF device was 350 μL of each mitochondria mixture, 150 μL of 40% Ampholine 3-10, and 100 μL of 2% HPMC.

### 3.2.6. Current Measurements

Current measurements were made with a digital multimeter (NI-4060) and LabView software from National Instruments (Austin, TX). To measure total current, a 100 ohm current shunt was used, with the corresponding voltage drop measured by LabView. From these measurements, changes in sample conductivity due to IEF and joule heating could be approximated. Once applied, the total current varied as a function of time, dropping as the buffer regions equilibrated and the ampholytes in the sample became focused.

### 3.2.7. Imaging and Analysis

Focusing behavior was observed with an inverted fluorescent microscope (Axiovert 200, Carl Zeiss, Inc, Thornwood, NY) with a high speed 8-bit color camera (MF-046C, Allied vision technology GMBH). A near-UV excitation filter was employed in pI marker focusing, and a FITC filter (green channel) was used to detect green fluorescence. Full frames were captured with a shutter time between 100 ms and 2.5 seconds, depending on the fluorescent intensity of the sample. The images captured by the camera were subsequently processed by programs written in MATLAB (The Mathworks, Natick, MA). Full-color images were desaturated prior to analysis. To find pixel intensity across the width of the channel, 100 to 500 pixels from a steady state image were averaged, and normalized to the maximum intensity.

### 3.2.8. Simulation of Species in an Idealized Ampholyte Buffer

For simplicity, the steady state two dimensional (2-D) focusing in the device may be approximated as a transient one dimensional (1-D) problem. A 1-D free flow IEF model was developed similar to Bier et al. [9, 97, 89]. Described in chapter 2, the IEF model is summarized here. Briefly, for an idealized ionic species undergoing electrophoresis, the general time dependent 1-D formulation is given by the following system of equations:

$$\frac{\partial C_i}{\partial t} = \frac{\partial}{\partial x}\cdot\left(D_i\frac{\partial C_i}{\partial x} - \mathbf{E}\frac{z_i D_i F}{RT}C_i\right) \qquad \textbf{3-1}$$

$$\mathbf{J} = -\mathbf{E}\frac{F^2}{RT}\sum_i z_i^2 D_i C_i - F\sum_i z_i D_i\frac{\partial C_i}{\partial x} \qquad \textbf{3-2}$$

$$\left[H^+\right] - \frac{K_w}{\left[H^+\right]} + \sum_i\left(z_i C_i\right) = 0 \qquad \textbf{3-3}$$

Equation 3-1 describes the species concentration, $C_i$, as both a function of position and time. Moreover, $C_i$ depends on the diffusion constant, $D_i$, charge number, $z_i$, temperature, $T$, and the local electric field, $\boldsymbol{E}$. Equation 3-2 is the current density within the device, assuming no ionic convection. Equation 3-3 enforces electroneutrality, which is assumed in the sample channel, where $K_w$ is the dissociation constant for water. In Equations 3-1 and 3-2, $F$ is Faraday's constant and $R$ is the ideal gas constant. The integral of the electric field was set equal to the applied voltage. In the case of isoelectric focusing, the sign of $z_i$ changes as the species enters regions of different pH, reversing the electrophoretic flux at the isoelectric point. From

Equation 3-1, it is apparent that the performance of IEF depends on both the diffusive and electrophoretic fluxes of the sample. The second term in Equation 3-2 describes the current density due to the diffusive flux of ions in the sample buffer. In order to simplify the system of equations; this diffusive current was assumed to be negligible compared to the current due to the applied field. To validate the model, previously published results [9, 97] were reproduced.

To model the formation of the pH gradient, the model considered phosphate ions (0, -1, and -2 valences), sodium ions, fluorescein, as well as 150 theoretical ampholytes. These ampholytes were assumed to be biprotic with pIs uniformly spanning the range of 3 to 10. The difference between the lower pKa and higher pKa was set to be 2 pH units. [89] Focusing of bovine serum albumin (BSA) was simulated with a protein model similar to Mosher et al. [90, 88] However, BSA titration data [17] was made continuous by a quartic/cubic rational fit. The system of equations used in the model constitutes a set of differential-algebraic equations (DAE), which were integrated numerically by DAE software (Jacobian, Numerica Technologies, Cambridge, MA).

## 3.3. Results and Discussion

### 3.3.1. Model Evaluation and Device Characterization

It is useful to identify the electric fields present in the sample channel versus the gel. By rapidly replacing the sample solution with a solution with a high, known conductivity, (1 M KCl) the resistance due to regions outside of the sample channel can be estimated. Depending on the original conductivity of the sample introduced to the device, the gel (which accounts for ~90% of the cross-sectional area) was measured to have a lower average electric field than the focusing sample. For samples with high conductivity, i.e. containing PBS, the electric field in the gel was determined to be 4.7 times lower than in the sample channel, presumably due to salt taken up by the gels. For the case of fluorescent IEF markers, which were dissolved in deionized water and 2% Ampholine, the electric field in the gel was half that in the sample channel. To demonstrate isoelectric focusing and modeling of proteins, FITC conjugated bovine serum albumin (FITC-BSA) was selected. BSA has a well-known titration profile [17], with a pI of approximately 4.8. Figure 3-2a shows the simulated and actual focusing of FTIC labeled BSA. The field strength was estimated to be 500 V/cm, with focusing complete in under 72 seconds. Despite the high level of surfactant, there was some adhesion of FITC-BSA at the anode and at its isoelectric

point. There was also a second, unknown peak that appeared at a more neutral pH, most likely an impurity or protein degradation product. Nonetheless, there was good agreement of simulation and experiment, both in the location of the focusing as well as peak width.

Another method of observing the pH gradient formed in the device is to use pH dependent fluorescent indicators such as fluorescein. Fluorescein has four relevant charge states: -2, -1, 0, and +1, that have different fluorescent properties. Fluorescein's pH behavior is well known and can be used to identify pH gradients. In IEF, a change in fluorescent intensity will identify the pH across the width of the channel, but fluorescein's own electrophoretic behavior cannot be ignored. To model fluorescein, values for absorbance, quantum yield, and proton dissociation were used from Sjoback et al. [111]. The pH gradient was assumed to be identical to the gradient determined by pI marker focusing, as the field strengths and sample compositions were similar. The resulting focusing (pixel intensities were in the linear range of the camera) agreed with model predictions (Figure 3-2b). The experiment was carried out with a 36 second residence time and an applied voltage of 100V, with the average field strength estimated at 530V/cm. The dashed line in Figure 3-2b is the calculated steady state concentration profile for average field strength of 530 V/cm. Using the quantum yield for the various forms of fluorescein results in a calculated fluorescent output plotted by the dotted line in Figure 3-2b. This calculated profile agrees with the experimental observations.

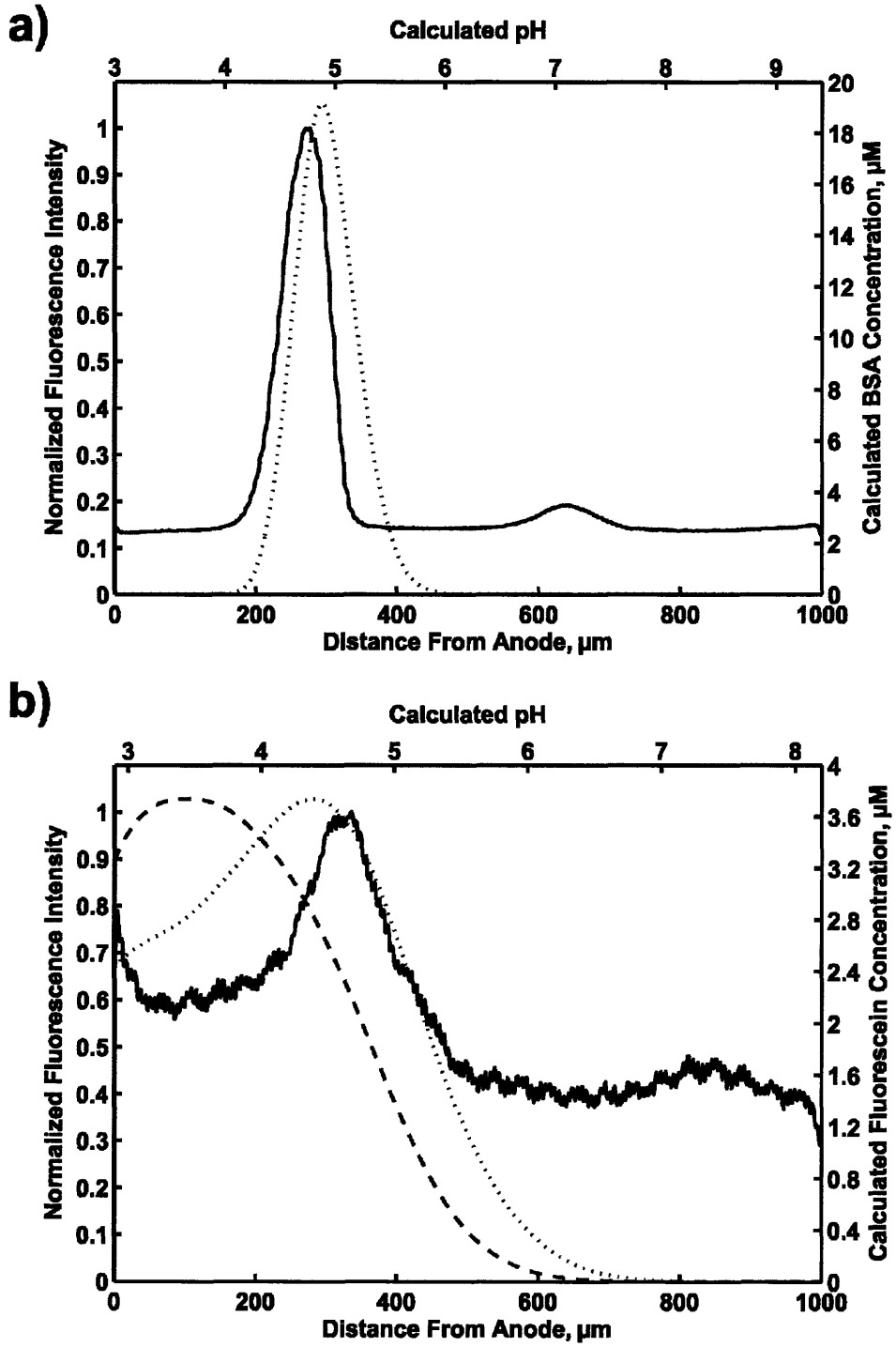


**Figure 3-2: Comparison of experimental results to theory. a) Focusing of FITC tagged BSA. Solid line indicates fluorescent intensity across channel after a 72 second residence time and an applied voltage of 150V. b) Focusing of fluorescein. Solid line shows the measured normalized fluorescent intensity across channel. The dotted line is the predicted fluorescence based on local pH. [111]**

### 3.3.2. Current Measurements

Understanding the potential drop across the channel is essential to quantifying device performance. Because IEF inherently lowers the sample conductivity, the resistance of the channel changes with time. Figure 3-3 shows the current measurement for the focusing of fluorescein (discussed in the following section). At time zero, 100V was applied to the device. The exponential decline in current is consistent with the simulation results. The residence time of the device was 36 seconds, whereas the current reached steady state after roughly three residence times. From this observation, it can be inferred that the gel has an additional effect on device performance. The gel regions were observed to loose conductivity over the course of the experiment. Suggesting that over time, ampholytes enter the gel and gradually change the pH to the extreme end of the ampholyte range. These extremes bracket the pKa's of the Immobilines, causing them to loose their charges. This effect works against the design goal of maintaining a high conductivity and complicates model comparisons. Nevertheless, the change in gel conductivity only reduces the efficiency of the device with respect to applied voltage, and can readily be compensated with greater applied voltages to achieve rapid focusing.

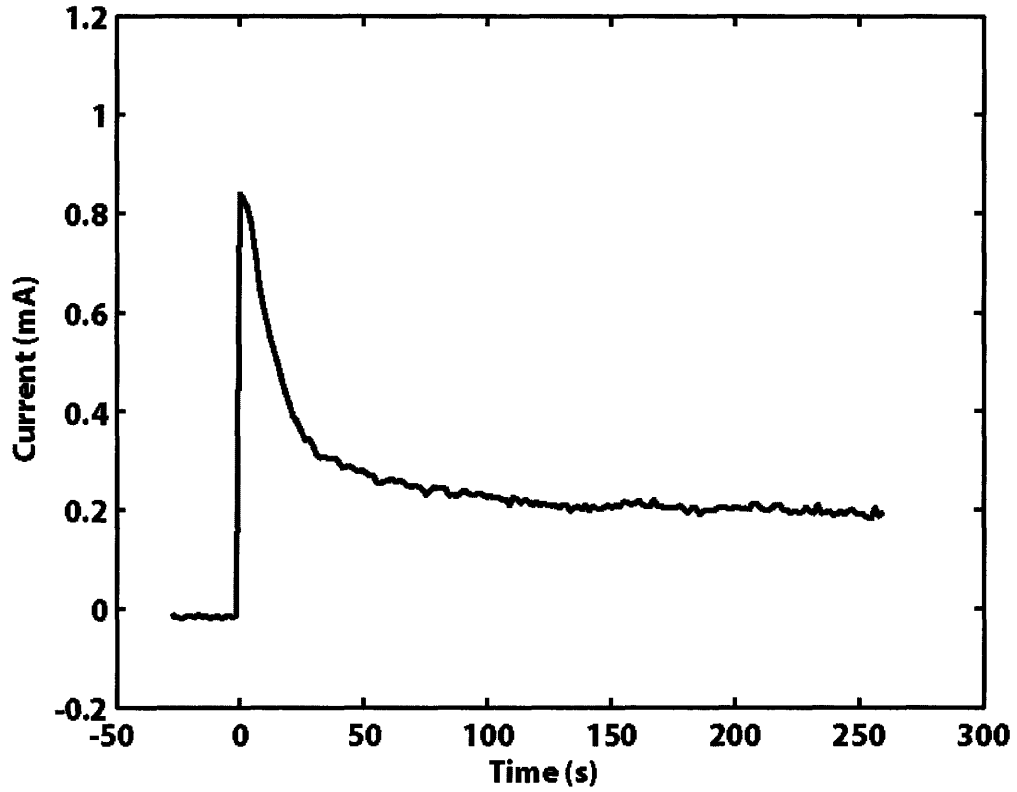


**Figure 3-3: Transient current profile for a typical focusing experiment. At time 0, 100 V are applied to the device. As species focus, the overall conductivity of the sample drops, resulting in a lower current passing through the system.**

### 3.3.3. Focusing of Amphoteric Dyes

Free-flow IEF can, in principle, focus anything with an isoelectric point, regardless of molecular weight. However, the high diffusivity of low molecular weight compounds imply that high electric fields are required to observe focusing of lower molecular weight compounds. As a demonstration of the high fields possible with the present design, low molecular weight pI markers [115, 114, 57] and fluorescein were successfully focused in the device.

Fluorescent IEF markers with pI's less than the anode or greater than the cathode gel pKa were selected, in order to better characterize the interaction between the sample and gel electrode. Figure 3-4 shows the focusing of a mixture of 5 different markers: 3.5, 5.1, 7.2, 7.6, and 9.5. As expected, species with pI's outside the pH range defined by the anode and cathode pKa's are driven out of the sample channel and into the corresponding gel sections by electrophoresis. Markers with pI's of 3.5 and 9.5 were focused inside the anode and cathode gels, respectively. In comparison with Kohlheyer et al. [67], the increased channel cross-section

(50x1000 versus 15x500 microns) reduces the overall resolution, but allows for higher volumetric flowrates (55 versus 20 nL/s) and a greater than 40-fold reduction in hydraulic resistance. Ampholine 3-10 used in the sample buffer is designed to create a linear pH gradient for IEF applications. Linear regression on the peaks (3.5, 5.1, 7.2, and 7.6) in Figure 3-4 (cooled device) yields a linear fit in Equation 3-4, ($R^2 = 0.985$).

$$pH = 5.29 \cdot 10^{-3} x + 2.94 \qquad \textbf{3-4}$$

Here, $x$ denotes the distance from the anode in microns. This fit implies that a linear pH gradient does form in the sample channel, but only in the range of 2.9 to 8.2. The absence of high pH markers and ampholytes leads to the conclusion that electroosmotic flow is responsible for shifting the focused bands towards the cathode. The asymmetric focusing of the pI 5.1 marker, which extends as far as pH 6.4, could be a characteristic of the dye, an impurity, or a degradation product.

For the experiment shown in Figure 3-4, a total of 168 mW of electrical power must be removed from the device. Under adiabatic conditions, this would heat 1 μL (the volume of the sample channel) of water at a rate of 40°C/s. In practice, the device was measured (with a thermocouple applied to the glass bottom of the device) to reach temperatures of at least 42°C, raising concerns of Joule heating. At high field strengths, increased Joule heating becomes disruptive to focusing as heat is generated faster than it can be dissipated by the device. Elevated operating temperatures are disruptive to device operation, creating bubbles and increasing electroosmotic flow. To prevent the device from overheating, a thermo-electric element was used to cool the top of the device. A cooling module with a water-cooled hot side and connected to the device via a silicon heat spreader affixed to the top of the device. This cooling rate was sufficient to more than compensate for Joule heating in the sample chamber. At excessive cooling rates, condensation formed on the surface of the glass coverslip, reducing the fluorescence signal from the channel. To compare focusing between devices with and without cooling, a second device was again operated at 200 V with the same sample mixture but without external cooling. Without cooling, the best results obtained were relatively broad peaks, with increased electroosmotic flow (Figure 3-4). Also, the channel was frequently blocked by the

formation of bubbles due to dissolved gasses loosing solubility at the elevated liquid temperatures.

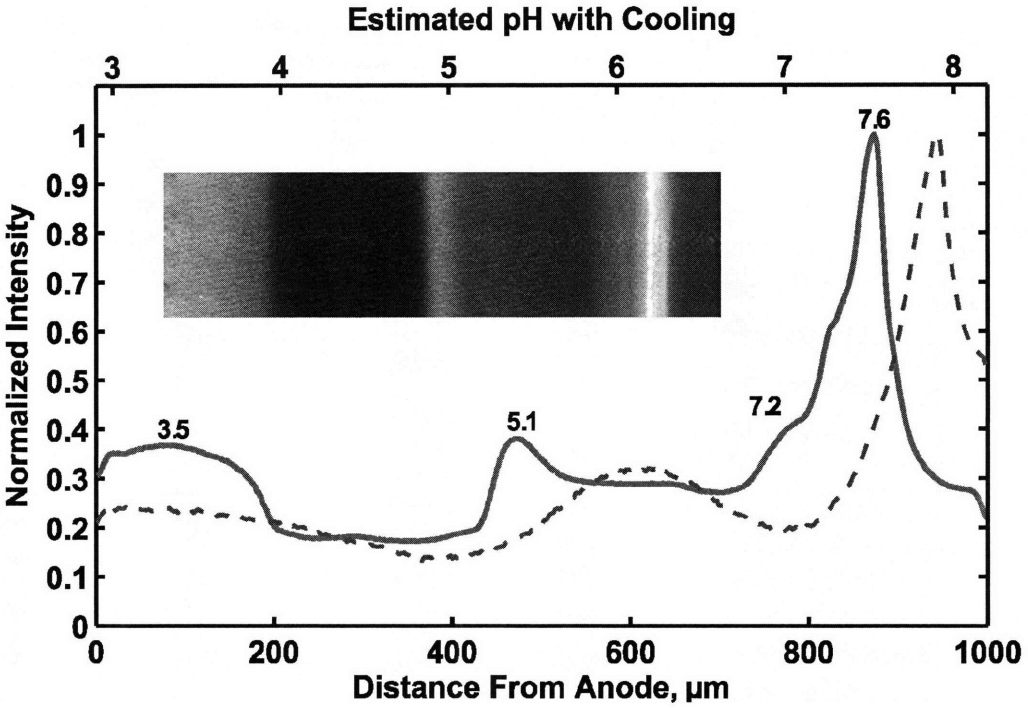


**Figure 3-4: Focusing of IEF markers with cooling (solid line) and without cooling (dashed line). Applied voltage was 200V with a focusing time of 14 seconds. Inset: Contrast enhanced microscope image with anode to the left, cathode to the right. Markers with pI's of 3.5, 5.1, 7.2 and 7.6 focus within the sample channel. Marker with pI 9.5 leaves the channel through the cathode side gel and accumulates in catholyte reservoir. The focusing occurs rapidly with an electric field estimated to be 520 V/cm. The estimated field strength without cooling is 140 V/cm. Both experiments were carried out at 200V.**

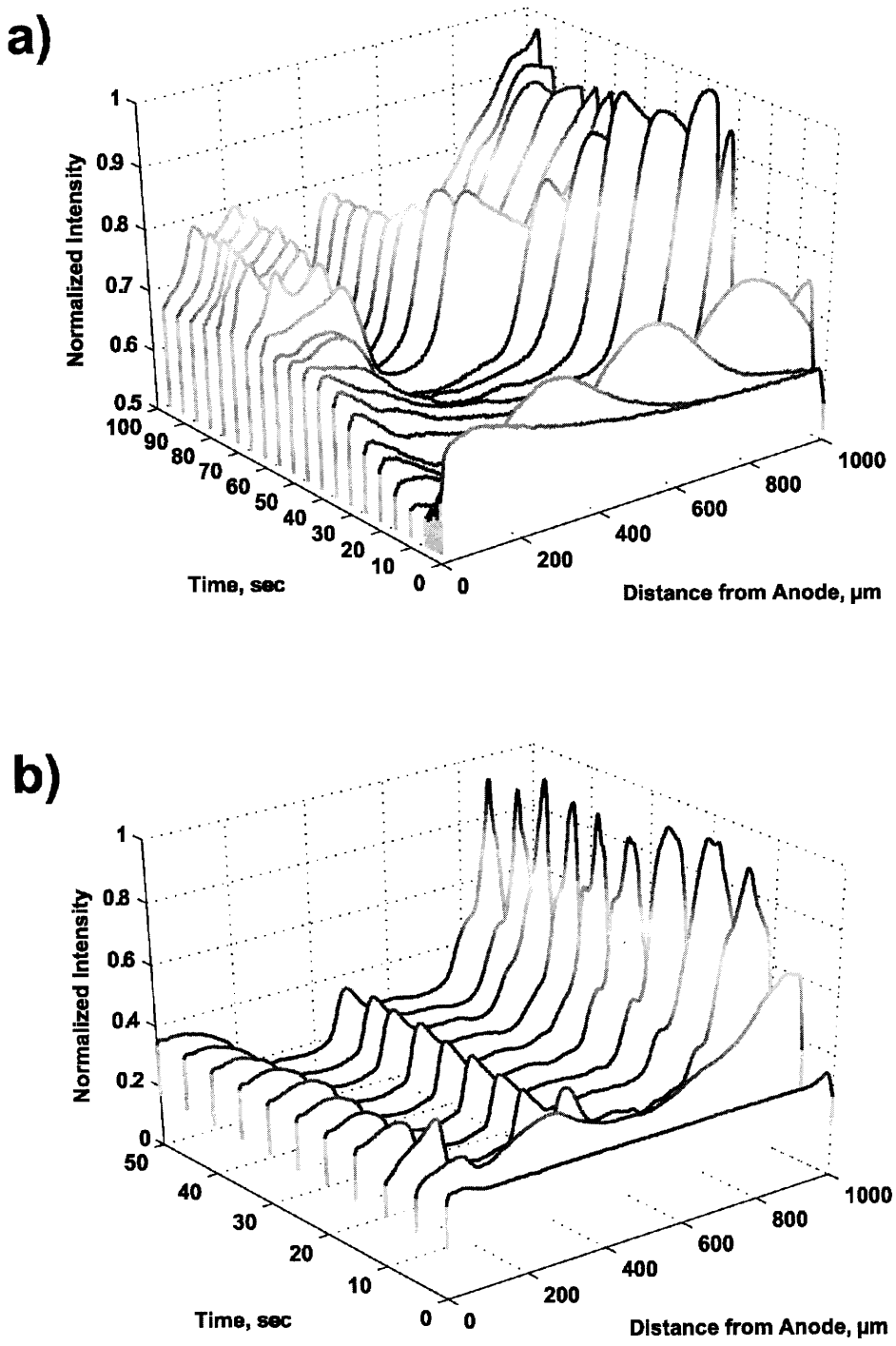


**Figure 3-5:** Time evolution of dye focusing with and without functional gels. a) Time course without immobilized pH groups. Here, plots spaced by one second for the first five seconds demonstrating the rapid electrophoresis of the dye mixture into the cathode. Subsequent plots spaced by 5 seconds. b) Time course with immobilized pH groups spaced by 5 seconds show a decreased time for pH gradient formation.

In order to test the effects of using Immobilines versus an unfunctionalized acrylamide gel, several devices were prepared using a 15% T, 3% C gel in both the anode and cathode regions, but without the addition of the Immobilines. The effect of Immobilines on device performance is shown in Figure 3-5. While the steady state results for both gel types were similar, the unfunctionalized gel typically required more than 60 seconds at 200V, and 15 minutes at 50 V to reach a steady state. For comparison, Hagedorn et al. [46] observed a 20 minute stabilization time for a channel formed from unmodified agarose gel. Because unfunctionalized gels have no buffering capacity, making them less effective for FF-IEF, Kohlheyer et al. [67, 66] used buffer side streams with their design. These side streams provide the pH stabilization in lieu of the plain acrylamide gel, which is used simply as a salt bridge.

### 3.3.4. Protein and Protein Complex Focusing

To demonstrate the focusing of labeled protein, streptavidin, Protein G, and cholera toxin subunit B were focused in the device. Figure 3-6 shows the focusing profile of the protein mixture. Protein G focuses sharply near the anode, streptavidin focuses and precipitates in the center of the channel, and cholera toxin subunit B focuses toward the cathode. Although no model for these proteins was formulated, owing to incomplete electrophoretic information, the manufacturers list the pI's of streptavidin and whole cholera toxin as "near-neutral" and 6.6, respectively. Monomers of cholera toxin subunit B have been found to have a heterogeneous pI between 8.1 and 7.9 [117]. From published results for cIEF [119], Alexa conjugated Protein G was measured to have a pI of 4.2.

An interesting application for free flow isoelectric focusing is not only protein focusing, but focusing of protein complexes. To demonstrate this in micro free-flow IEF, Protein G and mouse IgG were selected. Protein G exhibits a strong avidity for the Fc region in some mammalian immunoglobulins, especially mouse IgG. Figure 3-7 shows the fluorescent intensity of focused Protein G and Protein G-IgG complex at various concentrations of mouse IgG. At increasing concentrations of IgG, a second peak formed and became dominant, indicating that the Protein G-IgG complex had a higher pI than Protein G alone. This is consistent with the measured pI of Alexa conjugated Protein G (4.2), and the Protein G-IgG complex was observed to focus at a higher isoelectric point. Over the duration of this experiment (approximately one

hour) the Protein G band was observe to focus to the same point within the device, demonstrating the operational stability of the device over time.

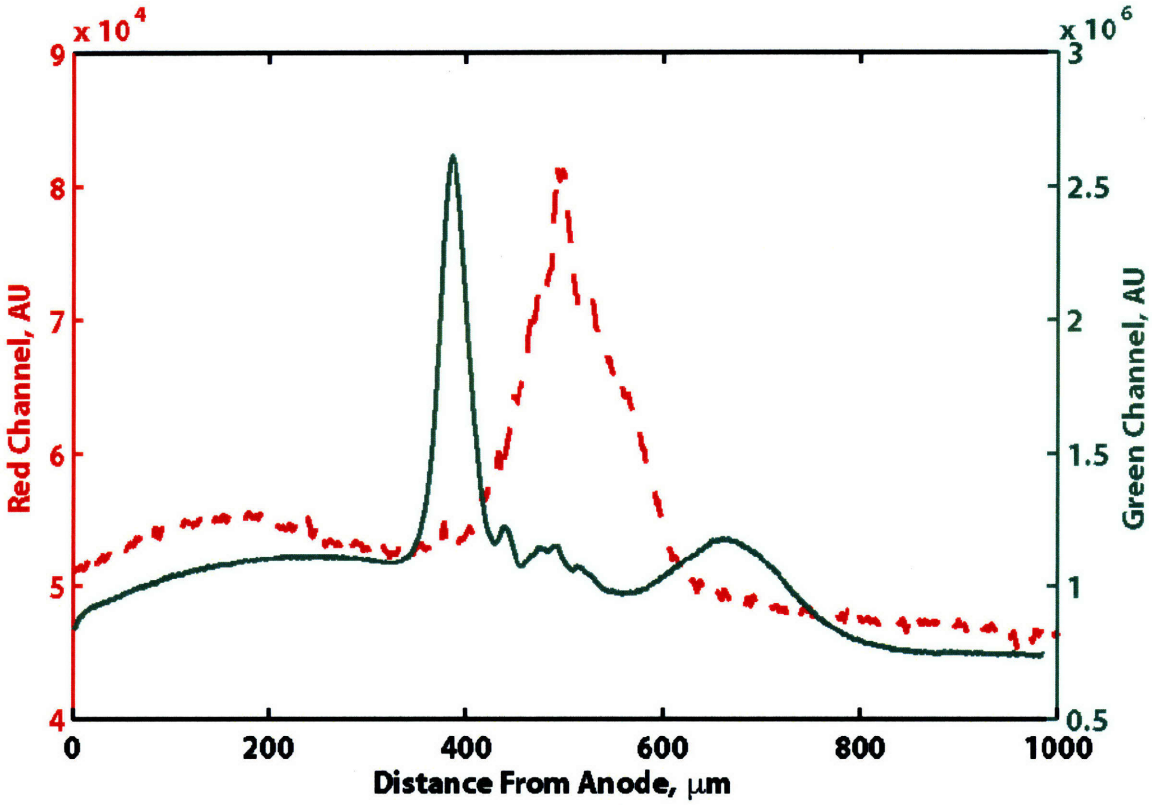


**Figure 3-6: Focusing of Texas Red conjugated streptavidin, FITC-conjugated cholera toxin subunit B, and Alexa 488 Protein G in PBS. The proteins were focused after 10 seconds with an applied voltage of 80 V. Plotted are normalized intensities for red (dashed line) and green (solid line) pixels. While cholera toxin subunit B focuses broadly, Protein G focuses strongly, and streptavidin focuses with some precipitation of the protein.**

Because of the high concentration of salt in the PBS buffer, the pH range is not expected to be linear over the entire width of the channel. Rather, the linear pH range created by the ampholytes will form in the center of the channel and will be bordered at both pH extremes by dissociated PBS ionic species (e.g. phosphoric acid and potassium hydroxide). This results in the narrower space that the proteins occupy in the sample channel, which is not consistent with the more linear pH profiles in Figure 3-2 through Figure 3-5. High ionic concentrations at the edges of the sample channel will also decrease the local electric field, reducing resolution near the

anode and cathode. However, the results are reproducible from run to run making the high voltage, free flow IEF device a promising tool for separating protein complexes.

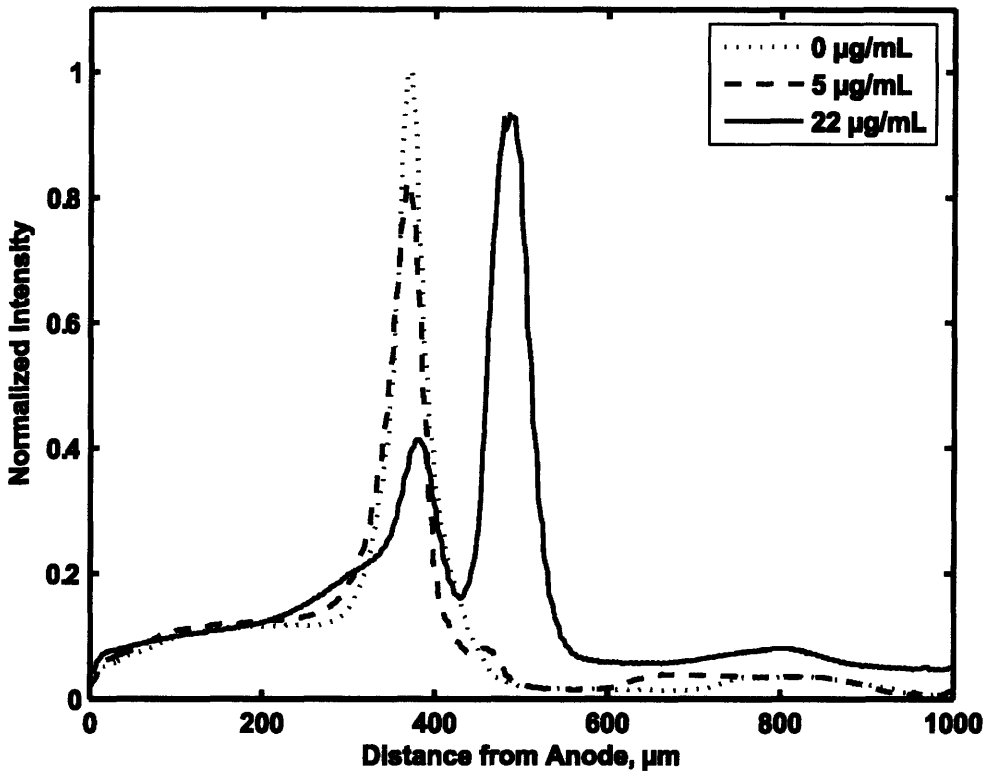


**Figure 3-7: Focusing of Alexa 488 conjugated Protein G at various levels of unlabeled mouse IgG. Plotted are fluorescent intensities normalized to Protein G alone (dotted line). The resolution of the dotted line was calculated to be 26. Plots of 5 µg/mL of IgG (dashed line) and 22 µg/mL (solid line) show the focusing of the IgG-Protein G complex. The proteins were focused in less than 20 seconds with an applied voltage of 30 V; the average electric field is estimated to be approximately 110 V/cm.**

Figure 3-8 shows the focusing of protein-DNA complexes. Here, purified transcription factor NF-κB is used with its consensus DNA binding sequence. By using a low concentration of fluorescently labeled DNA, the binding of NF-κB can be detected using IEF to focus the complex. Figure 3-8 shows the fluorescent profile under various conditions. Plotted are negative control (no NF-κB), and positive controls (NF-κB added), and competitor assays. A specific competitor, (unlabeled consensus sequence DNA) or a non specific sequence of DNA was used to confirm the specificity of the interaction. As expected, the positive control and non-specific (mutant) oligomers resulted in a focused peak. Interestingly, the NF-κB-DNA complex

focused to different areas within the channel depending on the presence or absence of the mutant oligomer. A small anomalous peak also appears at 0.7 mm for the positive control.

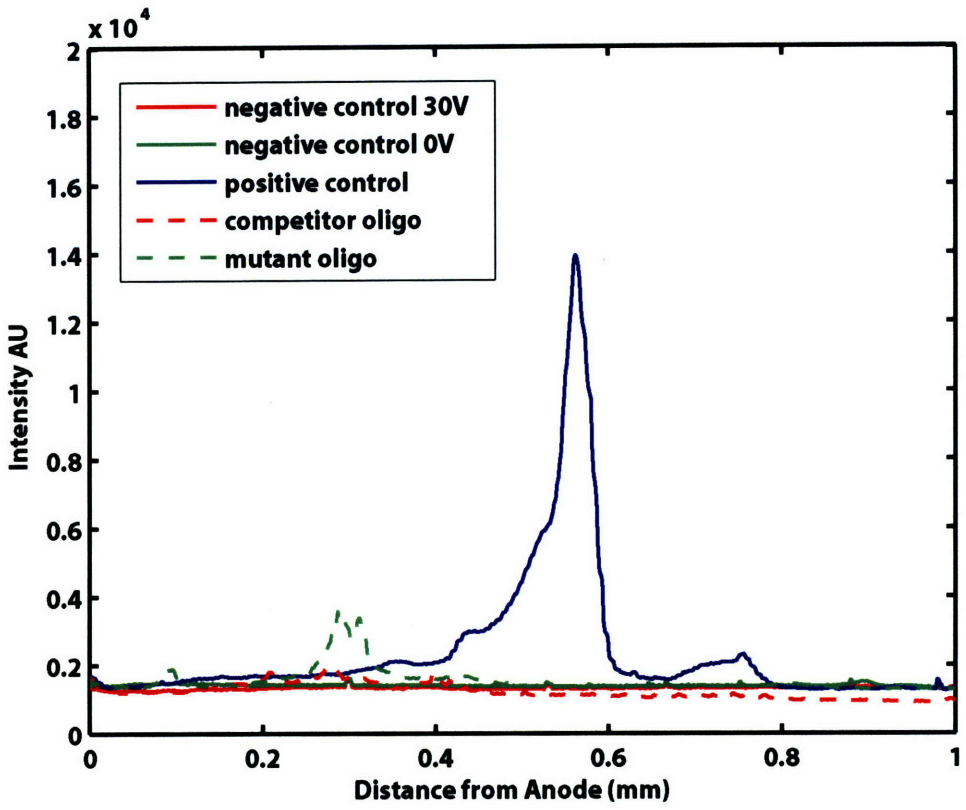


**Figure 3-8: Focusing of DNA-protein complexes. The interaction of NF-kB and its fluorescently labeled consensus binding sequence (5nM DNA) results in a fluorescent peak that is focused in 20s with an applied voltage of 30V.**

### 3.3.5. Electrokinetic Instabilities

At excessively high applied voltages, the differences in conductivities across sections of the channel can lead to unbalanced forces on the sample. Electrokinetic instabilities arise when these forces overcome the viscous resistance of the liquid. Section 2.2.6 discusses the theory behind electrokinetic instabilities, as well as defining an electric Rayleigh number proposed by Baygents and Baldessari. [6] Figure 3-9 shows a time course of device images for the focusing of Protein G for a step change in voltage from 30 to 90 V. After the focusing sharply, the Protein G band begins to break into periodic instabilities for several seconds before becoming randomly dispersed across the channel. The timescale and morphology of the instabilities agree qualitatively with the electrokinetic instabilities reported by Lin et al. [75].

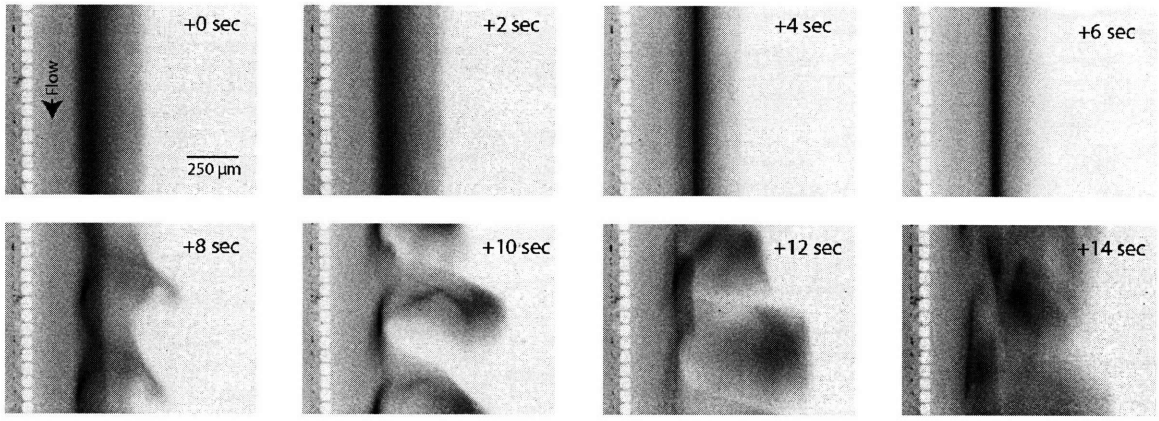


**Figure 3-9: Electrokinetic instability for focusing Alexa 488 conjugated Protein G. Applied voltage is stepped from 30V to 90V, flowrate 55nL/s. Images are inverted and contrast enhanced to illustrate the focusing and periodic instabilities.**

### 3.3.6. Organelle Focusing

Mitochondria were successfully focused at electric field strengths of less than 50 V/cm. At fields greater than this, surface adhesion and clumping severely inhibited device performance, even in PVA coated channels. The mitochondria were focused in tens of seconds, versus minutes as reported by Lu et al.[79]. In the negative control, the mitochondrial membrane is depolarized by CCCP, resulting in a shift in fluorescence from red to green. Figure 8 shows the fluorescent intensity across the sample channel after 24 seconds of focusing with an applied voltage of 100V. The mitochondria were observed to focus into two bands based on membrane potential. As in Lu et al.[79], the mitochondria with an intact transmembrane potential were focused to an acidic pH, while the mitochondria without a potential focused to a more neutral pH. For the cells untreated with CCCP, the vast majority of mitochondria kept their membrane potential for several hours while kept on ice, while most of those treated with CCCP had no membrane potential. Focusing experiments with either sample predominantly favored one peak, while an equal mixture of the two samples produced two peaks shown in Figure 8. The red peak focused to a lower pH, while the green peak was centered on a neutral pH. Mitochondria that are no longer polarized are more likely to breakdown, resulting in a population with a heterogeneous pI. Without this decomposition, the resulting peaks are expected to have similar distributions.

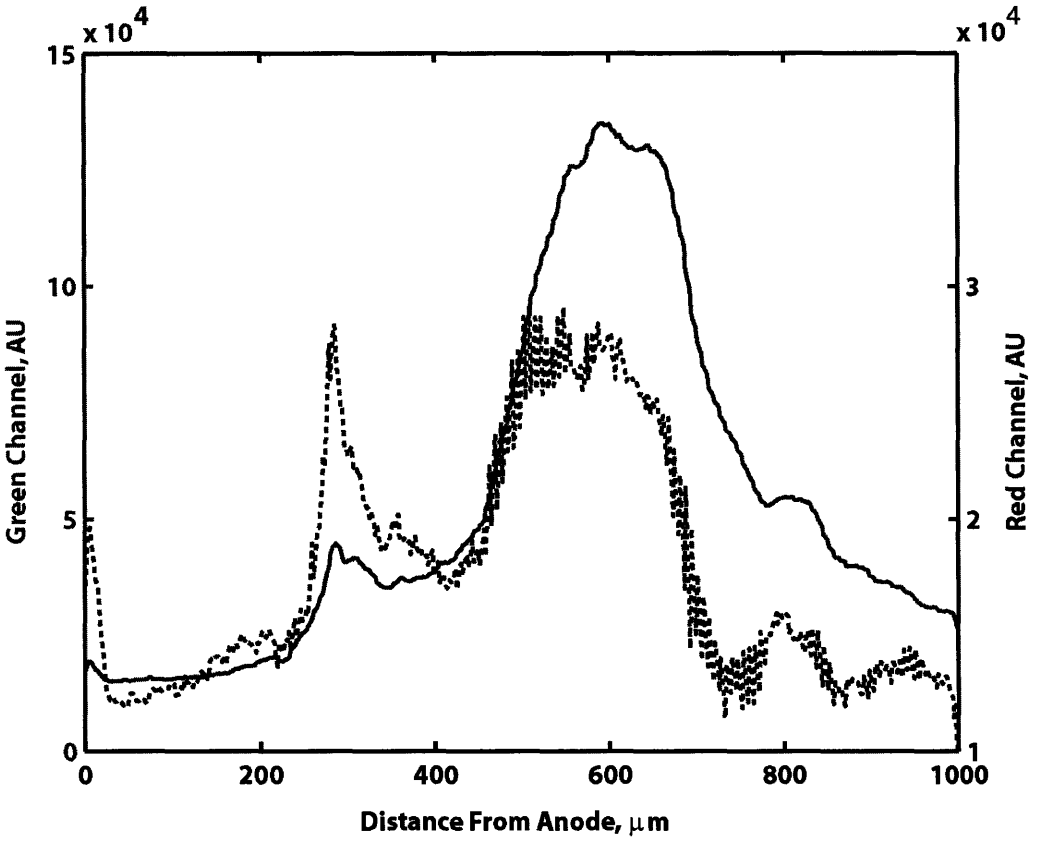


**Figure 3-10: Mitochondrial Focusing. Focusing of HeLa mitochondria after 24 seconds with an applied voltage of 100V, average electric field in the channel was estimated to be approximately 40 V/cm. Plotted are normalized intensities for red (dashed line) and green (solid line) pixels. Mitochondria that have retained their membrane potential appear red, while mitochondria without their potential appear green.**

## 3.4. Conclusions

The use of functionalized polyacrylamide as a conductive bridge as well as localized cooling of the sample has been demonstrated as a technique to enhance the performance of micro free-flow IEF devices. Electrode isolation permitted the hydrolysis reactions necessary for a high applied field, while preventing the gaseous hydrolysis products from interfering with the fluid flow. Here, functionalized gels have also been shown to be capable of providing the buffering capacity needed to for stable device operation. Incorporation of thermoelectric coolers with the micro-electrophoresis device mitigated the Joule heating effects that are problematic at high electric fields. Active cooling leads to more reliable device operation at high voltages. The chemical functionality of the gel, in conjunction with a thermoelectric cooling element enabled rapid separations, without excessive heating or buffer sheath flow.

The placement of these gels is easily defined by PDMS posts made from a relatively low resolution (~20 μm) SU-8 master. These posts eliminate the need for the extra masks and alignment necessary for UV-initiated polymerization. The fabrication in PDMS as well the ability to easily cast gels with different functionalities simplifies fabrication. Stable operation of the device presented here does not require buffer sheath flow; reducing the experimental complexity as well as setup labor. Also, the open sample channel lowers hydraulic resistance, and can pass large, non-ideal samples such as protein aggregates and organelles.

We also report the first application of micro free-flow IEF to focus protein complexes. The separation of free and complexed Protein G demonstrates how these devices may be used as tools for prefractionation or analytical separation of proteins and protein complexes. Non-denaturing separations of protein-protein and protein-DNA complexes may prove to be useful tools in elucidating protein complex formation in cellular signaling pathways.

Functionalized polyacrylamide as a conductive bridge could also form the basis for other high voltage microfluidic separation techniques. Thermal management in microfluidic systems is also a key concern for high voltage applications due to the high energies that must be dissipated. This combination of gel electrical interfaces and local cooling overcome two of the major barriers to high voltage microfluidics.

# Chapter 4: Cascaded FF-IEF

This chapter presents the implementation of cascaded stages for a microfabricated free-flow isoelectric focusing device with cascaded focusing stages. Both analytical and computational models for IEF suggest device performance will be improved by utilizing multiple stages to reduce device residence time. These models are shown to be applicable by using focusing of small IEF markers as a demonstration. We also show focusing of fluorescently tagged proteins under different channel geometries, with the most efficient focusing occurring in the cascaded design, as predicted by theory. An additional aim of this work is to demonstrate the compatibility of cascaded FF-IEF with common bioanalytical tools. As an example, outlet fractions from cascaded FF-IEF were analyzed by SDS-PAGE. Processing of whole cell lysate followed by immunoblotting for cell signaling markers demonstrates the reduction of albumin from samples, as well as the enrichment of apoptotic markers.

## *4.1. Introduction*

Isoelectric focusing (IEF) is a powerful technique to separate proteins on a basis independent of molecular weight. Most commonly IEF is performed in a gel format, as the first dimension of a 2-D gel, where immobilized pH gradient (IPG) strips are used to focus samples to high resolution, followed by a size based separation. The disadvantages of IPG strips include the limited sample composition, very low salt levels and highly denaturing conditions (8 M urea) are required to prevent gel burning and precipitation. Following the second dimension, the proteins must be removed from the gel for analysis by western blot or mass spectrometry, a time consuming process. Thus, the most promising routes for high throughput analysis lies with liquid phase separation techniques.[69]

Analytical separations by capillary IEF (CIEF) are an alternative to IPG strips as they offer the high resolution of IPG strips, but perform liquid phase separation.[65] This advantage of CIEF has been used with various orthogonal separation and detection schemes to speed analysis times and promote automation. The disadvantage of CIEF is that it is a batch separation technique, only small sample volumes may be processed. For multidimensional separations, IEF is attractive not only as an analytical technique, but as a prefractionation technique to coarsely resolve complex samples.

Free flow isoelectric focusing (FF-IEF) continuously focuses amphoteric molecules (e.g. proteins and peptides) to their isoelectric point (pI). In this technique, a sample solution is pumped through a rectangular chamber and an electric field is applied perpendicular to the fluid flow. Either an imposed or natural pH gradient is established across the width of the chamber and is stabilized by the electric field. Devices to perform FF-IEF have been in use since the 1960's [103]. FF-IEF is best suited as a preparative technique compared to capillary IEF or gel IEF, as it can fractionate large volumes of liquid with high recoveries (while maintaining protein biological activity) but with the trade-off of a lower separation resolution. Commercial FF-IEF devices have been developed [128, 15] and shown to be successful as a prefractionation tools for proteomic applications [56]. However, commercial systems FF-IEF require many inlets to establish a pH gradient with specialized buffer sheath flow, requiring extra equipment, extra reagents, and dilution of the purified sample.

Microfabricated FF-IEF devices are attractive as simple, inexpensive, and disposable prefractionation devices that can either be integrated with separation techniques on chip, process hazardous or radio-labeled samples, or compliment existing orthogonal separation techniques, such as SDS-PAGE or capillary electrophoresis. Micro FF-IEF devices have been shown to separate and concentrate fluorescent dyes [1, 67, 66, 2], proteins [81, 133], protein complexes [1], and organelles.[79] Practical challenges to micro-FF-IEF design and operation with a uniform electric field include removal or isolation of bubble-forming electrolysis products at the electrode interface, stable pH gradient formation, and Joule heating. To mitigate the effect of electrolysis, in these microdevices, researchers have used non-gassing electrodes [81], diffusion potentials at the junction of two different solutions [16, 80, 116], or electrode isolation using either fabricated structures with high hydrodynamic resistance [133] or photopatterned polyacrylamide.[67] To stabilize the pH gradient formation within the device, buffer sheath flow has been used.[67, 81] The previous Chapter reported using functionalized gels in conjunction with an active cooling module to perform FF-IEF in a PDMS device without sheath flow or Joule heating effects.[1] Another challenge for micro-FF-IEF devices is the task of collecting liquid fractions of different pI ranges for subsequent processing by orthogonal techniques such as capillary electrophoresis, SDS-PAGE, and immunoblotting (western blotting).

The notion of different focusing distances or multiple stages to design IEF tools within the scope of gel membrane or capillary IEF techniques has largely been ignored until recently,

chiefly due to the lack of suitable fabrication techniques. However, advances in microfabrication techniques and polymer machining now enable the fabrication of new and complex geometries for isoelectric focusing. Segmented IEF using parallel functionalized gels [139] was devised based on a simple analytical model. Das and Fan [25] observed the effects of capillary IEF channel length on focusing time and resolution within a microfabricated device. Cui et al. [24] controlled potentials across a channel with several T-junctions to perform multiple focusing operations while decreasing the pH gradient. By "zooming in" to a narrow pH range, higher resolution was obtained, but species outside of this range were lost.

Given the new freedom in microfabrication, design considerations for complex geometries are increasingly important. The mechanism of IEF results from the interplay of hundreds to thousands of charged species [103], making it difficult to model. Rigorous simulation tools [82, 88, 122, 123] for capillary IEF have shown good agreement with experiments and have offered insights into the dynamics of IEF, but are not yet used in the design of new IEF tools. In this chapter, we use simulations to determine the trade-offs of device geometry on FF-IEF performance in order to design faster and more efficient FF-IEF prefractionation tools. Figure 4-1 illustrates the concept of using cascaded IEF stages for more efficient FF-IEF. Micro FF-IEF rapidly establishes a steep pH gradient, enabling rapid focusing but with the consequence of lower resolution. Conventional FF-IEF tools use a shallower pH gradient, resulting in slower, but more resolved focusing. For cascaded FF-IEF, the final resolution is expected to be equivalent to focusing in a shallow pH gradient, but with the necessary residence time for focusing reduced. A shorter residence time in a free flow device equates to smaller device size and reduces losses associated with adsorption and electroosmotic flow. These efficient, simple devices could be fast and inexpensive enough to serve as a convenient technique to compliment many separation protocols.

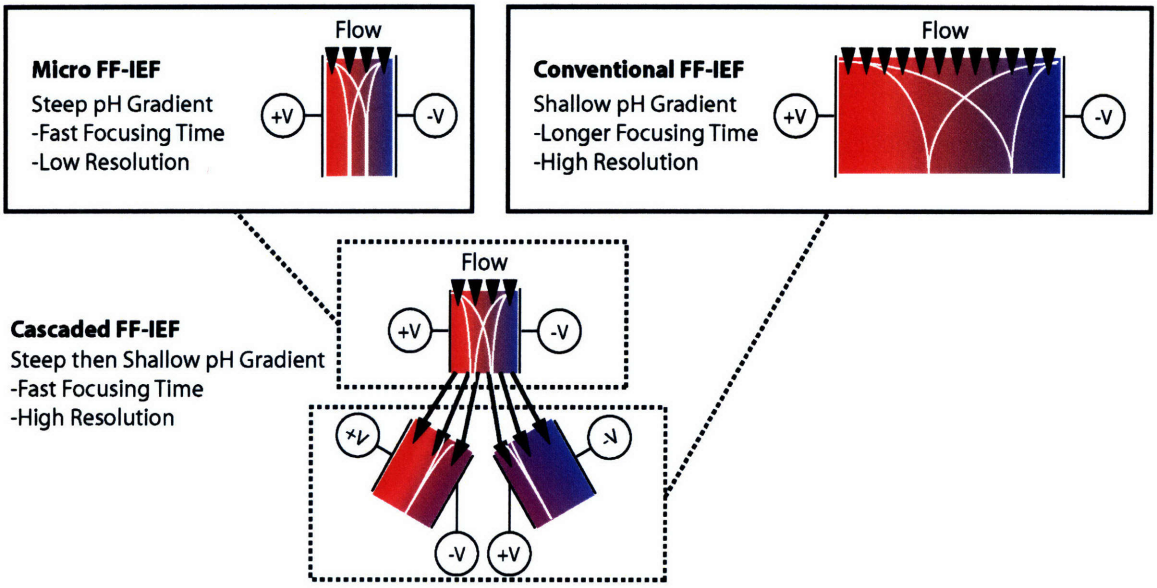


**Figure 4-1: Motivation for cascaded free-flow isoelectric focusing. Micro FF-IEF rapidly establishes a steep pH gradient, enabling rapid focusing but with the consequence of lower resolution. Conventional FF-IEF tools use a shallower pH gradient, resulting in slower, but more resolved focusing. Using cascaded FF-IEF stages to change the pH gradient midway through focusing results delivers resolution greater than micro FF-IEF designs and in less time than conventional FF-IEF.**

To explore the possibility of cascaded FF-IEF, the analytical expressions for IEF are first examined, followed by more rigorous numerical simulations of IEF for theoretical ampholytes in channels of different geometries. Following these analyses, devices are fabricated and tested. Our aims for cascaded IEF in a microfabricated device are: i) to demonstrate that focusing time can be reduced and ii) that the fractions produced these devices are compatible with existing molecular biology analytic techniques.

## *4.2. Theoretical Basis for IEF*

### 4.2.1. Analytical Scaling Approximations for IEF

Mass transport equations are used as the starting point to formulate expressions that coarsely describe isoelectric focusing. Chapter 2 outlines these expressions in more detail, but they are summarized here. The conservation equation for species in solution experiencing an electrophoretic force is given by Equation 4-1, below:

$$\frac{\partial C_i}{\partial t} = \underline{\nabla} \cdot \left( D_i \underline{\nabla} \cdot C_i - \underline{E} z_i \omega_i C_i \right) \qquad 4\text{-}1$$

In Equation 4-1 the concentration of a species $C_i$ is a function of position and time, electric field $E$, variable charge $z_i$, constant mobility $\omega_i$, and its diffusion constant $D_i$. In order to understand the effect of geometry and physical parameters on focusing, it is helpful to non-dimensionalize the conservation equation for one-dimensional transient focusing and make two assumptions: i) a linear pH gradient is established over the total length, $L$, and ii) the species has a linear charge behavior in the channel ($dz_i/dx = \Delta z_i/L$ = constant). Non-dimensionalizing and expanding the derivative results in Equation 4-2:

$$\frac{\partial \Theta}{\partial \tau} = \frac{1}{Pe_e}\frac{\partial^2 \Theta}{\partial \eta^2} - \Theta - \frac{\partial \Theta}{\partial \eta}\left(\eta - \eta_{pI}\right) \qquad 4\text{-}2$$

The dimensionless quantities in Equation 4-2 are defined as $\Theta = C_i / C_{i,0}$, $\eta = x/L$, $\tau = Et\omega\Delta z/L$, and $Pe_e = E\omega L\Delta z/D$. The location where the species focuses is defined by $\eta_{pI}$. The ratio of electrophoretic to diffusive fluxes, $Pe_e$, is similar to a Peclet number. This number must be >1 for electrophoresis to dominate the system.

At steady state, Equation 4-1 reduces to Equation 4-2, with the well known [103] solution given by Equation 4-3, in dimensionless form:

$$0 = \frac{1}{Pe_e}\frac{d^2 \Theta}{d\eta^2} - \Theta - \frac{d\Theta}{d\eta}\left(\eta - \eta_{pI}\right) \qquad 4\text{-}3$$

$$\Theta = \sqrt{\frac{Pe_e}{2\pi}}\exp\left(-\frac{\left(\eta - \eta_{pI}\right)^2}{2}Pe_e\right) \qquad 4\text{-}4$$

The Gaussian distribution of Equation 4-4 has a standard deviation of $Pe_e^{-1/2}$. By defining separation distance as three standard deviations (87% of the peak area), this leads to Equation 4-5, equivalent to the results of Vesterberg and Svensson [125] and Rilbe [104] for the minimum resolvable difference in pI. Here, we also define resolution, *Res*, as the minimum difference pI divided by the pH range within the channel:

$$\frac{\Delta pI_{min}}{\Delta pH} = 3\sqrt{\frac{D}{E\omega L\Delta z}} = \frac{1}{Res} \qquad 4\text{-}5$$

At excessively high electric fields, detrimental phenomena such as Joule heating, electroosmotic flow, and precipitation prevent ideal focusing. Therefore for any sample composition, there is an optimal electric field strength that maximizes resolution while minimizing negative effects. To examine focusing behavior in a variety of geometries, the electric field (as opposed to applied voltage) was assumed to be the same for every case. For the time scaling in Equation 4-2, the time scale of focusing ($t/\tau$) increases linearly with respect to channel length, $L$. From Equation 4-5, the resolution at steady state increases with $L^{1/2}$. These dependencies show that there is a trade-off between short focusing times and resolution when the applied field is constant. This trade-off can be exploited with multiple stages to deliver high resolution separations with a minimal focusing time, analogous to shifting gears in order to maximize a vehicle's acceleration.

Considering instead the case of constant applied voltage ($V = EL$), the time scale of focusing increases with $L^2$, whereas the steady state resolution is independent of distance, consistent with the findings of Das and Fan [25]. In practice, however, using a constant voltage for a range of channel lengths is less feasible than maintaining a constant electric field. Applying the high voltages typical in cm-scale IEF (200-500V) to a channel 1 mm in length would result in field strengths of 2-5 kV/cm. Electroosmotic flow would increase by a factor of 10, and Joule heating would increase by a factor of 100: an adiabatic 1 μL sample with conductivity similar to 2% Ampholine in deionized water (0.3 mS/cm) would be heated at a rate of 300-1800 °C/s.

### 4.2.2. Simulations of IEF in Channels of Varying Widths

Chapter 2 discusses various models for IEF, and presents the results of simulations in channels of varying widths; these results are summarized in this section. Because the analytical expressions for IEF must assume an established pH gradient, and do not consider nonlinear changes in sample conductivity, a 1-D transient IEF model using Jacobian (Numerica Technologies, Cambridge, MA) [1] was employed to explore the effect of distance on focusing dynamics. This model is based on published models [9, 82, 88], and assumes electroneutrality and instant pH equilibrium for a mixture of 140 biprotic ampholytes. The model was expanded to accommodate dynamic changes in channel width and applied voltage, to compare focusing dynamics for channels of various widths. A model with 240 spatial points (resulting in 137,613

coupled equations) was used to quickly simulate focusing at these widths, requiring only about 3 hours of CPU time on a 3.8 GHz personal computer. Custom MATLAB programs were used to provide Jacobian self-consistent initialization conditions, as well as to parse and post-process the simulation results.

To test the analytical predictions, several simulations were run at various widths and constant average electric field (100V/cm). Figure 2-18 shows the results of these simulations, plotting the time to reach steady state ($t_{ss}$, Figure 2-18a) and resolution *Res* (from a Gaussian fit of one of the ampholytes, Figure 2-18b) versus channel length for the simulations. Also plotted are power equations with two fitted parameters that were expected to describe the simulation results. A nearly linear relationship (exponent of 0.908) exists between focusing time and channel length, as predicted by scaling arguments. The relationship between resolution and channel length also follows the predicted power law behavior, with a fitted exponent of 0.488 versus 0.5 for the analytical case. From the solid lines in Figure 2-18, a wider FF-IEF channel has the effect of increasing both focusing resolution and focusing time. A simulation where the channel is instantly widened from 1 to 3 mm after 5 seconds (open circles) shows that the higher resolution of the 3 mm channel can be reached in half the time (8.70 versus 17.49 seconds to steady state) when the average electric field is held constant at 100 V/cm. These results indicate that the effects of pH gradient formation and changes in conductivity do not significantly alter the idealized focusing behavior of simple ampholytes, showing the usefulness of the analytical expressions for IEF.

The numerical model was also used to simulate the focusing of BSA in a channel either 1 or 3 mm long. Figure 2-19 shows the simulated focusing of BSA under three different geometry configurations at identical field strengths: 1 mm, 3 mm, and 1 mm followed by focusing at 3 mm. The protein focusing follows the "double-peak approach" observed by others [122, 20, 19, 7]: peaks form at both electrodes, move toward the pI, and coalesce. To better quantify focusing, the simulation used low electric fields (5 V/cm for each case) for slow, low resolution focusing. The resolution (from a Gaussian fit, $R^2 > 0.999$) of the focusing is 1.6 times greater for the longer channel. Transitioning from a shorter to a longer channel reaches this higher-resolution steady state in 40% less time than the 3 mm case. These results demonstrate that the predictions for small amphoteric molecules in terms of channel geometry and residence time also extend to large proteins with complicated electrophoretic behavior.

## 4.3. Experimental Materials and Methods

### 4.3.1. Design and Fabrication

Free flow IEF devices were designed to have a sample channel defined by a porous material capable of allowing ion conduction between the sample channel and the electrode buffer, while preventing fluid convection between the two regions. Our previous [1] single stage straight channel design 20 mm long by 1 mm wide was compared with a similar straight channel design that was a 30 mm long by 3 mm wide (Figure 4-2) as well as a cascaded design (Figure 4-3a). The channel height is nominally 50 microns in each of these designs. To demonstrate the speed and resolution advantages suggested by IEF modeling section, a device with cascaded IEF stages was designed and fabricated. The cascaded design consists of four focusing regions: the first IEF stage is a single channel (1 mm wide by 7.62 mm long) that branches into three secondary IEF stages with dimensions identical to the first stage. This split configuration was chosen over a 3 mm channel for two reasons: i) more uniform fluidic resistance for an improved flow field and sample collection and ii) more control over the electric field within the device. The anticipated pH range "zoomed in" for the three secondary stages (for Ampholine 3-10) is 3-5.3 (Figure 2a, $V_1$ to $V_2$), 5.3-7.7 ($V_2$ to $V_5$), and 7.7-10 ($V_5$ to $V_6$) from anode to cathode. The designs were based on a PDMS channel bordered by posts (Figure 4-3b) to define placement of the porous material without the need for a photo-polymerization mask. Small liquid reservoirs (2 for each straight design, 6 for the cascaded design) were manually cut out of the PDMS to contain catholyte and anolyte as well as platinum electrodes, which were connected to an external power source.

The body of the device was fabricated using standard soft lithography techniques.[33] Briefly, a silicon wafer was coated with a layer of SU-8 2050 (MicroChem, Newton, MA), which was pattered using a 5080dpi transparency mask (Pageworks, Cambridge, MA). Next, Sylgard 184, (Dow Chemicals, Midland, MI) was cast over the SU-8 mold and cured at 70°C for two hours. After curing, the PDMS was peeled off of the master; individual devices were cut out, and fluidic connections were punched using a 20 gauge Luer stub adapter (Becton-Dickinson, Sparks, MD).

When a 23 gauge Luer stub adapter was inserted in to these holes, the connection was self-sealing; no epoxy or glue was necessary. Next, the devices (two at a time) were treated with

oxygen plasma for 40 seconds prior to permanently bonding to a 50x75 mm microscope slide. After bonding, the microscope slide was scored and cut with a diamond scribe to separate pairs of devices. Next, the channels were filled with 1% v/v 3-(trimethoxysilyl)propyl methacrylate in ethanol and allowed to dry at room temperature overnight.

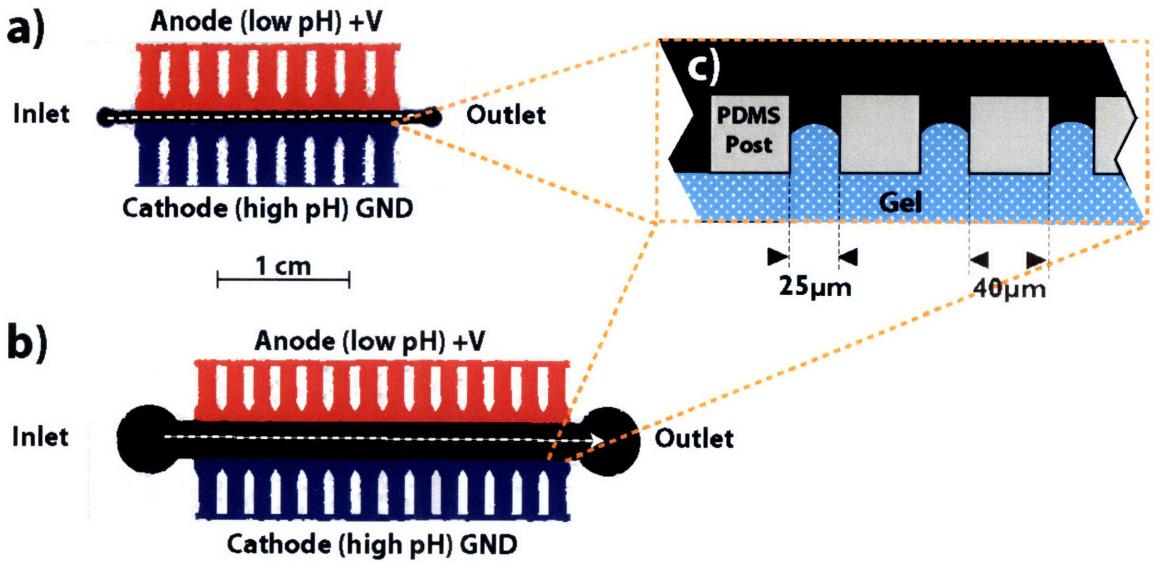


**Figure 4-2: Layout of single stage designs. Two straight channel designs were used: a) 1 mm channel width and b) 3 mm channel width. c) Detail of the PDMS post array.**

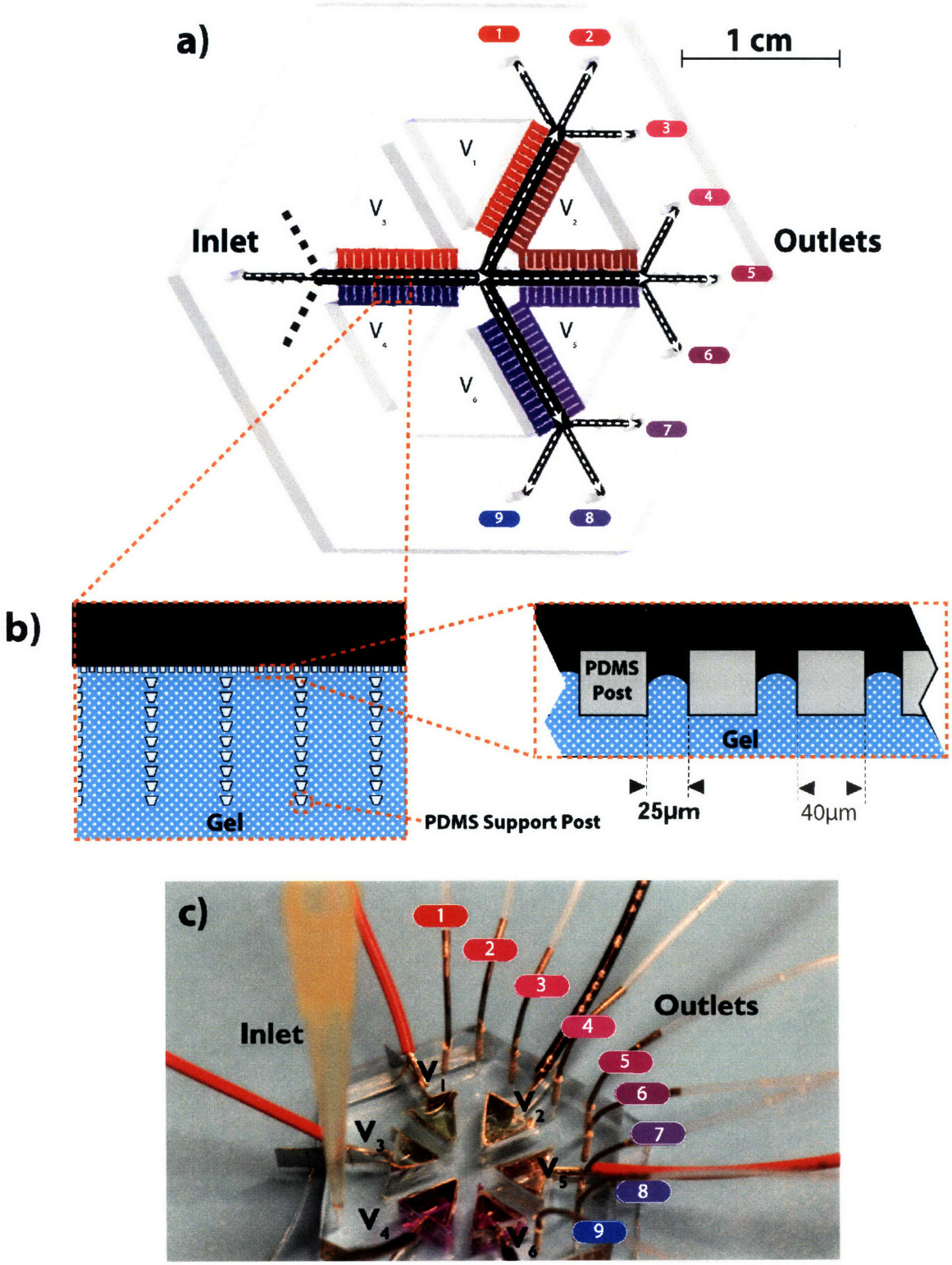


**Figure 4-3: Cascaded FF-IEF device design. a) Rendering of the cascaded device. b) Detail of square channel posts and trapezoidal support array. c) Photo of device in operation.**

### 4.3.2. Flow Balancing in Trifurcated Channels

The trifurcated geometry was chosen to increase the number of outlets from two IEF stages. Unlike channel bifurcation, a three-way split in a device may have an uneven pressure balance, leading to an uneven flow profile across the outlets. To ensure that each split in the device had an equivalent flow resistance; finite element modeling was used to properly balance the split geometry. Because of the computational cost of three dimensional Navier-Stokes simulations, two alternate approaches were used to quickly optimize split designs.

#### Electrical Analog to Laminar Flow

Because of the high aspect ratio and uniformity of the bulk fluid flow, the effects of no-slip at the channel sidewalls can be neglected in order to dramatically increase modeling time. For the ultimate goal of balancing flow resistance, the resulting system may be treated as an electrical conductor with an electrical potential between the "inlet" and "outlets" of the split. The "conductive media DC" module of COMSOL was used to solve Equation 4-6:

$$0 = \nabla \cdot d\sigma \nabla V \qquad 4\text{-}6$$

The "inlet" of the device was set to an arbitrary voltage (1V), while the "outlets" of the device were grounded. The "thickness" of the layer, $d$, and conductivity, $\sigma$, was set to unity. The current integral at each of the exits was calculated and compared. Figure 4-4 shows the models used for the splits after the first and second stages. Due to symmetry, only half of the split was modeled. In Figure 4-4 the surface color corresponds to the voltage (a proxy for pressure) and the streamlines correspond to current density (a proxy for flow profile). The speed of solver (0.44 seconds with a 2.8 GHz processor) allowed for iterative design of the "step" shape used to match the resistance for each of the outlets.

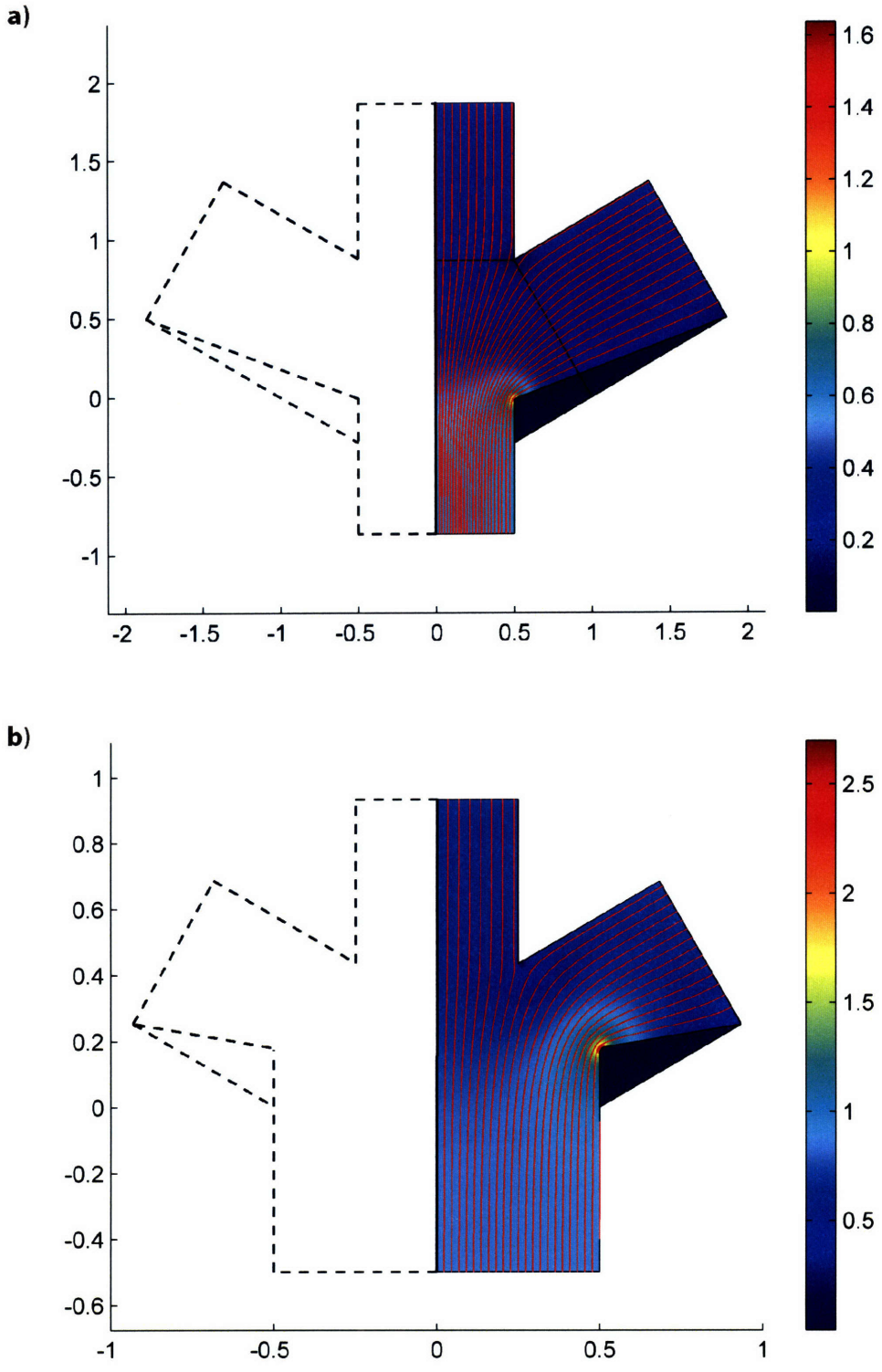


**Figure 4-4: Models for flow balancing using an electrical current analog. a) First trifurcation: 1 mm channel splits into three 1 mm channels. b) Second trifurcation, 1 mm channel splits into three 0.5 mm channels.**

## Full Stokes Flow Modeling

For vanishingly small Reynolds numbers, the Stokes equation for Newtonian fluids is given by Equation 4-7:

$$0 = \nabla \mathbf{P} + \mu \nabla^2 \mathbf{v} \qquad 4\text{-}7$$

Because Equation 4-7 is a linear PDE, it can be solved much more efficiently for 3-D fluid modeling. Although solving time is two orders of magnitude slower than a 2-D electrical analog, the model may still be solved without a high performance PC. Figure 4-5 shows the fluid flow for a fluidic split using the final designs from the 2-D modeling. Here, surface color corresponds to pressure, and the streamlines correspond to the fluid flow profile. Again, geometry was manually iterated to balance the pressure drop across the outlets. The values of the flow leaving the splits for these modified designs were found to be very close to the optimal geometry of the 2-D electrical analog to fluid flow.

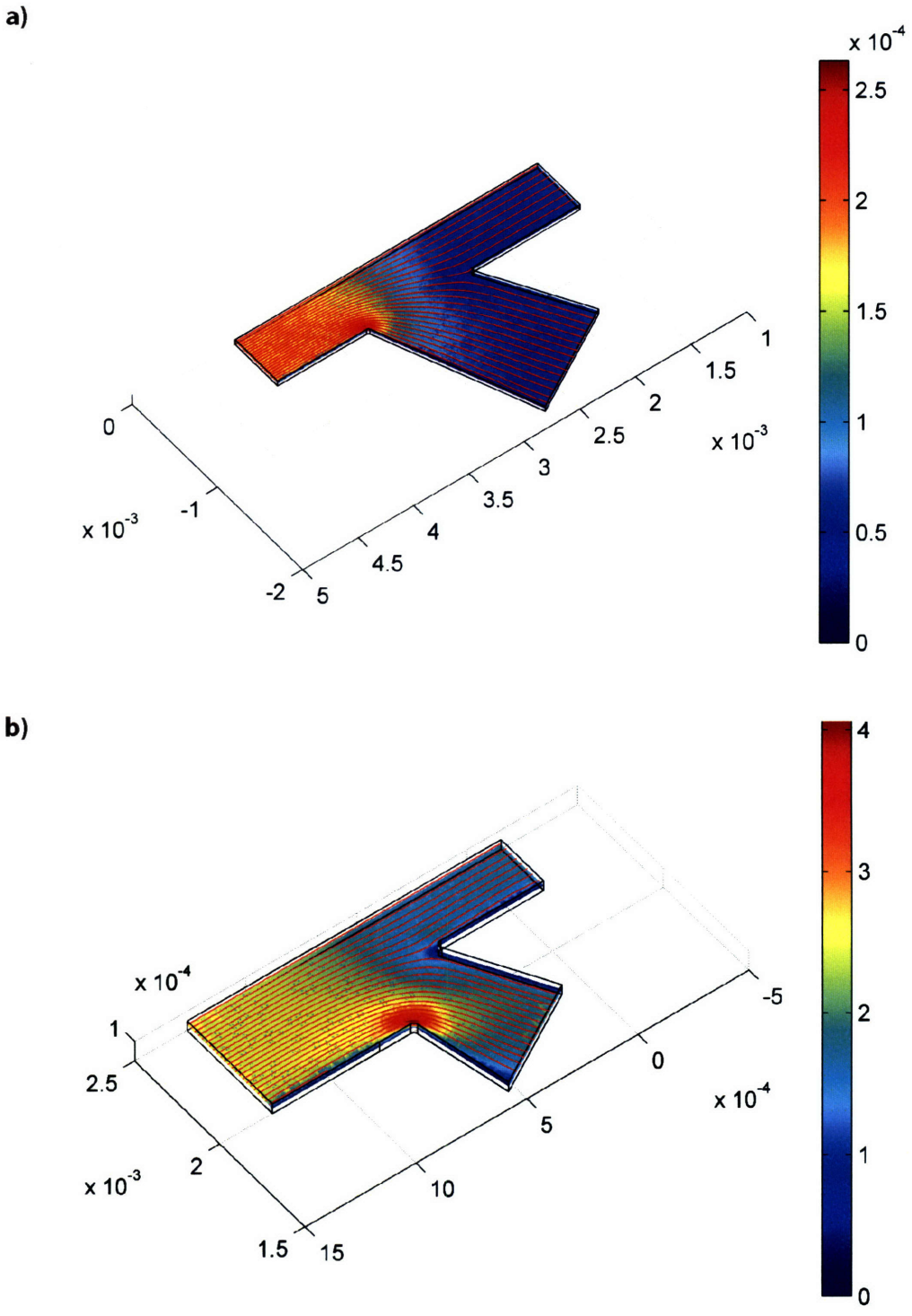


**Figure 4-5: Models for flow balancing using 3-D Stokes flow. a) First trifurcation: 1 mm channel splits into three 1 mm channels. b) Second trifurcation, 1 mm channel splits into three 0.5 mm channels.**

### 4.3.3. Gel Casting

To cast acrylamide within the devices, the devices were rinsed with ethanol, and degassed in a vacuum oven at 70°C and 50 mmHg for more than 2 hours. Subsequently, the devices were kept under nitrogen using an acrylic glove box (Air Control, Inc., Henderson, NC). The monomer solution used in the polyacrylamide devices tested was 15% total acrylamide (15% T), with 3% of the acrylamide present as bis-acrylamide (3% C) (PlusOne ReadySol IEF, GE Healthcare, Piscataway, NJ). Note: solutions containing acrylamide are neurotoxic and should be handled with caution. Immobilines (pKa 3.6 and pKa 9.3, GE Healthcare) were added to the monomer solution (anode and cathode respectively) to a final concentration of 12 mM. To fill the anode side of the device, 60 μL of 1% v/v Triton X-100 (EMD Chemicals, Gibbstown, NJ), and 6 μL of 10% w/v DMPA (2,2-Dimethoxy-2-phenylacetophenone, Sigma-Aldrich, St. Louis, MO) in acetone was added to 1mL of the anode (pKa 3.6) monomer mixture. For the cathode side, 30 μL of 1% Triton and 6 μL of 10% DMPA was added to 1 mL of the cathode (pKa 9.3) monomer mixture. These anode and cathode monomer mixtures with DMPA and Triton were mixed together at a 2:1 or 1:2 ratios to form the intermediate pH gels used in the cascaded design. These intermediate gels were used to provide some pH stability at values anticipated to be 5.3 and 7.7 without additional reagents. Across the second stages from anode to cathode, the low pH buffering capacity of the gels is incrementally reduced as the high pH buffering capacity is increased.

These monomer mixtures were cast inside the devices by introducing them to the electrolyte reservoirs, where they were drawn into the device by capillary action. Reaching the hydrophobic PDMS posts at the sample channel, the solution was held in place by surface tension, long enough to polymerize using a UV lamp (354nm, Spectroline ENF-280C, Spectronics Corporation, Westbury, NY). DMPA was observed to graft the polyacrylamide gel to the PDMS. However, because DMPA is highly soluble in PDMS, incomplete polymerization occurred for very shallow channels, and for long wait times (>5 min) before exposure. To correct for this, long exposure times (2 minutes at a distance of 3 cm) were used to ensure adequate polymerization. After polymerization, the devices were stored under 1% w/v solution of poly(vinyl alcohol) (PVA, MW 146-186kDa, 87-89% hydrolyzed, Sigma-Aldrich).

### 4.3.4. Device Packaging and Operation

Platinum wires or foil (0.5 mm diameter or 0.1 mm thickness, Alfa Asear, Ward Hill, MA) were used to connect the electrode reservoirs to a high voltage electrophoresis power supply (VWR, West Chester, PA). Silicone sealant (ASI 502, American Sealants Inc, Fort Wayne, IN) was used to fix the wires in place and to form reservoirs for the anolyte and catholyte buffers. The anolyte used was 100 mM phosphoric acid with 1% w/v hydroxypropyl methyl cellulose (HPMC, Fluka, Buchs, Switzerland) and 1% Triton; the catholyte was 200 mM lysine and 200 mM arginine (10X IEF Cathode Buffer, Bio-Rad, Hercules, CA) in 1% HPMC and 1% Triton. To buffer the second stages to an intermediate pH, 50 mM MES (adjusted to pH 5.35) and 50 mM HEPES (adjusted to pH 7.25) buffers each with 1% HPMC and 1% Triton were used. Samples were pulled through the device using a multi-channel syringe pump (EW-74901-10, Cole-Parmer, Vernon Hills, IL) equipped with nine 100 μL gas-tight syringes (Hamilton, Reno, NV) set to withdrawal mode. At the inlet of device, a 200 μL pipette tip was simply inserted into the PDMS. This sample reservoir was easily refilled by adding samples into the top of the pipette tip. The devices were checked for leaks before using. The average fabrication yield for the devices from casting to use was approximately 70%.

The size and layout of the cascaded device is too intricate to cool with commercially available thermoelectric elements. Therefore, two cooling strategies were employed. For fluorescent samples, the devices were cooled by venting nitrogen gas withdrawn from a liquid nitrogen cylinder over the glass underside of the device while it was mounted on the microscope stage. The forced convection proved to be sufficient to observe focusing, although it was not as effective as a thermoelectric cooling module [1]. For SDS-PAGE or immunoblot analysis, where no *in situ* observations were required, the devices were cooled by placing the device atop an aluminum heat sink (659-65AB, Wakefield Engineering, Pelham, NH) inverted (fins down) in a shallow dish. The dish was filled with enough ice water to immerse the fins of the heat sink, effectively keeping the device near 0°C.

To apply voltages to the cascaded devices, three power supplies were connected in parallel to apply up to 180V to one reservoir, ($V_1$ in Figure 3-1a), 120V ($V_2$ and $V_3$), or 60V to others ($V_4$ and $V_5$), while grounding the remaining reservoir ($V_6$). This configuration results in 60V across each focusing region within the device, and minimizes electrical interaction between regions.

### 4.3.5. Dye and Protein Preparation

Dye focusing experiments were conducted with fluorescent low molecular weight pI markers (isoelectric points: 5.1, 7.2, 7.6, and 9.5, Fluka, Buchs, Switzerland). Markers were used at a final concentration of 1 mg/mL. Ampholine 3-10 and NP-40 (Nonident P-40 substitute, Fluka) were added to deionized water (Millipore, Billerica, MA) to a final concentration of 2% and 0.5%, respectively.

To visualize the focusing of fluorescently labeled protein, Alexa 488 conjugated Protein G (Invitrogen, Carlsbad, CA) was mixed in phosphate buffered saline (PBS, Invitrogen) with 2% Ampholine 3-10 (Fluka) to a final concentration of 80 μg/mL (4 mM). For experiments where the fractions were subsequently processed by SDS-PAGE, the sample consisted of unlabeled protein standards for IEF: amyloglucosidase, carbonic anhydrase II, trypsin inhibitor, and trypsinogen (IEFM1A-1KT, Sigma-Aldrich) as well as Alexa labeled Protein G and Texas Red labeled streptavidin (Invitrogen) were mixed together in PBS with 2% Ampholine to a final concentration of 0.95 mg/mL for the unlabeled protein standards, and 0.24 mg/mL for Protein G and streptavidin. Approximately 0.4 mL of sample was used for each experiment.

Semi-quantitative immunoblot assays of total ERK2, phosphorylated AKT (pAKT), and cytochrome C were performed using HeLa cell lysates. HeLa cells (ATCC, Manassas, VA) were cultured in DMEM medium supplemented with 10% fetal serum, 100 units/mL penicillin, 100 μg/mL streptomycin, and 2 mM glutamine (Invitrogen) at 37 °C and 5% $CO_2$. For narrow pH range focusing, the cells were washed with PBS prior to lysis to remove albumin in the cell media. The lysis buffer consisted of: 1% Triton X-100, 150 mM NaCl, 10 mM β-glycerophosphate, 10 mM $Na_4P_2O_7$, 10 mM NaF, 1 mM $Na_3VO_4$, 10 μg/mL leupeptin, 10 μg/mL pepstatin, and 10 μg/mL chemostatin. To ensure both phosphorylated and unphosphorylated forms of ERK, half of the cell lysate originated from cells stimulated with 50 ng/mL TNF-α for 10 minutes. The insoluble (pellet) and soluble (supernatant) fractions were isolated by centrifugation (10min at 20000*g*). No other purification steps were performed. Before FF-IEF, the sample was mixed with an equal volume of 8M urea, adjusted to a final concentration of 0.45% NP-40 and 15 mM CHAPS (3-,-1-propanesulfonate, JT Baker, Phillipsburg, NJ) and 2% Ampholine pH 3-10.

### 4.3.6. Imaging and Analysis

Focusing behavior was observed with an inverted fluorescent microscope (Axiovert 200, Carl Zeiss, Inc, Thornwood, NY) with a high speed 8-bit color camera (MF-046C, Allied vision technology GMBH). A FITC filter was used to detect green fluorescence. Full frames were captured with a shutter time between 100 ms and 2.5 seconds, depending on the fluorescent intensity of the sample. Full-color images were desaturated and contrast enhanced prior to analysis. To find pixel intensity across the width of the channel, 50 to 500 pixels from a steady state image were averaged.

### 4.3.7. SDS-PAGE and Immunoblotting

Following FF-IEF, the collected fractions were removed from the collection syringes and were mixed with SDS-PAGE tricine sample buffer without any intermediate steps. The tricine sample buffer contained 2-mercaptoethanol as a reducing agent and was loaded on a precast 10 or 12 lane tricine gels according to the manufacturer's instructions. Following electrophoresis, the gel was stained using either a silver staining kit (Thermo Fisher, Portsmouth, NH) or Coomassie (Simply Blue, Invitrogen) according to the manufacturer's instructions. The setup and run time (approximately an hour) for the IEF separation was equivalent or less than the SDS-PAGE setup and run time.

Immunoblots of total ERK2 (SC1647, Santa Cruz Biotechnology, Santa Cruz, CA), phosphorylated AKT (pAKT, sc-33437-R, Santa Cruz Biotechnology), and cytochrome C (556433, BD Biosciences, San Jose, CA) were performed using the same primary antibodies as for flow cytometry at a 1:1000, 1:500, and 1:1000 dilution, respectively. Proteins were separated by SDS-PAGE and transferred to nitrocellulose. After blocking (30-60 min at room temperature), blots were probed overnight at 4 °C in primary antibody, washed 3 times for 5 min in TBS-T (20 mM Tris-HCl pH 7.5, 150 mM NaCl, 0.1% Tween-20), incubated 1 h at room temperature in secondary antibody (1:5000 IRDye800-conjugated donkey anti-rabbit IgG, Rockland Immunochemicals), and finally washed 3 x 5 min in TBS-T. Blots were scanned on an Odyssey imaging system (Li-Cor Biosciences)

## 4.4. Results and Discussion

### 4.4.1. Marker Focusing

Fluorescent IEF markers were focused in the device to determine if using cascaded stages could deliver increased resolution. To focus these markers, 75 to 85V were applied across each section of the device for inlet flowrates of 55nL/s. Figure 4-6 plots intensity versus position at the exit of the first and second stages. Gaussian fits to the pI 5.1 marker exiting both the first and second stage were used to calculate focusing resolution ( *Res* ) according to Equation 4-5. The improvement in resolution from the first to second stage (10.7 vs. 5.9) is a factor of 1.81, consistent with the expected value of 1.71 for a 3-fold increase in channel width. Under ideal conditions, using Ampholine 3-10, the pH range in the main channel should be 3-10 from the anode to the cathode. The pH range in the second channels should ideally be 3-5.3, 5.3-7.7, and 7.7-10. However, from Figure 4-6, it is clear that the pI 5.1 marker focuses in the second channel, illustrating a cathodic shift in the pH gradient.

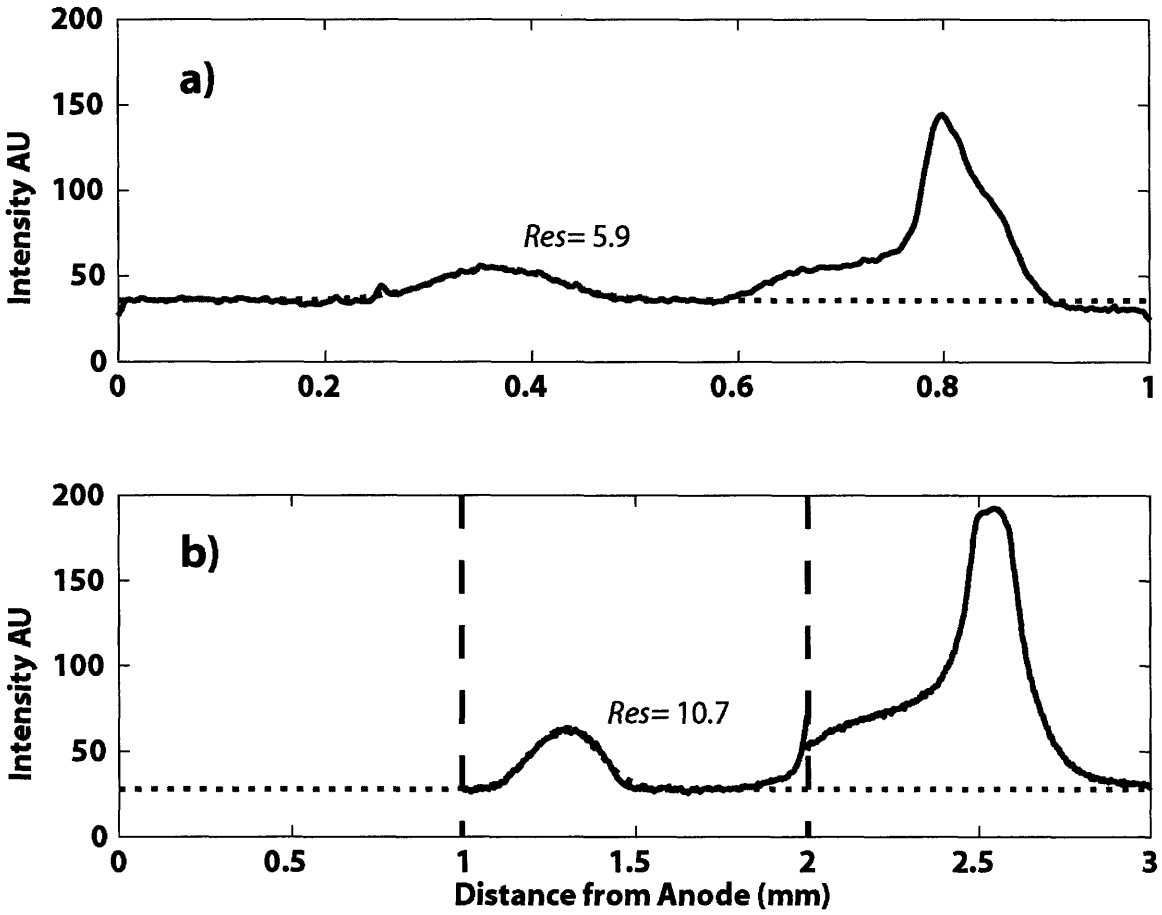


**Figure 4-6: Focusing of IEF markers in the cascaded design. Focusing at the exit of the first stage (a) shows a fluorescent profile (solid line) similar to our earlier work. Here, a Gaussian peak (dotted line) is fitted to the peak of the pI 5.1 marker, yielding a steady-state resolution of 5.9 after 6.8 seconds of focusing. Intensities at the exit of the second stages (b) show greater resolution and concentration of the markers after an additional 20.4s of focusing. A Gaussian fit to the pI 5.1 marker calculates a resolution of 10.7, consistent with theory.**

### 4.4.2. Protein Focusing in Each of the Designs

The ultimate goal of our work with micro FF-IEF devices is to develop a rapid separation tool that is compatible with current biological techniques. To demonstrate this, a mixture of proteins with known pI's and molecular weights were separated in the device. Figure 4-7 shows focusing of Protein G in each of the three designs with the same field strength. The 1 mm wide straight channel device reaches steady state before the other designs, but with the broadest peak. The 3 mm wide device required the longest residence time to reach steady state, approximately 22 seconds, as predicted by theory. The cascaded device required approximately 14s of focusing time, but had a final resolution comparable to the wider straight channel design. However,

incomplete fractionation of proteins in the semi-focused first stage results in Protein G buildup on the anode gel in the neighboring stages shown by the solid line in Figure 4-7b at $x/L$= 0.33 and 0.67.

The focusing of protein complexes was also observed, with the first trifurcation observed to separate Protein G unbound and bound to mouse IgG. Figure 4-8 shows the focusing profile of 20 μg/mL Alexa 488 labeled Protein G binding to 11 μg/mL of mouse IgG. Also plotted is the profile for focusing in the 1 mm straight channel design. There is excellent agreement for the focusing of the protein complex, however unbound Protein G exits predominantly in the acidic fraction, with some carryover into the neutral fraction. This carryover focuses to a position similar to the single stage device.

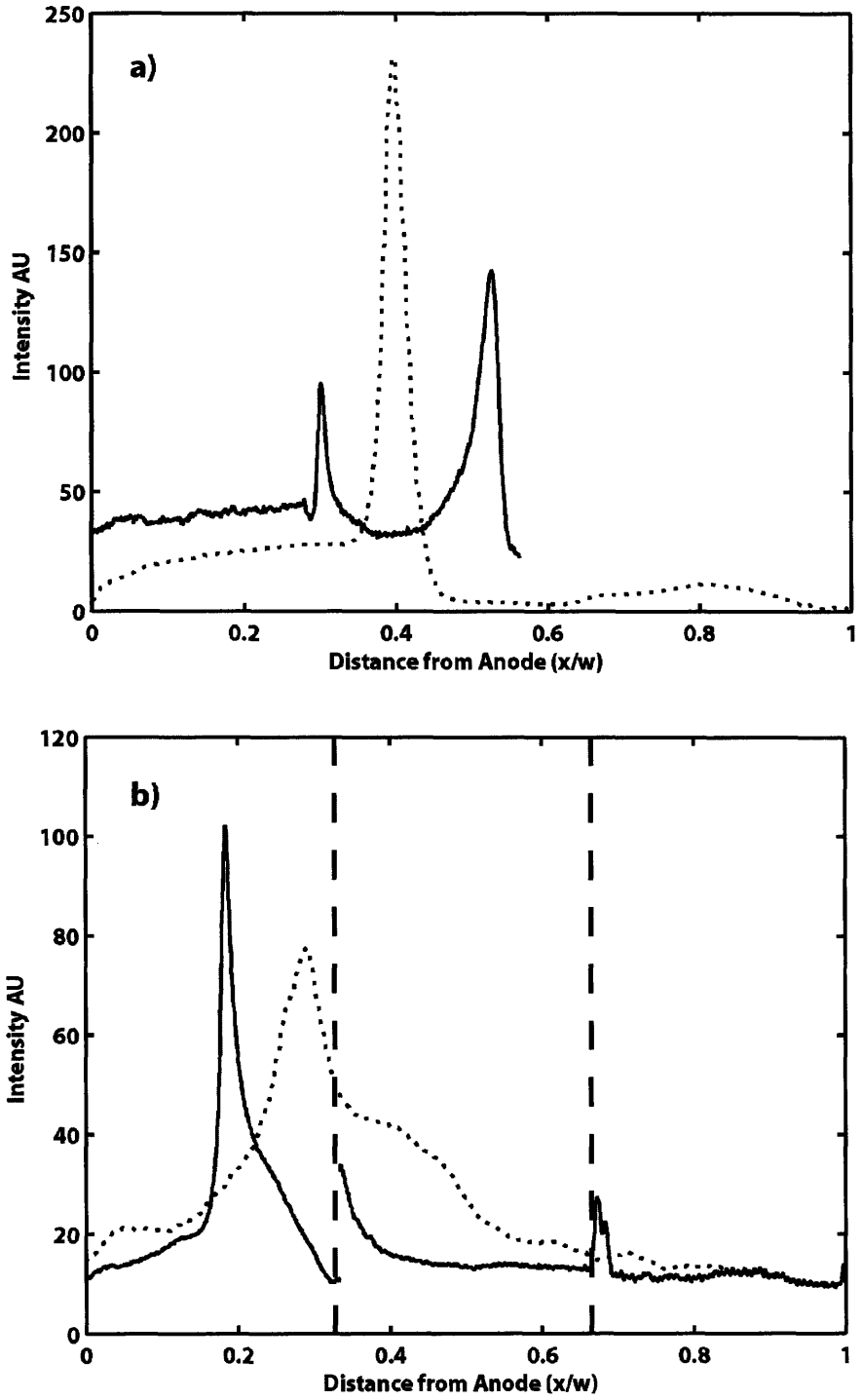


**Figure 4-7: Focusing of Alexa Protein G in channels of varying widths a) Focusing in a 3mm channel (solid green line, $L$ =3 mm – only part of the channel could be imaged) for 13s is still incomplete, while it reaches steady state in less than 9s in a 1mm device (dashed blue line, $L$ =1 mm). b) Focusing in the cascaded design shows incomplete focusing after 3.4 seconds in the first stage (black dashed line, $L$ =1 mm), but is tightly focused after an additional 10s in the second stage (solid blue line spliced from each stage, $L$ =3 mm)**

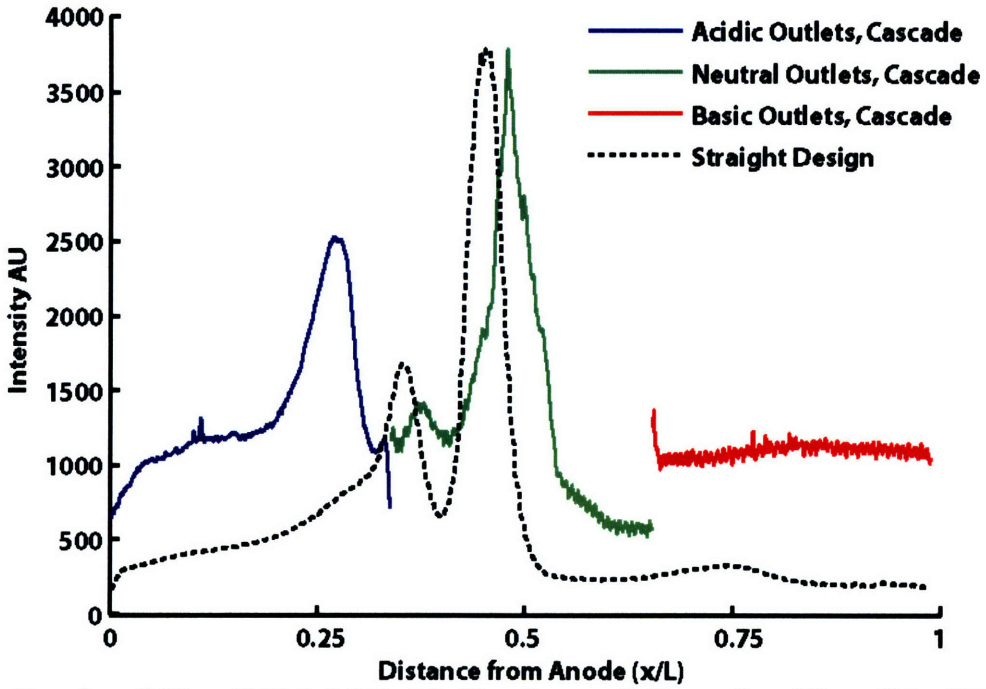


**Figure 4-8: Focusing of Alexa 488 labeled Protein G and mouse IgG complex. The outlets of the cascaded device are plotted straight lines for the acidic fraction (blue), the neutral fraction (green), and the basic fraction (red). For comparison, the focusing profile of Protein G-IgG complex in the 1 mm straight channel design is also shown (dashed line).**

### 4.4.3. SDS-PAGE and Immunoblotting

To demonstrate that the cascaded FF-IEF device can be used with other orthogonal separations, a mixture of proteins with known pI and molecular weight were separated in the device, and loaded on a SDS-PAGE gel. In all cases the outlets are numbered from 1 to 9 with outlet #1 corresponding to the lowest pH fraction and outlet #9 to highest pH fraction. Figure 4-9 shows the Coomassie stained gel where each IEF fraction 1-9 is separated in one lane of the gel. The gel shows that the proteins were focused into one, two, or three IEF fractions, and that no two fractions had the same protein composition. The labeled recombinant streptavidin was reduced by the tris-tricine sample buffer into its four subunits appearing at 13.2 instead of 57 kDa. The collected fractions are the integral of an hour of continuous focusing in the device; the consistent focusing shows that there is minimal drift in device performance. Of note is the compressed pH gradient observed in other focusing work.[1, 25, 24] The linear ampholyte pH range of 3-10 is expected to be bordered by more extreme, non-linear pH regions formed by dissociated ions from the salts present in the PBS. This results in the empty fractions near the anode and cathode (1, 8, and 9). Also, carrier ampholytes (which can interfere with detection

tools such as mass spectrometry) were easily separated from the proteins in the outlet fractions, staining as a low molecular weight (< 1 kDa) band just above the salt front. This coarse 2-D separation requires less labor and one-tenth the operating time of a 2-D gel.

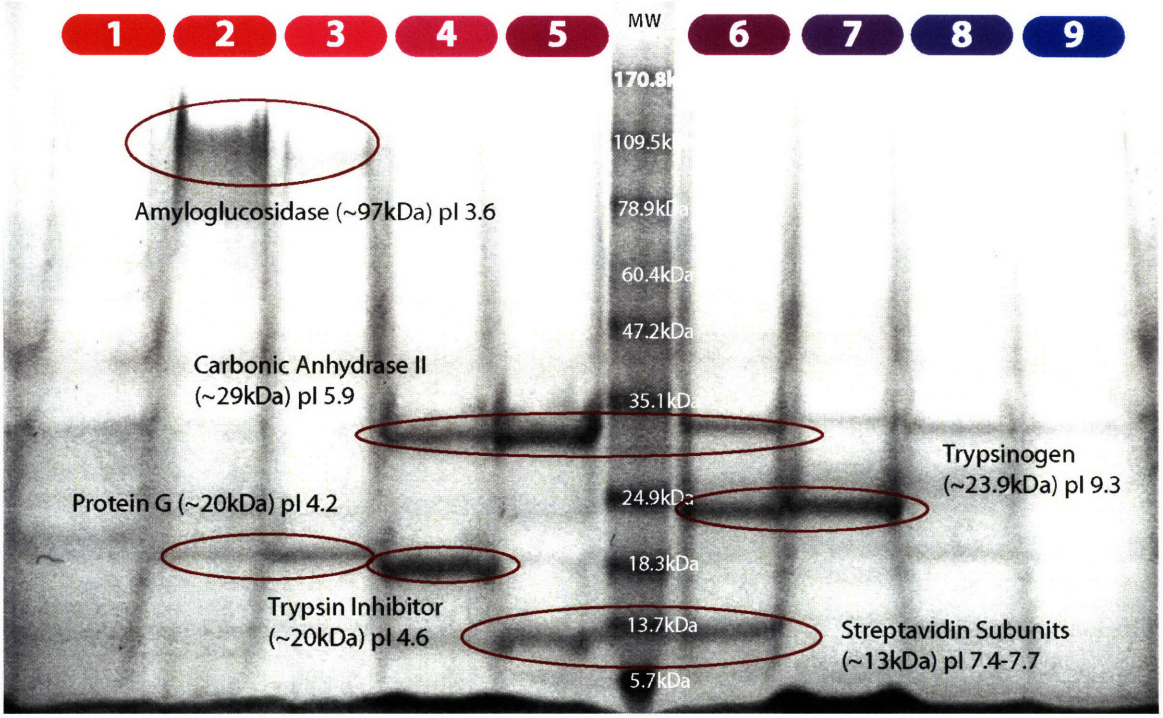


**Figure 4-9: Coomassie stained SDS-PAGE of five model proteins in PBS separated in a 3-10 pH gradient. Sample processed at 111 nL/s (18s residence time) and ~150V/cm.**

For low abundance proteins (such as signaling kinases) detection must be performed using affinity techniques such as immunoblotting. To demonstrate the ability of the cascaded devices to fractionate and simplify the most complex and challenging of samples, we chose to fractionate whole cell lysate in the devices. An additional application of the device is to remove major contaminants such as albumin from samples. As an example, Figure 4-10 shows western blots of the kinase JNK in lysate contaminated with cell medium where FF-IEF was used to reduce albumin in the sample. In addition to concentrating important proteins, FF-IEF prefractionation tools have utility in reducing the detection interference caused by common contaminants. Species present in cell culture media, such as albumin, can distort blotting results if the two proteins have similar sizes. The kinase JNK has a molecular weight near the bovine serum albumin in DMEM media, making it difficult to detect in samples rich in cell media. FF-IEF offers an orthogonal separation step to further reduce distortion. Figure 4-10 shows how

albumin can be separated from molecules of interest. For samples lysed in albumin-rich media, the albumin was observed to be concentrated in a few outlets (to the point of overloading the gel for #4), reducing the distortion in the rest of the pH fractions. In this case incomplete focusing at low field strengths was useful in reducing BSA and improving in the detection sensitivity of the other outlet fractions.

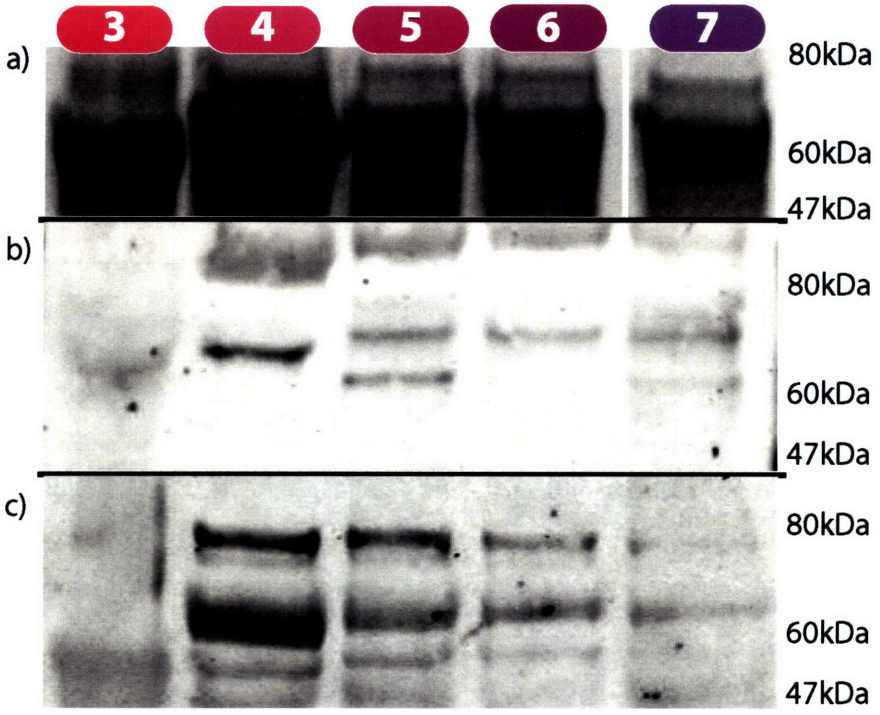


**Figure 4-10: Coomassie stained gel (a) and JNK western blots for (b) total JNK and (c) phospho-JNK. Whole HeLa cell lysed with 1% Triton in DMEM culture medium with 4M urea is processed at 111nL/s (18s of focusing) at ~150V/cm.**

Figure 4-11 shows pAKT, total ERK2, and Cytochrome *c* focusing in a 3-10 pH gradient under denaturing conditions as well as total protein (as determined by silver staining) present in each outlet. Band intensity was quantified and scaled to represent fold concentration over the averaged outlet signal and total protein levels. Here, Cytochrome *c* focuses well at its pI of ~9.6, with over a 200% (3-fold) enrichment for outlets 8 and 9. ERK2 and pAKT show 100% enrichment, presumably due to the short focusing time and multiple pIs across the 5-7 range for various isoforms.

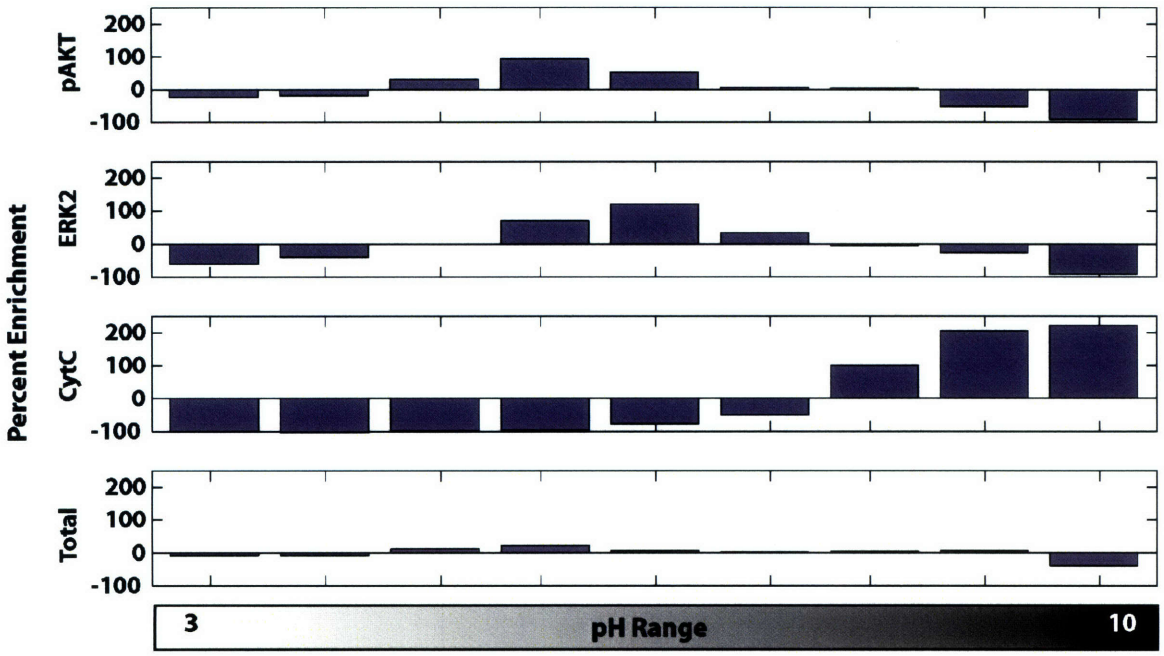


**Figure 4-11: Immunoblot and silver stain results for signaling proteins in HeLa cell lysate focused in a 3-10 pH gradient. Phospho-AKT and total ERK2 signal shows weaker focusing, with a maximum concentration factor of twofold. Cytochrome *c* is focuses strongly at a high pH, consistent with its high isoelectric point. As these proteins are focused, the total amount of protein, as determined by silver stain remains largely unchanged. These proteins are concentrated and collected from whole cell lysate at 83nL/s (18s of focusing) at ~300V/cm.**

The versatility of FF-IEF allows for many types of sample compositions, such as different pH ranges and denaturing conditions. Narrow pH ranges can be used in the device to separate proteins with similar pI, whereas milder surfactant conditions enable focusing of protein complexes. Figure 4-12 shows whole cell lysate focused in the 5-7 pH range in the presence of 4M urea. Bands were scaled to represent fold concentration over the averaged outlet signal. Here, protein bands corresponding to Cytochrome *c*, and pAKT show reasonable focusing and at least 2-fold enrichment over the lysate alone. However, ERK2 shows weaker focusing, presumably due to the multiple pIs across the 5-7 range for the various phosphorylated forms of ERK [92]. Of note is the focusing of Cytochrome *c* to an average pI of approximately ~5.7, far from the expected value of ~9.6. This apparent shift in pI is most likely due to the focusing of a protein heterocomplex (e.g. partially disrupted mitochondria) which includes Cytochrome *c* and is denatured by NP-40. Figure 4-11 shows Cytochrome *c* focusing normally at the high end of a 3-10 pH gradient in the presence of 4M urea as well as 0.45% NP-40. This shift in Cytochrome

*c* focusing in the presence of a surfactant supports the hypothesis that it participates in a protein complex that focuses at a more neutral pI.

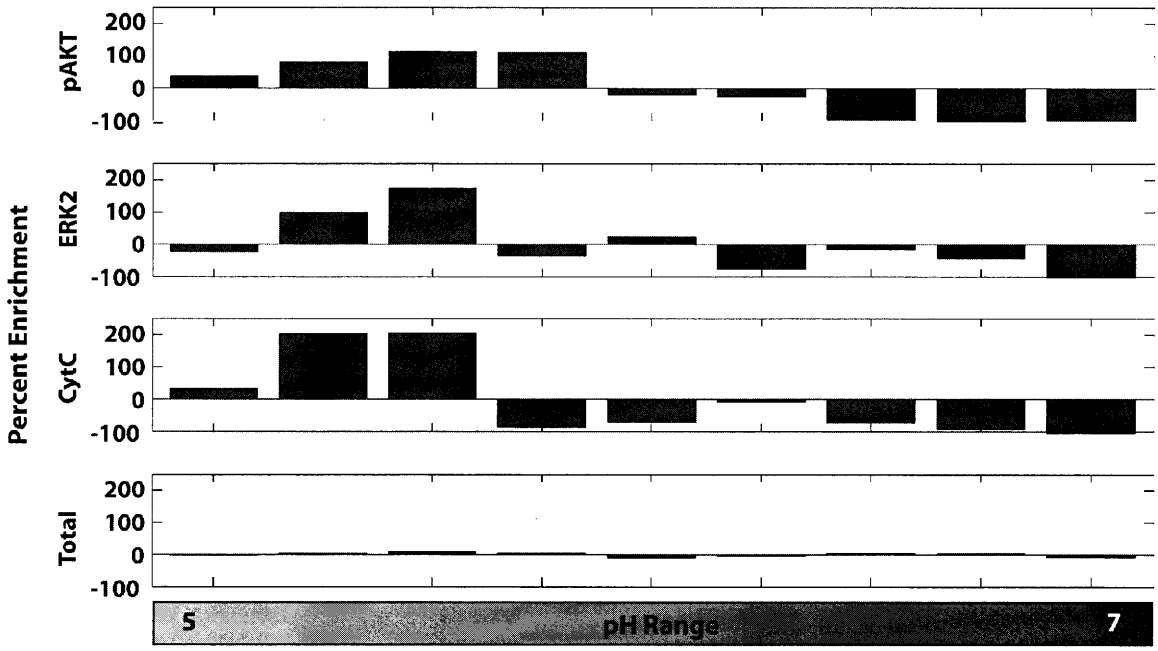


**Figure 4-12: Immunoblot and silver stain results for signaling proteins in HeLa cell lysate focused in a 5-7 pH gradient. Focusing of ERK2 and phospho-AKT is comparable to Figure 4-11, whereas Cytochrome *c* focuses to a pI estimated at ~5.7. These proteins are concentrated and collected from whole cell lysate at 111nL/s (14s of focusing) at ~300V/cm.**

## 4.5. Conclusions

We have demonstrated that the use of multiple stages for free flow isoelectric focusing can be used to more efficiently sort proteins in a complex mixture such as whole cell lysate. Using analytical expressions and numerical simulations, a cascaded design was proposed and fabricated to improve FF-IEF speed and resolution. Fabrication improvements, specifically maskless patterning of chemically different gels and gel-PDMS grafting with an UV initiator, were used to create devices. For cascaded FF-IEF the final resolution is expected to be equivalent to focusing in a shallow pH gradient; however, the necessary residence time for focusing is reduced. With a lower residence time, smaller device sizes are possible, reducing surface adsorption, Joule heating, and device manufacturing costs.

These simple, disposable FF-IEF devices have proven utility and reproducible performance, with operating times an order of magnitude faster than conventional techniques. FF-IEF has been shown to focus native model proteins, denatured proteins as well as protein complexes. Moreover, these FF-IEF devices tolerate messy, salty samples that present difficulties to other techniques such as IPG gel strips. Microfabricated FF-IEF devices have promise as disposable tools with reduced capital and operational costs compared to bench scale FF-IEF equipment, although this equipment can still benefit from cascaded stages. Although it is a relatively low-resolution technique, micro-FF-IEF with outlet collection is versatile and compatible with other common downstream techniques such as SDS-PAGE and immunoblotting. We have shown here that micro-FF-IEF performance can be improved with the use of cascaded stages that are easy to design and fabricate. For these reasons, micro-FF-IEF could become a very attractive "first step" separation tool for protein isolation and detection.

# Chapter 5: Preparative Scale FF-IEF

This chapter demonstrates the use of a diverging channel to enable preparative scale FF-IEF. These devices, larger than other disposable FF-IEF devices were designed, modeled, and tested with fluorescent dyes, protein IEF markers, and samples as complex as whole cell lysate. The fast liquid phase fractionation and collection was used to show compatibility with SDS-PAGE and western blotting. Comparing preparative scale FF-IEF to 2-D gel electrophoresis shows that IEF fractions are created much more quickly than conventional preparative techniques.

## 5.1. Introduction

For preparative separations on the milliliter scale, current FF-IEF tools require carefully cleaned and manually assembled apparatus to perform separations. These tools use multiple inlets to create a pH gradient across the width of the device [15, 129]. These inlets require multiple premixed proprietary pH buffers and a dedicated pumping system, increasing system cost and complexity. A sample introduced to this multiple buffer system is instantly diluted, reducing detection sensitivity even after focusing. Disposable, inexpensive IEF devices have the potential to become a new tool for research involving difficult proteins and protein complexes, reducing laborious sample preparation. Previous chapters have described devices with volumes in the range of 1-2 μL [1, 2], however, the flowrates (10 to 100 nL/s) are too low to process typical sample volumes experienced in biological research. Also, the nine outlets of the cascaded device may be too few for some applications where higher resolution is needed. Accordingly, a third generation of FF-IEF devices were developed and tested. These preparative scale FF-IEF devices are an order of magnitude (or more) larger than published μFF-IEF devices. [133, 81, 79, 67, 66, 1]

## 5.2. Design and Modeling

FF-IEF devices were redesigned towards a goal of fractionating 24 outlets and capable of processing samples as quickly as 300 nL/s (1 mL/hr). Because of the large number of outlets, cascaded FF-IEF stages would quickly become cumbersome to fabricate. Therefore, a new approach was taken to with these preparative scale devices. The devices are a single stage with a diverging channel, offering the benefits of the cascaded approach without a prohibitively large

and intricate footprint. However, the final footprint of the device is as large as the PDMS fabrication technique would allow. The limiting size of the devices is ultimately limited by the diameter of the oxygen plasma chamber, approximately 60 mm.

### 5.2.1. Device Layout

To demonstrate preparative scale FF-IEF and the benefit of a diverging sample channel, two device designs were fabricated. Table 5-1 lists the dimensions of the rectangular and divergent channel designs, shown in Figure 5-1. The rectangular device, shown in Figure 5-1a, has up to three optional inlets for sheath flow, similar to other FF-IEF designs [67, 66, 15, 129, 81, 133, 136, 116, 99]. The central inlet of the rectangular device design uses a branched structure defined by PDMS posts (white diamonds in Figure 5-1a) to balance the pressure drop and flowrate across the width of the channel.

The second design, consisting of a single inlet with a linearly diverging channel, is shown in Figure 5-1b. The diverging channel is bordered by triangular regions of polyacrylamide gel with either an acidic (red) or basic (blue) functional group incorporated into the polyacrylamide matrix. Diamond shaped posts (1 mm square) in the PDMS were used to support the gel regions.

The outlets of the device are an identical 2 by 12 array of channels with the endpoints roughly matching the pitch of a 384 well plate, 4.5 mm. The channel lengths were adjusted to keep the pressure drop through each of the channels equal. Each channel is 0.5 mm wide.

**Table 5-1: Comparison of preparative FF-IEF device designs.**

| Channel Type | Width (mm) | Length (mm) | Footprint ($mm^2$) | Height (μm) | Volume (μL) |
|---|---|---|---|---|---|
| Rectangular | 47 | 45 | 2108 | 165 | 348 |
| Divergent | 1.3 to 47 | 56.4 | 1360 | 160 | 218 |

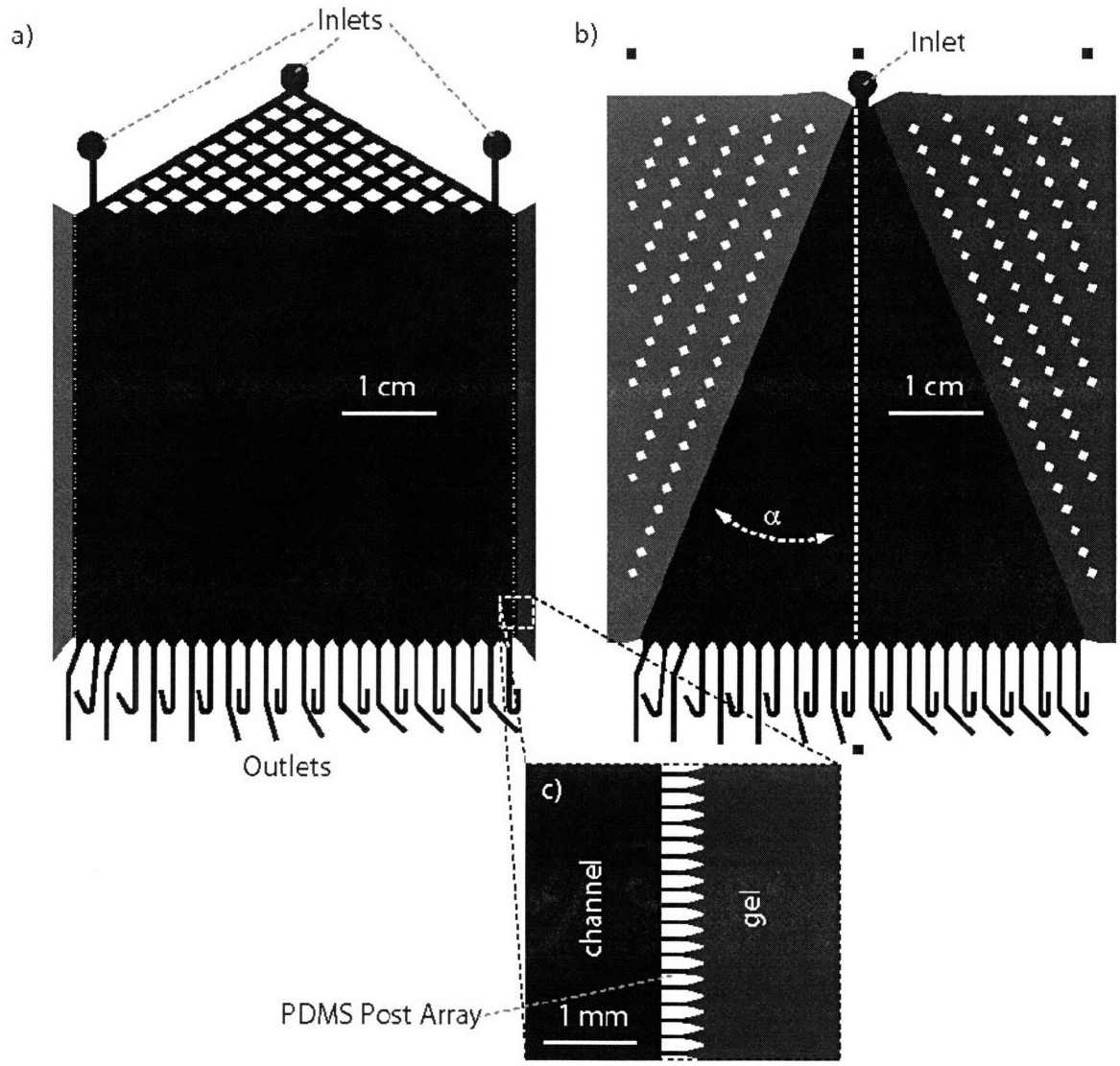


**Figure 5-1: Layout of the preparative scale FF-IEF devices. a) Rectangular channel and b) diverging channel designs were fabricated, modeled, and tested. c) Detail of the PDMS post array (white shapes) that allow for polyacrylamide gel pattering via surface tension. Each design has 24 outlets spaced in a 2x12 array and has a footprint slightly larger than 50x75mm.**

### 5.2.2. Laminar Flow Separation

For two-dimensional flow between infinite, diverging plates (Hamel flow), laminar separation can occur under some flow velocities [26, 29]. This leads to a reversal of flow direction near the walls. To ensure that laminar separation does not occur in the diverging channel design, the length scales and flow velocities were examined in a manner similar to that presented by Denn [29] using the radial component of the Navier-Stokes equation in cylindrical coordinates, Equation 5-1.

$$\rho\left[v_r\frac{\partial v_r}{\partial r}\right]=-\frac{\partial P}{\partial r}+\eta\left[\frac{\partial}{\partial r}\left(\frac{1}{r}\frac{\partial}{\partial r}(rv_r)\right)+\frac{1}{r^2}\frac{\partial^2 v_r}{\partial\theta^2}+\frac{\partial^2 v_r}{\partial z^2}\right] \qquad \textbf{5-1}$$

It is convenient to work with the flow rate per width (units: area per time) of the channel $q$, defined by Equation 5-2.

$$q=\int_{-H}^{H}\int_{-\alpha}^{\alpha}v_r r\,d\theta\,dz\Big/2H=\int_{-\alpha}^{\alpha}v_r r\,d\theta=\int_{-\alpha}^{\alpha}f(\theta)d\theta \qquad \textbf{5-2}$$

For convenience, Equation 5-2 also defines $f$ as the product of the radial distance, $r$, and the radial component of fluid velocity, $v_r$, a function of angular position and vertical ($z$-direction) only. Nondimensionalizing the distances and velocities and normalizing $f$ in Equation 5-1 results in Equation 5-3.

$$\tilde{r}=\frac{r}{L}\qquad \tilde{z}=\frac{z}{H}\qquad \tilde{v}=\frac{v_r}{U}=\frac{v_r L}{q}\qquad \tilde{f}=\frac{f\alpha}{q}\qquad \tilde{\theta}=\frac{\theta}{\alpha}$$

$$-\frac{\rho q^2}{L^3\alpha^2}\frac{\tilde{f}^2}{\tilde{r}^3}=-\frac{1}{L}\frac{\partial P}{\partial\tilde{r}}+\eta\left[\frac{q}{L^3\alpha}\left(\frac{\partial}{\partial\tilde{r}}\left(\frac{1}{\tilde{r}}\frac{\partial}{\partial\tilde{r}}\left(\tilde{f}\right)\right)\right)+\frac{q}{L^3\alpha^3}\frac{1}{\tilde{r}^3}\frac{\partial^2\tilde{f}}{\partial\tilde{\theta}^2}+\frac{q}{LH^2\alpha}\frac{1}{\tilde{r}}\frac{\partial^2\tilde{f}}{\partial\tilde{z}^2}\right] \qquad \textbf{5-3}$$

Rearranging Equation 5-3 yields Equation 5-4:

$$-\frac{\tilde{f}^2}{\tilde{r}^3}=-\frac{L^2\alpha^2}{q^2\rho}\frac{\partial P}{\partial\tilde{r}}+\frac{\mu\alpha}{q\rho}\left[\left(\frac{\partial}{\partial\tilde{r}}\left(\frac{1}{\tilde{r}}\frac{\partial}{\partial\tilde{r}}\left(\tilde{f}\right)\right)\right)+\frac{1}{\alpha^2\tilde{r}^3}\frac{\partial^2\tilde{f}}{\partial\tilde{\theta}^2}+\frac{L^2}{H^2}\frac{1}{\tilde{r}}\frac{\partial^2\tilde{f}}{\partial\tilde{z}^2}\right] \qquad \textbf{5-4}$$

For typical flowrate and sample properties $\rho=10^3\frac{kg}{m^3}$, $\mu=10^{-3}\frac{kg}{m\cdot s}$, and $q=10^{-5}\frac{m^2}{s}$. Using these values and the dimensions of the divergent device in Table 5-1, the first term inside the brackets on the right side of Equation 5-4 (radial derivative) is on the order of 1, the second term (angular derivative) is on the order of 100, and the third term is on the order of $10^5$. Because of the very different coefficients, the angular and radial derivatives of $\tilde{f}$ may be neglected, meaning that laminar flow separation does not occur within the device, due to the strong viscous damping from the narrow channel height.

An assumption for pressure drop is necessary to determine the order of magnitude for the first term on the right side of Equation 5-6. Using device and typical operating parameters, $\frac{q^2\rho}{L^3\alpha^2}$ is on the order of $10^{-3}$ Pa/m. Based on the height of the channel, and using the equation for pressure drop in parallel plate Poiseuille flow [26] shown here in Equation 5-5.

$$\frac{dP}{dx} = -\frac{3U\eta}{H^2} \qquad \textbf{5-5}$$

Using Equation 5-5 with the device parameters and typical flow rate, the pressure drop would be ~5 Pa/m, meaning that the order of magnitude for the first term (pressure drop) on the right side of Equation 5-4 is much greater than unity. Therefore, $\frac{\tilde{f}^2}{\tilde{r}^3}$ in Equation 5-4 may be neglected; thus only two terms may be considered with pressure solely a function of radial distance, resulting in Equation 5-6.

$$\frac{\partial^2 \tilde{f}}{\partial \tilde{z}^2} = \frac{H^2 \alpha \tilde{r}}{2q\mu}\frac{dP}{d\tilde{r}} \qquad \textbf{5-6}$$

This PDE can be solved analogously to parallel plate Poiseuille flow, with the solution given by Equation 5-7.

$$\tilde{f}(\tilde{r},\tilde{z}) = -\frac{H^2 \alpha \tilde{r}}{q\mu}\frac{dP}{d\tilde{r}}\left(1-\tilde{z}^2\right) \qquad \textbf{5-7}$$

Rearranging and dimensionalizing to solve for radial velocity results in Equation 5-8.

$$v_r = -\frac{H^2}{2\mu}\frac{dP}{dr}\left(1-\left(\frac{z}{H}\right)^2\right) \qquad \textbf{5-8}$$

Next, Equation 5-8 is substituted into Equation 5-2, shown as Equation 5-9 which is integrated to find $\frac{dP}{dr}$ in terms of $q$, with the solution presented in Equation 5-10. Rearranging to solve for pressure drop results in Equation 5-11.

$$q = \int_{-H}^{H} \int_{-\alpha}^{\alpha} -\frac{H^2}{2\mu}\frac{dP}{dr}\left(1-\left(\frac{z}{H}\right)^2\right) r\,d\theta\,dz \Big/ 2H \qquad \textbf{5-9}$$

$$q = -\frac{H^2\alpha}{3\mu}\frac{dP}{dr}r \qquad \textbf{5-10}$$

$$\frac{dP}{dr} = -\frac{3\mu q}{H^2\alpha r} \qquad \textbf{5-11}$$

Substituting Equation 5-11 into Equation 5-8, the relationship between velocity and radial distance is given by Equation 5-12.

$$v_r = \frac{3q}{2\alpha r}\left(1-\left(\frac{z}{H}\right)^2\right) \qquad \textbf{5-12}$$

As expected, Equation 5-12 is similar to the laminar flow between parallel plates, with the difference that the velocity is now also dependent on the radial distance. This feature will be explored in more detail using 3-D flow modeling in the following section.

### 5.2.3. Pressure Drop Variation

As the number of outlets increases, so does the challenge of achieving uniform outlet flowrates. To make fraction unloading more compatible with devices such as multi-well plates and multi-channel pipettes, as well as with the microscope slide used to seal the devices, the outlets were arranged in a 2x12 rectangular array. The outlet spacing was matched to roughly the pitch of a standard 384-well plate (4.5 mm).

The array was fabricated such that the outlet channels all had an equivalent length, to minimize on-chip pressure drop differences. To minimize off-chip pressure differences, the outlet flows were actively balanced by hydrostatic pressure. Gel loading pipette tips (VWR) were inserted into the outlet ports, resulting in a free standing array of reservoirs approximately 5 cm tall open to the atmosphere. During device operation, faster filling outlets would create a larger hydrostatic pressure than slower outlets. This difference actively works to balance the height of the reservoirs, resulting in more uniform outlet flowrates.

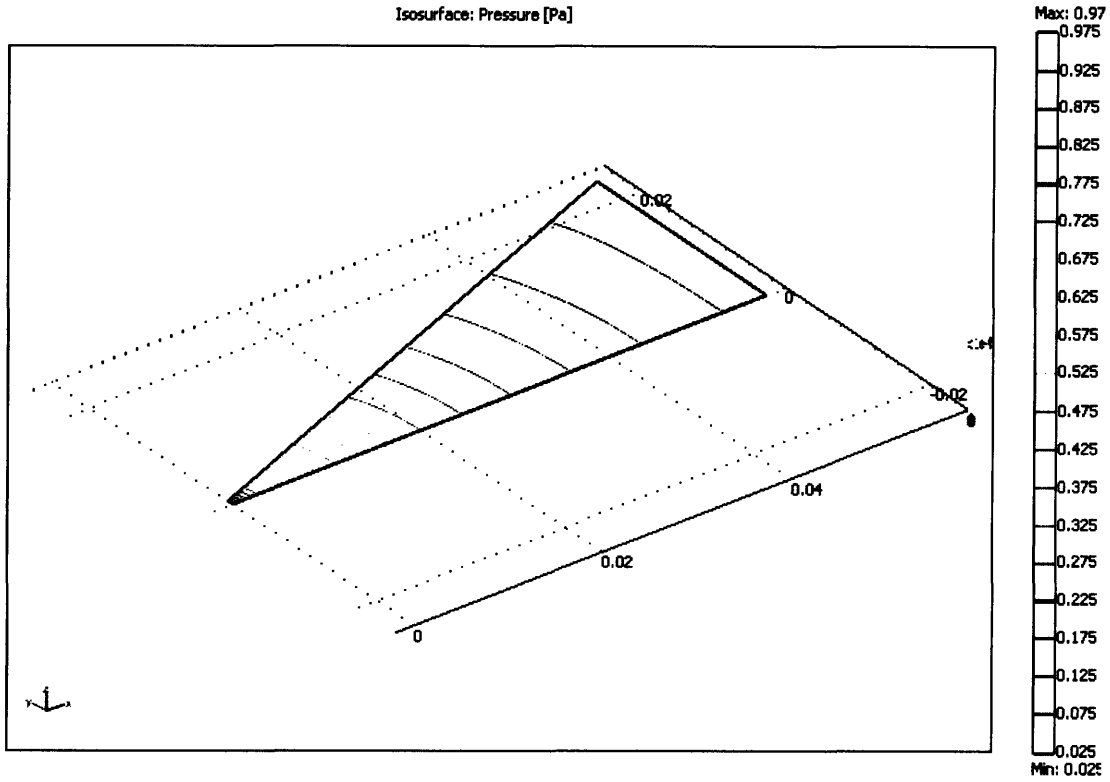


**Figure 5-2: FEMLAB Simulation of pressure drop in the divergent device design. Because of the symmetry of the device, only half of the channel was modeled. The simulation results confirm that in the absence of outlet pressure balancing, liquid will flow faster through the center of the channel.**

For the case of a channel that varies at a constant rate, $m$, with respect to time, Equation 5-13 was used.

$$w = mt + w_0 \qquad \textbf{5-13}$$

Substituting Equation 5-13 into Equation 2-53, Equation 5-14 shows the relationship between channel length, $L$, and width, $w$.

$$\frac{dL}{dt} = \frac{U_0 w_0}{mt + w_0} \qquad \textbf{5-14}$$

Solving Equation 5-14, the length of the channel must be a logarithmic function of channel width to satisfy the assumptions of Section 2.6.2 and Equation 5-13. Equation 5-15 describes the channel length as a function of width.

$$L = \frac{U_0 w_0}{m} \ln\left(\frac{mt + w_0}{w_0}\right) = \frac{U_0 w_0}{m} \ln\left(\frac{w}{w_0}\right) \qquad \textbf{5-15}$$

In creating a COMSOL model like Figure 5-2, it is more convenient to consider instead channel width as a function of the distance from the inlet. Rearranging Equation 5-15 yields Equation 5-17, below.

$$w = w_0 \exp\left(\frac{mL}{U_0 w_0}\right) \qquad \textbf{5-16}$$

From Equation 5-15, another model matching the overall footprint of the model in Figure 5-2 was created, using a factor of $m/U_0$ set to $4.12 \times 10^{-2}$ to correctly match the final widths of the channel. Figure 5-3 plots the pressure drop profile in the device, similar to Figure 5-2.

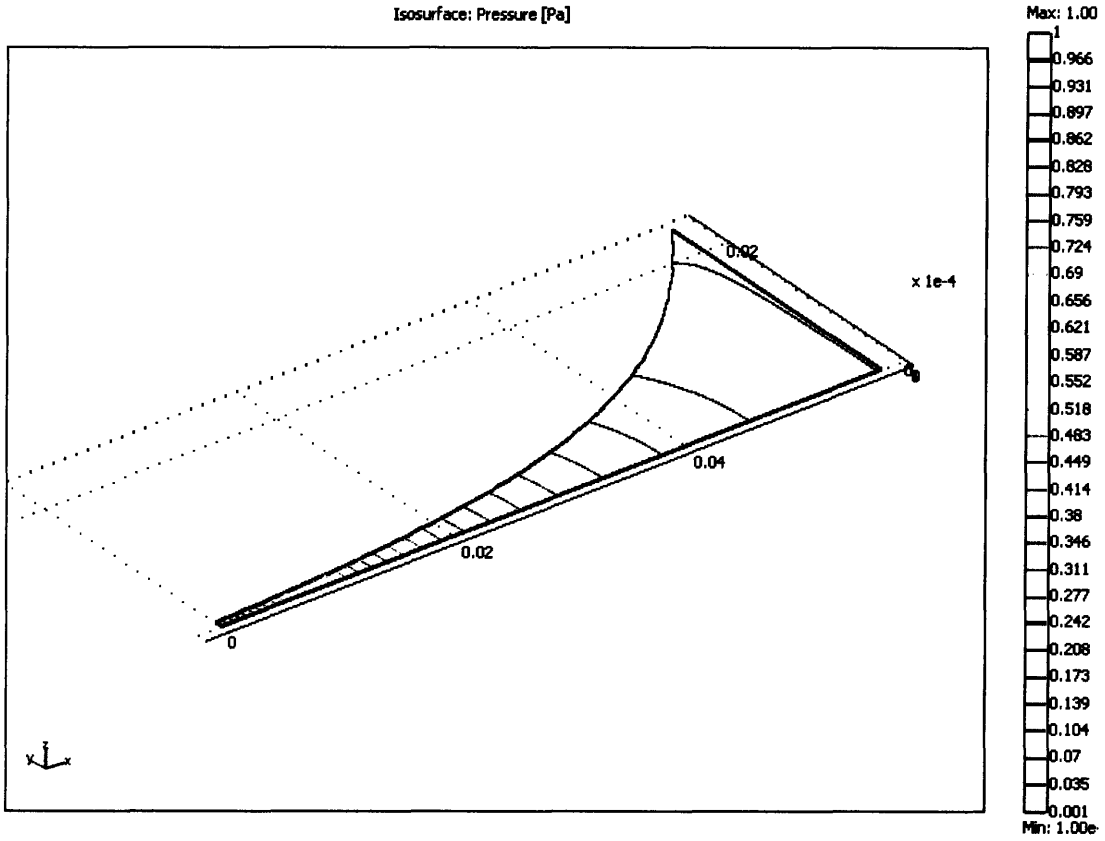


**Figure 5-3: FEMLAB simulation of pressure drop in an exponentially diverging device. Because of the symmetry of the device, only half of the channel was modeled. Inlet, outlet and channel length are identical to the divergent device design, but in this case the pressure drop profile is highly non-uniform.**

In Figure 5-3, as expected, the initial width of the channel experiences a large pressure drop, but as the channel widens the fluid will slow down dramatically. At the outlet of the device, the rapidly widening channel creates a stagnant region, driving most of the sample out through the center of the channel. While the linearly diverging channel is expected to require some back pressure to compensate for uneven flow, the exponentially diverging channel would require much more elaborate means to make uniform flow tractable.

Likewise, for a case where the channel widens with respect to a quadratic function, given by Equation 5-17, the relationship between length and width is presented in Equation 5-18.

$$w = mt^2 + w_0 \qquad \textbf{5-17}$$

$$L = U_0\sqrt{\frac{w_0}{m}}\tan^{-1}\left(\frac{mt}{\sqrt{mw_0}}\right) = U_0\sqrt{\frac{w_0}{m}}\tan^{-1}\left(\frac{\sqrt{w-w_0}}{w_0}\right) \qquad \textbf{5-18}$$

In this situation, reliable device operation the channel diverges so quickly that reliable pressure matching via external forcing is practically impossible.

## 5.3. Device Layout and Fabrication

### 5.3.1. Bulk Fabrication

The devices were fabricated using standard soft lithography techniques [33]. A mold was created from the photopaternable polymer SU-8 2050 (MicroChem, Newton, MA) spun cast on a featureless silicon wafer. The SU-8 was exposed to UV through a 20,000 dpi transparency mask (CAD/Art Services, Bandon, OR) to initiate polymerization. Once polymerized, two part PDMS (Sylgard 184, Dow Chemicals, Midland, MI) was mixed and poured on the wafer. Because of the large width of the channel, the soft, rubbery PDMS was found to collapse during device sealing. Therefore, a glass platform, a double-wide microscope side cut to approximately 50 x 50 mm was cured inside of the device, lending rigidity to the devices, while maintaining the advantages of soft lithography fabrication. Figure 5-4 outlines the two-curing step process used to cure the glass platform within the PDMS. After the device was removed from the master, holes (one inlet, 24 outlets) were punched using a 20 gauge Luer stub adapter (Becton-Dickinson, Sparks, MD). And were cleaned using cellophane tape prior to sealing.

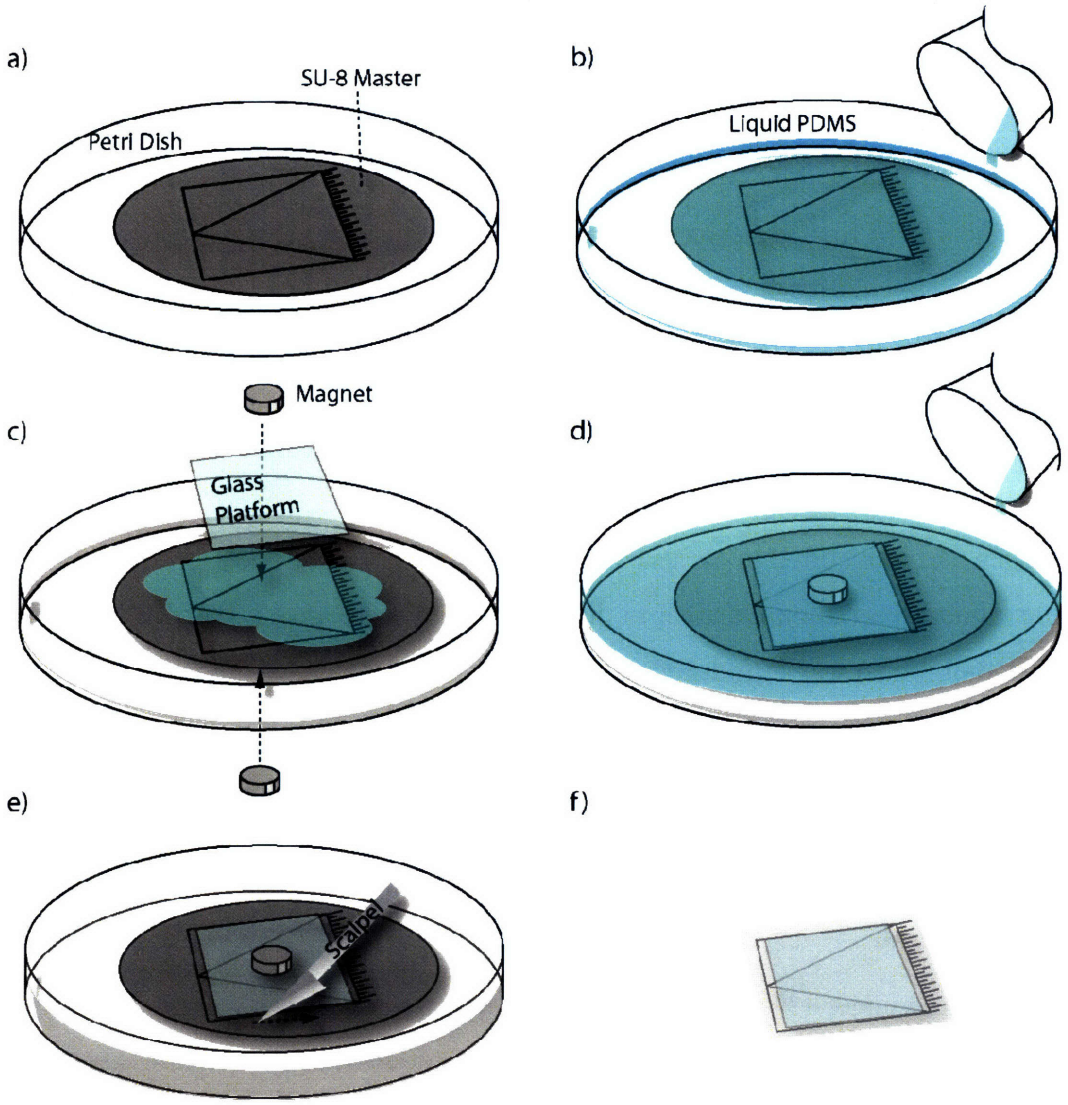


**Figure 5-4: Fabrication procedure for PDMS preparative devices. a) The SU-8 master, patterned on a 4-inch silicon wafer is placed inside a 6-inch Petri dish. b) Unpolymerized PDMS (20 g) is poured over the mold and cured for 2 hours at 70°C. c) To prevent the channel from collapsing, a glass platform approximately 50x50mm is positioned above the device and held in place with a magnet. d) More unpolymerized PDMS (60 g) is poured into the dish. e) After curing, the devices are cut out with a scalpel and carefully pried off the master using ethanol as a release agent. f) The magnet is removed, leaving the glass platform encased in the PDMS device.**

### 5.3.2. Sealing and Surface Modification

The devices were sealed by surface oxidation in oxygen plasma (Harrick, Ithaca, NY). A double wide microscope slide (75 x 50 mm) was exposed to plasma for one minute, following this, the PDMS device and the microscope slide were exposed to an additional 40 seconds of

plasma. The glass was brought into contact with the PDMS surface, forming a permanent bond. The freshly sealed devices were kept dry for at least 20 minutes to ensure complete bonding.

Next, the channels were filled with 1% 3-(trimethoxysilyl)propyl methacrylate (TSPM, Sigma Aldrich, St. Louis, MO) in anhydrous ethanol and allowed to dry at room temperature overnight. The TSPM treated devices now had a covalently bound methacrylate group, capable of being incorporated in to an acrylamide gel matrix.

### 5.3.3. Gel Casting

To cast polyacrylamide gel in the sealed devices, they were first degassed by placing them in a vacuum oven overnight at 70°C and 20 mmHg. After degassing, the devices were kept under nitrogen and transferred to an acrylic glove box (Air Control, Inc., Henderson, NC). And acrylamide monomer solution identical to that used in the cascaded FF-IEF devices (15% T, 3% C, 12mM Immobilines) was introduced to the anode and cathode gel regions at the edges of the device. The sample was drawn in by capillary action, and held in place at the array of small PDMS posts by surface tension, shown in Figure 5-1c. Care must be taken to prevent overflow of the monomer into the focusing chamber. The sample is held in place long enough to polymerize the acrylamide by exposing the UV initiator to long-wave UV (354 nm, Spectroline ENF-280C, Spectronics Corporation, Westbury, NY) for 2 minutes. After polymerization, the devices were stored under 1% w/v solution of poly(vinyl alcohol) (PVA, MW 146-186kDa, 87-89% hydrolyzed, Sigma-Aldrich). Prior to use, each device was checked for leaks and outlet flow. Some defects in casting were observed, but usually did not impact device performance. Device yields of 60-80% were typical.

## *5.4. Experimental Methods*

### 5.4.1. Sample Preparation

To evaluate the devices, a wide variety of biological and non-biological samples were evaluated. For all samples, Ampholine 3-10 (Fluka) was added to a final concentration of 2%. To evaluate the establishment of a pH gradient in the device, the pH indicators methyl red and bromothymol blue (Fluka) were used. For protein pI markers, a commercially available kit for IEF range 3.6-6.6 (l8012, Sigma Aldrich) was used with a high pI marker (Trypsinogen pI 9.3, T1146, Sigma Aldrich) added to an identical concentration as each of the kit components (20

μg/mL of each protein). The proteins were dissolved in 0.5x PBS with 0.05% w/v bromothymol blue to visualize focusing progress.

For whole cell lysate, two different buffer systems were examined. In some cases, chaotropic buffer consisting of 8 M urea (EMD Biosciences), 2 M thiourea (ACS, Sigma-Aldrich), and 4% CHAPS (3-[(3-Cholamidopropyl)dimethylammonio]-1-propanesulfonate, JD Baker) was used with HeLa, HCT 116, or U20S cell lysate to a final protein concentration of 0.5 to 1 mg/mL. For milder buffer conditions, 50 mM tris (EMD Biosciences), 5 mM EDTA (Mallinckrodt), 45 mM NaCl (Mallinckrodt), 0.5% NP-40, 20% glycerol was used as a sample buffer. The mouse macrophage line RAW 264.7 was lysed in this buffer of to a final protein concentration of 0.5 mg/mL. Fluorescent pI were markers spiked into the biological sample to better visualize focusing progress. Markers with pI 5.1 (Catalog #89478, Fluka), 7.6 (#89951) and 9.0 (#90699) were added to a final concentration of 25 μg/mL each.

### 5.4.2. Device Operation

Because of the large footprint and high cooling requirements, the preparative scale FF-IEF devices are not suitable for use on a microscope stage. The devices were operated with bench top equipment shown in Figure 5-5. The devices were placed atop a thermoelectric cold plate with a temperature controller (CP-036 and TC-24-10, TE Technology, Inc., Traverse City, MI) to cool the devices to a desired temperature. The sample is delivered to the device via a syringe pump. The device is powered by a high voltage power supply (EPS 3501, GE Healthcare). The bench top setup is small and inexpensive compared to conventional IEF equipment.

For biological samples that must be kept below room temperature, a jacketed syringe was used to simultaneously cool the sample without interfering with the syringe pump operation. This syringe was formed by inserting a 5 mL syringe into a 60 mL syringe. The 5 mL syringe was fitted with a 23 gauge Luer stub adapter to 0.5 mm ID polyethylene tubing. This fine tubing carried the sample, and was jacketed by ¼" ID silicone tubing attached to the 60 mL syringe. The larger tubing carried the cooling water which was introduced to the 60 mL syringe via a reservoir connected to a hole cut into the syringe barrel. The ¼" tubing drained into an ice bucked driven by hydrostatic pressure, requiring the sample reservoir to be occasionally refilled. The temperature difference between the ¼" tubing outlet and the reservoir was measured to be

4°C. The sample tubing exited through a hole in the larger tubing, exposing the sample to room temperature for 2 minutes or less depending on flowrate. Figure 5-5a shows a photograph of the jacketed syringe in operation, with a more detailed schematic in Figure 5-5b.

The use of a cold plate was found to be essential to the operation of the device. Nearly all the electrical energy from the power supply is converted to heat the sample through Joule heating. With a typical heating rate of 7 W under adiabatic conditions, 220 μL of pure water would be heated at a rate of about 8°C/s. The thermal conductivity of the sample is assumed to be 0.58 W/m-°K, that of the glass device bottom 1.0 W/m-°K, and the aluminum surface of the cold plate is 250 W/m-°K. Using thicknesses of 0.15, 1, and 10 mm respectively, and assuming that these heat transfer coefficients dominate the heat transfer, the overall heat transfer coefficient will be 768 $W/m^2$-°K. For a surface area of 25 x 75 mm, the heat transfer will be 1.44 W/°K. Thus there is a temperature difference between the device and the cold plate that will be at least 5 °C, but not much greater than this due to the good thermal contact between the cold plate, glass and sample.

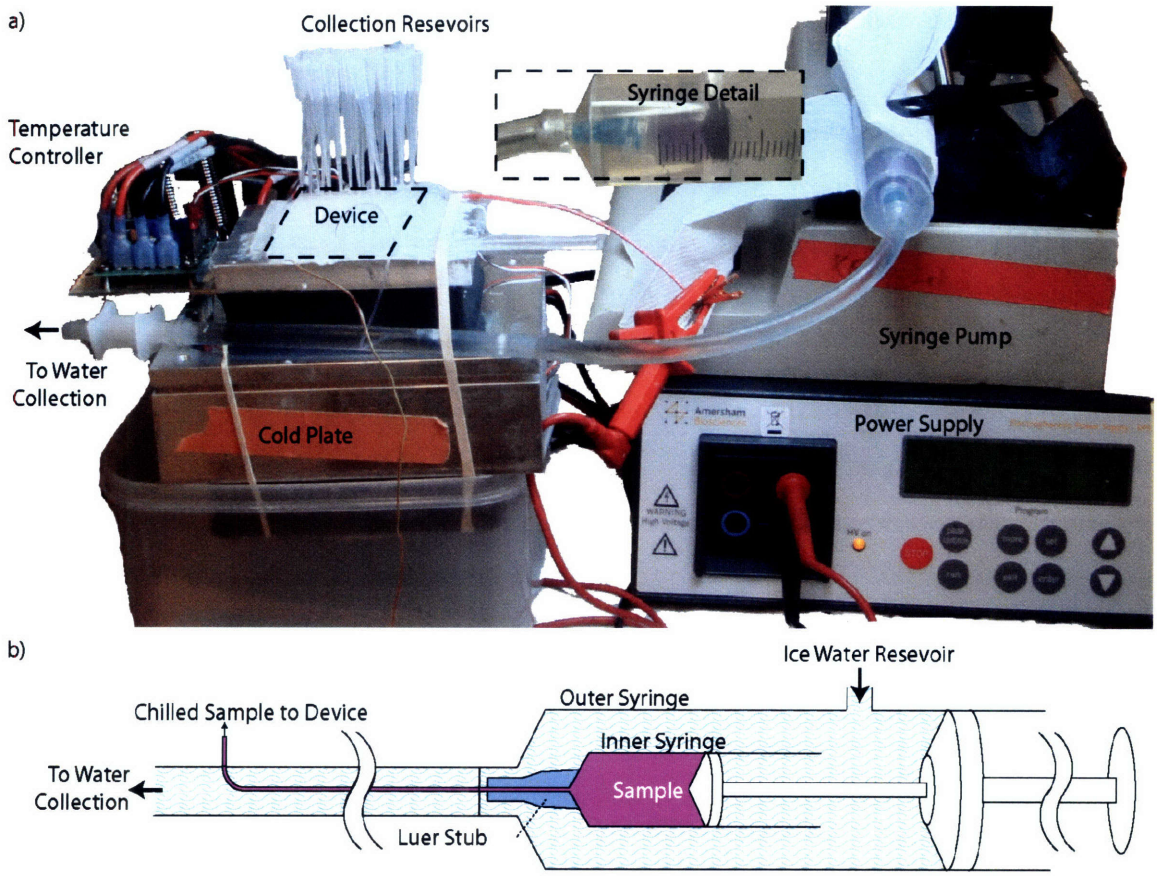


**Figure 5-5: Experimental setup for FF-IEF. a) Photo of device in operation showing the placement of the syringe pump, power supply, cold plate, and FF-IEF device. b) Cross-section of the jacketed sample syringe.**

### 5.4.3. Sample Collection

As shown by Figure 5-2, without an external pressure, the device outlets would have different flowrates. Therefore, hydrostatic pressure was used to ensure that the fractionated samples had roughly the same volume. This was accomplished by inserting a 200 µL gel loading pipette tip into the PDMS outlet. The fine plastic capillary of the pipette tip fit snugly into the 20 gauge hole, and was held in place without leaks for the duration of the experiment.

The pipette tip served to i) balance the volume of the collected fractions and ii) act as a collection reservoir for the fractionated sample. By introducing a negative hydrostatic pressure feedback to the central outlets, the height of the pipette tip promoted an equal volume collection of the outlet fractions. This feedback mitigated, but did not entirely prevent, irregular sample volumes due differences in pressure drop across the divergent channel, as well as irregularities in the device, such as channel height and the manually punched outlet holes. Protein precipitate or

PDMS fragments were also observed to interfere with the flow balancing effect of the vertical fraction reservoirs.

The fluidic connectivity between the reservoirs, which balanced the flow, also worked against the harvesting of the fractions. If the liquid in one outlet or the pipette tip itself was removed, hydrostatic pressure would cause the liquid in the other reservoirs to flow down and out of the perturbed outlet. To prevent this, the reservoirs must either be harvested simultaneously, or the fluidic communication between them must be prevented at the end of an experiment. Because of the irregular spacing of the pipette tips, simultaneous harvesting was not practical. Instead, the cold plate was used to freeze only the device and an insignificant part of the pipette tip. At maximum power, the cold plate could reach temperatures as low as -10°C in a 23°C ambient and -25°C in a 4°C ambient. At the maximum cooling rate, the liquid in the device was frozen in approximately 10 minutes. After freezing the pipette tips were removed and inserted into plastic vials and allowed to drain. The collected samples were labeled and either frozen or refrigerated for later analysis.

### 5.4.4. Imaging and Analysis

Because the devices were too large to image under a microscope, the whole device imaging was performed with a digital SLR camera (Canon Digital Rebel, 60 mm macro lens, f/16 aperture) during operation. For fluorescent marker visualization, the cold plate was enclosed with a UV source (also used for the acrylamide polymerization) positioned above. A ½" thick PMMA window was used to block reflected UV light and to allow imaging of the device.

Following FF-IEF, the collected fractions were mixed with SDS-PAGE tricine sample buffer containing 2-mercaptoethanol as a reducing agent and separated on a precast 10 or 12 lane tris-tricine gel (NuSep, Inc., Austell, GA) according to the manufacturer's instructions. Focused fractions were separated on a 10% acrylamide tris-tricine gel, and either stained for total protein content using Sypro Ruby stain (Invitrogen) and scanned using a gel scanner (Typhoon 9600, GE Healthcare, Piscataway, NJ) or transferred to nitrocellulose for western blotting. A small amount of sample (~5μL) was spotted onto pH indicator strips (0-14 range, EMD Chemicals, La Jolla, CA)

Immunoblots of total ERK2 (SC1647, Santa Cruz Biotechnology, Santa Cruz, CA), phosphorylated AKT (pAKT, sc-33437-R, Santa Cruz Biotechnology), and Cytochrome *c* (556433, BD Biosciences, San Jose, CA) were performed using the same primary antibodies as for flow cytometry at a 1:1000, 1:500, and 1:1000 dilution, respectively. After blocking (30-60 min at room temperature), blots were probed overnight at 4 °C in primary antibody, washed 3 times for 5 min in TBS-T (20 mM Tris-HCl pH 7.5, 150 mM NaCl, 0.1% Tween-20), incubated 1 h at room temperature in secondary antibody (1:5000 IRDye800-conjugated donkey anti-rabbit IgG, Rockland Immunochemicals), and finally washed 3 x 5 min in TBS-T. Blots were scanned on an Odyssey imaging system (Li-Cor Biosciences). Image quantification was performed by programs written in MATLAB. Western blot data was normalized to the average device outlet signal, and plotted as a percent enrichment over the outlet average.

## 5.5. *Focusing Results*

### 5.5.1. Design Comparison

The formation of a pH gradient by each of the two designs is shown in Figure 5-6. As expected, the rectangular design was less efficient compared to the diverging channel design. At an applied voltage of 480V, the mixture of methyl red and bromothymol blue resulted in a variety of colors across the outlets of the device, the indication of a pH gradient and migration due to indicator electrophoresis.

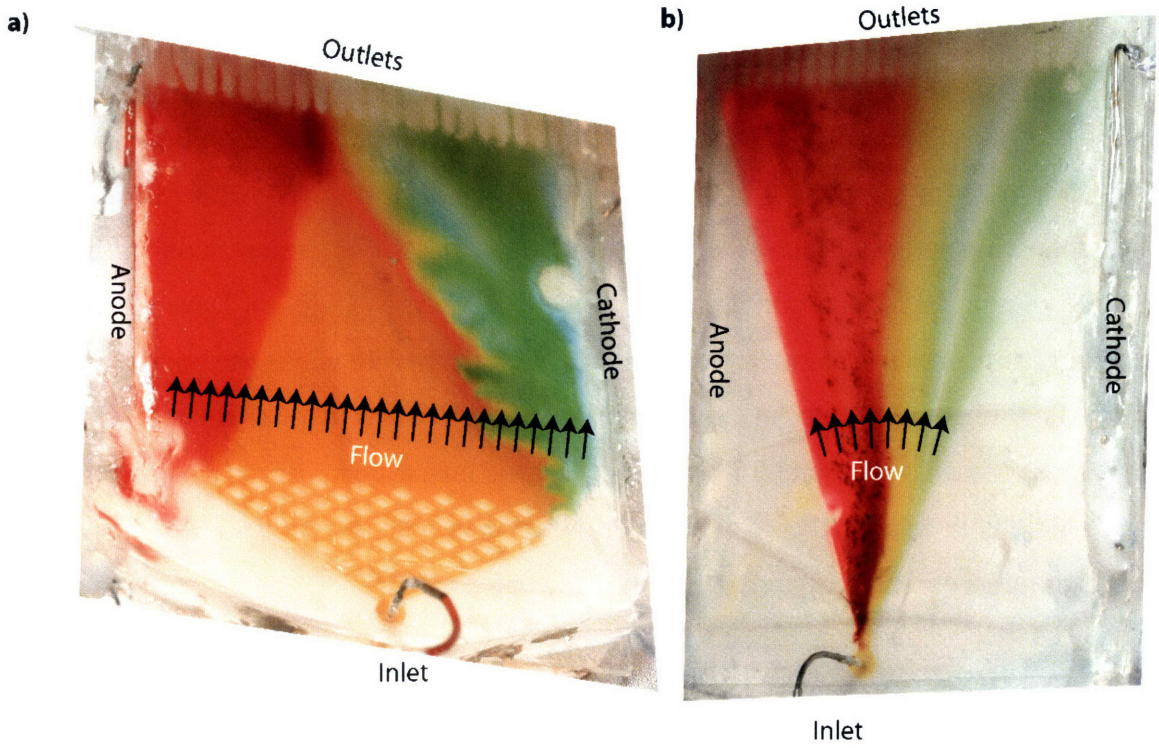


**Figure 5-6: Comparison of rectangular and divergent designs for a mixture of methyl red and bromothymol blue. The color gradient indicates the presence of an established pH gradient. Both devices are operated at 480V and a residence time of 6.5 minutes.**

As expected by theory, pH gradient formation begins at the gel-channel interface. This phenomenon poses a disadvantage for the rectangular device or any other rectangular FF-IEF device that uses a single inlet. In the case of Figure 5-6a, the time for the sample to respond and establish a pH gradient across the width of the channel is only slightly less than residence time of the device. The applied voltage is enough to cause some electrokinetic disturbances in the flow, appearing as color "wrinkles" near the cathode. In contrast, the divergent channel quickly establishes a pH gradient at the narrow inlet, which is continually refined as the channel diverges. Electrokinetic disturbances in the divergent channel were markedly reduced, and the device was less sensitive to higher applied voltages. The rapid initial focusing allowed for much higher flowrates as well, residence times as low as one minute were observed to have similar color gradients. Both devices show some cathodic shift due to electroosmotic flow.

In Figure 5-6, precipitation, typically a negative consequence of strongly focused samples, is an indicator of the improved focusing in the divergent channel. Methyl red precipitates near the inlet of the divergent channel appearing as dark specks in the channel. In

the rectangular device, there is also some precipitation, but only near the outlet where the pH gradient is finally established.

### 5.5.2. Separation of Protein Standards

Protein standards separated in 0.5x PBS were easily focused. Figure 5-7 shows the total protein content of all of the device outlets along with the original sample. The seven proteins were separated at a flowrate of 2 mL/hr (~6.5 min residence time) and an applied voltage of 270V. With the high sample conductivity, the device drew approximately 9 mA of electricity. Above 10 mA, arcing would occur in isolated parts of the device, typically near the cathode outlet.

From Figure 5-7, the 7 proteins, which only appear as 5 strong bands in the control lane, are concentrated into only 4 to 6 of the outlet fractions. This resolution of separation gives every outlet a unique protein composition. A faint band appears near the 47 kDa marker inconsistent with the size of the proteins known to be in solution. From the focusing behavior it is apparent that this unknown band is a dimer of trypsinogen. Also apparent is the expanded pH range due to the dissociation of the salt present in the PBS. This wide 2-13 pH range is not linear, as evidenced by location of the focused protein markers.

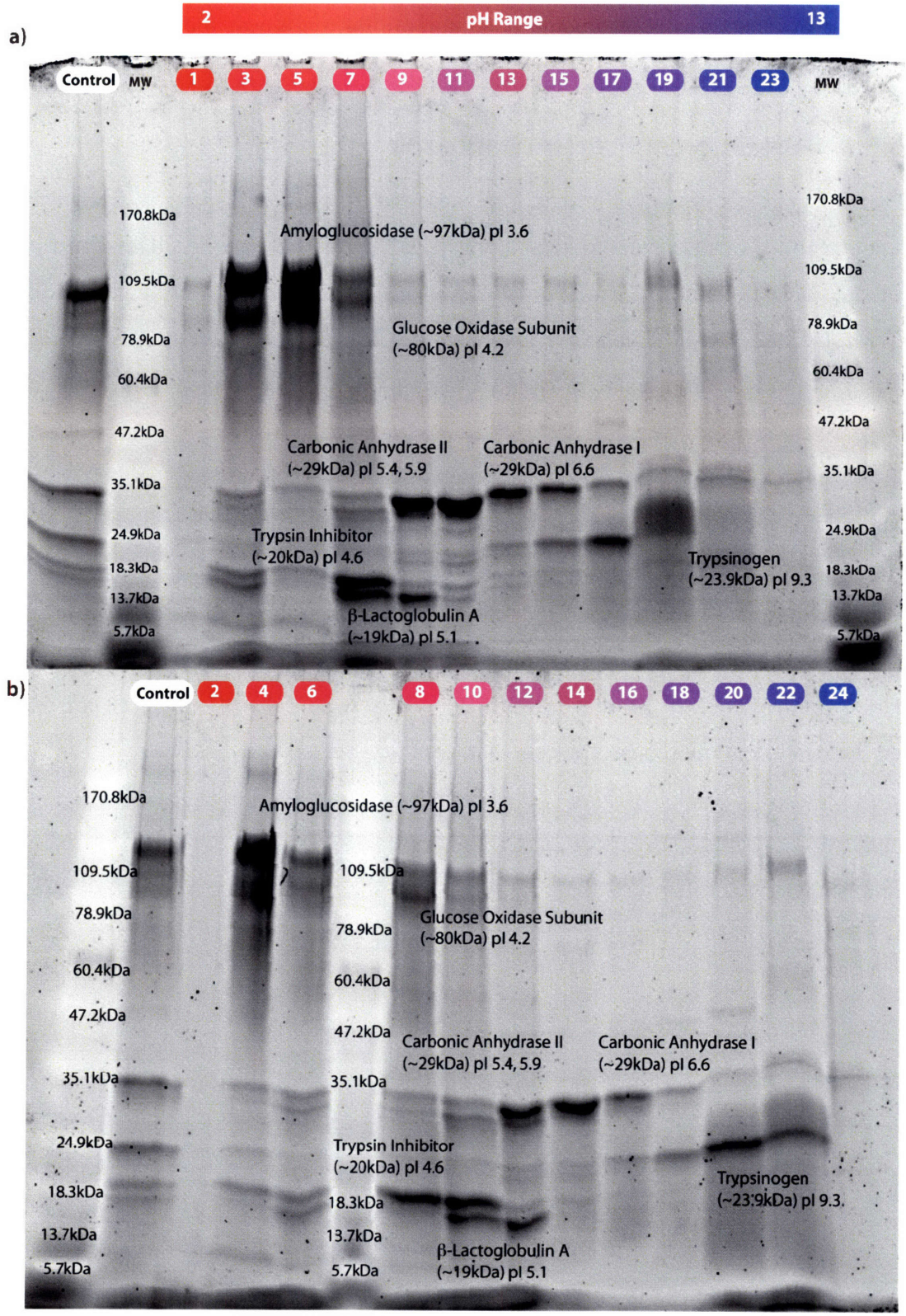


**Figure 5-7: Focusing of protein pI standards. Both a) odd fractions and b) even fractions with the original sample were separated on a 10% tricine gel. Seven known proteins with different pI and molecular weights were separated in 0.5x PBS.**

### 5.5.3. Focusing of Whole Cell Lysate

To use the preparative FF-IEF devices for "real world" samples, whole HeLa lysate was solublized in 8M urea and fractionated. Figure 5-8 shows the total protein content of the outlets. While the separation is not as resolved as for the protein markers, the gel shows some differential focusing of the most abundant proteins. Also of note is the narrow pH range, measured to be approximately 3.5 to 8. This narrow pH range is due to the cathodic shift for the low ionic strength sample buffer. The conductivity of 2% ampholyte in 8M urea was measured to be 0.75 mS/cm. This low sample conductivity required 2.5 mA of current at 1500 V.

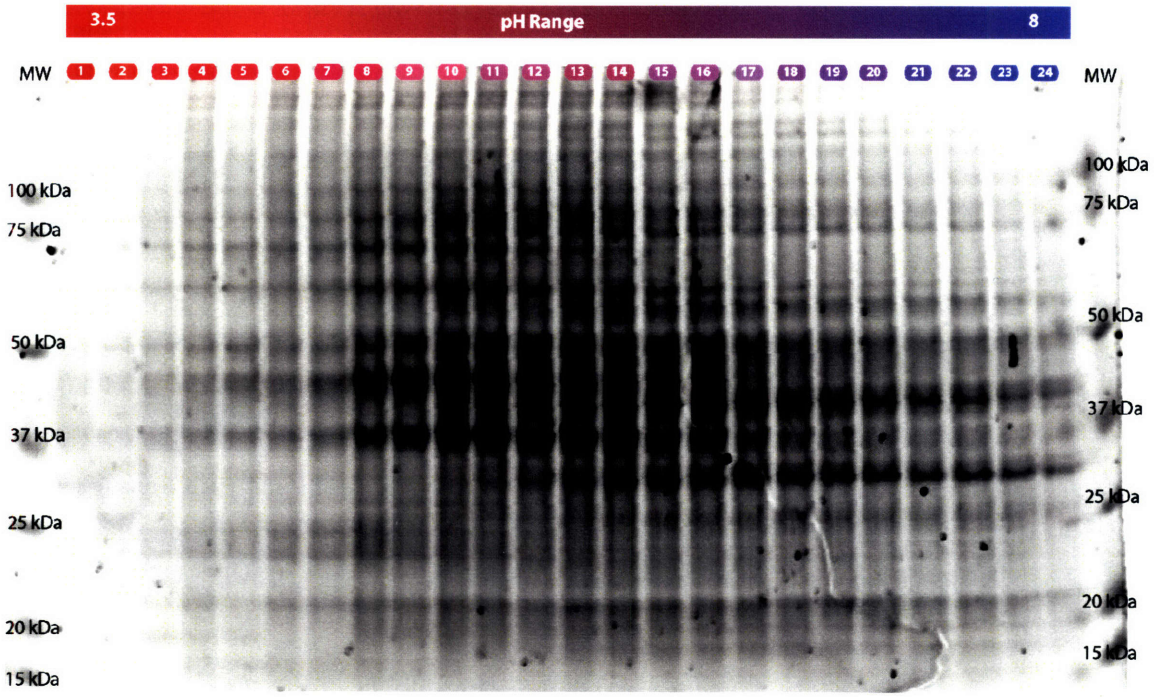


**Figure 5-8: Focusing of HeLa cell lysate. Whole cell lysate is fractionated at 1500 V for a 6.5 minute residence time.**

While the total protein stain showed very slight focusing, western blotting for specific proteins typically show more resolved focusing. From the samples in Figure 5-8, a second batch of gels were run for western blotting. Two important signaling kinases, ERK2 and AKT1 as well as Cytochrome *c* were probed. The results of the western blotting were quantified and are presented in Figure 5-9.

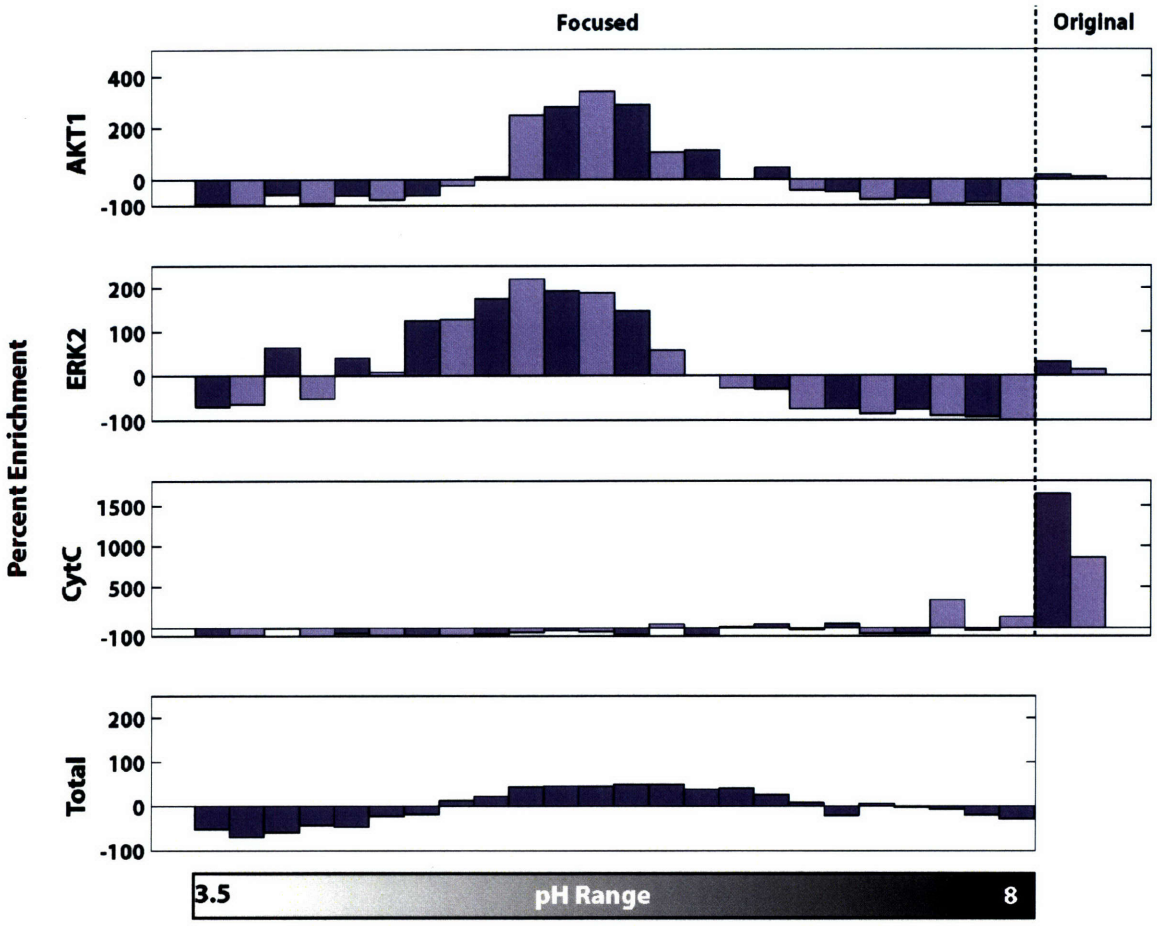


**Figure 5-9: Focusing of signaling proteins from HeLa lysate. Kinases AKT1 and ERK2 are focused within the channel, while Cytochrome *c* (CytC) is removed form the outlets entirely. Two 15 lane gels were used for blots of the odd (dark blue) and even (light blue) lanes. The total protein levels remain roughly constant.**

In Figure 5-9, the kinases are focused across 6-8 outlets in the middle of the pH range, and are enriched over the signal from the original unfocused sample. Quantifying the western blot signal confirms that 96% of the AKT1 concentration in the original sample leaves the device, and 82% of ERK2 leaves the device. However, Cytochrome *c*, with a pI of 9.6, does not focus in the device. Only 7% of the Cytochrome *c* present in the original sample is present in the outlet fractions. Presumably, the Cytochrome *c* entered the cathode gel and migrated into the catholyte. These results offer several interesting conclusions: i) that FF-IEF is capable of focusing rare signaling proteins, ii) FF-IEF with gel electrodes can extirpate proteins that are outside the fractionation pH range, and iii) that modest differential focusing for total protein staining underestimate focusing for less abundant proteins.

### 5.5.4. Two Dimensional Separations

To further validate device performance, FF-IEF fractions were refocused using conventional 2D gel techniques. To test this U2OS cells were lysed in 8 M urea, 2 M thiourea, and 4% CHAPS, and focused in the device at 0.5 mg/mL total protein content. Figure 5-10 shows the total protein stain of FF-IEF fractions, as well as 2-D gels of three outlet fractions, and acid fraction (outlet #3), a neutral fraction (#11), and a basic fraction (#21 combined with #23). Corrected for pH measured to be non linear, the SDS-PAGE of the outlet fractions compares with their focused pattern on the 2D gel. The acidic fraction contains the major spots from the low pH range of the original sample, while reducing the neutral and basic proteins. The neutral fraction contains the major spots around pH 5-7, as well as some streaks at the basic end of the gel. The basic fraction shows some proteins in the neutral range in addition to bands at the basic end of the gel.

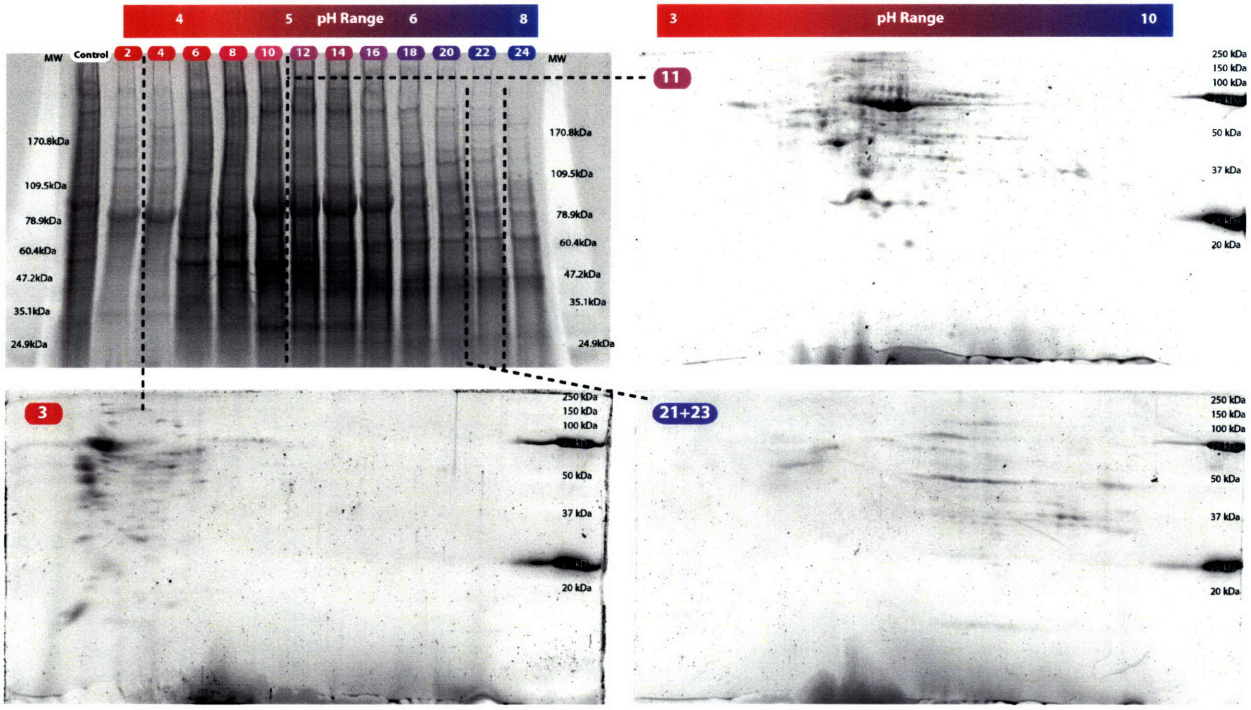


**Figure 5-10: Focusing of U20S cell lysate with FF-IEF followed by 2-D electrophoresis. Fractions 3, 13, and 21+23 were separated by 2-DE to show the effectiveness of the FF-IEF separation.**

## *5.6. Conclusions*

Commercial FF-IEF equipment requires multiple inlets to approximate the linear pH gradient commonly used in IEF. These inlets require many premixed pH buffers and a dedicated

pumping system, increasing system cost and complexity. In this chapter, a preparative scale FF-IEF device was designed and tested. The advantages of the divergent IEF design versus a rectangular design were demonstrated using pH indicators to visualize the formation of pH gradients within the devices. Theoretical and experimental observations indicate that using a divergent channel circumvents many of the difficulties associated with preparative FF-IEF equipment. Protein pI markers were used to demonstrate the devices ability to fractionate samples, even in the presence of salt levels too high for conventional IEF techniques. The devices were used to process complex biological samples, fractionating whole cell lysate at a rate of 2mL/hr. The device performance was further analyzed by 2-D gels of the fractionated outlets to show that cell lysate could be enriched based on pI. These findings show the promise of small, inexpensive, disposable FF-IEF devices in proteomics research.

# Chapter 6: Outlook for Free Flow Isoelectric Focusing

## 6.1. Thesis Contributions

This thesis has explored the use of microfabricated free flow isoelectric focusing devices in facilitating biological research. Research and development of these devices was performed with an emphasis on simple fabrication techniques and robust operation. This work resulted in disposable devices to fractionate samples ranging from simple molecules to proteins and organelles, up to fractioning whole cell lysate. Table 6-2 compares FF-IEF with other IEF techniques. Only FF-IEF is capable of focusing protein complexes and can perform coarse separations in a few hours.

**Table 6-1: Comparison of FF-IEF with other IEF techniques**

| | Protein Load | Liquid Phase | High Resolution | Time per Run | Large Proteins & Complexes | Labor |
|---|---|---|---|---|---|---|
| 2D Gel | 100 µg | No | Yes | 1.5 Days | No | Setup |
| Membrane Partitions | µg to g | Yes | No | 3-5 Hours | No | Setup and Cleanup |
| FF-IEF | 0.5 mg/mL | Yes | No | Minutes to Hours | Yes | Setup |

This work was the first to explore the use of hydrogels as ionic bridges to prevent electrolysis gasses from interfering with applied voltages above 3 V in microdevice operations. This innovation allows for fields of tens to hundreds of volts per centimeter to be applied to biological and chemical samples, even those with high salt content. This thesis also presents the use of functionalized acrylamide as well as the importance of active cooling for free flow isoelectric focusing. Functional modification of the polyacrylamide isolating the sample channel was shown to improve and stabilize the establishment of the pH gradient necessary for IEF. Joule heating, which can be neglected in most microdevices, was found to be significant for micro FF-IEF, where active cooling schemes were required to achieve improved performance.

This thesis was the first to use model driven design to propose, test, and validate the use of cascaded and divergent stages to enhance the performance of FF-IEF. This model driven approach avoids the use of a preestablished pH gradient for effective separations. To accomplish

this, a variety of models were created, ranging from simple analytical expressions to pseudo 3-D finite element models of simple systems, to rigorous models of systems as complex as the most advanced literature models. The understating and insight gained from the models make them the most informative tool in developing an intuition of the isoelectric focusing phenomena. These models were used not only as descriptive tools of IEF, but as a tool to experiment and rapidly test potential device designs. Table 6-1 compares the FF-IEF devices in this thesis to other devices in the literature and commercially available equipment. This work presents devices that are larger than other microfabricated FF-IEF devices, yet much smaller than commercial equipment. The devices have focusing resolution that is less than other techniques, with the aim of increasing protein concentration, simple operation, and downstream compatibility.

**Table 6-2: Comparison of FF-IEF devices**

| | Chamber Dimension (mm) | Residence Time | Flowrate | Concentration at Outlet | Cleaning Time | Outlets | Min ΔpI for 3-10 buffer |
|---|---|---|---|---|---|---|---|
| Functionalized μFF-IEF [1]* | 1x 20x 0.05 | 0.3 min | 0.2 mL/hr | 0 | 0 | 1 | 0.27 |
| Cascaded μFF-IEF [2]* | 2x 20x 0.05 | 0.3 min | 0.4 mL/hr | 5 | 0 | 9 | 0.65 |
| Preparative μFF-IEF* | ~22x 56x 0.15 | 2.3-23 min | 0.5-5 mL/hr | 8 | 0 | 24 | 0.29 max |
| BD's FFE | 100x 500x 0.5 | 15-20 min | 1-10 mL/hr | 0.5 | 30 min | 70 | 0.1 |
| Kohlheyer et al. [66] | 3.5x 10x 0.01 | 2.5 s | 0.2 mL/hr | 3 | 0 | 3 | 0.23 |

* This work

This thesis is also the first to demonstrate interfacing microfabricated separation tools with conventional biological techniques. Demonstrating microfabricated FF-IEF devices as tools that can be used in conjunction with other, more common, techniques is a departure from the "lab-on-a-chip" perspective espoused by the microdevice research community. However, it represents an opportunity to demonstrate the advantages of microdevices as complementary to, rather than superseding, well established protocols. The long term goal of integrated and

automated analysis systems is also possible. The design and fabrication of FF-IEF is simple enough to be easily integrated with other components should the opportunity arise, and this thesis has outlined the modeling tools necessary to adequately modify the designs used in this work.

## 6.2. *Future Applications of FF-IEF*

### 6.2.1. Optimization Options

There is still much work to do in improving the FF-IEF devices used here to achieve optimal performance for a given sample. The flowing list outlines the most straightforward optimization dimensions that impact the separation resolution of the devices:

- Device cooling
- Flow rate
- Voltage
- Salt concentration
- Ampholyte concentration
- Viscosity
- EOF suppression
- Protein concentration
- Chamber height

Of these, the two with the most potential for improvement are optimizing the way that the devices are cooled and adjusting the height of the chamber. Thermal management to mitigate the effects of Joule heating can be further developed for the preparative scale FF-IEF devices, possibly by modifying the cold plate arrangement, or by using materials with higher thermal conductivity. For example, the PDMS device could be bonded to a silicon wafer with an appropriately thick oxide layer. Alternatively, a thinner glass slide could simply be used to enhance the heat transfer and reduce the chance of localized overheating. With a properly tuned temperature controller, increasing the heat transfer is an opportunity to improve performance without negative consequences.

Channel height plays a critical role in preventing both overheating and minimizing electrokinetic instabilities through vicious damping. The thinner fluid layer in a reduced channel

height will have higher heat transfer, enabling rapid cooling. The higher flow resistance of the shallow channel will more effectively oppose the forces driving electrokinetic instabilities. However, the higher pressure drop across the device may require more effective external flow balancing. Also, the effect of channel height on efficiency versus throughput must be determined.

### 6.2.2. Particle Based Separations

Because of FF-IEF's ability to accommodate large particles and its ability to separate species on the basis of binding events, future applications of these disposable free flow electrophoresis devices include their application for particle based separations. Multi functional particles offer the potential to simultaneously assay the activities of several proteins or DNA oligomers simultaneously. Challenges remain to demonstrate the compatibility of these particles with free flow electrophoresis or with FF-IEF.

### 6.2.3. Integrated Devices for Biology

An attractive ultimate goal for microfabricated tools is the development of multicomponent, integrated unit operations. These integrated devices could potentially automate all aspects of biological assays, from cell culture to detection, as shown in Figure 6-1.

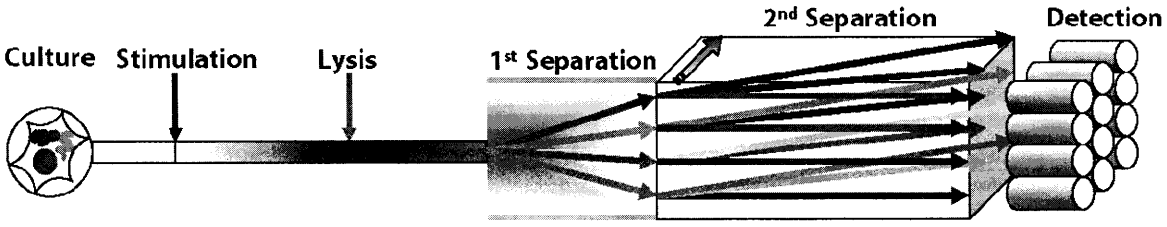


**Figure 6-1: Concept of an integrated stimulation and separation tool. It is conceivable to integrate devices to perform the steps necessary to assay cellular response to external stimulation.**

The obstacles to integration are not trivial, but there are many advantages of an integrated, automated system that would reduce many sources of experimental error and generate the large amounts of experimental data needed to probe cellular signaling networks. These advantages will continue to drive research and innovations in the field of integrated microdevices. In whatever capacity, FF-IEF has been shown to be a useful tool in the pursuit of understanding the intricacies of biology. It will continue to be an important area of device development for many years to come.

# Appendix A: Device Fabrication

## *A.1. Photolithography Mask Layout*

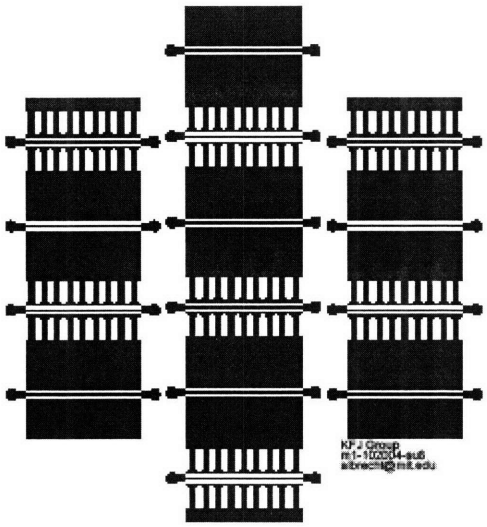


**Mask for single stage IEF devices**

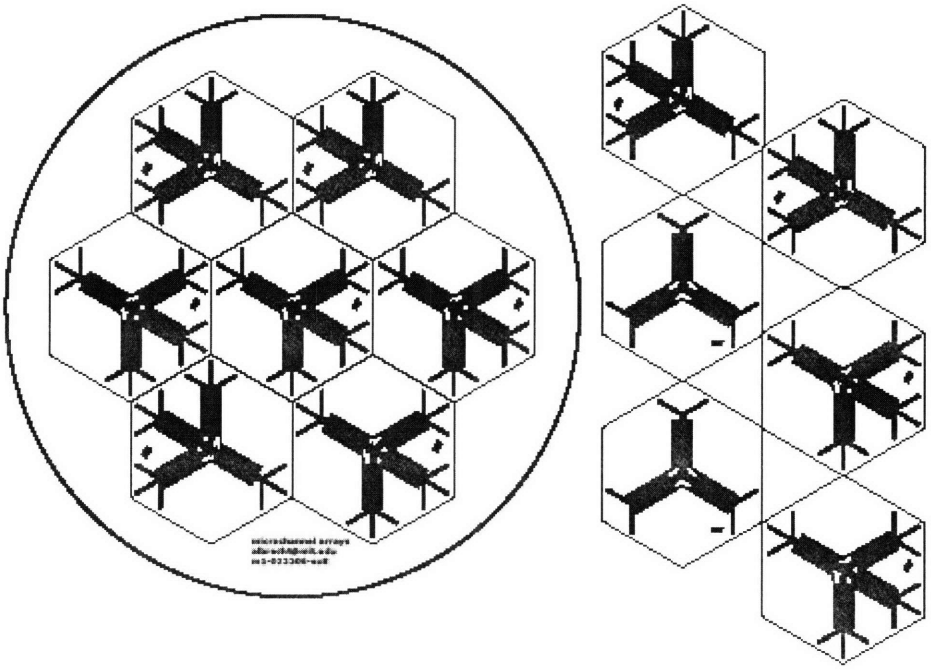

**Mask for cascaded IEF device**

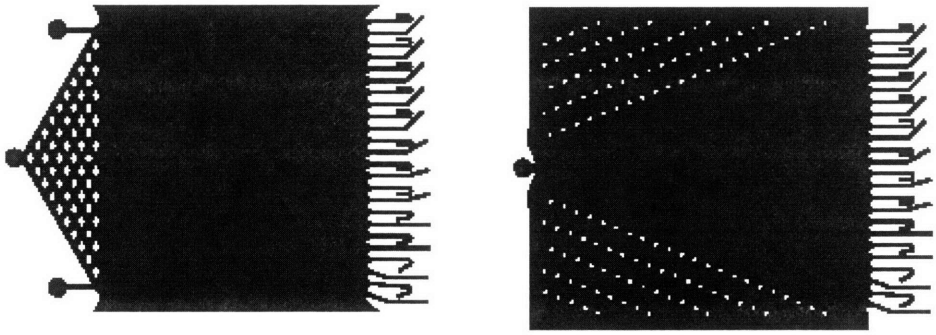

**Mask for the preparative scale IEF device**

## *A.2 PDMS Master Fabrication Process*

The process to fabricate a SU-8 master follows KFJ group recipe, with the exception that a single coating of SU-8 is used. The equipment names in the parentheses refer to machines in the Technology Research Laboratory (TRL) in MIT's Microsystems Technology Laboratories (MTL). The starting substrate is a 4" Silicon wafer (SSP, test grade). The entire process is code purple.

1. Dehydration Bake: Bake the wafers on a hotplate at 200 °C for 20 min. This step removes any adsorbed moisture on the silicon wafer.
2. Spin coating of SU-8(2050) layer: Transfer the wafers immediately from the dehydration bake hotplate to the spin coater (SU-8 spinner/ TRL) using a metallic wafer carrier. The wafer cools rapidly when placed on the metallic pin coater chuck. Use a nitrogen gun to blow away any dust particles on the wafer. Dispense a small amount (~20 mm diameter circle) of SU-8(2050) (Microchem Corp., MA) onto the wafer and start spinning immediately. SU-8(2050) has a quick evaporating solvent base, therefore immediate spinning is necessary. Spin at 650 rpm for 15s and 2100 rpm for 35s. This yields a layer of thickness ~40-50 μm.
3. Soft-bake of SU-8(2050) layer: Transfer the freshly coated wafer to a hot plate. Heat at 65 °C for 10 minutes, ramp up to 95 °C and hold for 45 minutes. Cool to at least 65 °C before transferring for photolithography.
4. Photolithography to define microchannel pattern: Interval exposure (5s x 7, 4s interval) (EV1/TRL).
5. Post-exposure bake: Place the freshly exposed wafer to a hot plate. Heat at 65 °C for 1 minute, ramp up to 95 °C and hold for 30 minutes. The SU-8 will reflow without fast polymerization if it is kept at 65 °C for too long. Cool to at least 50 °C before transferring for development.
6. Development: Develop in poly(glycol)mono ether acetate (PGMEA, Microchem.) for 45 min, replace with fresh solution every 15 min.
7. Wash: Rinse with Isopropyl alcohol and dry under a stream of nitrogen.

# Appendix B: Jacobian and MATLAB Code

## *B.1. Jacobian Tips and Tricks*

The GUI interface of Jacobian could not work with large (>2000 equations) systems of equations. Because of the large scale of the DAE system, the compiled mode of Jacobian was used. This command line mode translates the model into FORTRAN functions which can be more quickly integrated. However, the extra time required to create and compile the FORTRAN functions, typically 30 seconds, makes this mode more efficient only for larger models.

### B.1.1. Initialization with MATLAB

To avoid using Jacobian's slow initialization solver, the BLOCKSOLVE and ANALYSIS flags were set to false. MATLAB was then used to calculate the initial conditions for the system, and write a presets file. Because the initial conditions were slightly different for the two systems, MATLAB was used to give Jacobian consistent initial values under mild operating conditions < 20V/cm. The integration time course included a rapid increase in voltage to 100 V/cm over a brief period of time, typically 0.1 seconds.

### B.1.2. Adjusting the Integration Time Scale

For systems where the time derivative is too not steep enough, a "dsl_48" error may occur. In this case, increasing the time derivative may alleviate the error. Simulations used in this thesis used a time scaling factor of 10, meaning that simulating the system for 15 seconds is equivalent to 150 seconds for the physical system.

## B.2. Jacobian Model Code

```
# ====================================================================
#       coief5 USES APPLIED VOLTAGE, FIXED curr CALCULATION, ONE COMPARTMENT
#               many theoretical ampholytes
# This simulation uses code hijacked from of some of the ABACUSS PDE examples
#       its supposed to model isoelectric focusing (IEF) fairly rigorously
#       it assumes electro neutrality, ph equilibrium,
#               and an Einstein relation mobility for small molecules
#       it uses  a finite difference method to solve the spatial derivatives
#       similar to mao, anal chem 72,  2000 5493-5502
# ====================================================================
DECLARE
   TYPE
        Concentration     =       2.e-6           :   1e-40       :   1E1
        Derivatives       =       0.5E-50         :   -1E18       :   1E18
        PHtype            =       6.53            :   0           :   13
        Hconc             =       3.4064e-10      :   1e-16       :   1e-4
        extraHconc        =       1e-30           :   -1e-7       :   1e-7
        Voltage           =       1500            :   -1e6        :   1e6
        Efield            =       3.0298          :   1e-20       :   1e6
        current           =       4e-5            :   1e-20       :   10
        Conductivity      =       0.0021          :   1e-20       :   1
        charge            =       1.8938e-6       :   -200        :   200
        length            =       2e-7            :   1e-20       :   6
        henrys            =       .7196           :   .65         :   1
        channel           =       5               :   .05         :   6
        Axialrange        =       0.0125          :   1e-6        :   2
        proconc           =       1e-8            :   1e-20       :   1
END   # Declare
# ====================================================================
MODEL IEF_FDM
PARAMETER
        NoComp  as                              integer
        Nogrid  as                              integer
        Kw      as                              real
        pKp     as      array(2,NoComp)  of     real
        pKn     as      array(2,NoComp)  of     real
        Kp      as      array(2,NoComp)  of     real
        Kn      as      array(2,NoComp)  of     real
        F       as                              real
        Rt      as                              real
        Omega   as      array(NoComp+2)  of     real
        ee0,
        q       as                              real
        sig0    as                              real
        pi      as                              real
        D,
        mu      as                              real
        R       as                              real
        rat1    as      array(6)         of     real
        rat2    as      array(2)         of     real
VARIABLE
        Partial1_Eflux,
        Partial2_Comp           as      array(NoComp,Nogrid+1)    of      Derivatives
        Comp                    as      array(NoComp,Nogrid+1)    of      Concentration
        H                       as      array(Nogrid+1)           of      Hconc
        pH                      as      array(Nogrid+1)           of      PHtype
        Cond                    as      array(Nogrid+1)           of      Conductivity
        delV                    as      array(Nogrid+1)           of      Efield
        Cb                      as      array(NoComp,Nogrid+1)    of      charge
        curr                    as                                        current
        Applied_Voltage         as                                        voltage
        w                       as                                        channel
        Axial                   as                                        Axialrange
        Partial1_Eflux_bsa,
        Partial2_Comp_bsa       as      array(Nogrid+1)           of      Derivatives
        bsa                     as      array(Nogrid+1)           of      proconc
        zm                      as      array(Nogrid+1)           of      charge
        zeta                    as      array(Nogrid+1)           of      voltage
        fkr                     as      array(nogrid+1)           of      henrys
        kappa1                  as      array(nogrid+1)           of      length

SET
        sig0    :=      0;      #extra Conductivity from background salt
        Kw      :=      1e-14*1e-6;
        Kp(2,)  :=      10^(-(pKp(2,)))*1e-3;
        Kp(1,)  :=      10^(-(pKp(1,)))*1e-3;
        Kn(2,)  :=      10^(-(pKn(2,)))*1e-3;
        Kn(1,)  :=      10^(-(pKn(1,)))*1e-3;
```

```
        pi      :=      3.1415926535898;
        # these rational parameters avoid the charge explosion at pH 2:
        rat1    :=      [-1.184, 47.28, -748.5, 5858, -22640, 34370];      #rational parameters
        rat2    :=      [-18.55, 92.45];
        mu      :=      8.95e-6;          # viscosity kg/cm-s
        D       :=      4.1143e-21*10000/(R*6*PI*mu);  #5.94e-7; # bsa diffusivity in cm2/sec
        R       :=      4.1143e-21*10000/(6*PI*8.95e-6*5.94e-7);   # stokes radius (cm)
EQUATION
# Axial
        Axial=w/Nogrid;
# Governing equations for every fdm point
        # ph equation
        for j:=1 to Nogrid+1 do
                for i:=  1 to NoComp do
# Compute the average charge concentration for every species as a function of Kn, Kp and ph
        Cb(i,j)= ((H(j)/Kp(1,i))*(1+2*(H(j)/Kp(2,i)))
                -Kn(1,i)/H(j)*(1+2*(Kn(2,i)/H(j))))
                /((1+(H(j)/Kp(1,i)*(1+H(j)/Kp(2,i))+Kn(1,i)/H(j)*(1+Kn(2,i)/H(j)))))*Comp(i,j);
                End # i
# use electroneutrality to calculate H
        H(j)=Kw/H(j)-SIGMA(Cb(,j));                # BSA has no contribution to ph
#calcuate Conductivity (coul/mol*mol/cm3*cm2/s-V = A/cm-V = S/cm)
        Cond(j)=F*(H(j)*omega(1)+Kw/H(j)*omega(2)
                +SIGMA(((H(j)/Kp(1,))*(1+2*(H(j)/Kp(2,)))
                +Kn(1,)/H(j)*(1+2*(Kn(2,)/H(j))))
                *Comp(,j)/((1+(H(j)/Kp(1,)*(1+H(j)/Kp(2,))+Kn(1,)/H(j)*(1+Kn(2,)/H(j)))))
                *omega(3:NoComp+2)))+sig0;
# calcuate debye length (cm)
        kappa1(j)=sqrt(ee0*rt/(2*F^2
                *SIGMA(((H(j)/Kp(1,))*(1+4*(H(j)/Kp(2,)))
                +Kn(1,)/H(j)*(1+4*(Kn(2,)/H(j))))
                *Comp(,j)/((1+(H(j)/Kp(1,)*(1+H(j)/Kp(2,))
                +Kn(1,)/H(j)*(1+Kn(2,)/H(j))))))));
        pH(j)=-log10(H(j)*1000);
# calculate electic field (V/cm)
        delV(j) = curr/(Cond(j));
        end     #all j
# integrate Conductivity over channel to calulate current - # 10/8/06: took out border points
        Curr = 2*1/(SIGMA(2/Cond(2:Nogrid)))*Applied_Voltage/Axial;
# conservation equations
        for  j := 2 TO Nogrid Do
                for i:=1 to NoComp do
            $Comp(i,j) = 10*((omega(i+2)*rt/F) * Partial2_Comp(i,j)-Partial1_Eflux(i,j)*omega(i+2));
# Spatial approximation for derivatives
                Partial1_Eflux(i,j) = (curr/Cond(j+1)*Cb(i,j+1)
                                        -curr/Cond(j-1)*Cb(i,j-1))
                                       /(2*Axial);
                Partial2_Comp(i,j) = ( Comp(i,j+1) - 2*Comp(i,j) + Comp(i,j-1) ) / ( Axial^2 ) ;
                end # for i
        $BSA(j) = 10*(D * Partial2_Comp_BSA(j)-Partial1_Eflux_BSA(j));
# Spatial approximation for derivatives
        Partial2_Comp_BSA(j)    = ( BSA(j+1) - 2*BSA(j) + BSA(j-1) ) / ( Axial^2 );
        Partial1_Eflux_BSA(j)   = (Curr/cond(j+1)*ee0*zeta(j+1)*fkr(j+1)/mu*BSA(j+1)
                                  -Curr/cond(j-1)*ee0*zeta(j-1)*fkr(j-1)/mu*BSA(j-1))/(2*Axial);
        end # For j
for i:=1 to Nocomp do             # from coief3
# Boundary conditions     # use 2nd order no-flux
# At z = 0
  ( 4*Comp(i,2)-3*Comp(i,1)-Comp(i,3)) / (2*Axial)*rt/F -Curr/Cond(2)*Cb(i,2)= 0 ;
# At z = 1
   (3*Comp(i,Nogrid+1)-4*Comp(i,Nogrid)+Comp(i,Nogrid-1)) / (2*Axial) *rt/F -Curr/Cond(Nogrid)*Cb(i,Nogrid) =
0;
#       3*Comp(i,Nogrid+1)-4*Comp(i,Nogrid)+Comp(i,Nogrid-1)=0;
# derivatives at boundaries
    Partial2_Comp(i,1)          =       0;
    Partial1_Eflux(i,1)         =       (Curr/Cond(2)*Cb(i,2)
                                        -Curr/Cond(1)*Cb(i,1))
                                        /(Axial);
    Partial2_Comp(i,Nogrid+1)   =       0               ;
    Partial1_Eflux(i,Nogrid+1)  =       (Curr/Cond(Nogrid+1)*Cb(i,Nogrid+1)
                                                -Curr/Cond(Nogrid)*Cb(i,Nogrid))
                                                /(Axial);
end # for i

########  BSA equations ########
# re-fitted rational fit for the titration curve of BSA at zero ionic strength
        zm() =   (rat1(1)*(ph())^5+rat1(2)*(ph())^4+rat1(3)*(ph())^3
                                +rat1(4)*(ph())^2+rat1(5)*(ph())+rat1(6))
                                /((ph())^2+rat2(1)*(ph())+rat2(2));

# zeta potential as calculated by Debye-Huckel-Henry
```

```
#(factor of 10000 converts Joules to cm2-kg/s2)
        zeta()   =       10000*zm()*q/(4*PI*ee0*R*(1+R/kappa1())); # V
# henrys function approximation
        fkr()    =       2/3*(1+0.5*(1+2.5/(R/kappa1()*(1+2*exp(-R/kappa1())))))^(-3));
# UNIT CONFUSION:: A/cm2 * V-cm/A * coul/v-cm * V * cm-s/kg *mol/cm3 1/cm = V/cm *coul/cm *mol-s/kg-cm3 =
Joule-mol-s/cm4-kg = m2-mol/s-cm5 = 10000 mol/s-cm3

        Partial1_Eflux_BSA(1)           =       (Curr/cond(2)*ee0*zeta(2)*fkr(2)/(mu)
                                                        *BSA(2)
                                                -Curr/cond(1)*ee0*zeta(1)*fkr(1)/(mu)
                                                        *BSA(1))
                                                /(Axial);
        Partial2_Comp_BSA(1)            = 0;
        Partial2_Comp_BSA(Nogrid+1)     = 0;
        Partial1_Eflux_BSA(Nogrid+1)    = (Curr/cond(Nogrid+1)*ee0*zeta(Nogrid+1)
                                                *fkr(Nogrid+1)/(mu)*BSA(Nogrid+1)
                                                -Curr/cond(Nogrid)*ee0*zeta(Nogrid)
                                                *fkr(Nogrid)/(mu)*BSA(Nogrid))
                                                /(Axial);
   # Boundary conditions
   # At z = 0
  ( 4*BSA(2)-3*BSA(1)-BSA(3)) / (2*Axial)*D-Curr/cond(2)*ee0*zeta(2)*fkr(2)/(mu)*BSA(2)= 0 ;
   # At z = 1
  ( -4*BSA(Nogrid)+3*BSA(Nogrid+1)+BSA(Nogrid-1)) / (2*Axial)*D-
        Curr/cond(Nogrid)*ee0*zeta(Nogrid)*fkr(Nogrid)/(mu)*BSA(Nogrid)= 0 ;
############ END of BSA EQUATIONS ###############
END   # Model ief fdm
MODEL Flowsheet
PARAMETER
        NoComp                  as                              integer
        Nopre                   as                              integer  # number of specifically defined
species (e.g. sodium, phosphate and the Immobilines))
        pKp,pKn                 as array(2,NoComp)      of      real
        omega                   as array(NoComp+2)      of      real
        Nogrid, Nogel, Nogel90  as                              integer
        F                       as                              real
        rt                      as                              real
        ee0                     as                              real
        q                       as                              real
        maxpI,minpI             as                              real
        DT                      as                              real
UNIT
        AMPHY                   as      IEF_FDM
SET
        NoComp          :=      140;
        Nopre           :=      0;      # number of Components before the NoComp amphys begin
        Nogrid          :=      240;
        Nogel           :=      0; # grid points for the gel to occupy on either side of the channel
        Nogel90         :=      INT(Nogel*.9);
        F               :=      96485;   #coul/mol
        rt              :=      8.3145*(298);  #V*coul/mol 298*8.3145=2477.73  273.15*8.3145=2271.11
        DT              :=      0; # degrees above 25C; shift for omega to increase mobility as a function of
temperature; independent of rt;
        ee0             :=      80*8.8542e-12*0.01;       #permittivity of solution coul/v-cm
        q               :=      1.60e-19;         # elEctron charge (coul)
        omega(1)        :=      36.27e-4*(1+.02*DT);              # mobility, cm2/v-s
        omega(2)        :=      19.87e-4*(1+.02*DT);
        for i:=Nopre+3 to NoComp+2 do
            omega(i):=3e-4*(1+.01*DT);
        end
        maxpI:=10;
        minpI:=3.0;
        for i:=Nopre+1 to NoComp do
            pKp(2,i):=-1e10;
            pKp(1,i):= (i-Nopre-1)*((maxpI)-minpI)/(NoComp-Nopre-1) -1+ minpI;#defines pH range of amphys
            pKn(1,i):=2+pKp(1,i);
            pKn(2,i):=1e10;
        end
END
# ================================================================
SIMULATION coief5
OPTIONS
CSVOUTPUT               :=      true;
ALGRTOLERANCE           :=      1e-10;
ALGATOLERANCE           :=      1e-10;
dynrtolerance           :=      1e-11;
dynatolerance           :=      1E-11;
ALGMAXITERATIONS        :=      100;
REPORTINGINTERVAL       :=      0.1;
INIT_PRINT_LEVEL        :=      0;
CHECK_MATH_EXCEPTIONS   :=      true;
```

```
reinit_bounds             :=      false;   # see if this fixes the reinitialization problem
#DYNAMIC_SCALING          :=      FALSE;
BLOCK_SOLVE               :=      false;   # when true, the solving process is bad for large systems
ANALYSIS                  :=      false; # when true, the initialization process bad for large systems
NO_INTERPRETED_EVALUATIONS:=      TRUE;
UNIT
  Fs     as Flowsheet
report
         fs.amphy.ph,
         fs.amphy.Cond,
         fs.amphy.curr,
         fs.amphy.applied_voltage,
         #fs.amphy.cb(,),
         fs.amphy.Axial,
         fs.amphy.w,
         #fs.amphy.partial2_Comp,
         #fs.amphy.partial1_eflux,
         fs.amphy.bsa,
         fs.amphy.Comp(,)

Input
         fs.amphy.applied_voltage :=sqrt(4*0.3639*0.6*0.1*(time)*10+0.1*0.1)*(10+time*90/0.009); # v
         fs.amphy.w :=sqrt(4*0.3639*0.6*0.1*(time)*10+0.1*0.1);

PRESET
INCLUDE  coief5_INITCD
INITIAL
   WITHIN Fs DO
         WITHIN AMPHY DO
                  for j:=2 to Nogrid do
                     for i:=Nopre+1 TO NOCOMP DO
                           Comp(i,j)       =   .16e-6;
                           end
                  bsa(j)      =  4e-8;
                  end

         END   # Within AMPHY
   END # Within Fs
SCHEDULE
SEQUENCE
save presets coief5_INIT
    continue for 0.009
save presets coief5_INIT_0001
reset
         fs.amphy.applied_voltage:= sqrt(4*0.3639*0.6*0.1*(time)*10+0.1*0.1)*100;#20;
end # reset
         continue for 14.991
save presets coief5_END
   end  #sequence
END   # Process Simulation
# ============================================================================
```

## B.3. MATLAB Code to Prepare Presets File

```
function coief5

% ================================================================
%       coief5 USES APPLIED VOLTAGE, FIXED curr CALCULATION, ONE COMPARTMENT, AND BSA AFFECTS PH, viscosity
does not affecte omega
%               many theoretical ampholytes  and phosphate and gel species
% THis  simulation uses code hijacked from of seome of the ABACUSS PDE exampels
%       its supposed to model isoelectic focusing (IEF) fairly rigourously
%       it assumes electroneutrality, ph equilibruim,
%               and an einstein relation mobility for small molecules
%       it uses  a finite difference method to solve the spacial derivatives
%       based % ================================================================

runjac=true;
noflux=true;    % option for the fancy noflux boundary Condition
noflux2=true;   % option for simple noflux boundary condition, overwrites noflux to true, too

tic

sig0    =      0;       %extra Conductivity from background salt            _       this MUST BE PHASED OUT
Kw      =       1e-14*1e-6;
% bsa diffusivity in cm2/sec
viscosity_x             = 1;     % fold viscosity increase
mu      =       8.95e-6*viscosity_x;              % kg/cm-s
R       =       4.1143e-21*10000/(6*pi*8.95e-6*5.94e-7);   % radius (cm)    calculated from stokes drag
%       rat1    =       [-21.3868, 492.208, -2460.14, -16120.6, 91808.8];  %rational parameters
%       rat2    =       [-73.2781, 913.717, -1565.98];

% these rational parameters avoid the charge explosion at pH 2 - Dont forget to modify the variable's
definitions above
rat1    =       [-1.184, 47.28, -748.5, 5858, -22640, 34370];      %rational parameters
rat2    =       [-18.55, 92.45];

D       =       4.1143e-21*10000/(R*6*pi*mu);  %5.94e-7;

NoComp          =  140;
Nopre                   =       0;      % number of Components before the NoComp amphys begin
Nogrid                  = 80;
Nogel           =       double(fix(Nogrid*0.3));  % number of grid points for the gel to occupy on either
side of the channel

F                       =  96485;       %coul/mol
rt                      =  8.3145*(298);  %V*coul/mol             298*8.3145=2477.73  273.15*8.3145=2271.11
DT                      =  0;           % degrees above 25C; shift for omega to increase mobility as a
function of temperature; independent of rt;

ee0                     =  80*8.8542e-12*0.01;     %permittivity of solution coul/v-cm
q                       =  1.60e-19;       % elEctron charge (coul)
omega(1)        =36.27e-4*(1+.02*DT);             % mobility, cm2/v-s
omega(2)        =       19.87e-4*(1+.02*DT);
%       omega(:) =      3.3e-4*(1+.02*DT);  % fluorescein-viscosity dependence taken out
%       omega(:) =      1e-10*(1+.02*DT);         % mobility for immobilines
%       omega(:) =      1e-10*(1+.02*DT);         % mobility for immobilines
if ~or(noflux,noflux2)
    Nopre                       =       2;      % number of Components before the NoComp amphys begin
    NoComp      =   NoComp+Nopre;
    omega(3)    =       3.67e-4*(1+.02*DT);       % a guess.... mobility for phosphate depends on valence::
-1/z: 3.73 -2/z: 2.96, -3/z: 3.21 and the model can only handle 0, -1 and -2
    omega(4)    =       5.19e-4*(1+.02*DT);               % omega for sodium, ithink
end
%       omega(:) =      7.3e-4*(1+.02*DT);                % K+
%       omega(:) =      7.6e-4*(1+.02*DT);                % Cl-

Partial1_Eflux=zeros(NoComp,Nogrid+1);
Partial2_Comp  =      Partial1_Eflux   ;
Partial1_Eflux_BSA=zeros(1,Nogrid+1);
Partial2_Comp_BSA  =      Partial1_Eflux_BSA   ;

for i=Nopre+3:NoComp+2
    omega(i)=3e-4*(1+.01*DT);
end

maxpI=10;
minpI=3.0;

for i=Nopre+1:NoComp
    pKp(2,i)=-1e10;
    pKp(1,i)= (i-Nopre-1)*((maxpI)-minpI)/(NoComp-Nopre-1) -1+ minpI;%defines pH range of amphys
```

```
79          pKn(1,i)=2+pKp(1,i);
80          pKn(2,i)=1e10;
81      end
82
83      % the number of blocks here must match Nopre
84      %       pKp(2,1)=-1e10;          % values for fluorescein
85      %       pKp(1,1)=2.1;
86      %       pKn(1,1)=5;
87      %       pKn(2,1)=6.4;
88      if ~or(noflux,noflux2)
89          pKp(2,1)=-1e10;              % values for phosphate, just deals with -1 and -2 for now
90          pKp(1,1)=-1e10;
91          pKn(1,1)=2;
92          pKn(2,1)=1e10;
93
94          pKp(2,2)=-1e10;              % values for Na+
95          pKp(1,2)=100;
96          pKn(1,2)=1e10;
97          pKn(2,2)=1e10;
98      end
99      %       pKp(2,2)=-1e10;          % values for pka 3.6 immobiline
100     %       pKp(1,2)=-1e10;
101     %       pKn(1,2)=3.6;
102     %       pKn(2,2)=1e10;
103
104     %       pKp(2,3)=-1e10;          % values for pka 9.3 immobiline
105     %       pKp(1,3)=9.3;
106     %       pKn(1,3)=1e10;
107     %       pKn(2,3)=1e10;
108
109     %       pKp(2,6)=-1e10;          % values for K+
110     %       pKp(1,6)=100;
111     %       pKn(1,6)=1e10;
112     %       pKn(2,6)=1e10;
113
114     %       pKp(2,7)=-1e10;          % values for Cl-
115     %       pKp(1,7)=-1e10;
116     %       pKn(1,7)=.01;
117     %       pKn(2,7)=1e10;
118     Kp(2,:)  =       10.^(-(pKp(2,:)))*1e-3;
119     Kp(1,:)  =       10.^(-(pKp(1,:)))*1e-3;
120     Kn(2,:)  =       10.^(-(pKn(2,:)))*1e-3;
121     Kn(1,:)  =       10.^(-(pKn(1,:)))*1e-3;
122
123     %fs.amphy.applied_voltage = 75+75*(exp(2*(Time-20))-1)/(exp(2*(Time-20))+1);% v
124     w =0.1;  % account for extra length of gels
125     curr=30e-4;
126     Applied_Voltage=.1;
127
128     %INCLUDE coief5_INIT2
129
130     % INITIAL
131     %    WITHIN Fs DO
132     %       WITHIN AMPHY DO
133     BSA=zeros(1,1:Nogrid+1);
134     for j=1:Nogrid+1
135           BSA(j)      =  4e-8;
136     end
137     if or(noflux,noflux2)
138         % define NA AND PO4
139         for j=1:Nogel
140             Comp(1,j)= 100e-6;                % concentration of NA AND PO4-- should be 12.5e-6
141             Comp(2,j)= 1e-18;
142             for i=Nopre+1 :  NoComp
143                 Comp(i,j)       =   0.16e-6;
144             end
145         end
146
147         for j=Nogel+1:Nogrid-Nogel
148             Comp(1,j)=1e-18;
149             Comp(2,j)=1e-18;
150             for i=Nopre+1 : NoComp
151                 Comp(i,j)       =   0.16e-6;
152             end
153         end% for
154
155         for j=Nogrid-Nogel+1:Nogrid+1
156             Comp(1,j)= 1e-18;
157             Comp(2,j)= 40e-6;
158             for i=Nopre+1 : NoComp
159                 Comp(i,j)       =   0.16e-6;
```

```
        end
    end
else
    % define NA AND PO4
    for j=1:Nogel
        Comp(1,j)= 100e-6;                % concentration of NA AND PO4-- should be 12.5e-6
        Comp(2,j)= 1e-18;
        for i=Nopre+1 :  NoComp
            Comp(i,j)       =   0.16e-6;
        end
    end

    for j=Nogel+1:Nogrid-Nogel
        Comp(1,j)=1e-18;
        Comp(2,j)=1e-18;
        for i=Nopre+1 : NoComp
            Comp(i,j)       =   0.16e-6;
        end
    end% for

    for j=Nogrid-Nogel+1:Nogrid+1
        Comp(1,j)= 1e-18;
        Comp(2,j)= 40e-6;
        for i=Nopre+1 : NoComp
            Comp(i,j)       =   0.16e-6;
        end
    end
end

%  EQUATION
% axial
Axial=w/Nogrid;
% Governing equations for everyfdm point
% ph equation
H=ones(1,Nogrid+1)*10^-6.4677/1000;     % factor of a thousand to correct the mol/mL
use_findH=true;      %  flag to use the nonlinear solver to re caullate H, if false, Cb will be calulated from
the supplied pH
zm=ones(1,Nogrid+1)*-11;
Cond=ones(1,Nogrid+1);
[pH,H,Cb]= calcpH(H,Comp,Kp,Kn,Kw,BSA,zm,Nogrid,rat1,rat2,use_findH);
for j=1:Nogrid+1
    %calcuate Conductivity (coul/mol*mol/cm3*cm2/s-V = A/cm-V = S/cm)
    Cond(j)=F*(H(j).*omega(1)+Kw./H(j).*omega(2)...
        +sum(((H(j)./Kp(1,:)).*(1+2.*(H(j)./Kp(2,:)))...
        +Kn(1,:)./H(j).*(1+2.*(Kn(2,:)./H(j))))...
        .*Comp(:,j)'./((1+(H(j)./Kp(1,:).*(1+H(j)./Kp(2,:))+Kn(1,:)./H(j).*(1+Kn(2,:)./H(j)))))...
        .*omega(3:NoComp+2)))+sig0;

    Cond2(j)                =-sum(-abs(Cb(:,j)).*F.*omega(3:NoComp+2)')+F*(H(j).*omega(1)+Kw./H(j).*omega(2));

    % calcuate debye length (cm)
    kappa1(j)=sqrt(ee0*rt./(2*F^2 ...
        .*sum(((H(j)./Kp(1,:)).*(1+4*(H(j)./Kp(2,:)))...
        +Kn(1,:)./H(j).*(1+4*(Kn(2,:)./H(j))))...
        .*Comp(:,j)'./((1+(H(j)./Kp(1,:).*(1+H(j)./Kp(2,:))...
        +Kn(1,:)./H(j).*(1+Kn(2,:)./H(j))))))));
    % calculate electic field (V/cm)
end % for

for j=1:Nogrid+1
    for i=       1:NoComp
        % Compute the average charge concentration for every species as a function of Kn, Kp and ph
        Cb(i,j)= ((H(j)/Kp(1,i))*(1+2*(H(j)/Kp(2,i)))...
            -Kn(1,i)/H(j)*(1+2*(Kn(2,i)/H(j))))...
            /((1+(H(j)/Kp(1,i)*(1+H(j)/Kp(2,i))+Kn(1,i)/H(j)*(1+Kn(2,i)/H(j)))))*Comp(i,j);
    end
    % use electroneutrality to calculate H
    % calculate pH (H is in mol/cm3, hence the )
    pH(j)=-log10(H(j)*1000);

    % calculate electic field (V/cm)
    delV(j) = curr/(Cond(j));

end     %all j

% integrate Conductivity over length of channel and use to calulate
% the current - % fixed !
if noflux2
    curr=Applied_Voltage.*(2*1/(sum(2./Cond(2:Nogrid)))./Axial; % curr is decoupeld from the endpoints for
this noflux bc
else
```

```
241
242         curr=Applied_Voltage.*(2*1/(1./Cond(1)+1./Cond(Nogrid+1)+sum(2./Cond(2:Nogrid)))./Axial;
243         %Applied_Voltage=curr./(2*1/(1./Cond(1)+1./Cond(Nogrid+1)+sum(2./Cond(2:Nogrid)))).*Axial;
244     end
245
246     % conservation equations
247     for  j = 2:Nogrid
248         for i=1:NoComp
249
250             % Spatial approximation for derivatives
251
252             Partial1_Eflux(i,j)       =       (curr/Cond(j+1)*Cb(i,j+1)...
253                 -curr/Cond(j-1)*Cb(i,j-1))...
254                 /(2*Axial);
255
256             Partial2_Comp(i,j)        = ( Comp(i,j+1) - 2*Comp(i,j) + Comp(i,j-1) ) / ( Axial^2 ) ;
257             DComp(i,j) = (omega(i+2)*rt/F) * Partial2_Comp(i,j)-Partial1_Eflux(i,j)*omega(i+2);
258
259         end % for i
260         % conservation equations
261
262         %%%%%%%%  BSA equations %%%%%%%%
263         % rational fit for the titration curve of BSA at zero ionic strength -EXPLODES at pH<2
264         %    zm(:)            =       (rat1(1)*(pH(:))^4+rat1(2)*(pH(:))^3+rat1(3)*(pH(:))^2
265         %                                +rat1(4)*(pH(:))+rat1(5))
266         %                            /((pH(:))^3+rat2(1)*(pH(:))^2+rat2(2)*(pH(:))+rat2(3));
267
268         % re-fitted rational fit for the titration curve of BSA at zero ionic strength
269         zm(:)                =       (rat1(1)*(pH(:)).^5+rat1(2)*(pH(:)).^4+rat1(3)*(pH(:)).^3+...
270             rat1(4)*(pH(:)).^2+rat1(5)*(pH(:))+rat1(6))...
271             ./((pH(:)).^2+rat2(1)*(pH(:))+rat2(2));
272
273
274         % zeta potential as calculated by Debye-Huckel-Henry
275         %(factor of 10000 converts Joules to cm2-kg/s2)
276         zeta         =       10000*zm(:)*q./(4*pi*ee0*R*(1+R./kappa1(:))); % V
277         % henrys function approximation
278         fkr          =       2/3.*(1+0.5.*(1+2.5./(R./kappa1(:).*(1+2.*exp(-R./kappa1(:))))).^(-3));
279
280         % Spatial approximation for derivatives
281         Partial2_Comp_BSA(j)    = ( BSA(j+1) - 2*BSA(j) + BSA(j-1) ) /
282     ( Axial^2 )                              ;
283         Partial1_Eflux_BSA(j)   =     (curr/Cond(j+1)*ee0*zeta(j+1)*fkr(j+1)/mu*BSA(j+1)-curr/Cond(j-1)*ee0*zeta(j-
284     1)*fkr(j-1)/mu*BSA(j-1))/(2*Axial);
285         DBSA(j) = D * Partial2_Comp_BSA(j)-Partial1_Eflux_BSA(j);
286     end % For j
287
288     if or(noflux,noflux2)
289         if ~noflux2
290             j=1;
291             Comp=noflux_bc(H,Comp,j,Kp,Kn,Kw,Nogrid,NoComp,curr,Axial,rt,F,omega,BSA,zm,rat1,rat2,use_findH);
292             [pH(j),H(j),Cb(:,j)]= calcpH(H(2),Comp(j),Kp,Kn,Kw,BSA,zm,0,rat1,rat2,use_findH);
293             Cond(j)=F*(H(j).*omega(1)+Kw./H(j).*omega(2)...
294                 +sum((H(j)./Kp(1,:)).*(1+2.*(H(j)./Kp(2,:)))...
295                 +Kn(1,:)./H(j).*(1+2.*(Kn(2,:)./H(j))))...
296                 .*Comp(:,j)'./((1+(H(j)./Kp(1,:).*(1+H(j)./Kp(2,:))+Kn(1,:)./H(j).*(1+Kn(2,:)./H(j)))))...
297                 .*omega(3:NoComp+2)))+sig0;
298
299             j=Nogrid+1;
300             Comp=noflux_bc(H,Comp,j,Kp,Kn,Kw,Nogrid,NoComp,curr,Axial,rt,F,omega,BSA,zm,rat1,rat2,use_findH);
301             [pH(j),H(j),Cb(:,j)]= calcpH(H(j-1),Comp(j),Kp,Kn,Kw,BSA,zm,0,rat1,rat2,use_findH);
302             Cond(j)=F*(H(j).*omega(1)+Kw./H(j).*omega(2)...
303                 +sum((H(j)./Kp(1,:)).*(1+2.*(H(j)./Kp(2,:)))...
304                 +Kn(1,:)./H(j).*(1+2.*(Kn(2,:)./H(j))))...
305                 .*Comp(:,j)'./((1+(H(j)./Kp(1,:).*(1+H(j)./Kp(2,:))+Kn(1,:)./H(j).*(1+Kn(2,:)./H(j)))))...
306                 .*omega(3:NoComp+2)))+sig0;
307
308             Partial2_Comp(:,1)          =      0               ;
309             Partial1_Eflux(:,1)                =       (curr/Cond(2)*Cb(:,2)...
310                 -curr/Cond(1)*Cb(:,1))...
311                 /(Axial);
312
313             Partial2_Comp(:,Nogrid+1)          =       0                ;
314             Partial1_Eflux(:,Nogrid+1)=        (curr/Cond(Nogrid+1)*Cb(:,Nogrid+1)...
315                 -curr/Cond(Nogrid)*Cb(:,Nogrid))...
316                 /(Axial);
317         else
318             curr=Applied_Voltage.*(2*1/(sum(2./Cond(2:Nogrid)))./Axial;
319             j=1;
320             Comp(:,1)=-1/3*((2*Axial)*F/rt*curr/Cond(2).*Cb(:,2)+Comp(:,3)-4*Comp(:,2)); %WHAT IT SHOULD BE:
321     Comp(:,1)=(4*Comp(:,2)-Comp(:,3))./3;
```

```
        [pH(j),H(j),Cb(:,j)]= calcpH(H(2),Comp(:,j),Kp,Kn,Kw,BSA,zm,0,rat1,rat2,use_findH);
        Cond(j)=F*(H(j).*omega(1)+Kw./H(j).*omega(2)...
            +sum(((H(j)./Kp(1,:)).*(1+2.*(H(j)./Kp(2,:)))...
            +Kn(1,:)./H(j).*(1+2.*(Kn(2,:)./H(j))))...
            .*Comp(:,j)'./((1+(H(j)./Kp(1,:).*(1+H(j)./Kp(2,:))+Kn(1,:)./H(j).*(1+Kn(2,:)./H(j)))))...
            .*omega(3:NoComp+2)))+sig0;
        j=Nogrid+1;
        Comp(:,Nogrid+1)=1/3*((2*Axial)*F/rt*curr/Cond(Nogrid).*Cb(:,Nogrid)-Comp(:,Nogrid-
1)+4*Comp(i,Nogrid));%WHAT IT SHOULD BE: Comp(:,Nogrid+1)=(4*Comp(:,Nogrid)-Comp(:,Nogrid-1))./3;
        [pH(j),H(j),Cb(:,j)]= calcpH(H(j-1),Comp(:,j),Kp,Kn,Kw,BSA,zm,0,rat1,rat2,use_findH);
        Cond(j)=F*(H(j).*omega(1)+Kw./H(j).*omega(2)...
            +sum(((H(j)./Kp(1,:)).*(1+2.*(H(j)./Kp(2,:)))...
            +Kn(1,:)./H(j).*(1+2.*(Kn(2,:)./H(j))))...
            .*Comp(:,j)'./((1+(H(j)./Kp(1,:).*(1+H(j)./Kp(2,:))+Kn(1,:)./H(j).*(1+Kn(2,:)./H(j)))))...
            .*omega(3:NoComp+2)))+sig0;
        Partial2_Comp(:,1)          =      0               ;
        Partial1_Eflux(:,1)                =        (curr/Cond(2)*Cb(:,2)...
            -curr/Cond(1)*Cb(:,1))...
            /(Axial);

        Partial2_Comp(:,Nogrid+1)          =       0               ;
        Partial1_Eflux(:,Nogrid+1)=        (curr/Cond(Nogrid+1)*Cb(:,Nogrid+1)...
            -curr/Cond(Nogrid)*Cb(:,Nogrid))...
            /(Axial);


   % Boundary conditions
   % At z = 0
    BSA(:,1)=-1/3*((2*Axial)/D*curr/Cond(2).*ee0*zeta(2)*fkr(2)/(mu)*BSA(2)+BSA(3)-4*BSA(2));
 % ( 4*BSA(2)-3*BSA(1)-BSA(3)) / (2*Axial)*D       -curr/cond(2)*ee0*zeta(2)*fkr(2)/(mu)*BSA(2)= 0 ;

   % At z = 1
   BSA(Nogrid+1)=1/3*((2*Axial)/D*curr/Cond(Nogrid).*ee0*zeta(Nogrid)*fkr(Nogrid)/(mu)*BSA(Nogrid)-BSA(Nogrid-
1)+4*BSA(Nogrid));
%  ( -4*BSA(Nogrid)+3*BSA(Nogrid+1)+BSA(Nogrid-1)) / (2*Axial)*D     -
curr/cond(Nogrid)*ee0*zeta(Nogrid)*fkr(Nogrid)/(mu)*BSA(Nogrid)= 0 ;

                Partial1_Eflux_BSA(1)       =     (curr/cond(2)*ee0*zeta(2)*fkr(2)/(mu) ...
                                                        *BSA(2)...
                                                -curr/cond(1)*ee0*zeta(1)*fkr(1)/(mu)...
                                                        *BSA(1))...
                                                /(Axial);

        Partial2_Comp_BSA(Nogrid+1) = 0                                         ;
        Partial1_Eflux_BSA(Nogrid+1)= (curr/cond(Nogrid+1)*ee0*zeta(Nogrid+1)...
                                                        *fkr(Nogrid+1)/(mu)*BSA(Nogrid+1)...
                                                -curr/cond(Nogrid)*ee0*zeta(Nogrid)...
                                                        *fkr(Nogrid)/(mu)*BSA(Nogrid))...
                                                /(Axial);
    end %~if noflux2

else   %  if or(noflux,noflux2) is false

    for i=1:NoComp                %modified FOR MOSHER 1990
        % Boundary Conditions
        % At z = 0
        DComp(i,1) = (omega(i+2)*rt/F) * Partial2_Comp(i,1)-Partial1_Eflux(i,1)*omega(i+2);
        % Spatial approximation for derivatives
        Partial1_Eflux(i,1)        =       (curr/Cond(2)*Cb(i,2)...
            -curr/Cond(1)*Cb(i,1))...
            /(Axial);
        Partial2_Comp(i,1)         = ( Comp(i,3) - 2*Comp(i,2) + Comp(i,1) ) / ( Axial^2 ) ;   % a very sketchy
approximation
        % At z = 1
        DComp(i,Nogrid+1) = (omega(i+2)*rt/F) * Partial2_Comp(i,Nogrid+1)-
Partial1_Eflux(i,Nogrid+1)*omega(i+2);
        % Spatial approximation for derivatives
        Partial1_Eflux(i,Nogrid+1)=        (curr/Cond(Nogrid+1)*Cb(i,Nogrid+1)...
            -curr/Cond(Nogrid)*Cb(i,Nogrid))...
            /(Axial);
        Partial2_Comp(i,Nogrid+1) = ( Comp(i,Nogrid+1) - 2*Comp(i,Nogrid) + Comp(i,Nogrid-1) ) / ( Axial^2 ) ;
    end % for i

end % if or(noflux,noflux2)


% UNIT CONFUSION:: A/cm2 * V-cm/A * coul/v-cm * V * cm-s/kg *mol/cm3 1/cm = V/cm *coul/cm *mol-s/kg-cm3 =
Joule-mol-s/cm4-kg = m2-mol/s-cm5 = 10000 mol/s-cm3

% NEUMAN BOUNDARY CONDITIONS changed FOR MOSHER 1990
```

```
% z=0
DBSA(1) = D * Partial2_Comp_BSA(1)-Partial1_Eflux_BSA(1);
% Spatial approximation for derivatives
Partial2_Comp_BSA(1)    =Partial2_Comp_BSA(2)   ;  % AGAIN,
Partial1_Eflux_BSA(1)   = (curr/Cond(2)*ee0*zeta(2)*fkr(2)/mu*BSA(2)-
curr/Cond(1)*ee0*zeta(1)*fkr(1)/mu*BSA(1))/(Axial);

% Z=1
DBSA(Nogrid+1) = D * Partial2_Comp_BSA(Nogrid+1)-Partial1_Eflux_BSA(Nogrid+1);
% Spatial approximation for derivatives
Partial2_Comp_BSA(Nogrid+1)    = Partial2_Comp_BSA(Nogrid)   ;      % AGAIN,
Partial1_Eflux_BSA(Nogrid+1)   =  (curr/Cond(Nogrid+1)*ee0*zeta(Nogrid+1)*fkr(Nogrid+1)/mu*BSA(Nogrid+1)-
curr/Cond(Nogrid)*ee0*zeta(Nogrid)*fkr(Nogrid)/mu*BSA(Nogrid))/(Axial);

save(['coief5_' num2str(Applied_Voltage*1000) 'mV_' date])
plot(Comp')
[so, me, mID]=copyfile('D:\MATLAB701\work\coief5.m','\\Kfjtrio\kfj_swap\Jacob\matlab mfiles\coief5.m');
mat2presets('coief5',['coief5_' num2str(Applied_Voltage*1000) 'mV_' date],runjac); % build presets file /and
run jacobian
return % coief

% ====================================================================
function [pH,H,Cb]=calcpH(Hguess,Comp,Kp,Kn,Kw,bsa,zm,Nogrid,rat1,rat2,use_findH)
op=optimset('tolfun',1e-38,'tolx',1e-38,'display','off');
H=zeros(1,Nogrid+1);
pH=-log10(Hguess*1000);
H=Hguess;
Cb=Comp;
for j=1 : Nogrid+1
    if use_findH
        [H(j) fval
exitout]=fminbnd(@findH,Hguess(j)*.000001,Hguess(j)*100000,op,Comp,Kw,Kp,Kn,j,zm,bsa,rat1,rat2);
    end % if use_findH
    pH(j)=-log10(H(j)*1000);
    disp([j, pH(j)*100 fval exitout toc])
    while fval>1 && fval<1000
        Hguess(j)=0.1*Hguess(j);
        [H(j) fval
exitout]=fminbnd(@findH,Hguess(j)*.00001,Hguess(j)*10000,op,Comp,Kw,Kp,Kn,j,zm,bsa,rat1,rat2);
        pH(j)=-log10(H(j)*1000);
        disp([j, pH(j)*100 fval exitout toc])
    end % while
    for i=       1 : size(Comp,1)
        % Compute the average charge concentration for every species as a function of Kn, Kp and ph
        Cb(i,j)= ((H(j)/Kp(1,i))*(1+2*(H(j)/Kp(2,i)))...
            -Kn(1,i)/H(j)*(1+2*(Kn(2,i)/H(j))))...
            /((1+(H(j)/Kp(1,i)*(1+H(j)/Kp(2,i))+Kn(1,i)/H(j)*(1+Kn(2,i)/H(j)))))*Comp(i,j);
    end
end
return

function obj=findH(H,Comp,Kw,Kp,Kn,j,zm,bsa,rat1,rat2)
Cb=Comp;    % initialize

for i=  1 : size(Comp,1)
    % Compute the average charge concentration for every species as a function of Kn, Kp and ph
    Cb(i,j)=     ((H/Kp(1,i))*(1+2*(H/Kp(2,i)))...
        -Kn(1,i)/H*(1+2*(Kn(2,i)/H)))...
        /((1+(H/Kp(1,i)*(1+H/Kp(2,i))+Kn(1,i)/H*(1+Kn(2,i)/H)))*Comp(i,j);
end
pH=-log10(H*1000);
zm(:)            =       (rat1(1)*(pH(:)).^5+rat1(2)*(pH(:)).^4+rat1(3)*(pH(:)).^3+...
    rat1(4)*(pH(:)).^2+rat1(5)*(pH(:))+rat1(6))...
    ./((pH(:)).^2+rat2(1)*(pH(:))+rat2(2));

% use electroneutrality to calculate H
obj=1e10*(H-Kw/H+sum(Cb(:,j)))^2;%-zm*bsa(j))^2;

return

function Comp=noflux_bc(H,Comp,j,Kp,Kn,Kw,Nogrid,NoComp,curr,Axial,rt,F,omega,BSA,zm,rat1,rat2,use_findH)
op=odeset('RelTol',1e-6,'AbsTol',1e-9);
[t,C1]=ode15s(@odefun,[0,1000],Comp(:,j),op,j,H,Comp,Kp,Kn,Kw,Nogrid,NoComp,curr,Axial,rt,F,omega,BSA,zm,rat1,r
at2,use_findH);
Comp(:,j)=C1(end,:);
return

function DComp=odefun(t,C1,j,H,Comp,Kp,Kn,Kw,Nogrid,NoComp,curr,Axial,rt,F,omega,BSA,zm,rat1,rat2,use_findH)
Comp(:,j)=C1';
if j==1;
    [ppH,H(j),Cb(:,j)]= calcpH(H(1),Comp(:,j),Kp,Kn,Kw,BSA,zm,0,rat1,rat2,use_findH);
```

```
    Cond(j)=F*(H(j).*omega(1)+Kw./H(j).*omega(2)...
        +sum(((H(j)./Kp(1,:)).*(1+2.*(H(j)./Kp(2,:)))...
        +Kn(1,:)./H(j).*(1+2.*(Kn(2,:)./H(j))))...
        .*Comp(:,j)'./((1+(H(j)./Kp(1,:).*(1+H(j)./Kp(2,:))+Kn(1,:)./H(j).*(1+Kn(2,:)./H(j))))...
        .*omega(3:NoComp+2)));
    DComp=(( Comp(:,j+1) - Comp(:,j)) / Axial*rt/F-curr/Cond(j).*Cb(:,j));
elseif j==Nogrid+1
    [ppH,H(j),Cb(:,j)]= calcpH(H(j),Comp(:,j),Kp,Kn,Kw,BSA,zm,0,rat1,rat2,use_findH);
    if min2(Comp)<0
        ppH
    end
    Cond(j)=F*(H(j).*omega(1)+Kw./H(j).*omega(2)...
        +sum(((H(j)./Kp(1,:)).*(1+2.*(H(j)./Kp(2,:)))...
        +Kn(1,:)./H(j).*(1+2.*(Kn(2,:)./H(j))))...
        .*Comp(:,j)'./((1+(H(j)./Kp(1,:).*(1+H(j)./Kp(2,:))+Kn(1,:)./H(j).*(1+Kn(2,:)./H(j))))...
        .*omega(3:NoComp+2)));
    DComp= -(( Comp(:,Nogrid+1) - Comp(:,Nogrid)) / Axial*rt/F -curr/Cond(Nogrid+1)*Cb(:,Nogrid+1));
end % if j=1
return

function mat2presets(llamo,loadme,runjac)
%%%%%%%%%%%%%%%%%%%%%%%%%%%%%%%%%%%
%% special case of loading ICs simulated in coief.m or similar matlab code
%%%%%%%%%%%%%%%%%%%%%%%%%%%%%%%%%%%

if nargin==0
    runjac=true;       % command to actually run jacobian
    loadme='mao2000data_07-Sep-2006.mat';
    llamo='mao2000'; % name of jacobian model folder
end
%%
%%
tic

dir=['D:\Program Files\Jacobian\Models\' llamo '\input\'];
masterfield='FS.AMPHY'; % structure heading to use
file=[llamo '_INIT'];   % name of presets file
fid3=fopen([dir file 'CD.PRESETS'],'w');
    preset_var_names={'pH','Cond','curr','Cb','Partial1_Eflux','Partial2_Comp',...
        'delV','Comp','H','BSA','fkr','kappa1','zm','zeta','Partial1_Eflux_BSA','Partial2_Comp_BSA'};
    disp('DONE! Loading coiefdata...')
    load(loadme)

    newvar=0;
        for i=1:length(preset_var_names);
            try
            newvar=newvar+(numel(eval(preset_var_names{i})));
            catch
            end
        end

    q=1;
        for j=1:length(preset_var_names)

if exist(char(preset_var_names{j}),'var')

         matpoints=eval(preset_var_names{j}); % read in  data
         if min(size(matpoints))==1 && size(matpoints,2)==1;
             matpoints=matpoints';  % rotate if the 1D array is not the right orientation
         end
        for l=1:size(matpoints,1)       % over all components
         %       disp(['building ' char(preset_var_names{j}) ' point ' num2str(l)])
               for ii=1:size(matpoints,2)  % over all spactial points
                   if and(size(matpoints,2)==1,size(matpoints,1)==1);  % for single value variables i.e. CURR
                     %  Q{1}(q)=cellstr([masterfield '.' char(preset_var_names(j)) ' ']);
                     %  Q{3}(q)=matpoints;
                        fprintf(fid3,'%s\n',cell2mat([cellstr([masterfield '.' char(preset_var_names(j)) '
']))...
                            cellstr(':=') ...
                            cellstr(num2str(matpoints)) ...
                            cellstr(';') ...
                            cellstr('#') ...
                            cellstr(' ')]));
                       q=q+1;
                       break
                   elseif size(matpoints,1)==1;    %for spatial only varaibles like fkr and zeta
                    %   Q{1}(q)=cellstr([masterfield '.' char(preset_var_names(j)) '(' num2str(ii) ') ']);
                    %   Q{3}(q)=matpoints(ii);
                       fprintf(fid3,'%s\n',cell2mat([cellstr([masterfield '.' char(preset_var_names(j)) '('
num2str(ii) ') '])...
                            cellstr(':=')...
```

```
                                cellstr(num2str(matpoints(ii)))...
                                cellstr(';')...
                                cellstr('#')...
                                cellstr(' ')]));
                        else    % for 2-d variables like comp and cb
                          %  Q{1}(q)=cellstr([masterfield '.' char(preset_var_names(j)) '(' num2str(l) ','
num2str(ii) ') ']);
                           %   Q{3}(q)=matpoints(l,ii);
                                fprintf(fid3,'%s\n',cell2mat([cellstr([masterfield '.' char(preset_var_names(j))
'(' num2str(l) ',' num2str(ii) ') '])...
                                cellstr(':=')...
                                cellstr(num2str(matpoints(l,ii)))...
                                cellstr(';')...
                                cellstr('#')...
                                cellstr(' ')]));
                        end % if else
                        q=q+1;
                    end
                    disp([num2str((q/newvar)*100),' % Done after ', num2str(toc), ' seconds...',
num2str(toc*(newvar/q-1)), ' more!'])
            end   % l

end % if exists
            end% for preset var names
fclose(fid3);

disp('All Done!!')
newvar
if runjac
    disp('running jacoiban!')
    cd('D:\MATLAB701\work')
    dos(['cscript "' dir '"' llamo '.vbs &']); % wont work if screen is minimized or station is locked
end
```

# References


[1] J. Albrecht and K. F. Jensen, *Micro free-flow IEF enhanced by active cooling and functionalized gels*, Electrophoresis, 27 (2006), pp. 4960-4969.

[2] J. W. Albrecht, J. El-Ali and K. F. Jensen, *Cascaded Free-Flow Isoelectric Focusing for Improved Focusing Speed and Resolution*, Anal. Chem., 79 (2007), pp. 9364-9371.

[3] P.-A. Auroux, D. Iossifidis, D. R. Reyes and A. Manz, *Micro Total Analysis Systems. 2. Analytical Standard Operations and Applications*, Analytical Chemistry, 74 (2002), pp. 2637-2652.

[4] A. Ayala, J. Parrado and A. Machado, *Use of Rotofor preparative isoelectrofocusing cell in protein purification procedure*, Applied Biochemistry and Biotechnology, 69 (1998), pp. 11-16.

[5] H. E. Ayliffe, A. B. Frazier and R. D. Rabbitt, *Electric Impedance Spectroscopy Using Microchannels with Integrated Metal Electrodes*, IEEE Journal of Microelectromechanical Systems, 8 (1999), pp. 50-57.

[6] J. C. Baygents and F. Baldessari, *Electrohydrodynamic instability in a thin fluid layer with an electrical conductivity gradient*, Physics of Fluids, 10 (1998), pp. 301-311.

[7] J. N. Behnke, S. M. Dagher, T. H. Massey and W. C. Deal, Analytical Biochemistry, 69 (1975), pp. 1-9.

[8] M. Bier, R. A. Mosher and O. A. Paulinski, *Computer Simulation and Experimental Validation of Isoelectric Focusing in Ampholine-Free Systems*, Journal of Chromatography, 211 (1981), pp. 313-335.

[9] M. Bier, O. A. Paulinski, R. A. Mosher and D. A. Saville, *Electrophoresis: Mathematical Modeling and Computer Simulation*, Science, 219 (1983), pp. 1281-1287.

[10] U. Bilitewski, M. Genrich, S. Kadow and G. Mersal, *Biochemical analysis with microfluidic systems*, Analytical and Bioanalytical Chemistry, 377 (2003), pp. 556-569.

[11] J. S. Buch, Y. Li, F. Rosenberger, D. L. DeVoe and C. S. Lee, *Two-Dimensional Genomic and Proteomic Separations in a Plastic Microfluidic Network*, in M. A. Northrup, K. F. Jensen and J. D. Harrison, eds., *Proceedings of the 7th International Conference on Micro Total Analysis Systems*, Squaw Valley, CA, 2003, pp. 477-480.

[12] T. P. Burg, M. Godin, S. M. Knudsen, W. Shen, G. Carlson, J. S. Foster, K. Babcock and S. R. Manalis, *Weighing of biomolecules, single cells and single nanoparticles in fluid*, Nature, 446 (2007), pp. 1066-1069.

[13] T. P. Burg and S. R. Manalis, *Suspended microchannel resonators for biomolecular detection*, Applied Physics Letters, 83 (2003), pp. 2698-2700.

[14] T. P. Burg, A. R. Mirza, N. Milovic, C. H. Tsau, G. A. Popescu, J. S. Foster and S. R. Manalis, *Vacuum-packaged suspended microchannel resonant mass sensor for biomolecular detection*, Journal of Microelectromechanical Systems, 15 (2006), pp. 1466-1476.

[15] D. Burggraf, G. Weber and F. Lottspeich, *Free-Flow Isoelectric-Focusing of Human Cellular Lysates as Sample Preparation for Protein-Analysis*, Electrophoresis, 16 (1995), pp. 1010-1015.

[16] C. Cabrera, B. Finlayson and P. Yager, *Formation of Natural pH Gradients in a Microfluidic Device under Flow Conditions: Model and Experimental Validation*, Analytical Chemistry, 73 (2001), pp. 658-666.
[17] R. K. Cannan, A. Kibrick and A. H. Palmer, Annals of the New York Academy of Sciences, 41 (1941), pp. 243.
[18] M. Caron, N. Imam-Sghiouar, F. Poirier, J. P. Le Caer, V. Labas and R. Joubert-Caron, *Proteomic map and database of lymphoblastoid proteins*, Journal of Chromatography B-Analytical Technologies in the Biomedical and Life Sciences, 771 (2002), pp. 197-209.
[19] N. Catsimpoolas, ed., *Isoelectric Focusing*, Academic Press Inc., New York, 1976.
[20] N. Catsimpoolas, W. W. Yotis, A. L. Griffith and D. Rodbard, Archives of Biochemistry and Biophysics, 163 (1974), pp. 113-121.
[21] R. Y. Chein, Y. C. Yang and Y. S. Lin, *Estimation of Joule heating effect on temperature and pressure distribution in electrokinetic-driven microchannel flows*, Electrophoresis, 27 (2006), pp. 640-649.
[22] J. Chmelik, M. Deml and J. Janca, *Separation of 2 Components of Horse Myoglobin by Isoelectric-Focusing Field-Flow Fractionation*, Analytical Chemistry, 61 (1989), pp. 912-914.
[23] E. A. Cowles, N. Agrwal, R. L. Anderson and J. L. Wang, *Carbohydrate-Binding Protein-35 - Isoelectric Points of the Polypeptide and a Phosphorylated Derivative*, Journal of Biological Chemistry, 265 (1990), pp. 17706-17712.
[24] H. C. Cui, K. Horiuchi, P. Dutta and C. F. Ivory, *Multistage isoelectric focusing in a polymeric microfluidic chip*, Analytical Chemistry, 77 (2005), pp. 7878-7886.
[25] C. Das and Z. H. Fan, *Effects of separation length and voltage on isolectric focusing in a plastic microfluidic device*, Electrophoresis, 27 (2006), pp. 3619-3626.
[26] W. M. Deen, *Analysis of Transport Phenomena*, Oxford University Press, Oxford, 1998.
[27] A. Delgado, ed., *Interfacial Electrokinetics and Electrophoresis*, Marcel Dekker, New York, 2002.
[28] A. V. Delgado, E. Gonzalez-Caballero, R. J. Hunter, L. K. Koopal and J. Lyklema, *Measurement and interpretation of electrokinetic phenomena - (IUPAC technical report)*, Pure and Applied Chemistry, 77 (2005), pp. 1753-1805.
[29] M. M. Denn, *Process Fluid Mechanics*, Prentice-Hall, Englewood Cliffs, NJ, 1980.
[30] M. Dishon, G. H. Weiss and D. A. Yphantis, *Kinetics of Sedimentation in a Density Gradient*, Biopolymers, 10 (1971), pp. 2095-2110.
[31] V. Dolnik and K. M. Hutterer, *Capillary electrophoresis of proteins 1999-2001*, Electrophoresis, 22 (2001), pp. 4163-4178.
[32] V. Dolnik, S. R. Liu and S. Jovanovich, *Capillary electrophoresis on microchip*, Electrophoresis, 21 (2000), pp. 41-54.
[33] D. C. Duffy, J. C. McDonald, O. J. A. Schueller and G. M. Whitesides, *Rapid prototyping of microfluidic systems in poly(dimethylsiloxane)*, Analytical Chemistry, 70 (1998), pp. 4974-4984.
[34] J. El-Ali, P. K. Sorger and K. F. Jensen, *Cells on chips*, Nature, 442 (2006), pp. 403-411.
[35] S. B. Ficarro, M. L. McCleland, P. T. Stukenberg, D. J. Burke, M. M. Ross, J. Shabanowitz, D. F. Hunt and F. M. White, *Phosphoproteome analysis by mass spectrometry and its application to Saccharomyces cerevisiae*, Nature Biotechnology, 20 (2002), pp. 301-305.

[36] B. R. Fonslow and M. T. Bowser, *Free-flow electrophoresis on an anodic bonded glass microchip*, Analytical Chemistry, 77 (2005), pp. 5706-5710.
[37] J. K. Forwood and D. A. Jans, *Quantitative analysis of DNA-protein interactions using double-labeled native gel electrophoresis and fluorescence-based imaging*, Electrophoresis, 27 (2006), pp. 3166-3170.
[38] J. Fritz, E. B. Cooper, S. Gaudet, P. K. Sorger and S. R. Manalis, *Electronic detection of DNA by its intrinsic molecular charge*, Proceedings of the National Academy of Sciences of the United States of America, 99 (2002), pp. 14142-14146.
[39] S. Garbis, G. Lubec and M. Fountoulakis, *Limitations of current proteomics technologies*, Journal of Chromatography A, 1077 (2005), pp. 1-18.
[40] R. H. Garrett and C. M. Grisham, *Biochemistry*, Harcourt Brace & Company, Orlando, Florida, 1999.
[41] J. C. Giddings, *Concepts and Comparisons in Multidimensional Separation*, Journal of High Resolution Chromatography & Chromatography Communications, 10 (1987), pp. 319-323.
[42] J. C. Giddings, *Hyperlayer Field-Flow Fractionation*, Separation Science and Technology, 18 (1983), pp. 765-773.
[43] J. C. Giddings, *The Role of Lateral Diffusion as a Rate-Controlling Mechanisim in Chromatography*, J. Chromatogr., 5 (1961), pp. 46-60.
[44] J. C. Giddings, *Unified Separation Science*, Wiley, New York, 1991.
[45] D. Gioeli, S. B. Ficarro, J. J. Kwiek, D. Aaronson, M. Hancock, A. D. Catling, F. M. White, R. E. Christian, R. E. Settlage, J. Shabanowitz, D. F. Hunt and M. J. Weber, *Androgen receptor phosphorylation - Regulation and identification of the phosphorylation sites*, Journal of Biological Chemistry, 277 (2002), pp. 29304-29314.
[46] R. Hagedorn, T. Schnelle, T. Muller, I. Scholz, K. Lange and M. Reh, *Electrophoresis in gel channels*, Electrophoresis, 26 (2005), pp. 2495-2502.
[47] J. Han and A. K. Singh, *Rapid protein separations in ultra-short microchannels: microchip sodium dodecyl sulfate-polyacrylamide gel electrophoresis and isoelectric focusing*, Journal of Chromatography a, 1049 (2004), pp. 205-209.
[48] J. D. Harrison, K. Fluri, K. Seiler, Z. Fan, C. S. Effenhauser and A. Manz, *Micromachining a Miniaturized Capillary Electrophoresis-Based Chemical Analysis System on a Chip*, Science, 261 (1993), pp. 895-897.
[49] D. C. Henry, *Cataphoresis of Suspended Particles. Part I.-The Equation of Cataphoresis*, Proceedings of the Royal Society of London. Series A, 133 (1931), pp. 106-129.
[50] A. E. Herr, *Isoelectric Focusing for Multi-Dimensional Separations in Microfluidic Devices, Mechanical Engineering*, Stanford University, Stanford, CA, 2002, pp. 265.
[51] A. E. Herr, J. I. Molho, K. A. Drouvalakis, J. C. Mikkelsen, P. J. Utz, J. G. Santiago and T. W. Kenny, *On-Chip Coupling of Isoelectric Focusing and Free Solution Electrophoresis for Multidimensional Separations*, Analytical Chemistry, 75 (2003), pp. 1180-1187.
[52] A. E. Herr and A. K. Singh, *Photopolymerized cross-linked polyacrylamide gels for on-chip protein sizing*, Analytical Chemistry, 76 (2004), pp. 4727-4733.
[53] J. F. Hoburg, *Internal Electrohydrodynamic Instability of Liquids with Collinear Field and Conductivity Gradients*, Journal of Fluid Mechanics, 84 (1978), pp. 291-&.
[54] J. F. Hoburg and J. R. Melcher, *Electrohydrodynamic Mixing and Instability Induced by Colinear Fields and Conductivity Gradients*, Physics of Fluids, 20 (1977), pp. 903-911.

[55] J. F. Hoburg and J. R. Melcher, *Internal Electrohydrodynamic Instability and Mixing of Fluids with Orthogonal Field and Conductivity Gradients*, Journal of Fluid Mechanics, 73 (1976), pp. 333-&.

[56] P. Hoffmann, H. Ji, R. L. Moritz, L. M. Connolly, D. F. Frecklington, M. J. Layton, J. S. Eddes and R. J. Simpson, *Continuous free-flow electrophoresis separation of cytosolic proteins from the human colon carcinoma cell line LIM 1215: A non two-dimensional gel electrophoresis-based proteome analysis strategy*, Proteomics, 1 (2001), pp. 807-818.

[57] M. Horka, T. Willimann, M. Blum, P. Nording, Z. Friedl and K. Slais, *Capillary isoelectric focusing with UV-induced fluorescence detection*, Journal of Chromatography a, 916 (2001), pp. 65-71.

[58] P. H. Huang, A. Mukasa, R. Bonavia, R. A. Flynn, Z. E. Brewer, W. K. Cavenee, F. B. Furnari and F. M. White, *Quantitative analysis of EGFRvIII cellular signaling networks reveals a combinatorial therapeutic strategy for glioblastoma*, Proceedings of the National Academy of Sciences of the United States of America, 104 (2007), pp. 12867-12872.

[59] S. C. Jacobson, C. T. Culbertson, J. E. Daler and J. M. Ramsey, *Microchip Structures for Submillisecond Electrophoresis*, Analytical Chemistry, 70 (1998), pp. 3476-3480.

[60] D. Janasek, M. Schilling, J. Franzke and A. Manz, *Isotachophoresis in free-flow using a miniaturized device*, Analytical Chemistry, 78 (2006), pp. 3815-3819.

[61] J. Janca and J. Chmelik, *Focusing in Field-Flow Fractionation*, Analytical Chemistry, 56 (1984), pp. 2481-2484.

[62] K. A. Janes, J. G. Albeck, S. Gaudet, P. K. Sorger, D. A. Lauffenburger and M. B. Yaffe, *Systems model of signaling identifies a molecular basis set for cytokine-induced apoptosis*, Science, 310 (2005), pp. 1646-1653.

[63] G. M. Janini, T. P. Conrads, T. D. Veenstra and H. J. Issaq, *Development of a two-dimensional protein-peptide separation protocol for comprehensive proteome measurements*, Journal of Chromatography B, 787 (2003), pp. 43-51.

[64] P. K. Jensen, L. Pasa-Tolic, K. K. Peden, S. Martinovic, M. S. Lipton, G. A. Anderson, N. Tolic, K. K. Wong and R. D. Smith, *Mass spectrometric detection for capillary isoelectric focusing separations of complex protein mixtures*, Electrophoresis, 21 (2000), pp. 1372-1380.

[65] F. Kilar, *Recent applications of capillary isoelectric focusing*, Electrophoresis, 24 (2003), pp. 3908-3916.

[66] D. Kohlheyer, J. C. T. Eijkel, S. Schlautmann, A. vandenBerg and R. Schasfoort, *Microfluidic High-Resolution Free-Flow Isoelectric Focusing*, Anal. Chem., 79 (2007), pp. 8190-8198.

[67] D. B. Kohlheyer, Geert A. J.; Schlautmann, Stefan; Schasfoort, Richard B. M., *Free-flow zone electrophoresis and isoelectric focusing using a microfabricated glass device with ion permeable membranes*, Lab on a Chip, 6 (2006), pp. 374-380.

[68] A. Kolin, *Isoelectric Spectra and Mobility Spectra: A New Approach to Electrophoretic Separation*, Proceedings of the National Academy of Sciences, 41 (1955), pp. 101-110.

[69] J. Kraly, M. A. Fazal, R. M. Schoenherr, R. Bonn, M. M. Harwood, E. Turner, M. Jones and N. J. Dovichi, *Bioanalytical applications of capillary electrophoresis*, Analytical Chemistry, 78 (2006), pp. 4097-4110.

[70] L. Krivankova and P. Bocek, *Continuous free-flow electrophoresis*, Electrophoresis, 19 (1998), pp. 1064-1074.

[71] N. Kumar, A. Wolf-Yadlin, F. M. White and D. A. Lauffenburger, *Modeling HER2 effects on cell behavior from mass Spectrometry phosphotyrosine data*, Plos Computational Biology, 3 (2007), pp. 35-48.
[72] J. P. Landers, *Molecular Diagnostics on Electrophoretic Microchips*, Analytical Chemistry, 75 (2003), pp. 2919-2927.
[73] V. Levich, *Physicochemical Hydrodynamics*, Prentice Hall, 1963.
[74] D. R. Lide, ed., *Handbook of Chemistry and Physics*, Taylor and Francis, Boca Raton, FL, 2007.
[75] H. Lin, B. D. Storey, M. H. Oddy, C. H. Chen and J. G. Santiago, *Instability of electrokinetic microchannel flows with conductivity gradients*, Physics of Fluids, 16 (2004), pp. 1922-1935.
[76] K. Linderstrom-Lang and S. O. Nielsen, *Acid-Base Equilibria of Proteins*, in M. Bier, ed., *Electrophoresis: theory, methods, and applications.*, Academic Press, New York, 1959, pp. 85.
[77] Z. Liu, A. P. Drabovich, S. N. Krylov and J. Pawliszyn, *Dynamic kinetic capillary isoelectric focusing: A powerful tool for studying protein-DNA interactions*, Analytical Chemistry, 79 (2007), pp. 1097-1100.
[78] H. Lu, *Microfluidic Biomechanical and Electrical Devices for Rapid Analysis of Cells and Organelles*, *Chemical Engineering*, Massachusetts Institute of Technology, Cambridge, MA, 2003, pp. 145.
[79] H. Lu, S. Gaudet, M. A. Schmidt and K. F. Jensen, *A microfabricated device for subcellular organelle sorting*, Analytical Chemistry, 76 (2004), pp. 5705-5712.
[80] K. Macounova, C. Cabrera, M. R. Holl and P. Yager, *Generation of Natural pH Gradients in Microfluidic Channels for Use in Isoelectric Focusing*, Analytical Chemistry, 72 (2000), pp. 3745-3751.
[81] K. Macounova, C. R. Cabrera and P. Yager, *Concentration and separation of proteins in microfluidic channels on the basis of transverse IEF*, Analytical Chemistry, 73 (2001), pp. 1627-1633.
[82] Q. L. Mao, J. Pawliszyn and W. Thormann, *Dynamics of capillary isoelectric focusing in the absence of fluid flow: High resolution computer simulation and experimental validation with whole column optical imaging*, Analytical Chemistry, 72 (2000), pp. 5493-5502.
[83] S. E. Martin, J. Shabanowitz, D. F. Hunt and J. A. Marto, *Subfemtomole MS and MS/MS peptide sequence analysis using nano-HPLC micro-ESI Fourier transform ion cyclotron resonance mass spectrometry*, Analytical Chemistry, 72 (2000), pp. 4266-4274.
[84] T. C. Merkel, V. I. Bondar, K. Nagai, B. D. Freeman and I. Pinnau, *Gas sorption, diffusion, and permeation in poly(dimethylsiloxane)*, Journal of Polymer Science Part B-Polymer Physics, 38 (2000), pp. 415-434.
[85] P. E. Michel, F. Reymond, I. L. Arnaud, J. Josserand, H. H. Girault and J. S. Rossier, *Protein fractionation in a multicompartment device using Off-Gel (TM) isoelectric focusing*, Electrophoresis, 24 (2003), pp. 3-11.
[86] H. Mohr and A. Volkl, *Isolation of peroxisomal subpopulations from mouse liver by immune free-flow electrophoresis*, Electrophoresis, 23 (2002), pp. 2130-2137.
[87] R. A. Mosher, D. Dewey, W. Thormann, D. A. Saville and M. Bier, *Computer Simulation and Experimental Validation of the Electrophoretic Behavior of Proteins*, Analytical Chemistry, 61 (1989), pp. 362-366.

[88] R. A. Mosher, P. Gebauer, J. Caslavaska and W. Thormann, *Computer Simulation and Experimental Validation of the Electrophoretic Behavior of Proteins. 2. Model Improvement and Application to Isotachophoresis*, Analytical Chemistry, 64 (1992), pp. 2991-2997.

[89] R. A. Mosher and W. Thormann, *High-resolution computer simulation of the dynamics of isoelectric focusing using carrier ampholytes: The post-separation stabilizing phase revisited*, Electrophoresis, 23 (2002), pp. 1803-1814.

[90] R. A. Mosher, W. Thormann, R. Kuhn and H. Wagner, *Experimental and Theoretical Dynamics of Isoelectric Focusing*, Journal of Chromatography, 478 (1989), pp. 39-49.

[91] L. J. Nagels and I. Poels, *Solid state potentiometric detection systems for LC, CE, and microTAS methods*, Trends in Analytical Chemistry, 19 (2000), pp. 410-417.

[92] R. A. O'Neill, A. Bhamidipati, X. H. Bi, D. Deb-Basu, L. Cahill, J. Ferrante, E. Gentalen, M. Glazer, J. Gossett, K. Hacker, C. Kirby, J. Knittle, R. Loder, C. Mastroieni, M. MacLaren, T. Mills, U. Nguyen, N. Parker, A. Rice, D. Roach, D. Suich, D. Voehringer, K. Voss, J. Yang, T. Yang and P. B. Vander Horn, *Isoelectric focusing technology quantifies protein signaling in 25 cells*, Proceedings of the National Academy of Sciences of the United States of America, 103 (2006), pp. 16153-16158.

[93] H. Obara, A. Takayanagi, J. Hirahashi, K. Tanaka, G. Wakabayashi, K. Matsumoto, M. Shimazu, N. Shimizu and M. Kitajima, *Overexpression of truncated I kappa B alpha induces TNF-alpha-dependent apoptosis in human vascular smooth muscle cells*, Arteriosclerosis Thrombosis and Vascular Biology, 20 (2000), pp. 2198-2204.

[94] H. Ohshima, *A Simple Expression for Henrys Function for the Retardation Effect in Electrophoresis of Spherical Colloidal Particles*, Journal of Colloid and Interface Science, 168 (1994), pp. 269-271.

[95] D. R. Olander, *Simultaneous Mass Transfer and Equilibrium Chemical Reaction*, A.I.Ch.E. Journal, 6 (1960), pp. 233-239.

[96] C. Pasquali, I. Fialka and L. Huber, *Subcellular fractionation, electromigration analysis and mapping of organelles*, Journal of Chromatography B, 722 (1999), pp. 89-102.

[97] O. A. Paulinski, A. Graham, R. A. Mosher, M. Bier and D. A. Saville, *Theory of Electrophoretic Separations Part II: Construction of a Numerical Simulation Scheme and Its Applications*, AIChE Journal, 32 (1986), pp. 215-223.

[98] T. Rabilloud, *Two-dimensional gel electrophoresis in proteomics: Old, old fashioned, but it still climbs up the mountains*, Proteomics, 2 (2002), pp. 3-10.

[99] D. E. Raymond, A. Manz and H. M. Widmer, *Continuous Sample Pretreatment Using a Free-Flow Electrophoresis Device Integrated onto a Silicon Chip*, Analytical Chemistry, 66 (1994), pp. 2858-2865.

[100] P. Reschiglian, A. Zattoni, B. Roda, E. Michelini and A. Roda, *Field-flow fractionation and biotechnology*, Trends in Biotechnology, 23 (2005), pp. 475-483.

[101] D. R. Reyes, D. Iossifidis, P.-A. Auroux and A. Manz, *Micro Total Analysis Systems. 1. Introduction, Theory, and Technology*, Analytical Chemistry, 74 (2002), pp. 2623-2636.

[102] P. H. Rhodes, R. S. Snyder and G. O. Roberts, *Electrohydrodynamic Distortion of Sample Streams in Continuous-Flow Electrophoresis*, Journal of Colloid and Interface Science, 129 (1989), pp. 78-90.

[103] P. G. Righetti, *Isoelectric Focusing: Theory, Methodology and Applications*, Elsevier, Amsterdam, 1983.

[104] H. Rilbe, *Historical and Theoretical Aspects of Isoelectric Focusing*, Annals of the New York Academy of Sciences, 209 (1973), pp. 11-22.
[105] A. Ros, M. Faupel, H. Mees, J. van Oostrum, R. Ferrigno, F. Reymond, P. Michel, J. S. Rossier and H. H. Girault, *Protein purification by Off-Gel electrophoresis*, Proteomics, 2 (2002), pp. 151-156.
[106] O. A. Saleh and L. L. Sohn, *Direct detection of antibody-antigen binding using an on-chip artificial pore*, Proceedings of the National Academy of Sciences of the United States of America, 100 (2003), pp. 820-824.
[107] D. A. Saville and O. A. Paulinski, *Theory of Electrophoretic Separations, Part I: Formulation of a Mathematical Model*, AIChE Journal, 32 (1986), pp. 207-214.
[108] Y. F. Shen, S. J. Berger and R. D. Smith, *High-efficiency capillary isoelectric focusing of protein complexes from Escherichia coli cytosolic extracts*, Journal of Chromatography A, 914 (2001), pp. 257-264.
[109] Y. F. Shen, R. Zhao, M. E. Belov, T. P. Conrads, G. A. Anderson, K. Q. Tang, L. Pasa-Tolic, T. D. Veenstra, M. S. Lipton, H. R. Udseth and R. D. Smith, *Packed capillary reversed-phase liquid chromatography with high-performance electrospray ionization Fourier transform ion cyclotron resonance mass spectrometry for proteomics*, Analytical Chemistry, 73 (2001), pp. 1766-1775.
[110] K. Shimura, *Recent advances in capillary isoelectric focusing: 1997-2001*, Electrophoresis, 23 (2002), pp. 3847-3857.
[111] R. Sjoback, J. Nygren and M. Kubista, *Absorption and Fluorescence Properties of Fluorescein*, Spectrochimica Acta Part A-Molecular and Biomolecular Spectroscopy, 51 (1995), pp. L7-L21.
[112] K. Slais, *Electrophoretic Focusing in a Natural Steady-State Moving Ph Gradient*, Journal of Microcolumn Separations, 5 (1993), pp. 469-479.
[113] K. Slais, *Model of electrophoretic focusing in a natural pH gradient moving in a tapered capillary*, Journal of Chromatography A, 684 (1994), pp. 149-161.
[114] K. Slais and Z. Friedl, *Ampholytic Dyes for Spectroscopic Determination of Ph in Electrofocusing*, Journal of Chromatography a, 695 (1995), pp. 113-122.
[115] K. Slais and Z. Friedl, *Low-Molecular-Mass Pi Markers for Isoelectric-Focusing*, Journal of Chromatography a, 661 (1994), pp. 249-256.
[116] Y. A. Song, S. Hsu, A. L. Stevens and J. Y. Han, *Continuous-flow pl-based sorting of proteins and peptides in a microfluidic chip using diffusion potential*, Analytical Chemistry, 78 (2006), pp. 3528-3536.
[117] B. D. Spangler and E. M. Westbrook, *Crystallization of Isoelectrically Homogeneous Cholera-Toxin*, Biochemistry, 28 (1989), pp. 1333-1340.
[118] H. Svensson, *Isoelectric Fractionation, Analysis, and Characterization of Ampholytes in Natural pH Gradients. I. The Differential Equation of Solute Concentrations at a Steady State and its Solution for Simple Cases*, Acta Chemica Scandinavica, 15 (1961), pp. 325-341.
[119] W. Tan, Z. H. Fan, C. X. Qiu, A. J. Ricco and I. Gibbons, *Miniaturized capillary isoelectric focusing in plastic microfluidic devices*, Electrophoresis, 23 (2002), pp. 3638-3645.
[120] G. I. Taylor and A. D. McEwan, *The stability of a horizontal fluid interface in a vertical electric field*, J. Fluid Mech., 22 (1965), pp. 1-15.

[121] W. Thormann, M. A. Firestone, M. L. Dietz, T. Cecconie and R. A. Mosher, *Focusing Counterparts of Electrical-Field Flow Fractionation and Capillary Zone Electrophoresis - Electrical Hyperlayer Field Flow Fractionation and Capillary Isoelectric-Focusing*, Journal of Chromatography, 461 (1989), pp. 95-101.

[122] W. Thormann, T. M. Huang, J. Pawliszyn and R. A. Mosher, *High-resolution computer simulation of the dynamics of isoelectric focusing of proteins*, Electrophoresis, 25 (2004), pp. 324-337.

[123] W. Thormann and R. A. Mosher, *High-resolution computer simulation of the dynamics of isoelectric focusing using carrier ampholytes: Focusing with concurrent electrophoretic mobilization is an isotachophoretic process*, Electrophoresis, 27 (2006), pp. 968-983.

[124] W. Thormann, C. X. Zhang, J. Caslavska, P. Gebauer and R. A. Mosher, *Modeling of the impact of ionic strength on the electroosmotic flow in capillary electrophoresis with uniform and discontinuous buffer systems*, Analytical Chemistry, 70 (1998), pp. 549-562.

[125] O. Vesterberg and H. Svensson, *Isoelectric fractionation, analysis, and characterization of ampholytes in natural pH gradients. IV. Further studies on the resolving power in connection with separation of myoglobins.h*, Acta Chemica Scandinavica, 20 (1966), pp. 820-834.

[126] A. Volkl, H. Mohr, G. Weber and H. D. Fahimi, *Isolation of peroxisome subpopulations from rat liver by means of immune free-flow electrophoresis*, Electrophoresis, 19 (1998), pp. 1140-1144.

[127] D. B. Wall, M. Kachman, S. Gong, R. Hinderer, S. Parus, D. E. Misek, S. M. Hanash and D. M. Lubman, *Isoelectric Focusing Nonporous RP HPLC: A Two-Dimensional Liquid-Phase Separation Method for Mapping of Cellular Proteins with Identification Using MALDI-TOF Mass Spectrometry*, Analytical Chemistry, 72 (2000), pp. 1099-1111.

[128] G. Weber and P. Bocek, *Optimized continuous flow electrophoresis*, Electrophoresis, 17 (1996), pp. 1906-1910.

[129] G. Weber and P. Bocek, *Optimized continuous flow electrophoresis*, Electrophoresis, 17 (1996), pp. 1906-1910.

[130] G. Weiss, N. Catsimpoolas and D. Rodbard, *Transient State Isoelectric Focusing: Theory*, Archives of Biochemistry and Biophysics, 163 (1974), pp. 106-112.

[131] D. P. Wu, Y. Luo, X. M. Zhou, Z. P. Dai and B. C. Lin, *Multilayer poly(vinyl alcohol)-adsorbed coating on poly(dimethylsiloxane) microfluidic chips for biopolymer separation*, Electrophoresis, 26 (2005), pp. 211-218.

[132] D. Q. Xiao, T. Van Le and M. J. Wirth, *Surface modification of the channels of poly(dimethylsiloxane) microfluidic chips with polyacrylamide for fast electrophoretic separations of proteins*, Analytical Chemistry, 76 (2004), pp. 2055-2061.

[133] Y. Xu, C. X. Zhang, D. Janasek and A. Manz, *Sub-second isoelectric focusing in free flow using a microfluidic device*, Lab on a Chip, 3 (2003), pp. 224-227.

[134] N. F. Yin, K. Killeen, R. Brennen, D. Sobek, M. Werlich and T. V. van de Goor, *Microfluidic chip for peptide analysis with an integrated HPLC column, sample enrichment column, and nanoelectrospray tip*, Analytical Chemistry, 77 (2005), pp. 527-533.

[135] A. L. Zarling, S. B. Ficarro, F. M. White, J. Shabanowitz, D. F. Hunt and V. H. Engelhard, *Phosphorylated peptides are naturally processed and presented by major histocompatibility complex class I molecules in vivo*, Journal of Experimental Medicine, 192 (2000), pp. 1755-1762.

[136] C. X. Zhang and A. Manz, *High-speed free-flow electrophoresis on chip*, Analytical Chemistry, 75 (2003), pp. 5759-5766.

[137] Y. Zhang, A. Wolf-Yadlin, P. L. Ross, D. J. Pappin, J. Rush, D. A. Lauffenburger and F. M. White, *Time-resolved mass spectrometry of tyrosine phosphorylation sites in the epidermal growth factor receptor signaling network reveals dynamic modules*, Molecular & Cellular Proteomics, 4 (2005), pp. 1240-1250.

[138] B. Zhao, Y. Li, H. L. Tong, Y. Q. Zhuo, L. Zhang, H. Shi and C. H. Chen, *Study on the reaction rate of sulfite oxidation with cobalt ion catalyst*, Chemical Engineering Science, 60 (2005), pp. 863-868.

[139] G. V. Zilberstein, E. M. Baskin and S. Bukshpan, *Parallel processing in the isoelectric focusing chip*, Electrophoresis, 24 (2003), pp. 3735-3744.

[140] H. Zischka, G. Weber, P. J. A. Weber, A. Posch, R. J. Braun, D. Buhringer, U. Schneider, M. Nissum, T. Neitinger, M. Ueffing and C. Eckerskorn, *Improved proteome analysis of Saccharomyces cerevisiae mitochondria by free-flow electrophoresis*, Proteomics, 3 (2003), pp. 906-916.